Imperial College London

Measuring Crack Initiation and Growth in the Presence of Large Strains using the Potential Drop Technique

A Thesis submitted for the Degree of Doctor of Philosophy

of Imperial College London

and

Diploma of Imperial College

by

Keith Michael Tarnowski

February 2016

Department of Mechanical Engineering
Imperial College London
SW7 2AZ

Declaration of Originality

Unless stated otherwise, the work contained in this thesis is that of the author, Keith Michael Tarnowski. All work pertaining to other authors has been referenced accordingly.

Copyright Declaration

Abstract

Accurate laboratory measurements of crack initiation and growth are of vital importance for characterising material behaviour for use in the residual life assessment of structural components. The Potential Drop (PD) technique is one of the most common methods of performing these measurements, but such measurements are also sensitive to large inelastic strains which are often erroneously interpreted as crack growth. Despite the maturity of the PD technique, the extent of these errors is not fully understood and the most appropriate method of suppressing them is unknown.

In this thesis typical errors in the measurement of crack extension due to large inelastic strains have been quantified experimentally. These errors depend on the PD configuration and in some cases the configurations recommended in the standards are susceptible to particularly large errors. Optimum configurations for common fracture specimens have been identified but despite these mitigating measures, when testing ductile materials, the errors due to strain remain large compared to other sources of error common to the PD technique.

A sequentially coupled structural-electrical FE modelling approach has been developed which is capable of predicting the influence of strain on PD. This provides a powerful tool for decoupling the effects of strain from crack extension. It has been used in conjunction with experimental measurements, performed using a novel low frequency ACPD system (which behaves in a quasi-DC manner), to develop procedures for accurately measuring crack initiation and growth during fracture toughness and creep crack growth testing. It is demonstrated that some of the common methods of interpreting PD measurements during these tests are not fit for purpose. The proposed method of interpreting creep crack growth data has been used to re-validate creep crack initiation prediction models provided in the R5 assessment procedure.

Acknowledgments

I would like to thank my academic supervisors Dr Davies and Professor Nikbin as well as my industrial supervisor Professor Dean for their guidance and support throughout the course of this research. Your knowledge and advice has been invaluable and greatly appreciated.

I would also like to thank Professor Webster and Professor Nagy for regular technical discussions and critical feedback as well as Dr Priyesh Kapadia, Dr Ali Mehmanparast and Dr Joe Corcoran for your views on numerous experimental and analytical aspects of this work. Additional thanks to Amit Choda and Tony Willis for your advice regarding the manufacture of various fixtures and specimens. I would also like to acknowledge the support I have received from EDF Energy Ltd. In particular I would like to thank Marc Chevalier, Louise Allport, Dave McLennon and Mike Spindler, all of whom have taken the time to provide the information and support necessary for me to complete this research.

Finally I would like to thank my family. Ruth for her constant support and encouragement throughout but especially during the long days and late nights towards the end, and May for always greeting me with a smile and not holding it against me if I didn't make it home for bath time!

Contents

List of Tables

List of Figures

Nomenclature

a	Instantaneous crack length
a_0	Initial crack length measurement
a_{ave}	Average crack length
a_{eff}	Effective crack length
a_{max_res}	Crack length predicted from V_{norm_res}
a_{remote}	Crack length predicted from V_{norm_remote}
a_p	Predicted instantaneous crack length
a_{pf}	Predicted final crack length
a_f	Final crack length
a_n	Normalising crack length
$\dot{a}$	Creep crack growth rate
$\dot{a}_0$	Initial crack growth rate
$\dot{a}_s$	Steady state crack growth rate
Δa	Increment of crack growth
Δa_b	Crack extension due to blunting
$\Delta a_{b\_FE\_disp}$	Crack extension due to blunting predicted from the FE displacement field
$\Delta a_{b\_FE\_PD}$	Crack extension due to blunting predicted from the FE electric potential field
Δa_{b_ASTM}	Crack extension due to blunting predicted from the ASTM E1820 blunting line
Δa_{b_ESIS}	Crack extension due to blunting predicted from the ESIS P2-92 blunting line
Δa_{b_ISO}	Crack extension due to blunting predicted from the ISO 12135 blunting line
Δa_i	Increment of crack growth associated with initiation (typically 0.2 mm)
Δa_{limit}	Validity limit of ASTM E1820
Δa_{min}	Validity limit of ASTM E1820
Δa_{remote}	Remote reference error in the crack extension measurement
Δa_{res}	Resolution of crack extension measurement
A	Creep power-law coefficient
A_0, A_1, A_2, A_3	Potential drop correlation curve coefficients
A_A	Average creep power-law coefficient
A_c	Crack area
A_{eff}	Effective area
B	Specimen thickness
B_N	Net specimen thickness (between side-grooves)
B_e	Effective specimen thickness
B_r	Creep rupture power-law coefficient

c	Characteristic length of a specimen
C	Primary + secondary creep law coefficient
C_1	Primary + secondary creep law coefficient
C_2	Primary + secondary creep law time exponent
C_3	Primary + secondary creep law coefficient
C_{LL}	Elastic unloading compliance
$C(t)$	Transient creep crack tip characterising parameter
C^*	Steady state creep crack tip characterising parameter
d	Distance directly ahead of a crack or notch
d_N	Non-dimensional constant used to relate J and δ
d_N^*	Non-dimensional constant used to relate J and δ
D_N	Non-dimensional constant used to relate J and δ
D	Coefficient in power-law correlation between creep crack growth rate and C^*
E	Young's modulus
$\overline{E}$	$= 3E/\left(2(1+\nu)\right)$
E'	Effective Young's Modulus
f	Frequency
f_i	Original area fraction of cavities
$f_{ij}(\theta)$	Linear elastic crack tip stress variation
$g_{ij}(\theta,\nu)$	Linear elastic crack tip strain variation
G	Strain energy release rate
G_C	Critical strain energy release rate
G_{IC}	Critical strain energy release rate for mode I loading
h_1	Non-dimensional geometric function
H	Non-dimensional function of N or n
H	Coefficient in power-law correlation between creep toughness and time
I	Electrical current
I_n	Non-dimensional function of n
I_N	Non-dimensional function of N
j	Exponent in power-law correlation between creep toughness and time
J	Elastic-plastic crack tip characterising parameter
J_{max}	Validity limit of ASTM E1820
J_{limit}	Validity limit of ASTM E1820
J_C	Elastic-plastic fracture toughness
J_{IC}	Elastic-plastic fracture toughness for mode I loading
J_0	Elastic-plastic crack tip characterising parameter at time zero.

$J_{0.2}$	Elastic-plastic fracture toughness corresponding to 0.2 mm of crack extension
J_R	Resistance to stable tearing
J^e	Elastic component of J
J^p	Plastic component of J
k_t	Linear elastic stress concentration factor
K	Linear elastic stress intensity factor
K_r	Measure of the proximity to failure of a defected body by fracture
K_{sg}	Strain gauge total gauge factor
K_m	Strain gauge material gauge factor
K_g	Strain gauge geometric gauge factor
K_C	Critical stress intensity factor
K_{IC}	Critical stress intensity factor for Mode I loading
K_{mat}	Fracture toughness
K^c_{mat}	Creep toughness
L	Specimen length (or half length)
L_r	Measure of the proximity to failure of a defected body by plastic collapse (or creep rupture)
$L_r^{\max}$	Maximum value of L_r at the cut-off point in FAD and TDFAD
m	Non-dimensional constant used to relate J and δ
n	Creep power-law stress exponent
n_1	Primary + secondary creep law stress exponent
n_3	Primary + secondary creep law stress exponent
n_A	Average creep power-law stress exponent
N	Power-law hardening stress exponent
P	Load
P_0	Normalising load based on σ_0
P_L	Limit Load
P_{p0}	Normalising load based on σ_{p0}
q	Exponent in power-law correlation between initiation time and C^*
r	Radial distance from crack tip
r_c	Creep process zone size
r_p	Plastic zone size (including stress redistribution)
r_y	Plastic zone size (excluding stress redistribution)
R	Instantaneous resistance measurement
ΔR	Change in resistance
R_0	Initial resistance measurement
R_f	Final resistance measurement

R'	Geometrical length scale
s	Length of crack tip contour Γ
t	Time
t_0	Time to the onset of crack growth
t_0^{ASTM}	Time to the onset of crack growth as predicted by the method of interpreting PD data in ASTM E1457-13
t_0^{MOD}	Time to the onset of crack growth as predicted by the proposed modified method of interpreting PD data
$t_{0.2}$	Time for 0.2 mm of crack extension
$t_{0.2}^{ASTM}$	Time for 0.2 mm of crack extension as predicted by the method of interpreting PD data in ASTM E1457-13
$t_{0.2}^{MOD}$	Time for 0.2 mm of crack extension as predicted by the proposed modified method of interpreting PD data
t_f	Time to failure
t_i	Initiation time
t_{fp}	Transition time from primary to secondary creep
t_r	Uni-axial time to creep rupture
$t_{r,ref}$	Uni-axial time to creep rupture at the reference stress
t_r^*	Multi-axial time to creep rupture
t_{red}	Stress redistribution time
t_T	Transition time from small scale creep to widespread creep conditions
T	Temperature
T_i	Traction vector
u_i	Displacement vector
$\dot{u}_i$	Displacement rate vector
U_c	Creep strain energy
U_e	Elastic strain energy
U_p	Plastic strain energy
U_T	Total strain energy
V	Instantaneous potential drop measurement
ΔV	Change in potential drop
V_0	Initial potential drop measurement
V_1	Instantaneous Potential drop measurement at location 1
V_2	Instantaneous Potential drop measurement at location 2
V_{10}	Initial potential drop measurement corresponding to V_1
V_{20}	Initial potential drop measurement corresponding to V_2
V_f	Final potential drop measurement
V_{noise}	Amplitude of the noise on the potential drop measurement

V_{norm}	Normalised potential drop measurement
V_{norm_max}	Maximum normalised potential drop measurement including noise
V_{norm_remote}	Normalised potential drop measurement including remote reference measurement
V_n	Normalising potential drop measurement
V_{ref}	Reference potential drop measurement
V_{ref0}	Initial reference potential drop measurement
V_{corr}	Corrected instantaneous potential drop measurement
w	Strain energy density
$\dot{w}$	Strain energy density rate
W	Specimen width (or half width)
W_s	Work required to form new fracture surfaces
x	Cartesian coordinate axis
y	Cartesian coordinate axis
Y	Shape function describing the geometry dependency of K
Z	Impedance
α	Power-law hardening coefficient
β	Constant in plastic zone size expression
γ	Coefficient in power-law correlation between initiation time and *C**
δ	Crack tip opening displacement
δ_C	Critical crack tip opening displacement
δ_0	Initial crack tip opening displacement
δ_i	Crack tip opening displacement at initiation
δ_s	Skin depth
Δ	Displacement
Δ^c	Creep component of displacement
Δ^e	Elastic component of displacement
Δ^p	Plastic component of displacement
Δ_{CMOD}	Crack mouth opening displacement
Δ_{LLD}	Load line displacement
ε	Strain
ε_d	Strain at a distance *d* ahead of a crack
ε_f	Uni-axial creep ductility
ε_f^*	Multi-axial creep ductility
ε_i^c	Creep strain at the initiation time and reference stress
ε_{p0}	Power-law hardening normalising strain
ε_{ref}	Strain at reference stress

ε^c	Creep component of strain
ε^e	Elastic component of strain
ε^p	Plastic component of strain
ε^p_{ref}	Plastic component of strain at the reference stress
ε^e_{ij}	Elastic strain tensor
ε_{ij}	Strain tensor
$\tilde{\varepsilon}_{ij}$	Non-dimensional strain tensor
$\overline{\varepsilon}$	Equivalent strain
$\overline{\varepsilon}_{nom}$	Nominal equivalent strain
$\overline{\varepsilon}_{\max}$	Maximum at a notch tip
$\overline{\varepsilon}^e_d$	The equivalent elastic strain at a distance *d* ahead of a crack
$\overline{\varepsilon}^p$	Equivalent plastic strain
$\dot{\varepsilon}$	Strain rate
$\dot{\varepsilon}^c$	Creep strain rate
$\dot{\varepsilon}^c_{ref}$	Creep strain rate at the reference stress
$\dot{\varepsilon}^c_{ij}$	Creep strain rate tensor
$\dot{\varepsilon}_0$	Creep power-law normalising strain rate
$\dot{\varepsilon}^c_A$	Average creep strain rate
$\dot{\varepsilon}^c_s$	Secondary (or minimum) creep strain rate
Γ	Crack tip contour
η	Factor relating *J* or *C** to load and displacement measurements
λ	Function in Cocks and Ashby void growth model
μ	Plane stress/strain parameter
μ	Magnetic permeability
ν	Poisson's ratio
ν_r	Stress exponent in a creep rupture power-law
Π	Potential energy in a cracked body due to the internal strain and external forces
ϕ	Exponent in power-law correlation between creep crack growth rate and *C**
θ	Angular position
ρ	Resistivity
$\Delta\rho$	Change in resistivity
ρ_0	Initial resistivity
σ	Stress
σ_1, σ_2, σ_3	Principal stress components (where $\sigma_1 > \sigma_2 > \sigma_3$)
σ_0	Creep power-law normalising stress
$\sigma_{0.2}$	0.2% proof stress

$\sigma_{0.2}^{c}$	Stress corresponding to 0.2% inelastic (creep and plastic) strain
σ_d	Stress at a distance *d* ahead of a crack
σ_f	Flow stress
σ_{ij}	Stress tensor
$\tilde{\sigma}_{ij}$	Non-dimensional stress tensor
σ_m	Mean or hydrostatic stress
σ_{p0}	Power-law hardening normalising stress
σ_r	Rupture stress
σ_{ref}	Reference stress
σ_u	Ultimate tensile stress
σ_y	Yield stress
$\bar{\sigma}$	Equivalent stress
$\bar{\sigma}_{nom}$	Nominal equivalent stress
$\bar{\sigma}_{\max}$	Maximum equivalent stress at a notch tip
$\bar{\sigma}_d^e$	Equivalent linear-elastic stress at a distance *d* ahead of a crack
∇	Laplacian
ACPD	Alternating Current Potential Drop
CCI	Creep Crack Initiation
CCG	Creep Crack Growth
CMOD	Crack Mouth Opening Displacement
COD	Crack Opening Displacement
CS(T)	C-shaped Tension
C(T)	Compact Tension
CTOD	Crack Tip Opening Displacement
DCPD	Direct Current Potential Drop
DC(T)	Disc-shaped Compact Tension
DEN(T)	Double Edge-Notched Tension
EPFM	Elastic-Plastic Fracture Mechanics
FAD	Failure Assessment Diagram
FE	Finite element analysis
HRR	Hutchinson-Rice-Rosengren elastic-plastic crack tip field solution
LEFM	Linear-Elastic Fracture Mechanics
LLD	Load Line Displacement
M(T)	Middle Tension
PD	Potential Drop
SEN(T)	Single Edge-Notched Tension
SEN(B)	Single Edge-Notched Bend

SSY	Small-Scale Yielding
SZH	Stretch Zone Height
SZW	Stretch Zone Width
$TDFAD$	Time-Dependent Failure Assessment Diagram
$TDFM$	Time-Dependent Fracture Mechanics

Chapter 1: Introduction

All metal structures contain defects as a result of manufacturing processes. In order to assess the residual life of a structure it is necessary to understand the initiation and growth behaviour of these defects. This is typically characterised under laboratory conditions where an artificial defect is introduced into a specimen and simplified loading conditions are applied. Data obtained from such tests is also used to validate analytical models for predicting crack initiation and growth in situations where empirical test data is not available. Accurate methods of measuring crack behaviour in the laboratory are therefore critical for the continued safe operation of existing structures.

One of the most common methods of measuring crack behaviour in the laboratory is the Potential Drop (PD) technique, primarily due to its versatility; it can be used to monitor a wide variety of crack growth mechanisms and can be implemented in hostile environments. Although this is a mature technique, some limitations have yet to be fully addressed. For applications such as fracture toughness and creep crack growth testing of ductile materials, large inelastic strains can influence the PD measurement and are often erroneously interpreted as crack growth. The extent of these errors is not fully understood and the most appropriate method of suppressing them is unknown. Also, the most common variant of the PD technique, Direct Current Potential Drop (DCPD), tends to be susceptible to electrical noise which can reduce the accuracy of the measurement of crack extension.

Recently a low frequency Alternating Current Potential Drop (ACPD) system, which behaves in a quasi-DC manner, has been developed for monitoring creep strains on plant. This system demonstrates reduced noise and increased thermal stability compared to a typical DCPD system. In addition, advances in Finite Element (FE) techniques permit computationally inexpensive analyses to be performed which may be used to predict the PD response due to strain. This work combines these two technologies to address the limitations of the PD technique identified above and provide recommendations for the measurement of crack initiation and growth during fracture toughness and creep crack growth testing of ductile materials. These recommendations have been implemented to assess the accuracy of the analytical Creep Crack Initiation (CCI) models included in the R5 high temperature structural integrity assessment procedure.

1.1 Objectives

The main objectives of this research are:

- Review methods of measuring crack initiation and growth suitable for room temperature and high temperature applications, in particular the PD technique.
- Quantify the errors associated with the PD technique due to large inelastic strains and identify their significance by comparing them to other typical sources of error.
- Develop numerical tools for predicting the influence of strain on PD measurements.
- Use these tools to develop experimental methods for accurately measuring crack initiation and growth during fracture toughness and Creep Crack Growth (CCG) testing of ductile materials.
- Use these experimental methods to assess the accuracy of the analytical CCI models included in the R5 assessment procedure.

1.2 Structure of the Thesis

Chapters 2 and 3 provide a review of the literature and concepts relevant to this research. Chapter 2 presents a review of fracture mechanics concepts including Linear-Elastic Fracture Mechanics (LEFM), Elastic-Plastic Fracture Mechanics (EPFM) and Time-Dependent Fracture Mechanics (TDFM). Analytical models for predicting CCI and Creep Crack Growth (CCG) are also included. Chapter 3 reviews experimental techniques used to measure crack extension. Only techniques which are suitable for both room temperature and high temperature applications are considered because this research is related to both.

Chapters 4 and 5 investigate the typical errors associated with the PD technique and ways to mitigate them. The influence of the PD configuration is assessed in Chapter 4 and optimum configurations are identified for Compact Tension, C(T), and Single Edge-Notched, SEN, specimen geometries. Errors associated with calibrating the PD measurement with a crack extension are quantified in Chapter 5. Consideration is also given to a possible unified calibration function for the most common fracture specimen geometries.

Chapter 6 presents the development and validation of an FE based tool for predicting the influence of strain on PD measurements. This tool and the experimental validation have been used to identify the significance of plastic strain on PD measurements in the absence of crack extension. These are compared to the other common sources of error identified in Chapters 4 and 5 and recommendations are provided regarding methods to limit the influence of strain on PD measurements.

The most appropriate method of interpreting PD data during fracture toughness testing of ductile materials is assessed in Chapter 7. A combination of empirical and finite element analysis has been used to critically assess the two main methods proposed in the literature and standards [1, 2]. Anecdotally observed limitations of the PD technique for this application are also investigated.

The most appropriate method of interpreting PD data during CCG testing of ductile materials is assessed in Chapter 8. A modified method of interpreting the data is proposed which is analogous to the method used for fracture toughness testing. Possible limitations of this method have been investigated using FE.

PD data from a series of CCG tests has been reinterpreted using the proposed new method in Chapter 9. The measured initiation times and the subsequent crack growth rates are compared to those obtained using the current method defined in ASTM E1457-13 [3]. The experimental measurements are also compared to the analytical CCI models included in the R5 assessment procedure [4] to assess the accuracy of these models.

A discussion of the results is presented in each individual chapter whilst overall conclusions are provided in Chapter 10. Recommendations for future work are also provided. All references are provided at the end of the thesis.

Chapter 2:

Review of Fracture Mechanics Concepts

2.1 Introduction

This chapter reviews the fundamental fracture mechanics concepts relevant to this research. The mechanisms associated with elastic, plastic and creep deformation are considered first, along with the associated material models. This is followed by a review of Linear-Elastic Fracture Mechanics (LEFM), Elastic-Plastic Fracture Mechanics (EPFM) and Time-Dependent Fracture Mechanics (TDFM). The chapter concludes with a review of the analytical Creep Crack Initiation (CCI) and Creep Crack Growth (CCG) models which are assessed towards the end of this thesis.

2.2 Deformation Mechanisms

When a tensile load is applied to a uniaxial specimen at high temperature it will deform. The resulting strain, ε, will be a combination of elastic strain, ε^e, plastic strain, ε^p, and creep strain, ε^c, as defined in Equation (2.1). The elastic and plastic strain components are generally independent of time whilst the creep strain is time dependent.

$$\varepsilon = \varepsilon^e + \varepsilon^p + \varepsilon^c \qquad \textbf{(2.1)}$$

A uniaxial, one dimensional, explanation of these different strain components is provided in the following sections. This is extended to multi-axial, three dimensional, conditions later in this chapter.

2.2.1 Elastic Deformation

Up to the elastic limit of the material, the time independent deformation is purely elastic. This is due to distortion of the atomic lattice and is fully recoverable. It is described by Equation (2.2) where σ is the applied stress and E is the Young's modulus of the material.

$$\varepsilon^e = \frac{\sigma}{E} \tag{2.2}$$

2.2.2 Plastic Deformation

Above the elastic limit, the time independent deformation consists of elastic and plastic strain where the plastic component is due to dislocations in the atomic lattice and is non-recoverable. Plastic strain is often represented by a power-law as defined in Equation (2.3) where N is the stress exponent, α is a material constant and σ_{p0} and ε_{p0} are the normalising stress and strain respectively. The normalising stress is typically the 0.2% proof stress, $\sigma_{0.2}$, (the stress corresponding to 0.2% plastic strain) which is often used to approximate the yield stress, σ_y, of the material. The normalising strain is the corresponding elastic strain calculated from Equation (2.2).

$$\frac{\varepsilon^p}{\varepsilon_{p0}} = \alpha\left(\frac{\sigma}{\sigma_{p0}}\right)^N \tag{2.3}$$

2.2.2.1 Ramberg-Osgood Material Model

The Ramberg-Osgood material model is often used to approximate the elastic-plastic tensile behaviour of a strain hardening material. This model combines Equations (2.2) and (2.3) to produce Equation (2.4):

$$\frac{\varepsilon}{\varepsilon_{p0}} = \frac{\sigma}{\sigma_{p0}} + \alpha\left(\frac{\sigma}{\sigma_{p0}}\right)^N \tag{2.4}$$

2.2.3 Creep Deformation

Time dependent creep is most significant at high temperatures. At low temperatures logarithmic creep can occur but only produces small strains and does not lead to eventual failure [5]. The temperature at which creep becomes significant is approximately 50% of the absolute melting point, although it varies with material [6].

There are two main mechanisms which control creep: dislocation movement and diffusion of atoms. At stresses too low for dislocations to occur, diffusion dominates the creep process which results in an approximately linear dependence of creep strain rate on stress [6]. At higher stresses, the generation and movement of dislocations dominate the creep process and results in a power-law dependence of the creep strain rate on stress [6]. This is known as dislocation or power-law creep. For a given material, applied stress and temperature, the dominant mechanism may be obtained from a deformation mechanism map. The following

research focuses on materials, loads and temperatures for which dislocation creep is the dominant mechanism so the following discussion focuses on power-law creep.

A typical uniaxial creep curve for a polycrystalline material is provided in Figure 2.1. It consists of three stages: Primary, Secondary and Tertiary. During the primary stage, the creep strain rate reduces due to the introduction of dislocations which strain hardens the material. This strain hardening is competing with thermal recovery processes which soften the material. When a balance is obtained between these two mechanisms, a constant creep rate occurs. This is known as secondary or steady-state creep. The final stage is tertiary creep where the strain rate accelerates due to microstructural and/or mechanical instability [5]. Sources of microstructural instability include grain growth, recrystalisation and coarsening of precipitate dispersion. Sources of mechanical instability include necking and the formation of micro-voids along grain boundaries which coalesce to form micro-cracks and eventually lead to inter-granular failure [6].

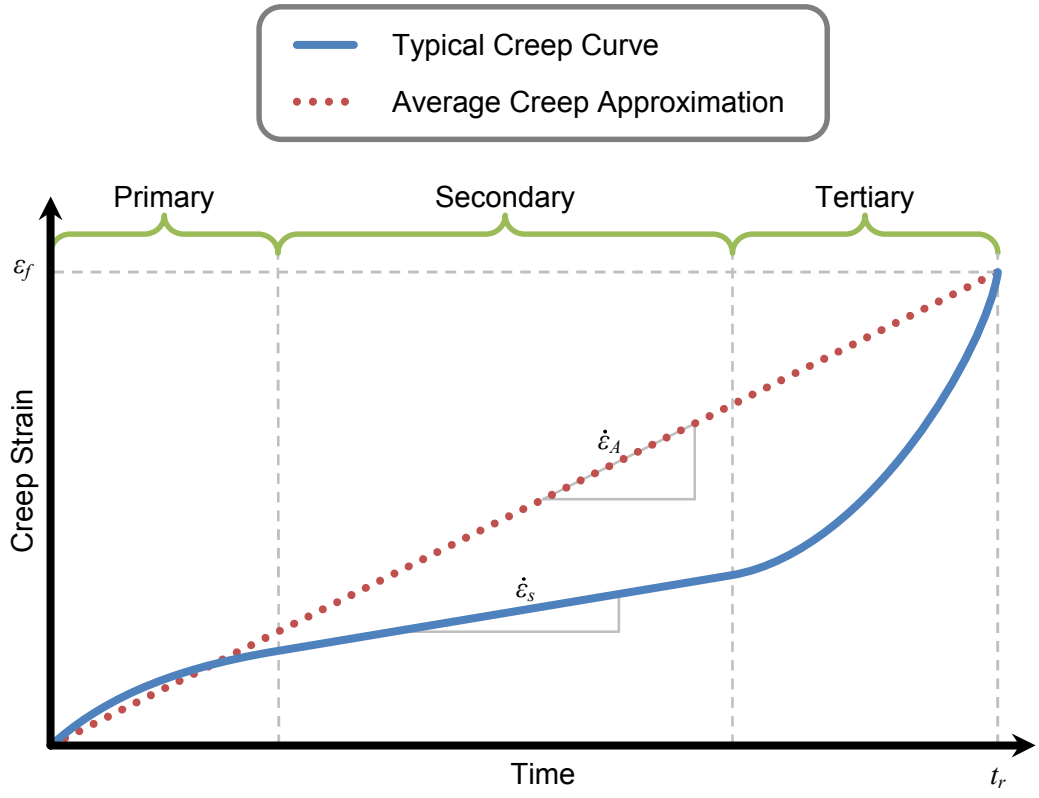

Figure 2.1: Typical uniaxial creep curve.

Uniaxial creep tests are typically performed at a constant temperature and a constant load but empirical creep laws required to assess the residual life of structural components must be applicable to wide range of temperatures and stresses. A significant number of tests are required to derive these creep laws.

2.2.3.1 Power-Law Creep

Power-law creep is so-called because of the power-law relationship between creep strain rate, $\dot{\varepsilon}^c$, and stress. A typical power-law relationship is provided in Equation (2.5) where n is the strain rate stress exponent, σ_0 is the normalising stress and $\dot{\varepsilon}_0$ is the normalising strain rate. The normalising stress and strain rate may alternatively be expressed as a temperature dependent material constant, A. The secondary creep strain rate, $\dot{\varepsilon}_s^c$, shown in Figure 2.1, is often related to the applied stress by a power-law relationship in the form of Equation (2.5).

$$\dot{\varepsilon}^c = \dot{\varepsilon}_0 \left(\frac{\sigma}{\sigma_0} \right)^n = A\sigma^n \tag{2.5}$$

The time to rupture, t_r, is also related to the applied stress by a power-law relationship. This is shown in Equation (2.6) where v_r is the stress rupture exponent and B_r is a temperature dependent material constant.

$$t_r = \frac{B_r}{\sigma^{v_r}} \tag{2.6}$$

2.2.3.2 Primary and Secondary Creep Laws

Power-law creep models have also been derived which include the different stages of creep. Equation (2.7) is an example of a primary and secondary creep law originally derived for austenitic Type 316LN stainless steel taken from the French nuclear design code RCC-MR [7].

$$\varepsilon^c = \begin{cases} C_1 t^{C_2} \sigma^{n_1} & t \le t_{fp} \\ C_1 t_{fp}{}^{C_2} \sigma^{n_1} + C\sigma^n \left(t - t_{fp} \right) & t > t_{fp} \end{cases} \tag{2.7}$$

The total creep strain, ε^c, is in mm/mm, time, t, is in hours, stress is in MPa and C_1, C_2, C, n_1 and n are material constants. The transition from primary to secondary creep occurs at time t_{fp}. This is the time at which the primary and secondary creep strain rates are equal and can be calculated from Equation (2.8) where constants C_3 and n_3 are calculated from Equations (2.9) and (2.10) respectively.

$$t_{fp} = C_3 \sigma^{n_3} \tag{2.8}$$

$$C_3 = \left(\frac{C}{C_1 C_2} \right)^{\frac{1}{C_2 - 1}} \quad \textbf{(2.9)}$$

$$n_3 = \frac{n - n_1}{C_2 - 1} \quad \textbf{(2.10)}$$

At times up to t_{fp} the total creep strain calculated from Equation (2.7) is due to primary creep only. At times greater than t_{fp} it is equal to the primary creep strain at the transition time plus a secondary creep component. This creep law is valid for creep strains up to 1% and temperatures up to 700ºC.

2.2.3.3 Average Creep Rate

To avoid complex creep laws which model the separate stages of creep, laws based on the average creep strain, $\dot{\varepsilon}_A^c$, shown in Figure 2.1, are often used. This is calculated from the creep ductility, ε_f, and the rupture time, t_r, as shown in Equation (2.11). It is often related to the applied stress by the power-law relationship, also shown in Equation (2.11), where n_A is the average stress exponent and A_A is a temperature dependent material constant.

$$\dot{\varepsilon}_A^c = \frac{\varepsilon_f}{t_r} = A_A \sigma^{n_A} \quad \textbf{(2.11)}$$

Equation (2.12) combines Equations (2.6) and (2.11). It demonstrates that an increase in stress results in an increase in creep ductility when $n_A > v_r$ and when $n_A = v_r$ it is independent of stress. These observations can be particularly useful when analysing creep ductility data, where experimental scatter can be significant, e.g. [8].

$$\varepsilon_f = A_A B_r \sigma^{(n_A - v_r)} \quad \textbf{(2.12)}$$

2.2.3.4 Variable Stress and Temperature

For an element of material at a constant stress and temperature the accumulated creep strain at a given time may be easily obtained from the creep laws presented above; however, the operating conditions of real components often result in fluctuating stresses and temperatures. To assess the residual life of such components, it is necessary to calculate the total accumulated creep strain for these complex operating conditions.

When the operating conditions change, the creep curve which describes the deformation behaviour will also change. In order to determine the location of an element of material on the creep curve for the new conditions it is necessary to use some parameter to capture the current 'state' of this element. The two most common parameters used are strain and time.

These are known as strain hardening and time hardening respectively and are shown schematically in Figure 2.2.

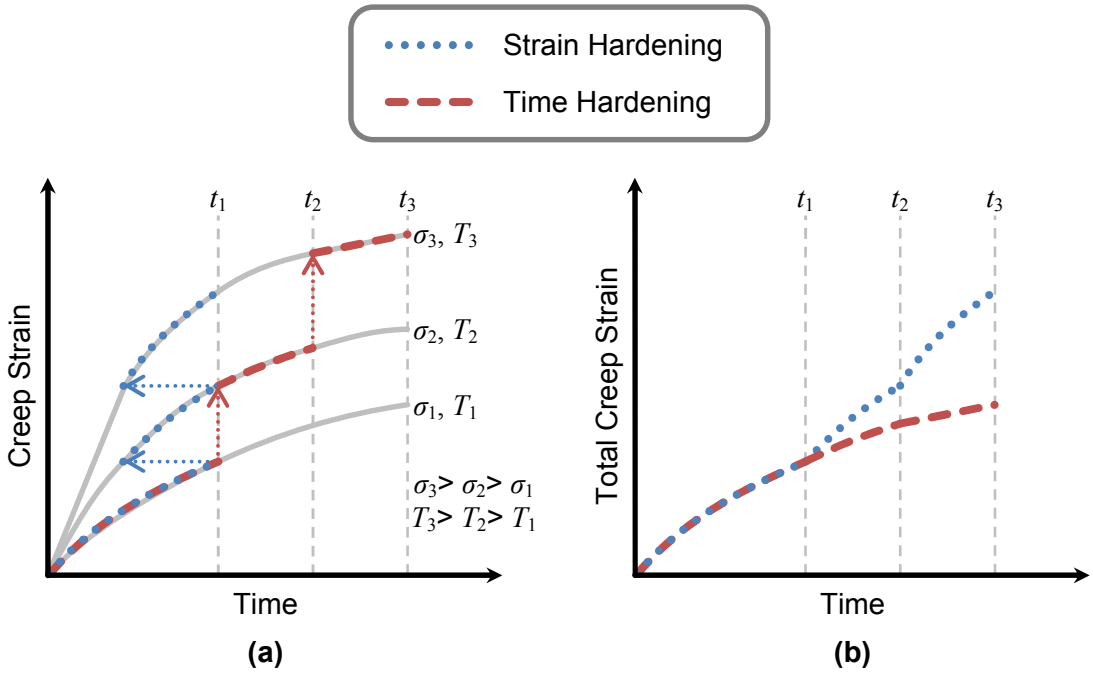

Figure 2.2: Accumulation of creep strain based on strain hardening and time hardening assumptions showing (a) instantaneous jumps between creep curves when the component conditions change, and (b) the total creep strain.

In Figure 2.2 the initial (primary) stage of three creep curves are shown corresponding to different operating conditions. In this example, the operating conditions change from condition 1 (σ_1, T_1), to condition 2 (σ_2, T_2), to condition 3 (σ_3, T_3) which represent progressively more onerous conditions. When the conditions change, the strain hardening law uses the current strain to characterise the 'state' of the material and the location on the new creep curve is obtained by moving horizontally in Figure 2.2(a). The time hardening law uses the total creep time to characterise the 'state' of the material and the location on the new creep curve is obtained by moving vertically in Figure 2.2(a). The strain hardening law and time hardening laws are demonstrated mathematically in Equations (2.13) and (2.14) respectively.

$$\dot{\varepsilon}^c = f\left(\sigma, T, \varepsilon^c\right) \tag{2.13}$$

$$\dot{\varepsilon}^c = f\left(\sigma, T, t\right) \tag{2.14}$$

Neither of these approaches is consistently conservative so the method of characterising the 'state' of the material should be selected with caution. The difference between the two depends on the shape of the creep curve and the stress and temperature history of the

component. In Figure 2.2, where the creep strain rate is reducing with time, and the changes in stress and temperature result in progressively more onerous conditions, the strain hardening law predicts a larger accumulated creep strain, as shown in Figure 2.2(b). If the creep strain rate was increasing with time (typical of tertiary creep) or the changes in stress and temperature resulted in less onerous conditions, the opposite would be true. For secondary creep, where the creep strain rate is constant, the two methods are identical.

2.2.4 Multi-axial Deformation

The constitutive relationships provided above are all derived from uniaxial tensile tests, but real components (and fracture specimens) tend to experience multi-axial stress states. For these complex stress states it is necessary to define an equivalent stress and an equivalent strain which may be compared to the uniaxial data. The von Mises yield criterion is the most common method used in fracture mechanics problems [9] although the Tresca yield criterion is also sometimes used. Both methods are presented here.

2.2.4.1 Von Mises Yield Criterion

The stresses experienced by an element of material can be separated into hydrostatic (or mean) and deviatoric components. An element of material which experiences only hydrostatic stress will experience a change in volume but not a change in shape, i.e. it will not plastically deform. This is because plasticity is driven by shear which results from deviatoric stresses [10]. The hydrostatic stress, σ_m, is the mean of the three principal stresses, σ_1, σ_2 and σ_3, as defined in Equation (2.15).

$$\sigma_m = \frac{\sigma_1 + \sigma_2 + \sigma_3}{3} \tag{2.15}$$

The deviatoric stresses in the three principal directions, σ'_1, σ'_2 and σ'_3, may be calculated from (2.16).

$$\begin{aligned} \sigma'_1 &= \sigma_1 - \sigma_m \\ \sigma'_2 &= \sigma_2 - \sigma_m \\ \sigma'_3 &= \sigma_3 - \sigma_m \end{aligned} \tag{2.16}$$

An element of material which experiences deviatoric stresses will experience shear and at some critical point, this will result in plastic deformation which occurs at constant volume, i.e. the effective Poisson's ratio, ν, is 0.5. The von Mises yield criterion states that an element of material will plastically deform when the shear strain energy attains a critical value.

Alternatively this may be stated as when the equivalent stress, $\bar{\sigma}$, defined by Equation (2.17), attains a critical value.

$$\bar{\sigma} = \frac{1}{\sqrt{2}}\left[\left(\sigma_1 - \sigma_2\right)^2 + \left(\sigma_2 - \sigma_3\right)^2 + \left(\sigma_3 - \sigma_1\right)^2\right]^{\frac{1}{2}} \quad \textbf{(2.17)}$$

In a uniaxial tensile test, where σ_2 = σ_3 = 0, Equation (2.17) reduces to Equation (2.18). The yield stress obtained from a uniaxial test is therefore this critical value of equivalent stress.

$$\bar{\sigma} = \sigma_1 \quad \textbf{(2.18)}$$

Using the von Mises definition of equivalent stress in Equation (2.17), it can be shown that the equivalent plastic strain, $\bar{\varepsilon}^p$ for a power-law hardening material may be defined by Equation (2.19). By comparing this to the uniaxial definition of plastic strain in Equation (2.3) it can be seen that a uniaxial stress-strain curve may also be applied to multi-axial conditions based on the von Mises definition of equivalent stress [9]. The same is also true for power-law creep properties derived from uniaxial creep tests.

$$\frac{\bar{\varepsilon}^p}{\varepsilon_{p0}} = \alpha\left(\frac{\bar{\sigma}}{\sigma_{p0}}\right)^N \quad \textbf{(2.19)}$$

2.2.4.2 Tresca Yield Criterion

The Tresca yield criterion states that plastic deformation will occur at a critical value of shear stress. The corresponding definition of equivalent stress is provided in Equation (2.20) assuming $\sigma_1 > \sigma_2 > \sigma_3$. For a uniaxial specimen, this again reduces to Equation (2.18), such that plastic deformation will occur when the equivalent stress is equal to the yield stress obtained from a uniaxial test.

$$\bar{\sigma} = \left|\sigma_1 - \sigma_3\right| \quad \textbf{(2.20)}$$

2.2.4.3 Flow Rule

To determine the deformed shape of an element of material in a multi-axial stress state a so-called flow rule is applied. A typical flow rule for metals assumes that the increment in plastic strain is proportional to the deviatoric stress in the same direction, i.e. the principal axes of plastic strain increment and deviatoric stress are coincident.

2.2.4.4 Multi-axial Creep Ductility

Creep rupture is often associated with the nucleation, growth and coalescence of voids forming along grain boundaries. The creep strain rate of a material is related to the

equivalent stress, whilst the rate of growth of these voids is also related to the ratio $\sigma_m/\bar{\sigma}$ [11]. This is often referred to as the triaxiality ratio and depends on the stress state of the material. The creep ductility of the material must therefore also depend on the stress state. Various models have been developed to capture this dependency e.g. [11, 12]. The one proposed by Cocks and Ashby [12] is often applied to Type 316H stainless steel [13-15] which is the main material considered in this research. This model is discussed here.

The multi-axial rupture time, t_r^*, for a power-law creeping material at a constant stress, due to the nucleation, growth and coalescence of evenly spaced voids along grain boundaries is given by Equation (2.21) [12]. In this equation t_n is the void nucleation time, f_i is the original area fraction of cavities and λ is defined by Equation (2.22). The multi-axial stress state is captured by the triaxiality ratio in Equation (2.22).

$$t_r^* = t_n + \frac{\lambda}{(n+1)\dot{\varepsilon}_s} ln\left(\frac{1}{(n+1)f_i}\right) \tag{2.21}$$

$$\lambda = \frac{1}{Sinh\left[2\frac{(n-1/2)}{(n+1/2)}\frac{\sigma_m}{\bar{\sigma}}\right]} \tag{2.22}$$

From equations (2.15) and (2.18) the triaxiality ratio is 1/3 under uniaxial conditions so the ratio of the uniaxial rupture time and multi-axial rupture time may be obtained from Equation (2.23) assuming that the void nucleation time is negligible.

$$\frac{t_r^*}{t_r} = \frac{Sinh\left[\frac{2(n-1/2)}{(n+1/2)}\frac{1}{3}\right]}{Sinh\left[\frac{2(n-1/2)}{(n+1/2)}\frac{\sigma_m}{\bar{\sigma}}\right]} \tag{2.23}$$

As discussed previously, creep laws derived from uniaxial tests are also applicable to multi-axial conditions so the average creep rate, defined in Equation (2.11) may also be expressed in terms of the multi-axial creep ductility, ε_f^*, and the multi-axial rupture time as demonstrated in Equation (2.24).

$$\dot{\varepsilon}_A^c = \frac{\varepsilon_f}{t_r} = \frac{\varepsilon_f^*}{t_r^*} \tag{2.24}$$

By combining Equations (2.23) and (2.24), the ratio of the uniaxial and multi-axial creep ductility may be defined by Equation (2.25).

$$\frac{\varepsilon_f^*}{\varepsilon_f} = \frac{t_f^*}{t_f} = \frac{Sinh\left[\frac{2(n-1/2)}{(n+1/2)}\frac{1}{3}\right]}{Sinh\left[\frac{2(n-1/2)}{(n+1/2)}\frac{\sigma_m}{\bar{\sigma}}\right]} \quad \textbf{(2.25)}$$

2.3 Fracture Mechanics

The stress and strain fields in a loaded body can be calculated by solving the equilibrium and compatibility equations for given set of boundary conditions. If that body contains a crack, it can be shown that the stress and strain fields local to the crack tip often depend only on the properties of the material and a single scaling parameter. This single scaling parameter depends on the geometry and the applied loading. For linear-elastic materials, this parameter is the stress intensity factor, K, and for elastic-plastic materials it is the J contour integral. In the presence of creep, this parameter may be $C(t)$ or C^* depending on the extent of the creep. Each of these different regimes is discussed below. The discussion focuses on mode I loading, i.e. the applied load is normal to the plane of the crack. This is the loading experienced by the fracture specimens considered in this research and is typical of cracks in most real components. The polar co-ordinate system used to describe the stress and strain fields around the crack tip is shown in Figure 2.3 for a crack of length $2a$ in an infinite body.

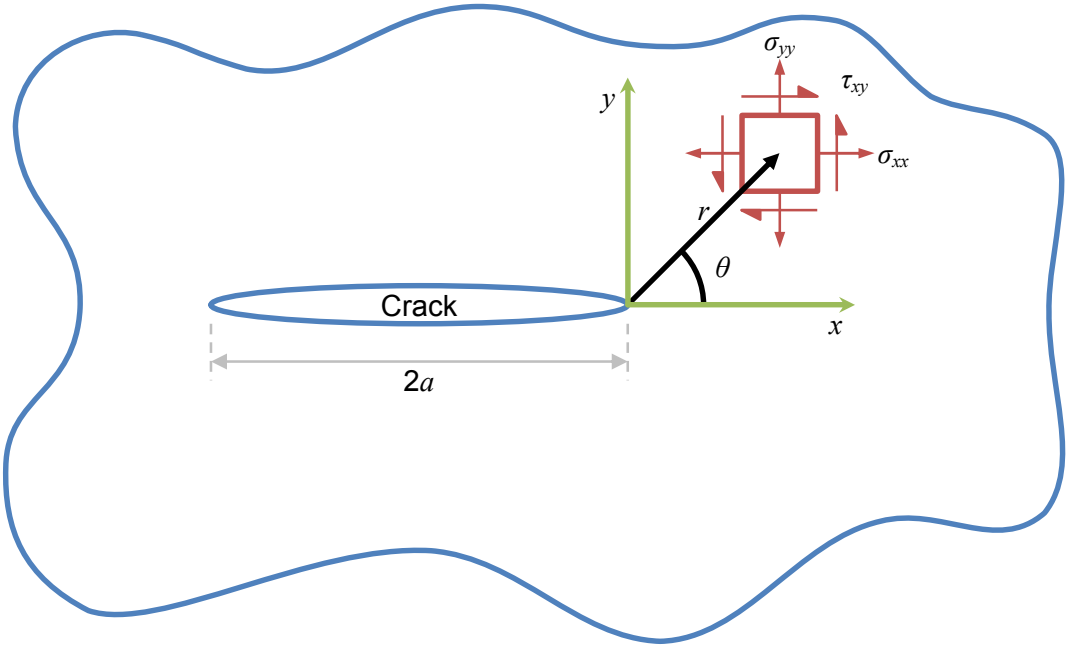

Figure 2.3: Crack tip co-ordinate system.

2.3.1 Linear-Elastic Fracture Mechanics (LEFM)

LEFM is applies to structures which fail in a predominantly elastic manner. It does not account for plasticity or time dependent effects although the concepts have been extended to account for small amounts of plasticity. Two different parameters are commonly used to describe the behaviour of cracks in LEFM. These are the strain energy release rate, G, and the stress intensity factor, K.

2.3.1.1 Strain Energy Release Rate, G

Griffith [16] identified that a crack would grow in a linear elastic material when the resulting release in strain energy is equal to, or more than, the energy required to break the atomic bonds necessary to form the new fracture surfaces. Based on Griffiths theory, strain energy release rate, G, was later proposed as a measure of the available energy to produce crack growth. The term 'rate' refers to the strain energy that would be released per unit area of crack growth. It is defined by Equation (2.26), where Π is the potential energy due to the internal strain and external forces and A_c is the crack area. The strain energy release rate, G, is sometimes called the crack driving force.

$$G = -\frac{d\Pi}{dA_c} \tag{2.26}$$

According to Griffith's theory, crack growth occurs when the crack driving force reaches a critical value, G_C (or G_{IC} for mode I loading). This critical value is the work done to break the atomic bonds and form the new fracture surfaces, W_s, per unit area of crack growth and is defined in Equation (2.27).

$$G_C = \frac{dW_s}{dA_c} \tag{2.27}$$

2.3.1.2 Stress Intensity Factor, K

By solving the equilibrium and compatibility equations, it can be shown that the stress distribution close to a perfectly sharp crack tip in a linear-elastic material can be approximated from Equation (2.28), where f_{ij} describes the variation of the stress field with angle θ, and K is the stress intensity factor which is the magnitude of the field.

$$\sigma_{ij} = \frac{K}{\sqrt{r}} f_{ij}(\theta) \tag{2.28}$$

This is the first term of a series expansion. In the vicinity of the crack tip, where r is small compared with the specimen geometry, this term dominates, but remote from the crack tip,

the higher order terms become significant and the stresses are governed by the remote boundary conditions. In some cases the second term, which contains the so-called T stress, can also influence the stresses close to the crack tip [17]. The elastic strain field around the crack tip is described by Equation (2.29).

$$\varepsilon_{ij}^{e} = \frac{K}{E\sqrt{r}} g_{ij}(\theta, v) \tag{2.29}$$

The value of K depends on the geometry, including the size of the crack, and the applied loading. Handbook solutions for many standard configurations are available in the literature (e.g. [18]). These are often in the form of Equation (2.30), where Y is a shape function which describes the geometry dependency.

$$K = Y\sigma\sqrt{a} \tag{2.30}$$

Given that K fully describes the conditions at the crack tip for a linear-elastic material, it follows that fracture will occur at a critical value, K_C. This is known as the fracture toughness and for mode I loading, the critical value is K_{IC}.

2.3.1.3 Small Scale Yielding

Equation (2.28) predicts infinite stresses at the crack tip. In real materials, this is not possible because plasticity will occur when the stress exceeds yield and a plastic zone will form at the crack tip. If this plastic zone is small compared to the region dominated by the crack tip singularity, the stress and strain fields inside the plastic zone will be driven by the surrounding material which behaves according to Equations (2.28) and (2.29). The conditions in the plastic zone therefore remain characterised by, K, albeit not described by Equations (2.28) and (2.29). This is called small-scale yielding.

Assuming an elastic-perfectly plastic material, the stress at the crack tip cannot exceed the yield stress. Irwin [19] demonstrated, from Equation (2.28), that the region of material ahead of the crack tip where the equivalent stress is predicted to exceed yield, r_y, may be obtained from Equation (2.31)

$$r_y = \frac{1}{\beta\pi}\left(\frac{K}{\sigma_y}\right)^2 \tag{2.31}$$

For plane stress conditions β = 2. For plane strain conditions, where plasticity at the crack tip is suppressed by stress triaxiality, β = 6. Accounting for the redistribution of the stress within this region, it can be shown that the size of the plastic zone, r_p, is double the value of r_y.

In the presence of small scale yielding, Irwin [19] postulated that the plastic zone increased the effective size of the crack and the corresponding stress intensity factor. He proposed that the effective crack length, a_{eff}, could be approximated from Equation (2.32).

$$a_{eff} = a + r_y \tag{2.32}$$

For a Ramberg-Osgood material a modified version of this approach has been proposed to account for strain hardening [20]. The corresponding values of r_y and a_{eff} are calculated from Equations (2.33) and (2.34) respectively, where P is the applied load and P_{p0} is a normalising load.

$$r_y = \frac{1}{\beta\pi}\left(\frac{N-1}{N+1}\right)\left(\frac{K}{\sigma_{p0}}\right)^2 \tag{2.33}$$

$$a_{eff} = a + \frac{1}{1+\left(P/P_{p0}\right)^2} r_y \tag{2.34}$$

2.3.1.4 Relationship between G and K

Irwin [21] performed a crack closure analysis to demonstrate the unique relationship between G and K. This relationship is provided in Equation (2.35) where E' is the effective Young's modulus.

$$G = \frac{K^2}{E'} \tag{2.35}$$

For plane stress conditions E' is simply the Young's modulus obtained from a uniaxial tensile test, E. For plane strain conditions it is corrected for the multi-axial stress state using Equation (2.36) where ν is the Poisson's ratio.

$$E' = \frac{E}{1-\nu^2} \tag{2.36}$$

2.3.2 Elastic-Plastic Fracture Mechanics (EPFM)

For an elastic-plastic material, small scale yielding conditions exist as long as the plastic zone is small compared to the K dominated zone around the crack tip as shown in Figure 2.4(a). As the load increases the plastic zone size increases engulfing the K dominated zone as shown in Figure 2.4(b). In these conditions, LEFM is no longer applicable and EPFM is required. The main parameter used to characterise the conditions at the crack tip in the elastic-plastic regime is the J contour integral. EPFM remains applicable as long as the large strain region (strains greater than ~10%) at the crack tip remains small compared

to the region characterised by J. At very large loads, this region engulfs the J dominated zone and the crack tip conditions can no longer be characterised by a single parameter. This is shown schematically in Figure 2.4(c). The Crack Tip Opening Displacement (CTOD) is sometimes used as alternative to the J contour integral. Both parameters are discussed here.

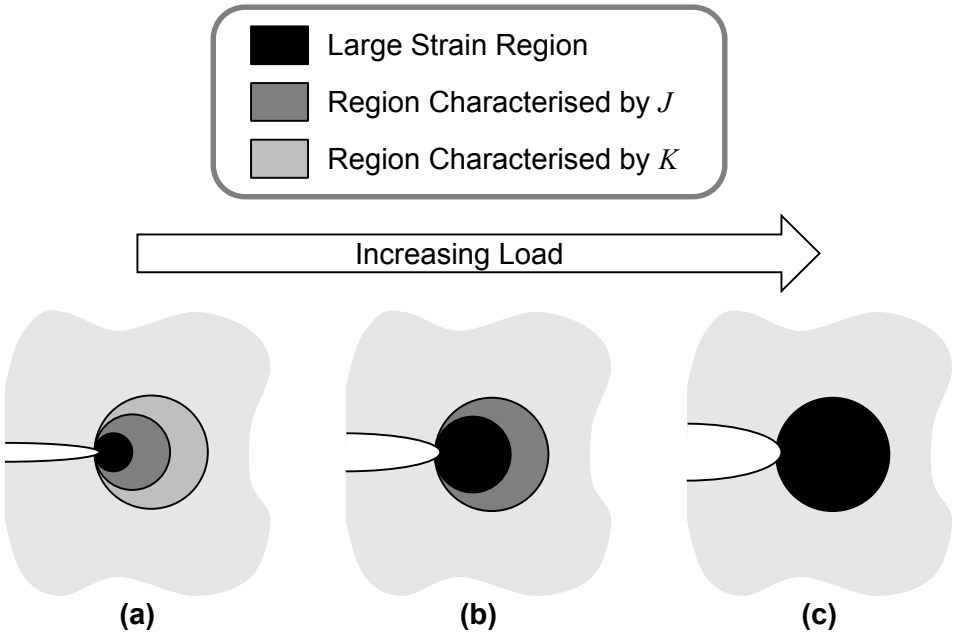

Figure 2.4: Schematic representation of the crack tip stress and strain fields for (a) LEFM regime (small scale yielding), (b) EPFM regime, and (c) crack tip conditions no longer characterised by a single parameter.

2.3.2.1 J Contour Integral

The J contour integral was originally derived by Rice [22] as a line integral taken anti-clockwise around the crack tip. It is defined in Equation (2.37) where s is the length of the contour Γ, w is the strain energy density given by Equation (2.38) and T_i and u_i are components of the traction and displacement vectors acting on the contour.

$$J = \int_{\Gamma} \left[w dy - T_i \left(\frac{\partial u_i}{\partial x} \right) ds \right] \tag{2.37}$$

$$w = \int_0^{\varepsilon_{ij}} \sigma_{ij} d\varepsilon_{ij} \tag{2.38}$$

This derivation was based on the deformation theory of plasticity which assumes a non-linear elastic material. For monotonic loading, this is a reasonable approximation of an elastic-plastic material. Rice [22] also demonstrated that this contour integral is equal to the strain energy release rate for a non-linear elastic material so crack growth will occur when J

reaches come critical value J_C (or J_{IC} for mode I loading). This is similar to the linear elastic strain energy release rate identified above such that for a linear elastic material:

$$J = G = \frac{K^2}{E'} \tag{2.39}$$

2.3.2.2 HRR Field

Hutchinson [23] and Rice and Rosengren [24] independently demonstrated that the stress and strain fields around a sharp crack in a power-law hardening material are described by Equations (2.40) and (2.41). This is known as the HRR field and is based on the deformation theory of plasticity similar to the derivation of J. The J contour integral provides the magnitude of these fields, in a similar manner to K for a linear elastic material.

$$\sigma_{ij} = \sigma_{p0}\left(\frac{J}{I_N \alpha \sigma_{p0} \varepsilon_{p0} r}\right)^{\frac{1}{N+1}} \tilde{\sigma}_{ij}\left(N,\theta\right) \tag{2.40}$$

$$\varepsilon_{ij} = \alpha\varepsilon_{p0}\left(\frac{J}{I_N \alpha \sigma_{p0} \varepsilon_{p0} r}\right)^{\frac{N}{N+1}} \tilde{\varepsilon}_{ij}\left(N,\theta\right) \tag{2.41}$$

In Equations (2.40) and (2.41) I_N is a non-dimensional function of N and $\tilde{\sigma}_{ij}$ and $\tilde{\varepsilon}_{ij}$ are non-dimensional functions of N and θ. Tables of values of I_N, $\tilde{\sigma}_{ij}$ and $\tilde{\varepsilon}_{ij}$ for plane stress and plane strain conditions are available [25]. Polynomial fits to this tabulated data have been used to derive Equations (2.42) and (2.43) for plane strain and plane stress conditions respectively [6].

$$I_N = 10.3\left(0.13 + \frac{1}{N}\right)^{\frac{1}{2}} - \frac{4.6}{N} \tag{2.42}$$

$$I_N = 7.2\left(0.12 + \frac{1}{N}\right)^{\frac{1}{2}} - \frac{2.9}{N} \tag{2.43}$$

The HRR field predicts infinite stresses at the crack tip. In real materials, large stresses at the crack tip result in a large strain region and crack blunting as demonstrated in Figure 2.4. The stress and strain field inside this region are not captured by the HRR field but, as long as this region is small compared to the region dominated by the crack tip singularity, Figure 2.4(b), the stress and strain fields inside the large strain region will be driven by the surrounding material. This material behaves according to the HRR field, so the conditions in

the large strain region will be characterised by, J, albeit not described by Equations (2.40) and (2.41). This is analogous to small scale yielding.

2.3.2.3 Crack Tip Opening Displacement

Wells [26] measured the Crack Tip Opening Displacement (CTOD), δ, which occurred due blunting in the large strain region. He identified that at the point of failure it was proportional to the material toughness. This led him to propose that a critical value of CTOD, δ_C, could be used as an alternative to J_C as a measure of fracture toughness. Both J and CTOD are incorporated into most fracture toughness testing standards e.g. [1, 2, 27].

When a crack blunts, some crack extension occurs which can make the definition of CTOD somewhat ambiguous and has led to various definitions. The two most commonly used are provided in Figure 2.5. In Figure 2.5(a) it is distance measured perpendicular to the crack plane at the original crack tip. In Figure 2.5(b) it is the distance measured between the intercepts of two 45º lines, originating from the current crack tip, with the crack profile. The latter definition is often used to measure CTOD from FE analyses [17].

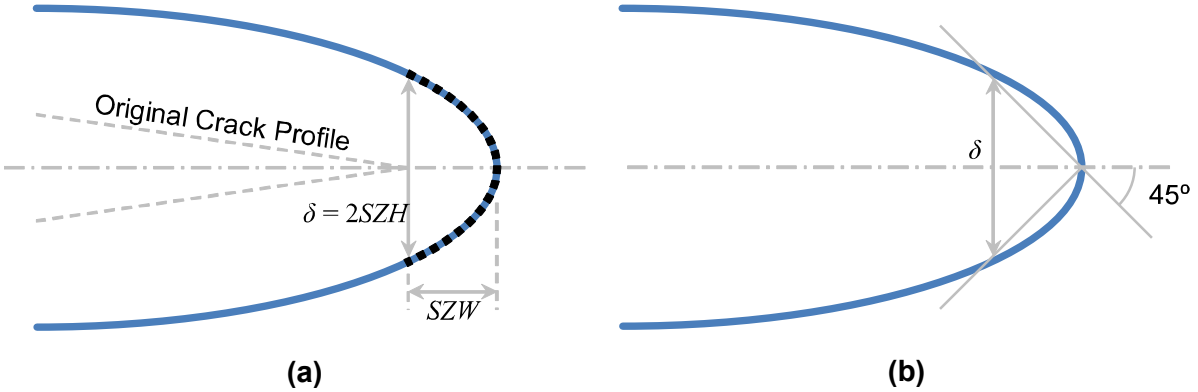

Figure 2.5: Definitions of CTOD based on (a) original crack tip location, and (b) Intercept of two 45º lines from the current crack tip with the crack profile.

The region of blunting is sometimes referred to as the Stretch Zone which is also shown in Figure 2.5(a). The size of this zone can be measured from the post-test fracture surface, using a Scanning Electron Microscope (SEM). When viewed from directly above the fracture surface, the extent of this zone is called the Stretch Zone Width (SZW) and is sometimes used as a measure of crack extension due to blunting although the subjectivity of such measurements can result in significant scatter [28]. The extent of this region perpendicular to the crack plane is twice the Stretch Zone Height ($2SZH$).

2.3.2.4 Relationship between J and CTOD

For a power-law hardening material which deforms according to Equation (2.3), the CTOD may be related to J by Equation (2.44) where d_N is the non-dimensional constant defined in

Equation (2.45) that is strongly dependent on the stress exponent, N, and weakly dependent on the other material constants α and ε_{p0} [29]. In Equation (2.45) D_N is a non-dimensional constant that is only dependent on the stress exponent. Tables of values of this constant are available [29].

$$\delta = d_N \frac{J}{\sigma_{p0}} \tag{2.44}$$

$$d_N = \left(\alpha \varepsilon_{p0}\right)^{\frac{1}{N}} D_N \tag{2.45}$$

In the limit of rigid plasticity, where $N \to \infty$, $d_N \to D_N$ and Equation (2.44) may be simplified to Equation (2.46). The constant m represents the constraint at the crack tip. For plane stress and plane strain conditions it may be assumed that m = 1 and m = √3 respectively [6].

$$\delta = \frac{J}{m\sigma_y} \tag{2.46}$$

2.3.2.5 Resistance Curves

Crack extension occurs when the crack driving force, J, attains a critical value, J_C, but the subsequent crack growth may be stable or unstable. This depends on how the resistance to crack extension, J_R, and the crack driving force vary with crack extension. A typical plot of the material resistance with crack extension for a ductile material is shown in Figure 2.6(a). This is known as a resistance or J-R curve.

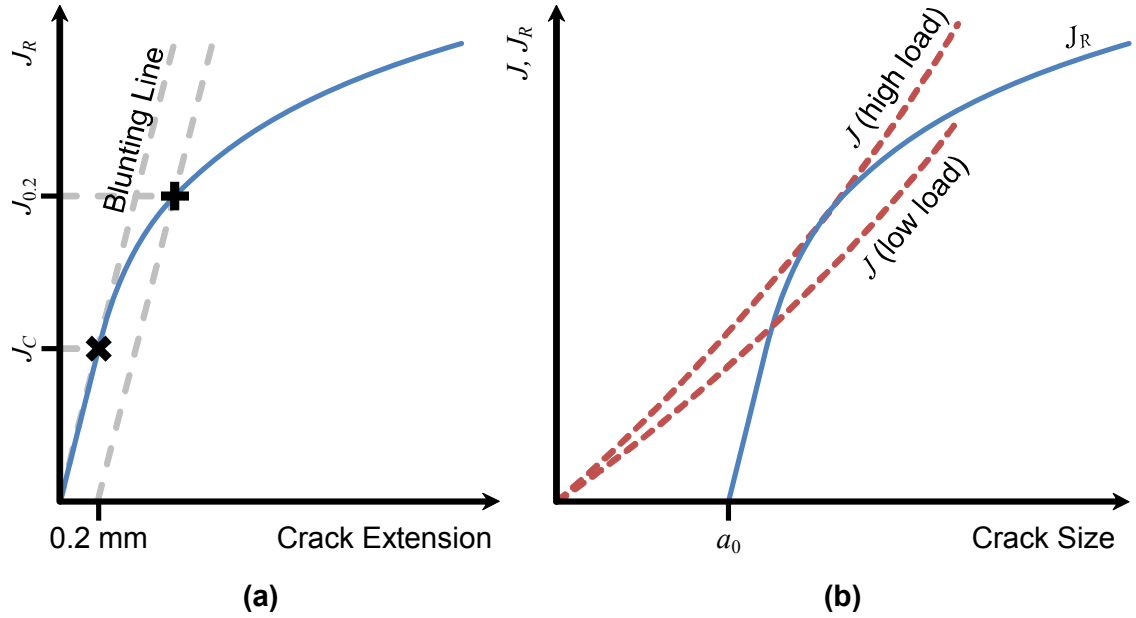

Figure 2.6: Schematic representation of (a) a J-R curve, and (b) the variation of crack driving force for two different load levels relative to the J-R curve.

For brittle materials, crack extension is generally unstable. This results in a flat resistance curve and a single value of fracture toughness which is a material property. For ductile materials, stable tearing can occur because the material resistance increases with crack extension. This results in a rising resistance curve such as the one shown in Figure 2.6(a). At low loads, the crack will extend due to blunting as discussed above and the resistance curve follows the so-called blunting line. The point at which the resistance curve deviates from the blunting line, labelled '×' in Figure 2.6, corresponds to the initiation fracture toughness, J_C, and the onset of stable tearing. The value of J_C is generally independent of geometry and may be considered a material property but the exact value is difficult to identify experimentally so an alternative, engineering definition is often used, $J_{0.2}$, e.g. [1, 2, 27]. This is the toughness corresponding to 0.2 mm of crack extension, which is a small but measurable amount of crack extension. It is labelled '+' in Figure 2.6(a) and is obtained from the point where the resistance curve intersects a line drawn parallel to the blunting line, offset by 0.2 mm of crack extension.

It is possible to determine whether crack growth is stable or unstable by comparing the relationship between crack driving force and crack length with the resistance curve. This is shown in Figure 2.6(b) for two different load levels. For the 'low load' at the initial crack length, a_0, the crack driving force, J, is above the resistance curve so some crack extension will occur, but this will stop when J_R becomes greater than J. This is stable crack extension and occurs when:

$$\begin{aligned} &J > J_R \\ &and \\ &\frac{dJ}{da} \leq \frac{dJ_R}{da} \end{aligned} \qquad \textbf{(2.47)}$$

At the 'high load' the variation of the crack driving force with crack length is such that it always remains above the resistance curve. This is unstable crack extension and occurs when:

$$\begin{aligned} &J > J_R \\ &and \\ &\frac{dJ}{da} > \frac{dJ_R}{da} \end{aligned} \qquad \textbf{(2.48)}$$

2.3.2.6 Blunting Lines

In order to determine the value of $J_{0.2}$, a blunting line is required which accurately describes the crack tip behaviour prior to stable tearing. Various different equations are presented in

the literature, derived from the relationships between J and CTOD discussed in Section 2.3.2.4.

The implementation of a blunting line was originally proposed by Landes and Begley [30], in the form of Equation (2.49).

$$\Delta a = \frac{J}{2\sigma_y} \tag{2.49}$$

This is based on Equation (2.46) assuming plane stress conditions and that the blunt crack tip has a semi-circular profile. To account for strain hardening, it was proposed that the yield stress could be replaced with the flow stress, σ_f, calculated from Equation (2.50) where σ_u is the ultimate tensile stress. This approach is included in the fracture toughness standard ASTM E1820-13 [27].

$$\sigma_f = \frac{\sigma_y + \sigma_u}{2} \tag{2.50}$$

Measurements of the SZW have demonstrated that Equation (2.49) can overestimate crack blunting [28, 31], particularly for materials which exhibit significant strain hardening. To address this problem Equation (2.51) was derived based on the HRR field and Equation (2.44) [31]. Equation (2.51) is slightly different from its original form for consistency with Equations (2.3) and (2.44).

$$\Delta a = 0.4 d_N \frac{J}{\sigma_{p0}} \tag{2.51}$$

The coefficient of 0.4 is based on two experimental observations:

1. The "operational" definition of CTOD implemented by Shih is very similar to the double stretch zone height, $2SZH$.
2. The relationship between the stretch zone width, SZW, and the double stretch zone height, $2SZH$, is approximately constant at 0.4. This is also in agreement with FE calculations [32].

Equation (2.51) suggests that the crack tip does not deform in a semi-circular manner which explains why Equation (2.49) tends to overestimate crack blunting, even for materials which approximate rigid-plasticity. This blunting line has been incorporated into the fracture toughness standard ESIS P2-92 [1] assuming plane strain conditions but the required methodology is quite complex due to the need to derive power-law material properties. To avoid this complexity, Landes [33] identified that the same blunting line could be approximated to within 5% for most engineering materials from the ultimate tensile stress using Equation (2.52).

$$J = 3.75\sigma_u \Delta a \quad \textbf{(2.52)}$$

This simplified blunting line is used in ISO 12135 [2], BS 7448-4:1997 [34] and is provided in ESIS P2-92 [1] as an “approximate method”.

2.3.2.7 Limit Load Analysis

The load bearing capacity of a flawed structure in the elastic-plastic regime may be limited by fracture or plastic collapse. Failure of the structure due to plastic collapse is said to occur when the applied load, P, exceeds some limit load, P_L. This limit load typically corresponds to gross yielding of the remaining ligament assuming rigid plasticity. Limit load solutions can be derived analytically, numerically or empirically, although handbook solutions are readily available for most standard specimen geometries e.g. [35]. The limit load solutions depend on the stress state and the yield criterion. Solutions based on plane stress conditions produce lower plastic collapse loads than those based on plane strain conditions. Solutions based on the Tresca yield criterion produce lower plastic collapse loads than those based on the von Mises yield criterion.

2.3.2.8 Failure Assessment Diagram

The Failure Assessment Diagram (FAD) was originally proposed to assess the interaction between elastic fracture and plastic collapse [36]. This was later extended to include J based EPFM which removed some of the conservatism from the assessment method [37]. This approach forms the basis of the R6 procedure for the assessment of the integrity of structures containing defects [35]. The main benefits of the FAD approach are that no prior knowledge of the failure mechanism is required, it is easy to implement and it can be applied to combined primary and secondary loads. Primary loads are those which contribute to plastic collapse whilst secondary loads only contribute to fracture, e.g. residual stresses.

In the R6 assessment procedure, the proximity of a component containing a flaw to fracture is described by the term K_r. This is calculated from Equation (2.53) where K_{mat} is calculated from Equation (2.54) for mode I loading. For elastic materials, K_{mat} is the linear-elastic fracture toughness, K_{IC}.

$$K_r = \frac{K}{K_{mat}} \quad \textbf{(2.53)}$$

$$K_{mat} = \sqrt{E' J_{IC}} \quad \textbf{(2.54)}$$

The proximity of a component containing a flaw to plastic collapse is described by the term L_r which is calculated from Equation (2.55) where σ_{ref} is the reference stress which is discussed further in Section 2.3.2.10.

$$L_r = \frac{\sigma_{ref}}{\sigma_y} = \frac{P}{P_L} \qquad \textbf{(2.55)}$$

The so-called Option 1 FAD is defined in Equation (2.56) and shown in Figure 2.7. This is a general curve suitable for all materials. The reduction in the critical value of K_r at higher values of L_r accounts for the increase in the crack driving force due to plasticity compared to the linear elastic value used to calculate K_r. The L_r cut-off (the vertical part of the FAD) is known as L_r^{max} and is defined in Equation (2.57).

$$K_r = \left[1 + 0.5{L_r}^2\right]^{-\frac{1}{2}} \left[0.3 + 0.7e^{-0.6{L_r}^6}\right] \qquad \textbf{(2.56)}$$

$$L_r^{max} = \frac{\sigma_f}{\sigma_y} \qquad \textbf{(2.57)}$$

The values of L_r and K_r, calculated from Equations (2.53) and (2.55) respectively, provide the co-ordinates of the assessment point (L_r, K_r) on the FAD. If the assessment point is inside the FAD, the structure is considered safe. Conversely, if it is outside the FAD it is unsafe. The proximity of an assessment point to the FAD may be used as a measure of proximity to failure.

The FAD is a particularly powerful tool for performing sensitivity studies to identify which of the input parameters most significantly influences the proximity of the assessment point to failure. Also by progressively increasing one of these parameters and plotting the locus of the assessment point it is possible to predict the failure mechanism from where the locus intercepts the FAD. At low values of L_r, (L_r < 0.3) failure occurs when $K_r \approx 1$ which corresponds to elastic failure and LEFM applies. For 0.3 < L_r < 0.8 failure typically corresponds to small scale yielding [35], for 0.8 < L_r < L_r^{max} EPFM applies and at large values of L_r (L_r > L_r^{max}) failure is due to plastic collapse.

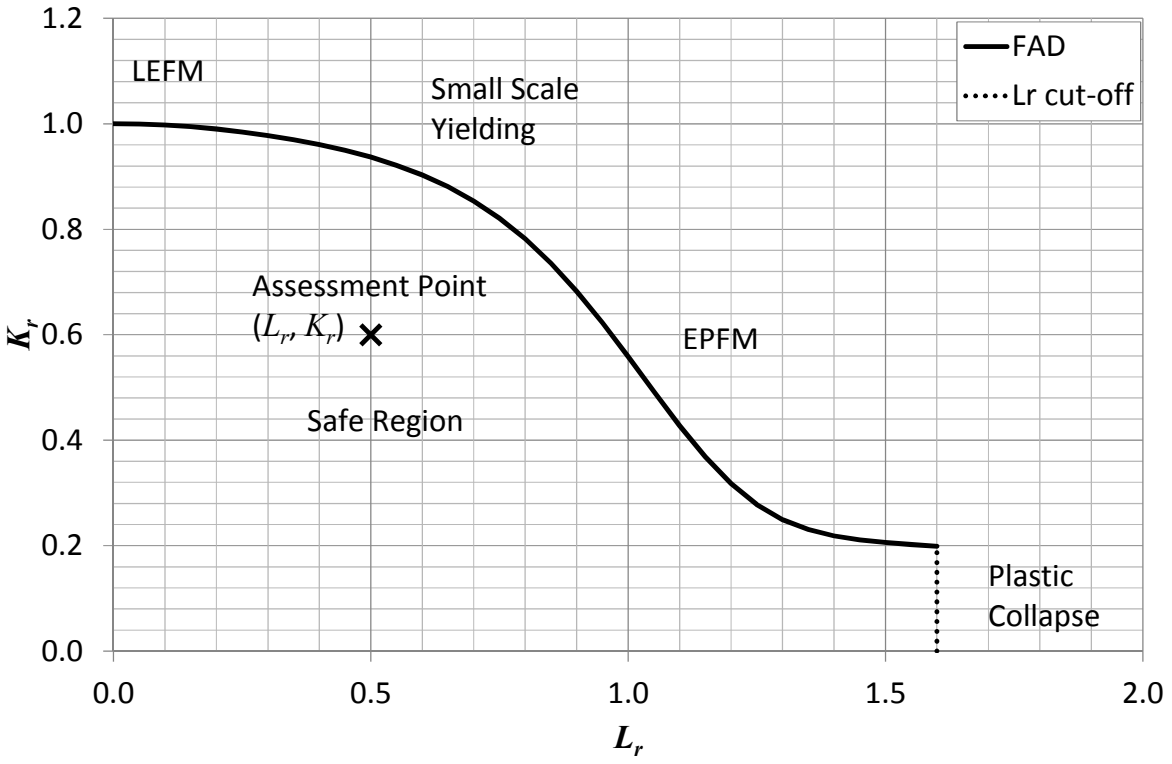

Figure 2.7: Option 1 failure assessment diagram [35].

For materials where the full uniaxial stress-strain curve is available a material specific (Option 2) FAD may be calculated from Equation (2.58). The main difference between the Option 1 and Option 2 curves exist for values of L_r > 0.8 where EPFM characterises failure [35]. These are the two main approaches proposed in R6 although a material and geometry specific Option 3 FAD is also available.

$$K_r = \left[\frac{E\varepsilon_{ref}}{L_r\sigma_{0.2}} + \frac{L_r^{\,3}\sigma_{0.2}}{2E\varepsilon_{ref}} \right]^{-\frac{1}{2}} \qquad \textbf{(2.58)}$$

2.3.2.9 EPRI solutions of J Contour Integral

For a crack in a non-linear elastic power-law hardening material, deforming according to Equation (2.3), the stress at every point within that body is directly proportional to the applied load, P. It follows from Equation (2.40) that J must be proportional to P^{N+1} and also to constants α, σ_{p0} and ε_{p0}. The value of J may therefore be evaluated from Equation (2.59) where c is an appropriate length scale often taken as the ligament ahead of the crack, P_{p0} is a normalising load which is a function of σ_{p0} and h_1 is a non-dimensional function of a/W and N. W is the characteristic width of the specimen.

$$J^p = \alpha \sigma_{p0} \varepsilon_{p0} c h_1 \left(\frac{P}{P_{p0}} \right)^{N+1} \quad \textbf{(2.59)}$$

The power-law relationship defined in Equation (2.3) and used to derive Equation (2.59) only accounts for the plastic component of strain in a Ramberg Osgood material. Equation (2.59) therefore accounts for only the plastic component of J, as identified by the superscript 'p'. The full value of J is calculated from Equation (2.60) where the elastic component is based on the effective crack length, from Equation (2.34).

$$J = J^e + J^p = \frac{K\left(a_{eff}\right)^2}{E'} + J^p \quad \textbf{(2.60)}$$

The Electric Power Research Institute (EPRI) have published tables of values of h_1 for a range of values of N and a/W for common specimen geometries [20]. These have been obtained from a suite of 2D FE analyses for both plane strain and plane stress conditions. In the same document, similar equations are provided for Crack Mouth Opening Displacement (CMOD), Load-Line Displacement (LLD) and Crack Tip Opening Displacement (CTOD).

2.3.2.10 Reference Stress Methods

The EPRI solutions are limited to common test geometries and power-law materials. For other geometries or materials Ainsworth [38] proposed an alternative approach based on the reference stress, σ_{ref}, which is defined in Equation (2.61).

$$\sigma_{ref} = \left(\frac{P}{P_{p0}} \right) \sigma_{p0} \quad \textbf{(2.61)}$$

For a Ramberg-Osgood material, the reference stress can be incorporated into Equation (2.60) to produce Equation (2.62) where ε_{ref} is the reference strain corresponding to the reference stress.

$$J = \frac{K^2\left(a_{eff}\right)}{E'} + c h_1\left(a/W, N\right) \sigma_{ref} \left(\varepsilon_{ref} - \frac{\sigma_{ref}}{E} \right) \quad \textbf{(2.62)}$$

When the stress exponent N = 1, the plastic component of Equation (2.62) corresponds to the elastic solution for ν = 0.5 as shown in Equation (2.63) where μ = 1 for plane stress conditions and μ = 0.75 for plane strain conditions which accounts for the change in the effective Young's modulus for the multi-axial stress state.

$$J^p = \mu \frac{K^2(a)}{E} = ch_1(a/W, N=1)\frac{\sigma_{ref}^2}{E} \quad \textbf{(2.63)}$$

By careful selection of the normalising load, P_{p0}, the value of h_1 becomes approximately independent of the stress exponent N. It has been shown that this normalising load is close to the limit load based on the von Mises yield criterion [38]. For this value of P_{p0}, the corresponding value of h_1 can be approximated from Equation (2.63) and the value of J approximated from Equation (2.64).

$$J = \frac{K^2(a_{eff})}{E'} + \mu\sigma_{ref}\left(\frac{K(a)}{\sigma_{ref}}\right)^2\left(\varepsilon_{ref} - \frac{\sigma_{ref}}{E}\right) \quad \textbf{(2.64)}$$

For a power-law hardening material, rather than a Ramberg-Osgood material, this simplifies to Equation (2.65) [6].

$$J = \mu\left(\frac{K(a)}{\sigma_{ref}}\right)^2 \sigma_{ref}\varepsilon_{ref} \quad \textbf{(2.65)}$$

The benefit of this approach is that it may be applied to any material for which the uniaxial stress-strain data is available and is not limited to common fracture specimen geometries.

2.3.2.11 Empirical Methods

Rice et al. [39] demonstrated that the value of J could also be obtained experimentally from a plot of load vs. displacement for a single point on a specimen. They derived solutions for a range of standard fracture specimens in the form of Equation (2.66) where H is a dimensionless constant which depends on the stress exponent, N, η is a dimensionless constant which depends on the specimen geometry, Δ^p is the plastic component of displacement and B_n is the net specimen thickness measured between the roots of the side-grooves. For specimens without side-grooves the net specimen thickness is equal to the specimen thickness, B.

$$J^p = \frac{P\Delta^p}{B_n(W-a)}H\eta \quad \textbf{(2.66)}$$

A detailed review of η solutions is provided by Davies et al. [40] along with numerical derivation of η for a range of standard test specimens, crack sizes and stress exponents. These solutions are provided for displacement measurements taken at the load-line, Δ_{LLD}, and the crack mouth, Δ_{CMOD}.

2.3.3 Time-Dependent Fracture Mechanics (TDFM)

When a load is applied to a cracked body at elevated temperature, the instantaneous stress and strain distribution around the crack tip is governed by LEFM or EPFM depending on the material properties and the applied loading as shown in Figure 2.4. Due to the high stresses at the crack tip a creep zone will form and start to grow which will tend to relax the stresses in this region. When this creep zone is small compared to the dimensions of the component and the crack, this is known as small scale creep and is shown schematically in Figure 2.8(a). This is analogous to small scale yielding for LEFM and the material surrounding the creep zone will still be characterised by K or J. The material in the creep zone is characterised by a parameter known as $C(t)$ which is time dependent. As time progresses, this creep zone grows and eventually engulfs the region originally characterised by J and/or K as shown in Figure 2.8(b). This is known as transient creep and the crack tip conditions remain characterised by $C(t)$. After a long period of time the creep zone extends across the entire ligament ahead of the crack and wide-spread creep occurs. At this time, steady-state creep conditions exist and the parameter characterising the crack tip conditions tends to a constant value, C^*, shown schematically in Figure 2.8(c).

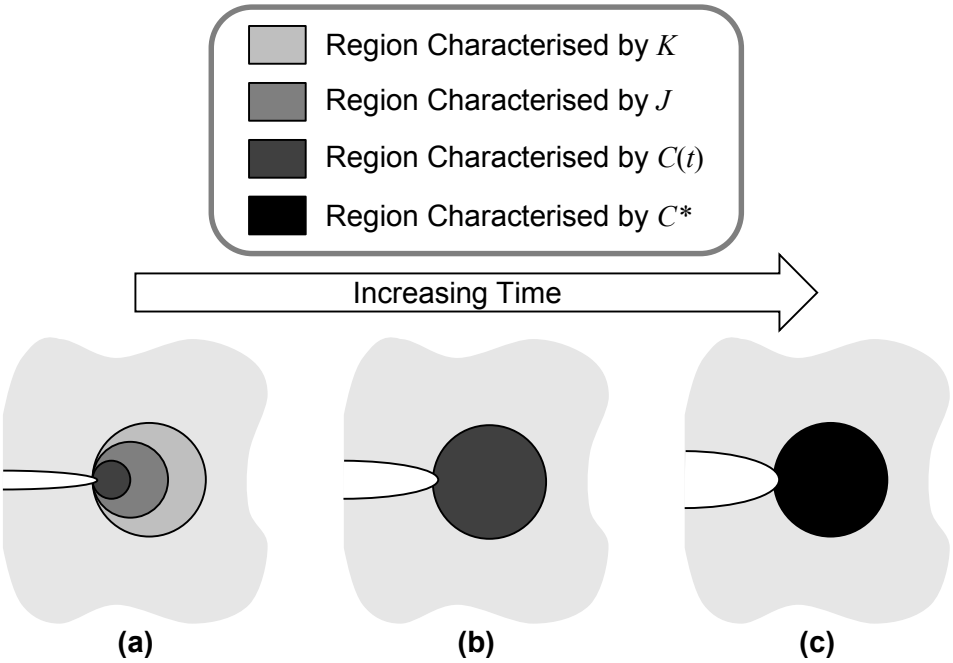

Figure 2.8: Schematic representation of the development of the creep zone showing (a) small scale creep, (b) transition creep, and (c) steady-state creep.

2.3.3.1 Steady State Creep

For steady-state creep conditions, the stress around the crack tip of a power-law creeping material is an HRR type field [41] similar to a power-law hardening material. For materials where $n = N$ the stress distributions are identical for the same load. This is because the

same equilibrium and compatibility equations are applicable except that the strain and displacement are replaced by strain rate and displacement rate.

For steady-state creep conditions the crack tip stress and strain rate fields are described by Equations (2.67) and (2.68) respectively. These are analogous to Equations (2.40) and (2.41) but the magnitude of the fields are defined by the parameter C^* rather than J. The close analogy between power-law hardening materials and power-law creeping materials is frequently used to explain the steady-state creep behaviour of a structure.

$$\sigma_{ij} = \sigma_0 \left(\frac{C^*}{I_n \sigma_0 \dot{\varepsilon}_0 r} \right)^{\frac{1}{n+1}} \tilde{\sigma}_{ij}(\theta, n) \tag{2.67}$$

$$\dot{\varepsilon}^c_{ij} = \dot{\varepsilon}_0 \left(\frac{C^*}{I_n \sigma_0 \dot{\varepsilon}_0 r} \right)^{\frac{n}{n+1}} \tilde{\varepsilon}_{ij}(\theta, n) \tag{2.68}$$

In Equations (2.67) and (2.68) I_n is a non-dimensional function of n and $\tilde{\sigma}_{ij}$ and $\tilde{\varepsilon}_{ij}$ are non-dimensional functions of n and θ. These are the same functions used for a power-law hardening material but N is replaced by n. The tables of values of I_N, $\tilde{\sigma}_{ij}$ and $\tilde{\varepsilon}_{ij}$ produced by Shih [11] for a power-law hardening material are therefore applicable, as are Equations (2.42) and (2.43).

2.3.3.2 C^* Contour Integral

Continuing the analogy between a power-law hardening material and a power-law creeping material, the crack tip characterising parameter during steady-state creep, C^*, may be determined in the same manner as J. That is a line integral taken anti-clockwise around the crack tip, as defined in Equation (2.69) where $\dot{w}$ is the strain energy rate density given by Equation (2.70) and $\dot{u}_i$ is the displacement rate vector acting on the contour.

$$C^* = \int_\Gamma \left[\dot{w} dy - T_i \left(\frac{\partial \dot{u}_i}{\partial x} \right) ds \right] \tag{2.69}$$

$$\dot{w} = \int_0^{\dot{\varepsilon}^c_{ij}} \sigma_{ij} d\dot{\varepsilon}^c_{ij} \tag{2.70}$$

2.3.3.3 Approximations of C^*

Similar methods to the ones used to approximate J can also be applied to C^*. For a power-law creeping material the value of C^* can therefore be estimated from EPRI handbook solutions [20] by substituting the normalising strain, ε_{p0}, with the normalising strain

rate, $\dot{\varepsilon}_0$, and the tensile stress exponent, N, for the creep stress exponent, n, as demonstrated in Equation (2.71).

$$C^* = \sigma_0 \dot{\varepsilon}_0 c h_1 \left(\frac{a}{W}, n \right) \left(\frac{P}{P_0} \right)^{n+1} \quad \textbf{(2.71)}$$

To overcome the limitations of the EPRI solutions discussed above, reference stress estimations of C^* can be calculated from a modified version of Equation (2.65) where the reference strain, ε_{ref}, is replaced by the reference strain rate, $\dot{\varepsilon}_{ref}$, which is the strain rate at the reference stress determined from Equation (2.5). This approximation of C^* is demonstrated in Equation (2.72) where R' is a characteristic length defined in Equation (2.73)

$$C^* = \sigma_{ref} \dot{\varepsilon}^c_{ref} R' \quad \textbf{(2.72)}$$

$$R' = \left(\frac{K(a)}{\sigma_{ref}} \right)^2 \quad \textbf{(2.73)}$$

Empirical estimations of C^* may be calculated from a modified version of Equation (2.66) where the plastic displacement, Δ^p, is replaced with the creep displacement rate, $\dot{\Delta}^c$, as demonstrated in Equation (2.74).

$$C^* = \frac{P \dot{\Delta}^c}{B_n (W - a)} H \eta \quad \textbf{(2.74)}$$

2.3.3.4 Small-scale and Transient Creep

During small scale creep and transient creep the stress and strain rate fields at the crack tip are defined by Equations (2.75) and (2.76) respectively [41]. They are similar in form to Equations (2.67) and (2.68) which describe the steady-state crack tip conditions, but because the crack tip parameter which describes the magnitude of these fields, $C(t)$, varies with time, the stresses and strain rates also vary with time.

$$\sigma_{ij} = \sigma_0 \left(\frac{C(t)}{I_n \sigma_0 \dot{\varepsilon}_0 r} \right)^{\frac{1}{n+1}} \tilde{\sigma}_{ij} (\theta, n) \quad \textbf{(2.75)}$$

$$\dot{\varepsilon}^c_{ij} = \dot{\varepsilon}_0 \left(\frac{C(t)}{I_n \sigma_0 \dot{\varepsilon}_0 r} \right)^{\frac{n}{n+1}} \tilde{\varepsilon}_{ij} (\theta, n) \quad \textbf{(2.76)}$$

Similar to C^*, the crack tip parameter, $C(t)$, can be defined as an anti-clockwise line integral around the crack tip, as defined in Equation (2.77).

$$C(t) = \int_{\Gamma \to 0} \left[\dot{w} dy - T_i \left(\frac{\partial \dot{u}_i}{\partial x} \right) ds \right] \quad \textbf{(2.77)}$$

Unlike C^*, $C(t)$ is path dependent. As demonstrated schematically in Figure 2.8, the region characterised by $C(t)$ is close to the crack tip, so the line integral must be evaluated in this region. At long times $C(t)$ tends towards C^*, so Equations (2.75) and (2.76) tend towards Equations (2.67) and (2.68).

2.3.3.5 Approximations of $C(t)$

For small-scale creep conditions, where the creep zone is surrounded by a region of material characterised by J, Riedel and Rice [41] demonstrated that the crack tip characterising parameter $C(t)$ could be approximated from Equation (2.78) where J_0 is the value of J at time $t = 0$. This equation is applicable to situations where the initial deformation is elastic or elastic-plastic.

$$C(t) = \frac{J_0}{(n+1)t} \quad \textbf{(2.78)}$$

2.3.3.6 Stress Redistribution

At long times $C(t) \rightarrow C^*$, but Equation (2.78) predicts that $C(t) \rightarrow 0$. This is because it is only valid for small scale creep conditions. Despite this it may still be used to approximate the time for wide-spread creep conditions to occur by replacing $C(t)$ with C^* and rearranging to make time the subject as demonstrated in Equation (2.79). This is often called the transition time, t_T,

$$t_T = \frac{J}{(n+1)C^*} \quad \textbf{(2.79)}$$

Due to the limited validity of Equation (2.78), the transition time underestimates the time for stress redistribution to occur. In reality the stresses never truly redistribute but asymptotically approach steady-state conditions; however, it may be shown that $C(t)$ is within 10% of C^* when $n \geq 2.5$ and $t \geq t_{red}$ as defined in Equation (2.80) [6]. This is known as the redistribution time.

$$t_{red} = (n+1)t_T = \frac{J}{C^*} \quad \textbf{(2.80)}$$

For elastic-creep conditions this may be rewritten in terms of the reference stress as demonstrated in Equation (2.81). This suggests that the time for stress redistribution to occur is approximately the time for the creep strain to equal the elastic strain at the reference stress [6].

$$t_{red} = \frac{\sigma_{ref}}{E\dot{\varepsilon}^{c}_{ref}} \tag{2.81}$$

2.4 Creep Crack Initiation and Growth Models

When a cracked body undergoes creep, the creep strains are largest at the crack tip. After some time, micro-voids will start to form along grain boundaries ahead of the crack tip which coalesce to form micro-cracks. Eventually these micro-cracks will link up with the pre-existing defect which is known as Creep Crack Initiation (CCI). This precise point can be difficult to measure experimentally so an engineering definition of initiation is often used which is the time for a small, measureable amount of crack extension to occur, Δa_i. Consistent with fracture toughness testing, this is often taken to be 0.2 mm which is the resolution of typical laboratory measurement techniques [3]. The time prior to initiation is the incubation period and can contribute to a significant portion of a components life [42]. After initiation, Creep Crack Growth (CCG) will occur until the remaining ligament fails due to fracture or creep rupture.

A wide variety of different models for predicting CCI and CCG have been proposed in the literature. The validation of these models for use with creep ductile materials requires accurate laboratory measurements in the presence of large strains. This will be addressed as part of this research, so the relevant models are reviewed here. There are a large number of CCI models available in the literature. The most common are included in the R5 assessment procedure [4] so only those will be considered in detail here although a brief discussion of the other models is also provided.

2.4.1 NSW Model

The main CCG model is the NSW model proposed by Nikbin, Smith and Webster [43]. It is based on a power-law creeping material under established steady-state creep conditions. It assumes a creep process zone ahead of the crack of size r_c, as shown in Figure 2.9, which is growing at a constant rate.

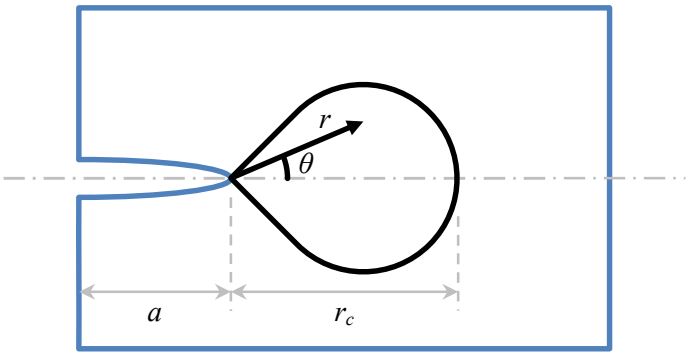

Figure 2.9: Schematic representation of the steady-state creep process zone ahead of the crack tip assumed by the NSW Model.

For an undamaged element of material entering the creep process zone at r = r_c, and time t = 0, the creep strain accumulated over time, t, may be calculated by Equation (2.82).

$$\varepsilon_{ij}^{c} = \int_0^t \dot{\varepsilon}_{ij}^{c} dt = \int_{r_c}^{r} \dot{\varepsilon}_{ij}^{c} \frac{dt}{dr} dr \qquad \textbf{(2.82)}$$

The steady-state crack growth rate, $\dot{a}_s$, is estimated from Equation (2.83) assuming: failure occurs when the element of material reaches the crack tip (r = 0) which corresponds to when the multi-axial creep ductility, ε_f^*, is exhausted in that element; crack growth does not influence the value of C*; and growth of the creep process zone is equal to the crack growth rate.

$$\dot{a}_s = (n+1)\frac{\dot{\varepsilon}_0}{\varepsilon_f^*}\left[\frac{C*}{I_n \sigma_0 \dot{\varepsilon}_0}\right]^{\frac{n}{n+1}} r_c^{\frac{1}{n+1}} = \frac{(n+1)}{\varepsilon_f^*}\left[\frac{C*}{I_n}\right]^{\frac{n}{n+1}} (A r_c)^{\frac{1}{n+1}} \qquad \textbf{(2.83)}$$

In this model failure is assumed to occur at the location around the crack tip, θ, where the equivalent strain is largest. This is where $\tilde{\varepsilon}_{ij}(\theta, n)$ obtains its maximum value of unity.

2.4.1.1 Alternative Versions of the NSW Method

A modification to the NSW model has been derived to incorporate the variation in triaxiality around the crack tip which will influence the multi-axial creep ductility [14]. Assuming that crack growth occurs at the location which corresponds to the maximum ratio of the equivalent strain to multi-axial creep ductility the growth rate may be estimated from Equation (2.84).

$$\dot{a}_s = (n+1)\dot{\varepsilon}_0 \left[\frac{C^*}{I_n \sigma_0 \dot{\varepsilon}_0} \right]^{\frac{n}{n+1}} r_c^{\frac{1}{n+1}} \left. \frac{\tilde{\tilde{\varepsilon}}(\theta,n)}{\varepsilon_f^*(\theta,n)} \right|_{max} \quad \textbf{(2.84)}$$

An alternative version of the NSW model, based on creep rupture data has also been proposed [44]. By using rupture data the model is based on average creep rates which account for primary and tertiary creep, albeit approximately, as demonstrated in Figure 2.1. The model also allows for any dependency of creep ductility on stress [45] by replacing the multi-axial creep ductility ε_f^* with the term ε_{f0}^* which is the multi-axial creep ductility at σ_0. The crack growth rate predicted by this version of the NSW model is calculated from Equation (2.85).

$$\dot{a}_s = \frac{n_A + 1}{n_A + 1 - \nu_r} \frac{\dot{\varepsilon}_0}{\varepsilon_{f0}^*} \left[\frac{C^*}{I_{n_A} \sigma_0 \dot{\varepsilon}_0} \right]^{\frac{\nu_r}{n_A+1}} r_c^{\frac{n_A+1-\nu_r}{n_A+1}} \quad \textbf{(2.85)}$$

For the case where n_A = ν_r, the creep ductility becomes independent of stress so ε_{f0}^* = ε_f^* and Equation (2.85) simplifies to Equation (2.86).

$$\dot{a}_s = \frac{(n_A+1)}{\varepsilon_f^*} \left[\frac{C^*}{I_{n_A}} \right]^{\frac{n_A}{n_A+1}} (A_A r_c)^{\frac{1}{n_A+1}} \quad \textbf{(2.86)}$$

2.4.1.2 Initial CCG Rates

The NSW model assumes established steady-state damage conditions exist at the crack tip but at time, t = 0, no creep strains exist in the region ahead of the crack tip. By approximating the creep process zone as a number of small elements ahead of the crack tip it is possible to analytically model the development of strain in the creep process zone [46]. From this it may be shown that the initial crack growth rate, $\dot{a}_0$, can be approximated from Equation (2.87) where $\dot{a}_s$ is the steady-state crack growth rate predicted by the NSW model.

$$\dot{a}_0 \approx \frac{1}{n+1} \dot{a}_s \quad \textbf{(2.87)}$$

This approach still assumes that the crack tip stress field is characterised by C^* and does not account for any stress redistribution.

2.4.2 Experimental CCG Rate Correlations

Experimental creep crack growth rates are often correlated to some crack tip parameter to produce empirical laws. For creep ductile materials, where failure occurs in the presence of significant creep strains, the crack growth rates are usually correlated to the steady-state crack tip parameter C^*. A power-law fit in the form of Equation (2.88) is most commonly used where D and ϕ are material constants which may be temperature and stress state dependent [6].

$$\dot{a} = DC^{*\phi} \tag{2.88}$$

For creep brittle materials where failure occurs prior to any significant creep strain, the elastic stress intensity factor, K, is sometimes correlated with crack growth rate. Correlations have also been performed to the other crack tip characterising parameters discussed above [6].

By comparing Equation (2.88) with Equation (2.83) it can be seen that for steady state conditions, D and ϕ may be predicted from Equations (2.89) and (2.90) respectively. For $n \gg 1$, typical of creep, ϕ should be close to but less than unity.

$$D = \frac{(n+1)}{\varepsilon_f^*}\left[\frac{Ar_c}{I_n{}^n}\right]^{\frac{1}{n+1}} \tag{2.89}$$

$$\phi = \frac{n}{n+1} \tag{2.90}$$

2.4.3 Sigma-d Model

The sigma-d model assumes that crack initiation occurs at the time required for a uniaxial specimen to fail with an applied stress, σ_d, which corresponds to the stress at some characteristic distance, d, ahead of the crack tip. This method is included in the R5 procedure [4] for assessing austenitic stainless steels. It is confined to this classification of steel because they exhibit significant work hardening. For materials which do not work harden, the predicted stress value, and therefore the initiation time would be independent of the applied load. The recommended value of the characteristic distance, d, is 50 μm which is approximately the grain size for this classification of steel [4]. This value is pessimistic compared to the guidance in RCC-MR which recommends 60 μm [7].

The sigma-d method has been validated against experimental CCG tests performed on parent material, heat affected zone (HAZ) and weld metal for two stainless steels: Type 316H and Esshete [4]. Predictions based on mean material properties were in good

agreement with experimental measurements of the time for 0.2 mm of crack extension to occur. Predictions based on lower-bound material properties were conservative. This validation was used to justify the use of the sigma-d method for predicting the time for 0.2 mm of crack extension to occur in austenitic stainless steels.

Various different methods of estimating the value of σ_d are available. For cracks in the linear elastic regime, it may be obtained from the K field. For cracks in the elastic-plastic regime it may be obtained from the HRR field. Alternatively the Neuber method may be used which is the method used in R5 and RCC-MR. Neuber proposed that for a sharply curved notch in an elastic-plastic material, the maximum equivalent stress, $\bar{\sigma}_{max}$, and maximum equivalent strain, $\bar{\varepsilon}_{max}$ may be related to the nominal equivalent stress, $\bar{\sigma}_{nom}$, and nominal equivalent strain, $\bar{\varepsilon}_{nom}$, by the linear-elastic stress concentration factor, k_t, by Equation (2.91) [47].

$$\bar{\sigma}_{max}\bar{\varepsilon}_{max} = k_t^{\,2}\bar{\sigma}_{nom}\bar{\varepsilon}_{nom} \qquad \textbf{(2.91)}$$

In R5, this approach is applied to a sharp crack. The equivalent elastic stress at a distance, d, ahead of the crack tip, $\bar{\sigma}_d^e$, is obtained from the K field solution using Equation (2.92). This conservatively implies plane stress conditions (no out of plane stress).

$$\bar{\sigma}_d^e = \frac{K}{\sqrt{2\pi d}} \qquad \textbf{(2.92)}$$

The corresponding equivalent strain, $\bar{\varepsilon}_d^e$, is calculated from Equation (2.93) where ε_{ref}^p is the plastic strain which occurs at the reference stress and is included to account for large scale yielding. The value of $\bar{E}$ is obtained from Equation (2.94).

$$\bar{\varepsilon}_d^e = \frac{K}{\bar{E}\sqrt{2\pi d}} + \varepsilon_{ref}^p \qquad \textbf{(2.93)}$$

$$\bar{E} = \frac{3E}{2(1+\nu)} \qquad \textbf{(2.94)}$$

The values of σ_d and ε_d at a distance, d, from the crack tip are obtained using the Neuber construction shown schematically in Figure 2.10. Mathematically, this is the point on the uniaxial tensile stress-strain curve which satisfies Equation (2.95), which is equivalent to Equation (2.91). The iterative procedure required to obtain these values may be simplified by applying a Ramberg Osgood fit to the uniaxial data.

$$\sigma_d\varepsilon_d = \frac{K}{\sqrt{2\pi d}}\left(\frac{K}{\bar{E}\sqrt{2\pi d}} + \varepsilon_{ref}^p\right) \qquad \textbf{(2.95)}$$

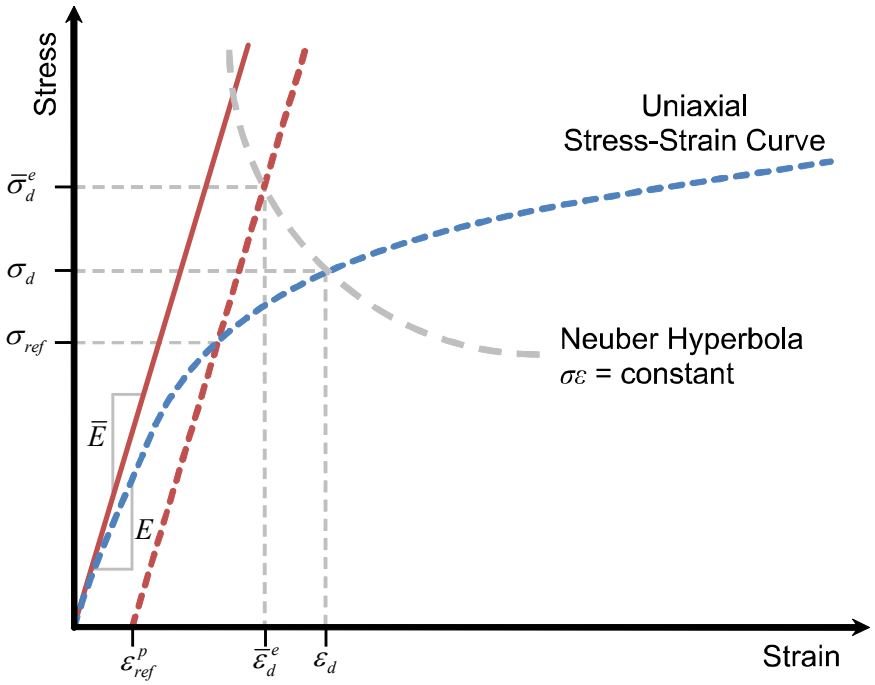

Figure 2.10: Schematic representation of the Neuber construction for the sigma-d method.

The time for 0.2 mm of crack growth to occur is then obtained from the uniaxial creep properties using Equation (2.96) which is based on Equation (2.6).

$$t_i = \frac{B_r}{\sigma_d^{\nu_r}} \tag{2.96}$$

As demonstrated above, the stress ahead of the crack tip is obtained from the elastic-plastic material properties. No account of the stress relaxation due to creep is considered in this model.

2.4.4 CTOD Model

For a component containing a pre-existing defect under creep conditions, large strains will accumulate at the crack tip causing it to blunt prior to crack extension. Ainsworth [48] postulated that this blunting continues until the ductility of the material ahead of the defect is exhausted at which point crack initiation occurs. Assuming that the crack tip blunts in a semi-circular manner and the initial CTOD, δ_0, is negligible compared to the CTOD at initiation, $\delta_{i,}$, which is a material property, it may be shown that δ_i is related to the initiation time, t_i, by Equation (2.97) where ε_i^c is the creep strain at the initiation time at the reference stress.

$$\delta_i^{\frac{n}{n+1}} = \left(\frac{\dot{\varepsilon}_0}{{\sigma_0}^n} \right)^{\frac{1}{n+1}} C*^{\frac{n}{n+1}} t_i \left(1 + \frac{\sigma_{ref}}{E\varepsilon_i^c} \right) \quad \textbf{(2.97)}$$

Substituting in the reference stress definition of C* from Equation (2.72), this can be simplified to Equation (2.98).

$$\left(\frac{\delta_i}{R'} \right)^{\frac{n}{n+1}} = \varepsilon_i^c + \frac{\sigma_{ref}}{E} \quad \textbf{(2.98)}$$

This form of the CTOD method is included in R5 [4]. For power-law creep the corresponding initiation time is calculated from Equation (2.99).

$$t_i = A^{\frac{-1}{n+1}} \left(\frac{\delta_i}{C*} \right)^{\frac{n}{n+1}} - \frac{1}{EA{\sigma_{ref}}^{n-1}} \quad \textbf{(2.99)}$$

One of the benefits of this method is that it is considered to incorporate the different stages of creep deformation [6] however, in order to implement it experimental measurements of the CTOD at initiation are required. Often this data is not available which restricts the use of this model. For this reason, a modified version, shown schematically in Figure 2.11, has been proposed which negates this limitation [8].

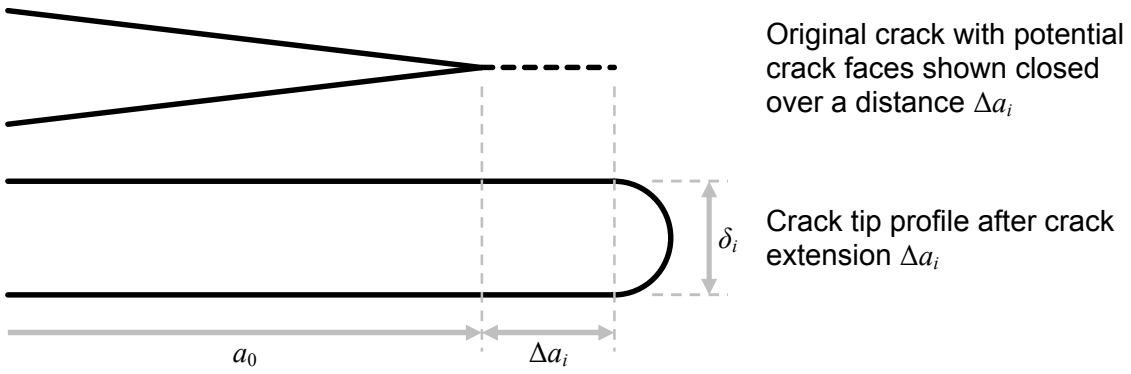

Figure 2.11: Schematic representation of creep crack initiation based on a critical CTOD

Assuming that for crack extension to occur, the creep ductility associated with the state of stress at the crack tip, ε_f^*, has been exhausted, the critical CTOD may be related to this creep ductility. If the creep strain along the new crack faces associated with crack extension, Δa_i, results in crack tip blunting, and again assuming a semi-circular crack tip, the critical CTOD may be related to the crack extension and the multi-axial creep ductility by Equation (2.100).

$$\frac{\pi\delta_i}{2} = 2\Delta a_i \varepsilon_f^* \quad \textbf{(2.100)}$$

From the analogy between J and C^*, it may be assumed that, for $n\rightarrow\infty$, Equation (2.46) may be rewritten in terms of C^* where δ is replaced with $\dot{\delta}$ and σ_y is replaced by σ_{ref} such that:

$$C^* = m\sigma_{ref}\dot{\delta} \quad \textbf{(2.101)}$$

Assuming that C^* and $\dot{\delta}$ are constant for the small crack increment associated with initiation, Δa_i, Equation (2.101) may be integrated over the incubation period to give:

$$C^* t_i \approx m\sigma_{ref}\delta_i \quad \textbf{(2.102)}$$

Estimating C^* from Equation (2.72) and combining Equations (2.100) and (2.102) gives:

$$t_i = \frac{4m}{\pi}\Delta a_i \varepsilon_f^* \dot{\varepsilon}_{ref}^c \left(\frac{K}{\sigma_{ref}}\right)^{-2} \quad \textbf{(2.103)}$$

Substituting Equation (2.11) for $\dot{\varepsilon}_{ref}^c$ and noting that for plane stress conditions $m \approx 1$ and for plane strain conditions $m \approx \sqrt{3}$ [6] it is conservative to rewrite Equation (2.103) as:

$$t_i = \Delta a_i \frac{\varepsilon_f^*}{\varepsilon_f}\left(\frac{K}{\sigma_{ref}}\right)^{-2} t_{r,ref} \quad \textbf{(2.104)}$$

This equation may be used to derive the initiation time without the need for experimental measurements of the critical CTOD.

2.4.5 Time Dependent Failure Assessment Diagram (TDFAD)

The TDFAD was originally proposed by Ainsworth [49] to extend the FAD approach described above to the creep regime. This approach is incorporated into R5 to assess if a small tolerable amount of crack extension, Δa, will occur in a given time, t, known as the assessment time [4].

The TDFAD approach uses a modified version of the Option 2 FAD, described in Equation (2.105), to incorporate time dependent material properties. Isochronous stress-strain data is required for its construction.

$$K_r = \left[\frac{E\varepsilon_{ref}}{L_r\sigma_{0.2}^c} + \frac{L_r^3\sigma_{0.2}^c}{2E\varepsilon_{ref}}\right]^{-\frac{1}{2}} \quad \textbf{(2.105)}$$

The stress corresponding to 0.2% inelastic strain (plastic plus creep), $\sigma_{0.2}^{c}$, is obtained from the isochronous stress-strain data at the assessment time. When the assessment time is short, this tends towards the 0.2% proof stress. When the assessment time is long, it tends towards the stress to produce 0.2% creep strain. The total strain at the reference stress, ε_{ref}, is also obtained from the isochronous stress-strain data. The L_r cut-off, equivalent to that shown in Figure 2.7, is calculated from Equation (2.106) where σ_r is the rupture stress at the assessment time obtained from Equation (2.6). The second part of Equation (2.106) is for consistency with the FAD approach in R6.

$$L_r^{max} = \frac{\sigma_r}{\sigma_{0.2}^{c}} \leq \frac{2\sigma_r}{\sigma_{0.2} + \sigma_u} \tag{2.106}$$

The assessment point on the diagram is defined by Equations (2.107) and (2.108) where K_{mat}^{c} is the creep toughness. The creep toughness may be obtained from a creep crack growth test using Equation (2.109) where η is same as the value used in Equations (2.66) and (2.74) and Δ_c is the experimental load-line displacement due to creep. A typical experimental force vs. load-line displacement plot for a creep crack growth test is provided in Figure 2.12. The crack length, a, in Equation (2.109) includes the crack extension Δa.

$$K_r = \frac{K}{K_{mat}^{c}} \tag{2.107}$$

$$L_r = \frac{\sigma_{ref}}{\sigma_{0.2}^{c}} \tag{2.108}$$

$$K_{mat}^{c} = \sqrt{K^2 + E' J^p + \frac{n}{n+1} \frac{EP\Delta_c}{B_N (W-a)} \eta} \tag{2.109}$$

A single creep crack growth test will provide a correlation between Δa and Δ_c but each set of data points will correspond to a different time. In order to obtain the dependence of K_{mat}^{c} on time for a given Δa or the dependence of K_{mat}^{c} on Δa for a given time, a number of tests at different reference stresses are required.

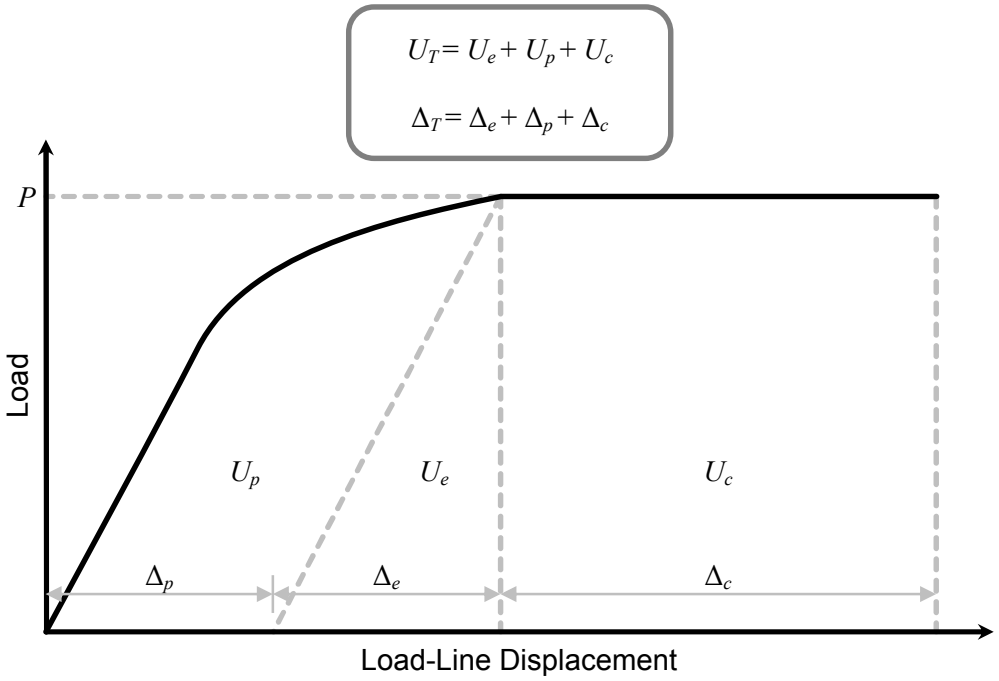

Figure 2.12: Schematic force vs. load-line displacement plot for a typical creep crack growth test.

An alternative approach to calculating K^c_{mat} has been implemented by some authors e.g. [50] based on the procedure for calculating J in ESIS P2-92 [1]. This approach uses the total strain energy, U_T, defined in Figure 2.12 which avoids the need to separate the various components of displacement. This calculation is provided in Equation (2.110).

$$K^c_{mat} = \sqrt{E' \frac{\eta U_T}{B_N (W - a)}} \qquad \textbf{(2.110)}$$

Based on the above definitions, the coordinates of the assessment point, L_r and K_r are both time dependent as is the TDFAD. For a given assessment time the crack extension is predicted to have exceeded Δa if the assessment point falls outside the TDFAD. If it falls inside the TDFAD then the crack extension is less than Δa. The time for the crack increment associated with initiation to occur, Δa_i, corresponds to the time when the assessment point falls on the TDFAD which can be obtained by iteration.

2.4.6 Experimental CCI Correlations

Similar to crack growth rates, initiation times may also be correlated to a suitable crack tip parameter to produce empirical laws. For creep ductile materials, this is usually the steady-state crack tip parameter C^*. A power-law fit in the form of Equation (2.111) is most commonly used where γ and q are material constants which may be temperature and stress state dependent [6].

$$t_i = \gamma C^{*-q} \quad \textbf{(2.111)}$$

2.4.7 Other CCI Models

Other CCI prediction models are also available in the literature, but are less widely used. Upper and lower bound predictions of the time for CCI to occur may be obtained from the initial and steady-state crack growth rates predicted by the NSW model [8]. Riedel and Rice [41] proposed a model which assumes that crack growth occurs when the equivalent strain at a small structural distance ahead of the crack tip achieves a critical value. Alternatively, Davies [51] proposed a more comprehensive model which accounts for stress redistribution from initial elastic or elastic-plastic conditions, to small scale creep, transition creep and eventually widespread creep.

Chapter 3:

Review of Techniques for Measuring Crack Initiation and Growth

3.1 Introduction

This chapter presents a review of the experimental techniques used to measure crack initiation and growth in the laboratory. The following research considers both room temperature and high temperature applications so the scope of this review is restricted to techniques capable of operating in both these environments. The Potential Drop (PD) is the most common technique for high temperatures applications [52], particularly in the field of creep [53]. For this reason it is the only method recommended in ASTM E1457-13 [3] and is the primary focus of this chapter. There are two main forms of the PD technique: Direct Current Potential Drop (DCPD) and Alternating Current Potential Drop (ACPD). ACPD can be further categorized into low frequency and high frequency. These three variants of the PD technique are reviewed in detail followed by the elastic unloading compliance and optical techniques which have also been implemented with some success. Each of these techniques is critically reviewed, with specific consideration given to the influence of strain. A brief discussion of some other techniques is also presented.

3.2 DCPD

All variants of the PD technique work on the principle that a constant current flowing through a specimen containing a crack generates an electrical field which is sensitive to changes in the geometry of the specimen, in particular crack extension. As the crack grows the PD, measured between two probes located either side of the crack, will increase. By using a suitable calibration function, this can be correlated to a crack extension. The following discussion relates specifically to DCPD.

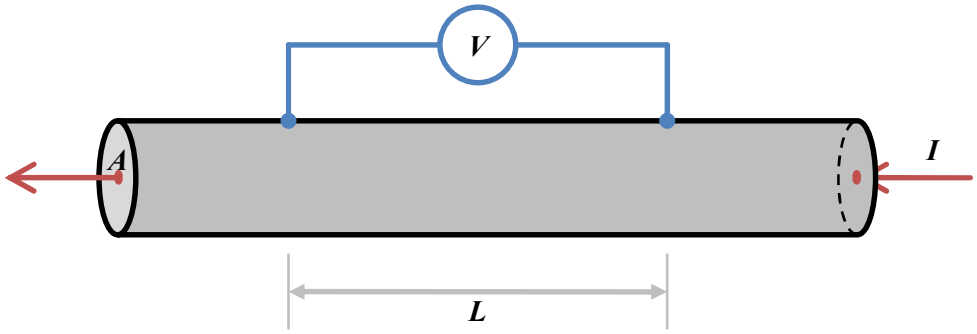

Figure 3.1: A direct current, I, applied to a rod of uniform cross-section, A, with the potential drop, V, measured over a central gauge length, L.

Figure 3.1 shows a rod of uniform cross-section, A, with a direct current, I, applied at a point source in the centre of one end, and a point sink at the centre of the other. The potential drop, V, is measured across a central gauge length, L. When a direct current is applied to a conductor, it tends to fill the cross section, limited only by the separation of the source and sink [54]. In Figure 3.1, if the ends of the rod are suitably remote from the gauge length, the current in the gauge region will be uniformly distributed and the resistance, R, can be calculated from Equation (3.1), where ρ is the resistivity of the material. This assumes an isotropic, homogeneous material.

$$R = \rho \frac{L}{A} \tag{3.1}$$

The potential drop measured across the gauge region, V, can then be calculated using Ohm's law, Equation (3.2):

$$V = IR \tag{3.2}$$

It can be seen from Equations (3.1) and (3.2) that for this simple case, the potential drop is inversely proportional to the cross section. Introducing a crack into the gauge region, as shown in Figure 3.2, creates a local reduction in cross-section which increases the resistance and therefore the PD measured along the gauge length. The crack also disturbs the electric field such that the current distribution local to the crack is no longer uniform and the relationship between PD and crack size is no longer simple. A calibration function is therefore required to convert potential drop to crack length.

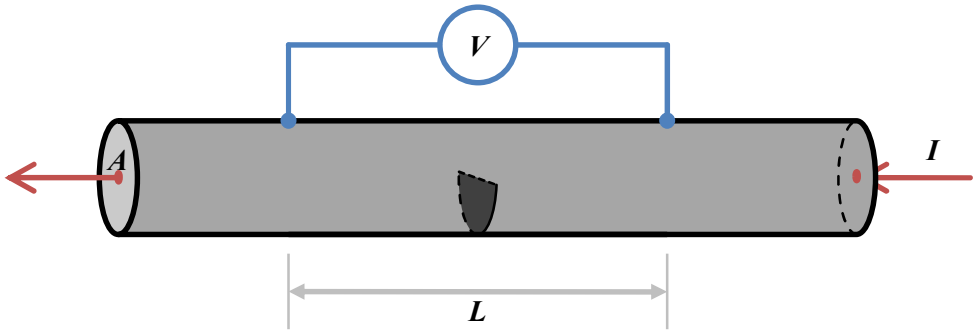

Figure 3.2: A direct current, I, applied to a rod with the potential drop, V, measured over a central gauge length, L, containing a semi-circular crack.

3.2.1 Calibration

Calibration functions are often expressed in terms of a normalised PD and a normalised crack length [55, 56]. The PD, V, is usually normalised with respect to a value, V_n, corresponding to a normalising crack length, a_n. This makes the calibration independent of the magnitude of the applied current and the material resistivity provided they remain constant. It is also independent of specimen thickness as long as the current is injected sufficiently remote from the crack and the PD probes. The crack length, a, is normalised with respect to another in-plane dimension [57-59]. This is usually the normalising crack length or the characteristic specimen width, W. This makes the calibration independent of specimen size, as long as the dimensions remain in proportion. This includes the configuration of the current injection and the PD probes,.

If the calibration function is normalised with respect to the initial crack length, a_0, and the corresponding PD, V_0, the initial crack length is usually obtained by optical measurement either from the surface of the specimen at the start of the test or from the fracture surface after the test. Assuming accurate measurement of this initial crack length, this normalisation will suppress small geometrical differences between the actual and nominal specimen geometry [57, 58]. If however this initial crack length is not measured accurately, it will be a source of systematic error for all crack length measurements [60].

3.2.1.1 Deriving Calibration Curves

For a specimen with an applied electric current, the static electric field is described by Equation (3.3) assuming there is no free charge [61].

$$\nabla^2 V = 0 \tag{3.3}$$

This is Laplace's equation where ∇^2 is the Laplacian. For a three dimensional conductor in a Cartesian co-ordinate system, this can be rewritten as Equation (3.4) [61].

$$\frac{\partial^2 V}{\partial x^2}+\frac{\partial^2 V}{\partial y^2}+\frac{\partial^2 V}{\partial z^2}=0 \qquad \textbf{(3.4)}$$

For fracture specimens, this is often simplified to a two dimensional problem by assuming the current distribution is uniform through the thickness [58, 60, 62] as shown in Equation (3.5).

$$\frac{\partial^2 V}{\partial x^2}+\frac{\partial^2 V}{\partial y^2}=0 \qquad \textbf{(3.5)}$$

To generate a calibration function for a given geometry it is necessary to find the solution to Laplace's equation. This can be achieved analytically, numerically or empirically.

3.2.1.2 Analytical Calibration

Where the boundary conditions of the specimen are known, Laplace's equation can be solved analytically using, for example, conformal mapping techniques [58, 62-64]. When performing such calculations the free surfaces of the specimen are generally assumed to be perfectly insulated with the exception of the current injection locations where a uniform current is assumed. Symmetry of the electric field about the plane of the crack is often utilised to simplify the calculation [60].

Analytical calibration functions provide an exact solution for the nominal specimen geometry and idealised boundary conditions. They also tend to be general solutions written in terms of the specimen dimensions making them highly suited to parametric studies, e.g. [62]. This general form also allows the user to select the normalising crack size to match the initial crack length which can usually be determined with a high degree of accuracy.

$$\frac{a}{W}=\frac{2}{\pi}\cos^{-1}\left[\frac{\cosh\left(\frac{\pi y}{2W}\right)}{\cosh\left(\frac{V}{V_0}\cosh^{-1}\left\{\frac{\cosh\left(\pi y/2W\right)}{\cos\left(\pi a_0/2W\right)}\right\}\right)}\right] \qquad \textbf{(3.6)}$$

One of the most common calibration functions referenced in the literature was derived by Johnson [58] for a Middle Tension, M(T), specimen using analytical methods. This calibration function is provided in Equation (3.6) and the corresponding geometry is shown in Figure 3.3 which includes an infinitesimally thin crack with a remotely applied uniform current. The analysis performed by Johnson was extended by Gilbey and Pearson [65] to

consider a point application of the current and PD probe locations off the centre-line of the specimen.

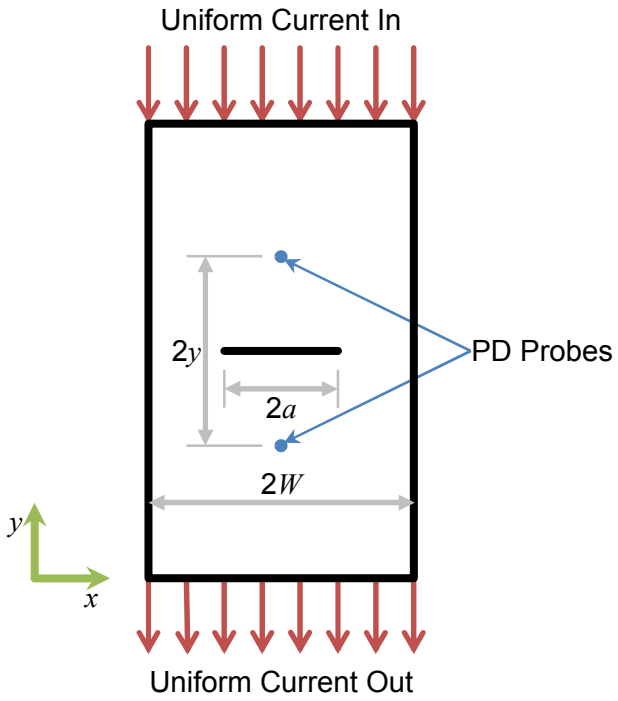

Figure 3.3: M(T) specimen geometry used to derive Equation (3.6) [58].

Although Johnson's formula was originally derived for the geometry shown in Figure 3.3, Schwalbe and Hellman [66] demonstrated experimentally that it could also be applied to Compact Tension, C(T), and Single Edge-Notch, SEN, specimens due to the geometric similarities shown in Figure 3.4. By splitting an M(T) specimen along its centre line, two SEN specimens are obtained as shown in Figure 3.4(a). Furthermore, a C(T) specimen is effectively a short SEN specimen as shown in Figure 3.4(b). The term SEN incorporates both Single Edge-Notch Bend, SEN(B), and Single Edge-Notch Tension, SEN(T), specimens which are geometrically equivalent for the purpose of calibration where deformation is not considered.

The main disadvantage of analytical calibration is that the mathematics is relatively complex [63]. As the complexity of the specimen geometry increases analytical techniques cannot be easily applied and an alternative method is often required [67].

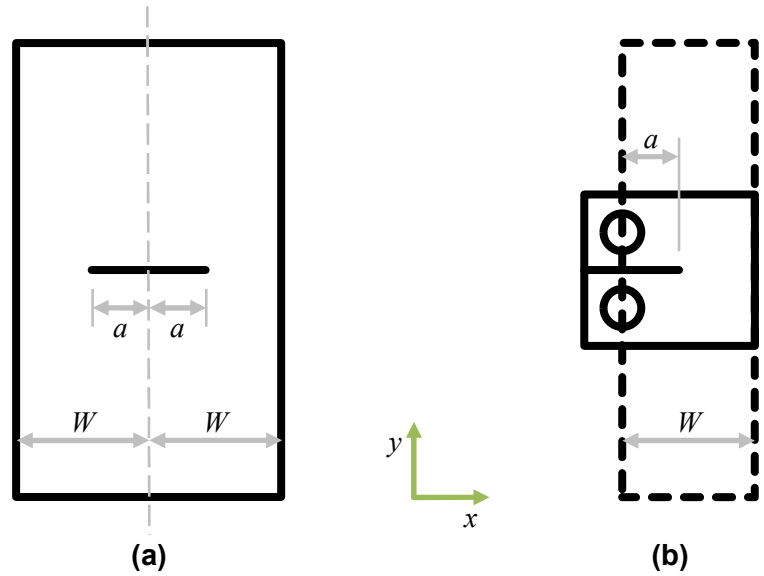

Figure 3.4: Similarities between (a) M(T) and SEN specimen geometries, and (b) SEN and C(T) specimen geometries.

3.2.1.3 Numerical Calibration

Numerical techniques such as FE analysis [56, 67-70] and finite boundary analysis [71] can also be used to solve Laplace's equation and, unlike analytical techniques, are not restricted to simple geometries. An example of a numerically derived calibration function for a C(T) specimen is provided in Equation (3.7) [55].

$$\frac{a}{W} = 0.0002398\left(\frac{V}{V_n}\right)^3 - 0.1398\left(\frac{V}{V_n}\right)^2 + 0.8857\left(\frac{V}{V_n}\right) - 0.5051 \qquad \textbf{(3.7)}$$

Equation (3.7) was originally derived by Hicks and Pickard [68] by fitting a third order polynomial to discrete data points calculated from multiple FE analyses of a C(T) specimen with different crack lengths. Unlike Equation (3.6) this is not a general solution and is only valid for a specific PD configuration and a normalising crack size, a_n, of $0.241W$. To use Equation (3.7) it is necessary to obtain the normalising PD, V_n, which corresponds to this crack size. If the initial crack length, a_0, is $0.241W$ then this is simply the initial PD, V_0, but if not then it must be calculated from the initial crack length and PD. This is achieved by rearranging the calibration function to make V_n the subject and substituting in a_0 and V_0 for a and V respectively. For simple calibration functions, e.g. a power law fit, this rearrangement is a trivial matter but for the polynomial in Equation (3.7) an easier approach is to fit another polynomial to the original numerical data with the abscissa and ordinate switched which produces Equation (3.8).

$$\frac{V_0}{V_n} = 1.6898\left(\frac{a_0}{W}\right)^3 - 1.0712\left(\frac{a_0}{W}\right)^2 + 1.9169\left(\frac{a_0}{W}\right) + 0.5766 \quad \textbf{(3.8)}$$

Numerical calibration has the advantage of being easily applied to complex geometry and non-uniform current distributions [67]. It is also easy to perform parametric studies to optimise the specimen geometry and the PD configuration [56, 71]. Other complexities such as deformation and loading pin contact can also be considered in the numerical analysis [72].

The main draw-back of this approach is that it relies on fitting a curve to the data or, in the case identified above, fitting *two* curves to the data. The accuracy of the calibration function is therefore limited by this fit which can introduce significant errors when measuring small crack extensions [62].

3.2.1.4 Empirical Calibration

The third method of deriving a calibration function is from empirical data. The PD is measured for a range of crack lengths on a physical specimen and, similar to the numerical approach, a curve is fitted to the discrete data points. Fatigue is often used to grow a crack in a controlled manner [56, 57, 63, 68, 73]. By recording the PD at various points throughout the test and marking the fracture surface at the same time, post-test crack length measurements can be correlated to the PD. A calibration function based on measurements from the fracture surface can correct for uneven crack growth, unlike optical surface measurements [73]. The fracture surface may be marked by varying the fatigue loading [56, 57, 68, 73] or by heat tinting [63]. An alternative approach is to use multiple nominally identical specimens and grow the crack to different lengths in each specimen although this requires a large amount of material [67, 74].

Rather than using fatigue crack growth, the crack can be incrementally machined into the specimen, often by Electrical Discharge Machining (EDM) or a saw cut [67, 69, 75, 76]. This approach ensures a straight crack front which negates the need to mark the fracture surface but it also introduces a blunt notch rather than a sharp crack which may influence the calibration [58, 75]. To avoid this some authors used graphitised conducting paper [71, 75] or aluminium foil [68, 77] cut to the shape of the specimen and produced a sharp crack using a scalpel or razor blade. This assumes that the current distribution is uniform through the thickness.

Empirical calibrations can be developed under the required experimental conditions, to incorporate test specific variables such as time dependent creep effects [78]. Despite this, they are considered less accurate than those developed using analytical or numerical

methods because they tend to be based on a limited number of data points with significant experimental scatter [62]. This scatter can be reduced by scaling up the specimen geometry [68] but this requires more material. They also suffer from many of the limitations experienced by numerical calibration because they also rely on a curve fitted to discrete data points. For these reasons, empirical data are often used to validate calibration curves derived by other methods rather than to define them [62, 67, 69, 71].

3.2.2 Suppressing Proportional Changes in PD

As discussed in Section 3.2.1, the PD measured across the crack, V, is usually normalised with respect to a value, V_n, corresponding to a normalising crack length, a_n, so the calibration is independent of current magnitude and material resistivity provided they remain constant. The normalising PD is usually determined at the start of a test, so the calibration will be sensitive to any subsequent changes in applied current magnitude and material resistivity which occur throughout the test. These variations can have a significant influence on the measurement of crack extension [79].

Fluctuations in input current due to, for example, amplifier drift [79] will produce a change in the measured PD which is proportional to the magnitude of the signal. The same is true for factors which influence the resistivity of the entire specimen such as global temperature fluctuations [59, 79-81]. These fluctuations will have the same proportional effect on another measurement performed at the same time, on the same material, in the same environment and with the same equipment. This observation can be used to supress proportional changes in PD using either of the two methods discussed below.

3.2.2.1 Reference Measurement Remote from the Crack

The first method uses a reference measurement, V_{ref}, taken at the same time as the measurement across the crack, V, with the same equipment but at a location which is not influenced by crack growth. This reference measurement can be taken from the test specimen at a location remote from the crack [57, 59, 79] or on a nominally identical specimen in the same environment but without a growing crack [81-83]. It is used to correct the measurement using Equation (3.9) where V_{corr} is the corrected measurement and V_{ref0} is the value of V_{ref} at the start of the test.

$$V_{corr} = V \frac{V_{ref\,0}}{V_{ref}} \qquad \textbf{(3.9)}$$

Whilst this will supress proportional changes in PD from the measurement signal, it will also increase the noise on the signal because the reference signal, like the measurement signal,

is susceptible to electrical noise. By ensuring $V_{ref} \geq V$, this additional noise should be acceptable [55].

3.2.2.2 Two Measurements across the Crack

McCartney et al. [60] proposed an alternative approach where two PD measurements, V_1 and V_2, are taken across the crack at different locations, at the same time. Assuming the relationship between PD and crack extension is different at these two locations, the ratio of the two measurements will be dependent on crack extension, but independent of proportional changes in PD. This approach requires a calibration function derived based on the ratio of these measurements such as Equation (3.10) which was derived for a C(T) specimen [60].

$$\frac{a}{W} = 5062\left(\frac{V_1}{V_2}\right)^5 - 10338\left(\frac{V_1}{V_2}\right)^4 + 8415\left(\frac{V_1}{V_2}\right)^3 - 3415\left(\frac{V_1}{V_2}\right)^2 + 694.1\left(\frac{V_1}{V_2}\right) - 56.32 \qquad \textbf{(3.10)}$$

A calibration in this form does not require further normalisation based on a known crack size. This avoids the need for an initial, usually optical, crack length measurement. Instead, the initial crack length is determined directly from the PD measurement. It also avoids the complications associated with taking a reference measurement at a location which is truly independent of crack extension.

A disadvantage of this approach is that a calibration based on the ratio of two measurements, both of which are sensitive to crack extension, will inevitably be less sensitive to crack extension than a single measurement. In the extreme, the ratio V_1/V_2 could remain constant for all crack lengths and the measurement would be completely insensitive to crack growth.

3.2.3 PD Configuration

Calibration functions are geometry specific which includes the PD configuration, i.e. the location of the current injection and PD probes. Whilst the specimen type is selected based on the test requirements such as crack tip constraint and material availability, the PD configuration can be selected to optimise the accuracy of the crack growth measurement.

Optimisation of the PD configuration has been the subject of much research [56, 65, 71, 76, 84]. When comparing configurations, the following metrics were generally used:

- *'Sensitivity':* Change in PD with crack extension. The higher the sensitivity, the more accurately small increments in crack extension can be measured.
- *'Repeatability':* Change in PD due to small errors in the PD configuration. The smaller this change in PD, the better repeatability of the measurement.

- *'Measurability':* The magnitude of the PD at the start of the test. This was used to infer the signal-to-noise ratio. The larger the magnitude, the larger the signal-to-noise ratio.

One study also considered the linearity of the calibration function [71]. This simplifies the calculation of crack extension and provides constant sensitivity for all crack lengths however, no configurations were identified with a truly linear calibration function.

The preferred PD configurations suggested by previous optimisation studies are provided in Figure 3.5. The rationale behind these locations is discussed below.

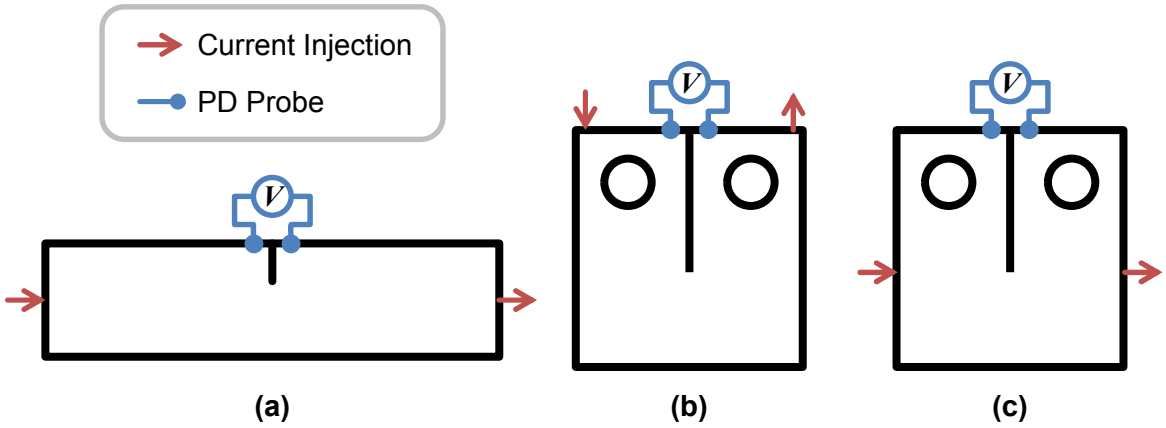

Figure 3.5: PD configurations suggested by previous optimisation studies for (a) a SEN specimen, (b) a C(T) specimen with current injection points on the front face, (c) a C(T) specimen with current injection points on the side flanks.

3.2.3.1 Current Injection

Injecting the current close to the crack generates a large local current density which provides good sensitivity but poor repeatability [71, 84]. Injecting the current remote from the crack generates a more uniform current distribution; reducing sensitivity but improving repeatability. The improved repeatability associated with remote current injection was typically preferred to the greater sensitivity which accompanies local current injection [56, 71, 84].

The large aspect ratio of a typical SEN specimen enables the current to be injected at a sufficiently remote location to produce a uniform current distribution in the region of the crack. These current injection points, shown in Figure 3.5(a), produce a calibration which is not sensitive to small changes in the current injection points [84]. The same is not possible for C(T) specimens. Due to the compact nature of the geometry, there is no equivalent location which is sufficiently remote from the crack [66, 84]. This suggests that C(T) calibration functions are sensitive to small variations in the location of the current injection

points however, such variations have not been considered in previous probe optimisation studies [56, 71]. The preferred current injection points are on the front face [69], or the side flanks [56, 71] as shown in Figure 3.5(b) and (c) respectively. Both of these locations have a similar sensitivity, but locating the current injection point on the front face improves the measurability [56].

Ritchie et al. [84] suggested applying the current by area contact to provide a more uniform distribution. This has been achieved experimentally by transmitting the current to the specimen using copper braid bolted to the specimen [71] or copper sheet soldered, brazed or screwed to the specimen [76, 84]. Whilst this approach will distribute the current over an area, difficulties have been identified with ensuring a consistent, uniform electrical contact for the duration of the test [76, 84].

3.2.3.2 PD Probes

Similar to the current injection, the most sensitive PD probe location is next to the crack tip however this reduces repeatability due to the sensitivity of the calibration function to small changes in probe location [84]. If the probes are moved behind the crack tip the sensitivity does not reduce significantly [65], but the repeatability is greatly improved [84]. For this reason, all of the probe optimisation studies identified have concluded that the preferred location is across the crack mouth, as close to the crack plane as possible [56, 65, 71, 76, 84]. Moving the probes ahead of the crack tip reduces sensitivity [65, 76] whilst moving the probes away from the crack plane reduces repeatability [56]. Locating the PD probes close to the current injection points also reduces repeatability [56].

3.2.3.3 Other Considerations

When selecting the optimum PD configuration, there is generally a compromise between sensitivity and repeatability. In all of the studies identified in the literature, this compromise is discussed in a purely qualitative manner [56, 71, 84] and the relative influence of these metrics on crack extension measurements has not been quantified. In addition, these previous studies did not consider other factors which may influence the optimum PD configuration such as the electrical resistivity of the specimen material, the amount of crack growth being measured (both of which will influence the magnitude of the PD signal) or the type of system used to take the measurements (which will influences the noise level on the PD signal). Also, they did not identify optimum configurations for a suitable reference measurement to suppress proportional changes in PD. It is therefore unclear from the existing research if the optimum PD configurations have been identified and if they are the same for all test conditions.

3.2.4 Influence of Strain

It is well known that strain can influence the electrical behaviour of materials since it is this phenomenon which is utilized in a typical resistance strain gauge. Using this as an example, the influence of strain on PD is discussed below. This is followed by a discussion of the influence of strain on crack length measurements performed using the DCPD technique.

3.2.4.1 A typical Strain Gauge

The gauge factor of a strain gauge, K_{sg}, is the sensitivity of the resistance, R, to the applied uniaxial strain, ε, as defined by Equation (3.11) [85]:

$$K_{sg} = \frac{\Delta R / R_0}{\varepsilon} \tag{3.11}$$

For isotropic materials, this can be written as Equation (3.12) [85] where ν is the Poisson's ratio and ρ and ρ_0 are the electrical resistivity of the strained and unstrained material respectively.

$$K_{sg} = 1 + 2\nu + \frac{\Delta \rho / \rho_0}{\varepsilon} \tag{3.12}$$

Alternatively, Equation (3.12) can be written as Equation (3.13) where K_g and K_m are calculated from Equations (3.14) and (3.15) respectively. K_g is the geometric gauge factor associated with a change in physical geometry. K_m is the material gauge factor associated with a change in the electrical resistivity.

$$K_{sg} = K_g + K_m \tag{3.13}$$

$$K_g = 1 + 2\nu \tag{3.14}$$

$$K_m = \frac{\Delta \rho / \rho_0}{\varepsilon} \tag{3.15}$$

The resistivity of the material depends on the number of charge carriers per unit volume, the total number of charge carriers and their mobility [85]. For elastic materials which undergo volumetric changes due to strain (ν < 0.5), the number of charge carriers per unit volume will change. It can therefore be shown that the material gauge factor, as calculated in Equation (3.15), contains a geometric term (1 - 2ν). When this is included in Equation (3.14), the total geometric gauge factor is 2 and is independent of Poisson's ratio [85].

For metal strain gauges operated in the elastic regime, the total gauge factor, K_{sg}, is material dependent and can range from -12.1 for Nickel to 6.1 for Platinum [86]. The material components of these gauge factors are therefore -14.1 and 4.1 respectively. In the plastic regime however, the influence of strain on resistivity is much smaller such that the gauge factor is often taken as 2 and material effects are ignored [85, 87, 88].

Madhi and Nagy [89] used non-contacting eddy current measurements to investigate the influence of elastic and plastic strain on the electrical conductivity of a uniaxial tensile specimen manufactured from type 304 stainless steel. The axial and lateral elastic material gauge factors, corresponding to Equation (3.15), were 1.35 and 1.95 respectively. Comparisons between an as-received specimen and one containing 15% plastic strain demonstrated negligible change in the axial direction and only a very small reduction in conductivity in the lateral direction. This was more than an order of magnitude less than the corresponding elastic value and reduced with temperature such that above 250ºC it was negligible. This is consistent with the findings of other authors who measured the PD along the gauge length of uniaxial tensile tests performed on 316L [83], X70 pipeline steel and S690 structural steel [90]. The measurements were in good agreement with hand calculations and FEA, both of which neglected material effects of strain on PD. These various studies confirm that the geometric effects dominate in the presence of significant plastic strain.

3.2.4.2 Influence of Strain on DCPD Crack Length Measurements

Strain has been identified as a significant source of error in crack length measurements using the DCPD technique [52, 57, 75, 78, 91]. It is most significant prior to initiation and the influence of strain is often ignored during crack growth [75, 91]. In some cases, such as low cycle fatigue, the majority of the strain effects can be identified from the first few cycles, which makes it relatively simple to suppress e.g. [83]. In other cases however, such as fracture toughness and creep crack growth testing, strain is constantly changing, particularly during the early stage of the test, so it is much more difficult to isolate the change in PD due to crack extension.

Research has been performed to decouple the effects of strain and crack extension during fracture toughness testing of tough, ductile materials. This has resulted in two separate methods of interpreting the PD data which are shown schematically in Figure 3.6. The method shown in Figure 3.6(a) is based on a plot of load vs. PD and is herein called the ‘load’ method. The method shown in Figure 3.6(b) is based on a plot of Crack Opening Displacement (COD) vs. PD and is herein called the ‘COD’ method. These methods are included in some fracture toughness standards e.g. [1, 2].

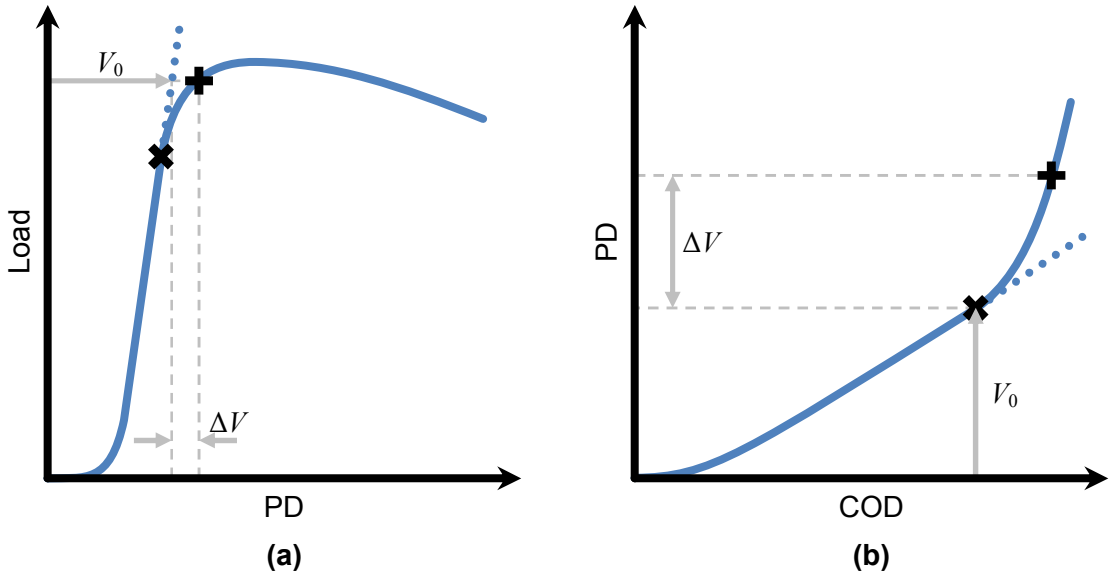

Figure 3.6: Interpretation of DCPD data during fracture toughness testing using (a) the 'load' method and (b) the 'COD' method. The point of crack initiation is identified by '×' and the PD values used to calculate crack extension at '+' are shown.

The 'load' method is based on a linear regression applied to the initial steep portion of the load vs. PD plot. The onset of crack blunting is assumed to correspond to the point where the data deviates from this linear trend, labelled '×' in Figure 3.6(a). The subsequent crack extension, which consists of crack blunting and stable tearing, is calculated using a standard calibration function, but the value of V_0 is assumed to be a function of the applied load, P. This function is the equation of the linear regression. The values of V_0 and ΔV used to calculate crack extension corresponding to the point labelled '+', are shown.

In this method, the DCPD is used to measure the total crack extension due to the combination of blunting and stable tearing. To calculate the initiation fracture toughness, J_{IC}, it is necessary to identify the onset of stable tearing. This is achieved by comparing a plot of J vs Δa, obtained experimentally, with a suitable blunting line. The onset of stable tearing is identified as the point where the two diverge. Alternatively the amount of blunting may be observed from post-test SEM measurements of the Stretch Zone Width (SZW).

The 'COD' method was originally proposed by Lowes and Fearnehough [75]. Unlike the 'load' method, the DCPD is only used to measure stable tearing. A linear regression is applied to a plot of PD vs. COD where COD could be CMOD or LLD. The onset of stable tearing is assumed to correspond to the point where the data deviates from this linear trend. This is labelled '×' in Figure 3.6(b). The subsequent tearing is calculated using a standard calibration function and a fixed value of V_0. The values of V_0 and ΔV used to calculate crack extension at the point labelled '+', are shown. The crack extension due to blunting is not

obtained from the PD technique and is instead assumed to follow a suitable blunting line. Alternatively it could be obtained from post-test SEM measurements of the SZW.

Crack length predictions from both of these methods have been compared with measurements from the final fracture surface for a range of materials [82]. Results from the 'COD' method were in better agreement with the fracture surface measurements, particularly for high toughness materials where the 'Load' method significantly over estimated crack extension and underestimated J_{IC}. Despite the general success of the 'COD' method, a limitation has been identified when testing high toughness, high tearing resistance and high hardening materials whereby the point of deviation from linear, labelled '×' in Figure 3.6(b), can be difficult to identify. Similar observations have been made by other authors [91, 92].

Although creep crack growth tests are likely to experience a similar increase in PD due to strain prior to the onset of crack growth [6, 78], an equivalent approach has not been developed. The current guidance in the most common creep crack growth standard, ASTM E1457-13 [3], states that the initial PD, V_0, used in the calculation of crack length, should correspond to the value at the end of load-up. This supresses the influence of any elastic or plastic strains which occurs during load-up, but not the subsequent creep strains. This is a potentially significant source of error when testing creep ductile materials.

To investigate the influence of strain on PD measurements, FE analyses of cracked specimens have been performed. Ljustell [83] performed a sequentially coupled structural-electrical FE analysis of a C(T) specimen with a stationary crack. Large plastic strains were demonstrated to have a significant influence on the PD in the absence of crack extension although validation of the results was not presented. Ke and Stahle [72] performed a similar analysis on a three point bend specimen. The model included gap elements to model electrical contact between the loading pins and the specimen. The results compared well with experimental data however; the amplification of the PD system in the experiment was unknown so the magnitude of the FE predictions could not be checked. Both of these studies only considered geometric effects of strain on PD and assumed that any change in material resistivity due to strain was negligible.

3.2.5 Other Sources of Error

3.2.5.1 Thermal EMF

Another potential source of error in DCPD measurements is thermal EMF [52, 57, 79]. A voltage or EMF is induced in a conductor that is subjected to a thermal gradient. The magnitude of the voltage is material specific. In an electric circuit consisting of a single material subject to a thermal gradient, all thermal EMFs will cancel each other out however,

if the circuit contains multiple materials e.g. different materials for the specimen and the PD leads, then a voltage will be induced in the measuring circuit which is not related to crack growth. The most common approach to mitigate this source of error is to switch the current off periodically throughout the test. The PD measured in the absence of the applied current is the error due to thermal EMF and can be subtracted from the measurements taken with the current applied [57]. A similar approach is to take two PD readings for each data point, one with the current polarity switched. The average of these two readings is the thermal EMF [3].

3.2.5.2 Crack Morphology

Calibration functions typically assume an ideal straight fronted, planar crack however, real cracks often do not to exhibit such behaviour. In cases where the crack faces are rough or the crack opening displacements are small, shorting can occur between the faces which results in the PD under-predicting crack extension [76]. Also, despite claims that DCPD measurements are related to some average crack extension, making it suitable for measuring tunnelling and discontinuous cracks [53], it has been shown that it tends to underestimate the mean crack extension [92].

In cases where crack morphology results in significant errors, a linear correction in the form of Equation (3.16) can be applied to the PD measurements where a_0 and a_f are the initial and final crack lengths obtained from the fracture surface and a_{pf} and a_p are the final and instantaneous predicted crack lengths based on the PD [76]. This approach is included in ASTM E1457-13 [3] for measuring creep crack growth where discontinuous cracking can result in significant errors in crack length measurements.

$$a = \left[\frac{\left(a_f - a_0\right)}{\left(a_{pf} - a_0\right)} \left(a_p - a_0\right) \right] + a_0 \qquad \textbf{(3.16)}$$

3.2.5.3 Noise

One of the main issues with DCPD is the difficulty in isolating the signal from any electrical noise. For this reason DCPD is generally unsuitable to noisy environments [93]. Even when implemented under laboratory conditions, large currents are required to obtain the necessary signal-to-noise ratio [52]. This can result in Joule heating of the specimen which can be a problem when trying to perform a test at room temperature although the current requirements of modern DCPD systems have significantly reduced [73].

3.2.5.4 Initial Drop in PD

Another complication specific to creep crack growth testing is an initial drop in PD which is sometimes observed early in the test. The cause of this behaviour remains unknown although it has been suggested that it may be related to dislocation rearrangement during primary creep and changes in precipitate size and spacing [78]. To mitigate this, the guidance in ASTM E1457-13 is to extrapolate the minimum value of PD back to zero time.

3.3 ACPD

When an alternating current (AC) passes through a conductor the distribution of this current is related to the geometry of the component, the material and the frequency of the applied current. The current density is highest at the surface which is known as the 'skin effect'. If the frequency is sufficiently high, the AC distribution through a cross-section of the gauge length of the conductor shown in Figure 3.1 is shown schematically in Figure 3.7.

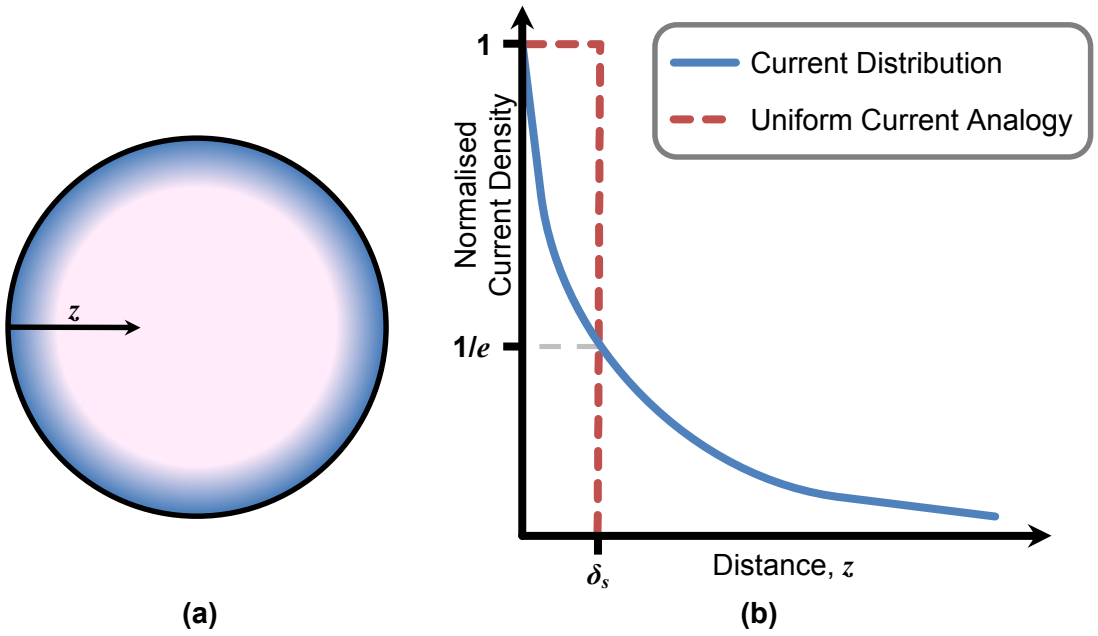

Figure 3.7: High frequency AC distribution through the cross-section of a cylinder

The current distribution is often simplified to a uniform current acting over a distance, δ_s. This distance is known as the skin depth and is shown in Figure 3.7(b). This is the depth at which the current amplitude reduces to 1/e (~37%) of the surface value. This simplification makes the AC analogous to a DC in the skin region only. For good conductors, e.g. metals, the skin depth can be calculated from Equation (3.17) where f is the frequency, ρ is the resistivity and μ is the magnetic permeability of the material.

$$\delta_s = \left(\frac{\rho}{\pi f \mu} \right)^{\frac{1}{2}} \quad \textbf{(3.17)}$$

Unlike DC, where the opposition to the flow of electric charge is due to the material resistivity only, the opposition to the flow of AC is a combination of resistive and reactive components. The resistive component is the same as the DC resistance, but the reactive component consists of capacitive reactance and inductive reactance which are both a function of frequency. The combination of the resistive and reactive components is known as the impedance, Z. Based on the skin depth analogy, the impedance of the gauge length of the cylinder shown in Figure 3.1 may be calculated from Equation (3.18) where A_{eff} is the effective area estimated from the skin depth using Equation (3.19) and r is the radius of the cylinder [79].

$$Z = \rho \frac{L}{A_{eff}} \quad \textbf{(3.18)}$$

$$A_{eff} = 2\pi r \delta_s \quad \textbf{(3.19)}$$

These equations are only applicable to situations where the frequency is sufficiently high, such that the skin depth is much smaller than the radius of the cylinder. At lower frequencies, where the skin depth calculated from Equation (3.17) is much greater than the radius of the cylinder, a quasi-DC current distribution exists.

There are two forms of the ACPD technique: high frequency and low frequency. High frequency ACPD applies to cases where the skin effect is significant. Low frequency ACPD applies to quasi-DC conditions where the skin effect is negligible. Whether a technique is considered high frequency or low frequency is dependent on the specimen geometry, the material and the applied frequency. For typical fracture specimen geometries, some materials, such as 2.25Cr-1Mo ferritic steels, experience a significant skin effect at frequencies as low as 50Hz [81], whilst others, such as Type 304 stainless steel, experience negligible skin effect at much higher frequencies [94].

3.3.1 High Frequency ACPD

By limiting the current to the skin region, the high frequency AC impedance of a specimen is significantly larger than its DC resistance. This reduces the input current required to produce a signal of a given magnitude [52, 79]. In addition, phase sensitive detectors (or lock-in amplifiers) which filter out noise at frequencies other than that of the applied current often result in a better signal-to-noise ratio than an equivalent DCPD system so the

magnitude of the current may be further reduced [52, 53, 73, 95]. This large signal-to-noise ratio makes ACPD particularly suited to noisy environments [96] and the low current requirements avoid the complications associated with Joule heating.

Another benefit of high frequency ACPD is current focusing [97]. By locating the current leads close to the surface of the specimen, but electrically isolated from it, the electrical current is focused in the region of the lead. This approach can be used to control current density thus further increasing the sensitivity of the ACPD technique [98].

3.3.1.1 Calibration

Assuming that the applied frequency, magnetic permeability and material resistivity remain constant such that the skin depth does not change throughout the test, the impedance is directly proportional to the length of free surface, L, between the two PD probes as demonstrated by Equation (3.18). It follows that the measured ACPD signal is approximately proportional to the crack length such that linear interpolation, based on Equation (3.20), is often used to estimate the crack length from the instantaneous PD, V, where a_0 and a_f are the initial and final crack lengths measured from the post-test fracture surface and V_0 and V_f are the corresponding PD measurements [79, 81, 99, 100].

$$a = a_0 + \frac{\left(V - V_0\right)}{\left(V_f - V_0\right)}\left(a_f - a_0\right) \qquad \textbf{(3.20)}$$

The assumption that the resistivity and magnetic permeability of the material remain constant is not always true, since both are sensitive to other factors, e.g. strain [79, 81, 99, 100]. Equation (3.20) also assumes that the only current path is via the crack tip however, alternative current paths which do not include the crack tip provide alternative parallel current paths e.g. such as via the back or side faces of the specimen [101]. For these reasons, the linearity of the calibration function is often confirmed experimentally [100, 101].

3.3.1.2 Suppressing Proportional Changes in PD

When using ACPD the most common method of supressing proportional changes in PD due to temperature fluctuations is to take a reference measurement on a nominally identical specimen which is not loaded [79, 81]. This is also the approach recommended in ESIS P2-92 [1]. The reference measurement also suppresses variations in current which occur during the test; however, this is less important for ACPD because the electronics tend to be inherently more stable than DCPD systems [81].

3.3.1.3 PD Configuration

The linear calibration function usually applied to high frequency ACPD measurements is derived based on post-test fracture surface measurements. It does not require a predetermined calibration function, so the location of the PD configuration is of less importance than DCPD and has not been addressed in the literature.

3.3.1.4 Influence of Strain

High frequency ACPD has been successfully implemented to measure stable tearing during fracture toughness testing of various steels at room temperature [79, 81, 99, 100]. The approach used by many of these studies is included in the ESIS P2-92 standard [1] and is described here.

A typical plot of ACPD and load against COD is provided in Figure 3.8; it consists of four separate stages. In Stage 1, on initial loading, there is an increase in PD. This is due to the elimination of shorting across the faces of the fatigue pre-crack [81, 99, 100]. For specimens where the pre-crack is introduced by Electrical Discharge Machining (EDM) such that the two faces of the pre-crack are not initially in contact, this increase in PD is not observed [81, 99]. Once this electrical shorting has been eliminated, a maximum in the PD occurs followed by a linear decrease (Stage 2). This corresponds to the elastic response of the structure and is caused by the dependence of the electrical resistivity and magnetic permeability of the material on elastic strain [79, 81, 99, 100]. Once the global response of the structure becomes non-linear due to significant plasticity, the reduction in PD also becomes non-linear. This is Stage 3 which continues until a minimum in the PD occurs, labelled '×' in Figure 3.8. This minimum is often associated with the onset of stable tearing and the subsequent increase in PD during Stage 4 is attributed to crack extension [79, 81, 99, 100] assuming that any further influence of strain is negligible. The instantaneous stable tearing corresponding to the point labelled '+' in Figure 3.8 is estimated from Equation (3.20) where the necessary PD values are shown.

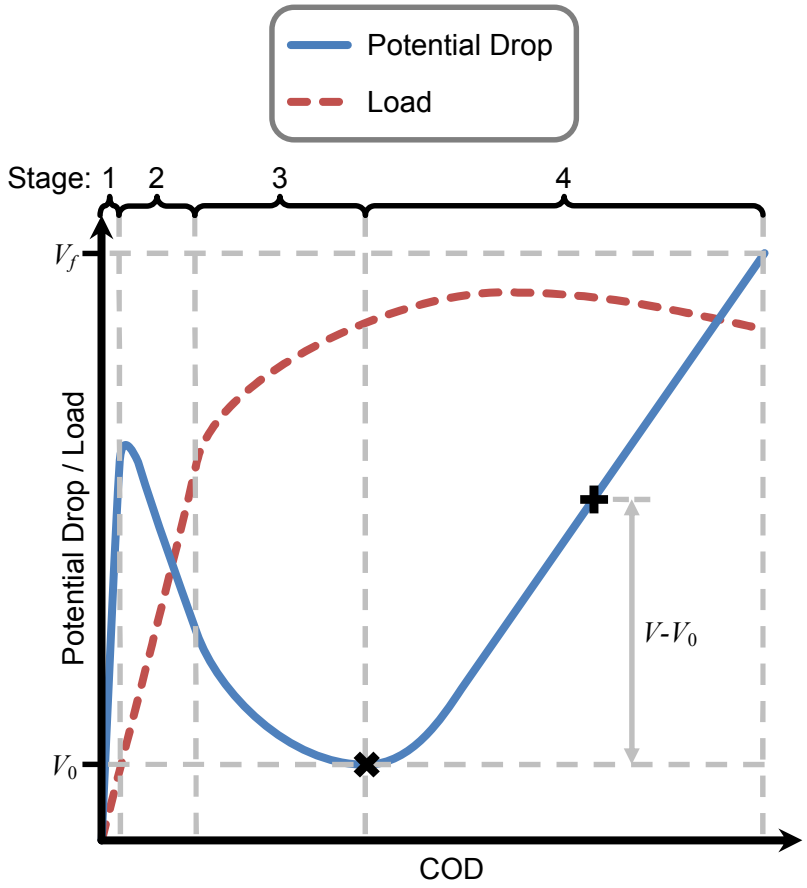

Figure 3.8: Typical ACPD/Load vs. COD plot obtained from a typical fracture toughness test performed on a tough, ductile material.

The value of J_{IC} measured using this approach can be dependent on the frequency of the applied current [100, 101]. This suggests that the minimum does not always correspond to the onset of stable tearing. One suggestion is that the minimum can occur when the plastic zone extends outside the skin depth such that it no longer has a significant influence on the magnetic permeability of the material in the skin region and the increasing distance between the PD probes due to blunting begins to dominate the PD response. To avoid this it was recommended that the frequency was selected such that the skin depth remains larger than the plastic zone size [100].

Alternatively, a different method of interpreting the high frequency ACPD data has been proposed [99]. It was suggested that by extrapolating the linear relationship between load and PD during Stage 2, the influence of strain on PD at higher loads could be determined. Using this to correct the PD data for strain effects (assuming that the influence of plastic strain on magnetic permeability is small) the onset of stable tearing was identified from a plot of corrected PD vs. J where it deviated from linear.

The interpretation of high frequency ACPD data during fracture toughness testing is more complex than for DCPD because of the dependence of the magnetic permeability on strain. This has resulted in some uncertainty regarding the most appropriate method of identifying the onset of stable tearing. For creep crack growth testing there is no comparable procedure for interpreting high frequency ACPD data.

3.3.1.5 High Frequency ACPD – Other sources of Error

One of the main disadvantages of high frequency ACPD is the relatively complex and therefore expensive electronics compared to DCPD [52, 80, 95]. It can also be sensitive to interference from other electrical equipment [52] or ferromagnetic material [79]. Cross-talk between the current and voltage leads can also produce signals not related to crack growth although this effect can be reduced by keeping the current and voltage leads separate, fixing all of the leads in position to prevent movement during the test, twisting the voltage leads together, twisting the current leads together and reducing the applied current [52]. Capacitance effects across the crack faces can further complicate the signal [52] but, such effects are only significant at very high frequencies [79].

Although high frequency ACPD has been applied to high temperature applications, e.g. [95, 102, 103], it is rarely used for measuring creep crack growth where DCPD is almost exclusively used [53]. As well as the strain effects discussed above, other complications include interference from the heating equipment [95] and measuring discontinuous cracking which, if separated from the crack tip by more than the skin depth, will remain undetected [104].

3.3.2 Low Frequency ACPD

Low frequency ACPD was originally developed as an alternative to DCPD to avoid thermal EMF effects and to reduce the high current requirements [96]. It combines some of the benefits of DCPD and High frequency ACPD, but also has some of the disadvantages of both. To avoid repetition a brief summary of low frequency ACPD is presented here with reference to the discussion above.

Similar to high frequency ACPD, the use of phase sensitive detectors (or lock-in amplifiers) improves the signal-to-noise ratio compared to DCPD [96] albeit at the expense of more sophisticated electronics. This reduces the required input current although it remains larger than high frequency ACPD because it is not confined to the skin region. Despite this, it tends to be sufficiently low to avoid any heating effects. Low frequency ACPD systems suffer from similar sources of interference to high frequency ACPD such as the proximity to

other electrical equipment or ferromagnetic material and cross-talk between the current and PD leads. To avoid this, the same mitigations may be implemented.

The quasi-DC current distribution enables calibration functions derived for DCPD to be applied to low frequency ACPD [105] although the same detailed consideration of the most appropriate PD configuration is required. The PD measurement is therefore related to the remaining ligament ahead of the crack thus providing some average crack length measurement and some sensitivity to crack tunnelling and sub-surface defects [53, 105]. Proportional changes in PD can also be suppressed in a similar way. The post-processing of the PD data in the presence of large strains is also the same as for DCPD. This avoids the additional complexity associated with variations in magnetic permeability.

The main limitation of low frequency ACPD is that it requires a frequency low enough to produce the required quasi-DC current distribution by ensuring that the skin depth, as calculated from Equation (3.17), is large compared to the specimen dimensions. Typical systems often have a minimum frequency 1-2 Hz because at frequencies lower than this flicker noise can become significant. This is sufficiently low for common fracture specimen geometries manufactured from materials with a low magnetic permeability, such as austenitic stainless steels, but for materials with a high magnetic permeability, such as ferritic steels, the skin depth may be small enough to prevent the required quasi-DC current distribution [54].

3.4 Elastic Unloading Compliance

When a cracked specimen is partially unloaded, the behaviour tends to be linear and independent of prior plastic deformation [106] and the unloading compliance can be easily obtained from the load-displacement plot. As the crack advances, this compliance increases and can be correlated to a crack length using solutions available in the literature. Most of these solutions, such as the one provided in Equation (3.21) for a standard C(T) specimen, are derived from small displacement elastic FE analyses [107]. In this equation u is obtained from Equation (3.22), C_{LL} is the ratio of the change in LLD and the change in load, and B_e is the effective specimen thickness, calculated from Equation (3.23).

$$\frac{a}{W} = 1.000196 - 4.06319u + 11.242u^2 - 106.043u^3 + 464.335u^4 - 650.677u^5 \qquad \textbf{(3.21)}$$

$$u = \frac{1}{\left(B_e E C_{LL}\right)^{0.5} + 1} \qquad \textbf{(3.22)}$$

$$B_e = B - \frac{\left(B - B_N\right)^2}{B} \tag{3.23}$$

Solutions such as this one are not directly applicable to materials where large deformations accompany crack extension such as austenitic stainless steels. In these materials the elastic unloading compliance can significantly underestimate the crack length so a rotational correction must be applied [108].

The elastic unloading compliance technique is the most common method of measuring stable tearing for single specimen fracture toughness tests. The main benefits of this method are that it is cheap, simple to automate and easy to implement [109] and can be applied to high temperature environments [110]. In a few instances it has been applied to creep crack growth tests [111, 112] and is included in the European code of practice for creep crack growth [113] although periodic unloading may cause stress redistribution at the crack tip which could influence the crack growth rate [6].

The elastic unloading compliance is related to some average crack length [114] although it has been shown that it can underestimate the mean crack extension by up to 40% in the presence of crack tunnelling [115, 116]. Other sources of error include elastic displacements of the testing fixture, misalignment of the load train, frictional effects and local indentations in the shackles/loading pin assembly which can result in negative crack growth predictions [92, 106]. These sources of error can be mitigated by using flat bottomed pin holes in the shackles, roller bearings, or other modifications which allow the pins to freely rotate, even when bending [111, 117]. Additional difficulties have been identified due to some materials having large inelastic strain responses and for application to low compliant test geometries where a change in crack length has a small influence in the overall response of the specimen [82].

Comparisons between the elastic unloading compliance method and the DCPD technique have been performed for fatigue crack growth with large scale plastic deformation [83] and fracture toughness testing [118]. Both authors observed good agreement between the two techniques although the scatter in the partial unloading data was typically higher. Fewer measurements are also obtained when using the elastic unloading compliance method.

3.5 Optical Techniques

Optical methods directly observe the surface of the specimen with equipment such as a travelling microscope [67]. They rely on surface measurements to characterise the through thickness crack length and cannot capture crack tunnelling. This can result in significant

errors and in extreme circumstances, cracking can occur inside the specimen with no observable growth on the surface until final fracture [119]. Whilst crack tunnelling can be reduced by applying side grooves, this can make the crack more difficult to observe. Optical methods are therefore most reliable when testing thin specimens. When testing thicker specimens they are often used in conjunction with other methods such as the PD technique [79, 80].

The effect of crack tunnelling can also be corrected for by inspection of the post-test fracture surface [120]. This is discussed in ASTM E1457-13 [3] where a 9 point average crack length is taken at the start and the end of the test. Additional data points can also be obtained from a single specimen by marking the fracture surface throughout the test by heat tinting, fatigue beach marks or dye penetrant. Cortie and Garrett [121] demonstrated highly accurate crack length measurements using this method; however, this approach is not always possible, particularly during sustained load creep crack growth tests.

3.6 Other Techniques

The techniques described above are the main methods of measuring crack growth in the laboratory, particularly at high temperature. Some studies have considered alternative techniques, but these technologies remain in their infancy. Such techniques include ultrasonics [122] and acoustic emissions [123] where waveguides have been used to locate the temperature sensitive transducers away from the hostile environment.

3.7 Discussion

The most suitable technique for measuring crack initiation and growth at room temperature and high temperature is the PD technique. In some situations the elastic unloading compliance technique may also be suitable, but fewer measurements are obtained per test and increased scatter in the data has been observed when compared with the PD technique. This scatter is probably due to friction and misalignment of the load train which the elastic unloading compliance technique is particularly sensitive to. In addition, questions remain with regards to the suitability of the elastic unloading compliance technique for creep crack growth testing where regular unloading may influence the test results.

The relative advantages and disadvantages of the different variants of the PD technique are summarised in Table 3.1. Low frequency ACPD provides a good compromise between DCPD and high frequency ACPD for measuring crack initiation and growth in the presence of large strains. It has a high signal-to-noise ratio suitable for measuring small crack extensions such as those associated with initiation whilst the PD data is relatively simple to

interpret in the presence of large strains because it is not sensitive to changes in magnetic permeability. In addition, the measurement is sensitive to discontinuous cracking which is of particular concern for creep crack growth testing.

	DCPD	High Frequency ACPD	Low Frequency ACPD
Input Current:	High	*Very low (skin effect and phase-sensitive detection)*	*Low (phase-sensitive detection)*
Electronics:	*Simple & inexpensive*	Complex & expensive	Complex & expensive
Signal-to-noise ratio:	Low	*High*	*High*
Influence of large strains:	*Geometry & resistivity*	Geometry, resistivity & magnetic permeability	*Geometry & resistivity*
PD interpretation due to large strains:	*Relatively simple*	Complex	*Relatively simple*
Measured crack length:	*Some average crack length including sub-surface cracking*	Less sensitive to crack tunnelling and sub-surface cracking	*Some average crack length including sub-surface cracking*
Calibration:	Calibration function required (linear calibration sometimes assumed)	*Linear calibration often assumed*	Calibration function required (linear calibration sometimes assumed)
PD configuration:	Careful selection of PD configuration required.	*PD configuration less critical.*	Careful selection of PD configuration required.
Thermal EMF errors:	Yes	*No*	*No*
Suitable Materials:	*All Metals*	Not metals with high magnetic permeability	*All Metals*

Table 3.1: Comparison of the three main variants of the PD technique. Relative advantages *highlighted*.

Recently a low frequency ACPD system has been developed for in-situ monitoring of creep on power plant components [94]. This system demonstrates reduced noise and increased thermal stability compared to a typical DCPD system at frequencies as low as 2 Hz. This system will be implemented in this research.

One of the main disadvantages of low frequency ACPD (and DCPD), compared to high frequency ACPD, is that careful selection of the PD configuration is required to optimise the accuracy of the crack length measurement. Although suitable PD configurations are suggested in the literature, some uncertainty remains with regards to the most appropriate configuration for a wide range of conditions. This uncertainty will be addressed as part of this research.

Another limitation of the low frequency ACPD technique is that it is not suitable for materials with high magnetic permeability. This research will therefore focus on Type 316H stainless steel which is a ductile, austenitic stainless steel with a low magnetic permeability that will ensure that the low frequency ACPD system behaves in a quasi-DC manner. Conclusions based on this PD system and material should be applicable to all conducting materials when tested using a typical DCPD.

Chapter 4: Optimisation of the PD Configuration

4.1 Introduction

To calculate crack extension from a PD measurement, a calibration function is required. This function is specific to the specimen geometry and the configuration of the current injection and PD probes. The location of these electrical connections must be carefully selected to optimise the accuracy with which crack extension may be determined.

PD configuration optimisation studies have been published on C(T), SEN and M(T) specimens [56, 65, 71, 76, 84]. These studies did not consider the mechanical behaviour of each specimen, so the results for the SEN specimen are applicable to both the tension, SEN(T), and bend, SEN(B), variants of this geometry. A review of this work is presented in the previous chapter. A variety of metrics have been used to assess different PD configurations but the qualitative nature of these previous studies prevented a direct comparison of the relative importance of these metrics. As such, the preferred configuration was typically selected based on a preference for 'repeatability' over 'sensitivity'. In addition, these previous studies did not consider other factors which may influence the optimum PD configuration such as the electrical resistivity of the specimen material, the amount of crack growth being measured (both of which will influence the magnitude of the electrical signal) or the PD system used to take the measurements (which will influences the noise level on the signal). Also, they did not identify optimum configurations for any additional measurements used to suppress proportional changes in PD due to, for example, temperature fluctuations and/or amplifier drift. Further work is needed to address these limitations and ensure that a suitable PD configuration is implemented in the subsequent studies.

This chapter builds on the existing research to present a finite element based PD configuration optimisation study for two of the most common specimen geometries: C(T) and SEN. The metrics used in previous studies have been revised so they each relate to an error in the measurement of crack extension which allows them to be directly compared.

The other limitations of the previous studies are addressed by considering suitable extremes of material resistivity as well as small and large amounts of crack extension. The different methods of suppressing proportional changes in PD, discussed in the previous chapter, have also been assessed. The results are presented for a typical DCPD system and the low frequency ACPD system used in the following research.

4.2 Calibration Functions

For each of the PD configurations considered in this study, a calibration function has been derived in the form of Equation (4.1) where A_0, A_1, A_2 and A_3 are coefficients and V_{norm} is the normalised PD. This format of calibration function has been used to adequately describe the relationship between PD and crack length in previous studies [55].

$$\frac{a}{W} = A_0 + A_1 V_{norm} + A_2 V_{norm}{}^2 + A_3 V_{norm}{}^3 \quad \textbf{(4.1)}$$

The normalised PD is generally calculated from Equation (4.2) where the instantaneous PD measured across the crack, V, is normalised by the initial value, V_0.

$$V_{norm} = \frac{V}{V_0} \quad \textbf{(4.2)}$$

4.2.1 Supressing Proportional Changes in PD

Temperature fluctuations and amplifier drift can be significant sources of error in the measurement of crack extension [79]; however, they produce proportional changes in all PD measurements obtained under the same conditions so this error can be easily suppressed by taking additional PD measurements which are incorporated into a modified version of Equation (4.2). Two methods of achieving this are discussed in the previous chapter. These are:

1. A reference measurement remote from the crack,
2. Two parallel measurements across the crack.

Whilst these methods will suppress errors due to proportional changes in PD they will inevitably introduce other sources of error to the normalised PD signal, e.g. noise. To investigate whether these additional errors are significant and identify which method of suppression is most appropriate both have been considered in this study. A brief overview of the two methods, including the required modifications to Equation (4.2), is provided below.

4.2.1.1 Reference Measurement Remote from the Crack

This method of suppressing proportional changes in PD requires a reference measurement taken at the same time as the measurement across the crack, with the same equipment but at a location which is not influenced by crack growth. Variations in the reference measurement which occur throughout the test are then used to correct the measurement taken across the crack. Using this method, the normalised PD, V_{norm}, is calculated from Equation (4.3) where V_{ref} is the reference signal and V_{ref0} is the initial reference signal.

$$V_{norm} = \frac{V/V_0}{V_{ref}/V_{ref\,0}} \tag{4.3}$$

The reference measurement can either be made on the test specimen at a location remote from the crack [57, 59, 79] or on a nominally identical specimen in the same environment but without a growing crack [81]. Due to the limited availability of the material used in this research, the use of additional reference specimens is not viable so this study focuses on a reference measurement on the same specimen as the growing crack.

4.2.1.2 Two Measurements across the Crack

This method involves two PD measurements, V_1 and V_2, taken across the crack at the same time but at different locations. The calibration is derived in terms of the ratio of these measurements. Using this method the normalised PD, V_{norm}, is calculated from Equation (4.4).

$$V_{norm} = \frac{V_1}{V_2} \tag{4.4}$$

4.3 Metrics

In order to compare PD configurations, a set of suitable metrics are required. In previous optimisation studies [56, 65, 71, 76, 84] the following metrics were used:

- *'Sensitivity':* Change in PD with crack extension. The higher the sensitivity, the more accurately small increments in crack extension can be measured.
- *'Repeatability':* Change in PD due to small errors in the PD configuration. The smaller this change in PD, the better repeatability of the measurement.
- *'Measurability':* The magnitude of the PD at the start of the test. This was used to infer the signal-to-noise ratio. The larger the magnitude, the larger the signal-to-noise ratio.

In this report, these have been revised to produce two new metrics called '*probe misplacement error*' and '*resolution'*. A third metric called '*remote reference error*' has also been included. Each of these metrics relate to an error in the crack extension measurement so they can be directly compared. They are described in the following sub-sections.

4.3.1 Probe Misplacement Error

Calibration functions are derived based on a nominal PD configuration, but when the current injection and PD probes are attached to a physical specimen, small deviations from this nominal configuration are inevitable. The difference in the relationship between PD and crack extension for the actual and nominal PD configurations introduces a '*probe misplacement error*'. This is related to the '*repeatability*' metric used in previous studies [56, 71, 84].

Based on experience, electrical connections can be attached to the specimen to within 0.5 mm of the nominal location. This is in agreement with observations by Aronson and Ritchie [56] and has been used as the basis for calculating probe misplacement error as shown schematically in Figure 4.1.

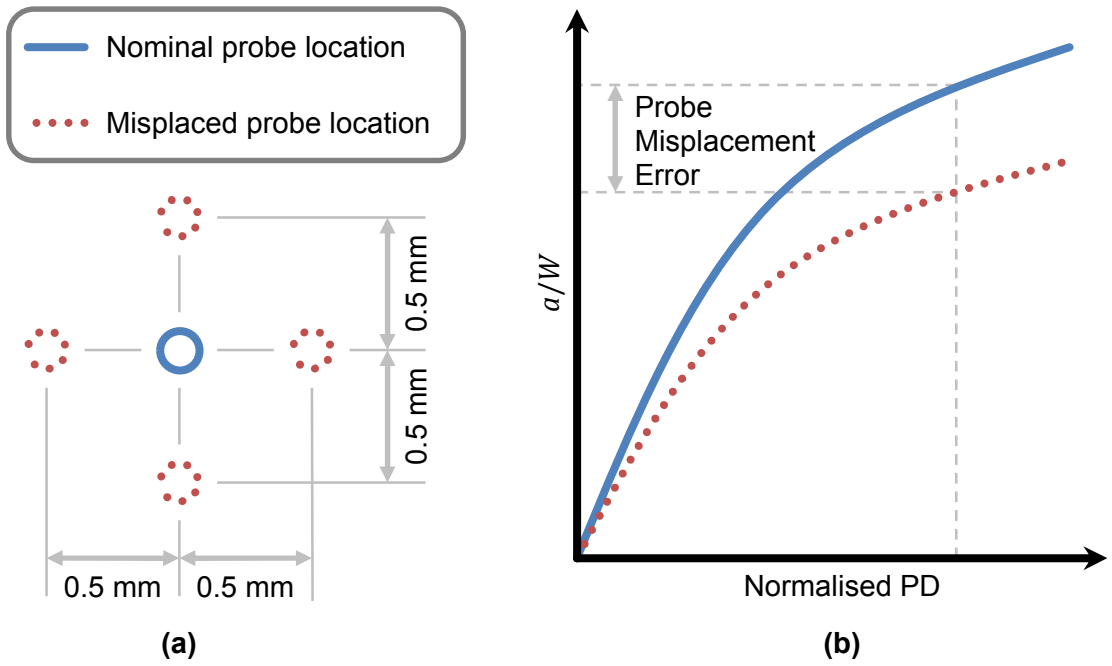

Figure 4.1: Schematic representation of the 'probe misplacement error' showing (a) the probe locations considered and (b) the calibration curves for the nominal and a 'misplaced' configuration.

The individual steps in the calculation of probe misplacement error are:

1. An FE analysis of the specimen was performed with the nominal PD configuration and the crack was grown in small increments. For each increment the change in PD

was recorded and a nominal calibration function was derived in the form of Equation (4.1).

2. The PD probe and current injection locations were then adjusted by 0.5 mm parallel to one of the axes of the co-ordinate system and a calibration function for the 'misplaced' configuration was derived.
3. For each crack increment with the 'misplaced' configuration, the change in PD was recorded and the crack extension was calculated from the calibration functions for the nominal and 'misplaced' configurations. The difference between these two values is the error due to probe misplacement.
4. Steps 2 & 3 were repeated for every combination of current injection and PD probe misplacement (including electrical connections used to suppress proportional changes in PD). The 'probe misplacement error' for each crack increment is the maximum value for all 'misplaced' configurations considered.

This metric is only related to the location of the PD configuration. It is independent of the magnitude of the electrical signal (i.e. the electrical resistivity of the specimen material) and the noise on the PD signal (i.e. the type of PD system used to perform the measurement).

4.3.2 Resolution

PD measurements are inherently susceptible to electrical noise which can mask changes in PD associated with small amounts of crack growth. The '*resolution*' is the crack extension which is necessary to produce a change in PD equal to the amplitude of the electrical noise, shown schematically in Figure 4.2.

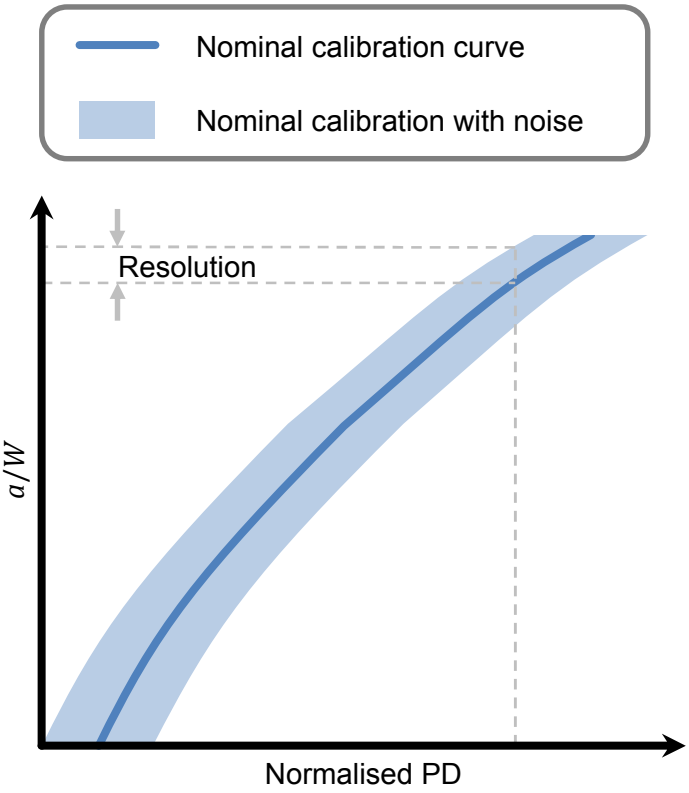

Figure 4.2: Schematic representation of the 'resolution'.

When no method of suppression is considered, the normalised PD is calculated from Equation (4.2) where the measurement signal, V, is susceptible to electrical noise. By including the amplitude of the electrical noise, V_{noise}, on this signal, the maximum value of the normalised PD due to noise, V_{norm_max}, can be calculated from Equation (4.5) for each increment of crack extension.

$$V_{norm\_max} = \frac{V + V_{noise}}{V_0} \tag{4.5}$$

The corresponding maximum crack length predicted by the calibration function, a_{max_res}, is calculated from Equation (4.6).

$$\frac{a_{max\_res}}{W} = A_0 + A_1\left(V_{norm\_max}\right) + A_2\left(V_{norm\_max}\right)^2 + A_3\left(V_{norm\_max}\right)^3 \tag{4.6}$$

The resolution, Δa_{res}, can therefore be calculated from Equation (4.7) where a is the nominal crack length calculated from Equation (4.1) based on the normalised PD, V_{norm}, from Equation (4.2).

$$\Delta a_{res} = a_{max\_res} - a \tag{4.7}$$

The resolution, as calculated in this study, is only influenced by signals which change throughout the test. It has been assumed that the initial measurement, V_0, is obtained from an average of a sufficient number of readings such that the influence of noise may be neglected. The value of the resolution depends on the magnitude of the electrical signal (i.e. the electrical resistivity of the specimen material) and the noise on the PD signal (i.e. the type of PD system used to perform the measurement). It is therefore related to the '*sensitivity'* and '*measurability*' metrics used in previous optimisation studies [56, 71, 84].

All PD measurements will be susceptible to electrical noise. This includes any additional measurements used to supress proportional changes in PD. The resolution is therefore dependent on the method of suppression. The calculation of resolution for the different methods of suppression considered in this study is provided below.

4.3.2.1 Reference Measurement Remote from the Crack

For this method of suppression, the normalised PD is calculated from Equation (4.3) where the measurement signal, V, and the reference signal, V_{ref}, are both susceptible to electrical noise. By including the amplitude of the electrical noise, V_{noise}, on these signals, the maximum value of the normalised PD due to noise, V_{norm_max}, can be calculated from Equation (4.8) for each increment of crack extension.

$$V_{norm\_max} = \frac{\left(V + V_{noise}\right)/V_0}{\left(V_{ref} - V_{noise}\right)/V_{ref\,0}} \qquad \textbf{(4.8)}$$

The corresponding maximum crack length predicted by the calibration function, a_{max_res}, is calculated from Equation (4.6) and the resolution, Δa_{res}, from Equation (4.7) where the nominal crack length, a, is the calculated from Equation (4.1) based on the normalised PD, V_{norm}, from Equation (4.3).

4.3.2.2 Two Measurements across the Crack

For this method of suppression, the normalised PD is calculated from Equation (4.4) where both signals, V_1 and V_2, are susceptible to electrical noise. The maximum value of the normalised PD, V_{norm_max}, due to noise can be calculated from Equation (4.9) for each increment of crack extension.

$$V_{norm\_max} = \frac{V_1 + V_{noise}}{V_2 - V_{noise}} \qquad \textbf{(4.9)}$$

The corresponding maximum crack length predicted by the calibration function, a_{max_res}, is calculated from Equation (4.6) and the resolution, Δa_{res}, from Equation (4.7) where the

nominal crack length, a, is the calculated from Equation (4.1) based on the normalised PD, V_{norm}, from Equation (4.4).

4.3.3 Remote Reference Error

When using a remote reference measurement to supress proportional changes in PD, it is assumed that this measurement is independent of crack extension; however, when this measurement is obtained from the same specimen as the growing crack it is likely to have some small dependence on crack extension. This dependence will influence the value of V_{norm} calculated from Equation (4.3) which will introduce a '*remote reference error*', shown schematically in Figure 4.3.

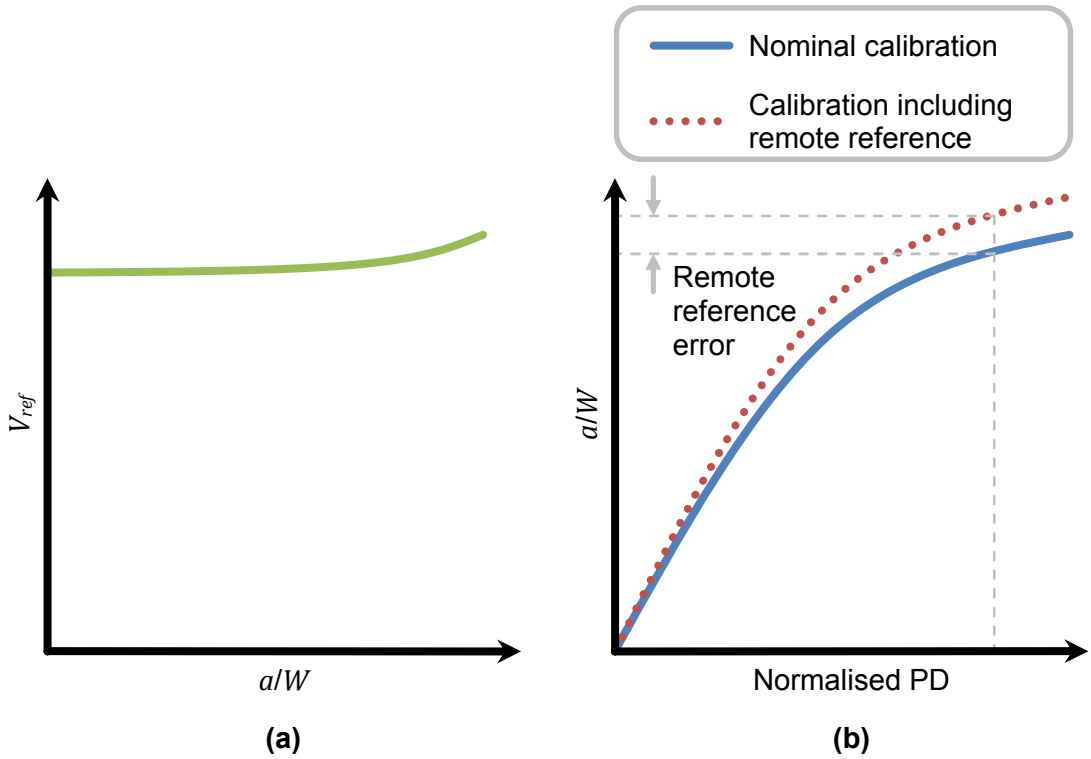

Figure 4.3: Schematic representation of the 'remote reference error' showing (a) variation of the reference measurement with crack extension and (b) the influence of the remote reference signal on the nominal calibration curve.

When using a remote reference measurement, the normalised PD is calculated from Equation (4.3). By including the reference measurement as a function of crack length, $V_{ref}(a)$, the normalised PD including the influence of crack length on the reference measurement, V_{norm_remote}, can be calculated from Equation (4.10).

$$V_{norm\_remote} = \frac{V(a)/V_0}{V_{ref}(a)/V_{ref\,0}} \qquad \textbf{(4.10)}$$

The corresponding crack length predicted by the calibration function, a_{remote}, is calculated from Equation (4.11).

$$\frac{a_{remote}}{W} = A_0 + A_1\left(V_{norm\_remote}\right) + A_2\left(V_{norm\_remote}\right)^2 + A_3\left(V_{norm\_remote}\right)^3 \quad \textbf{(4.11)}$$

The remote reference error, Δa_{remote}, can therefore be calculated from Equation (4.12) where a is the nominal crack length calculated from Equation (4.1) based on the normalised PD, V_{norm}, from Equation (4.3) where V_{ref} is assumed to be constant for all crack lengths.

$$\Delta a_{remote} = a_{remote} - a \quad \textbf{(4.12)}$$

This error does not apply when two parallel measurements across the crack are used to supress proportional changes in PD because the calibration function accounts for the dependence of both of these signals on crack extension.

4.4 General Methodology

Two of the most common specimen geometries have been considered in this study: Compact Tension, C(T), and Single Edge-Notch, SEN. This study does not consider the mechanical behaviour of each specimen, so the results for the SEN specimen are applicable to both the tension, SEN(T), and bend, SEN(B), variants of this geometry. This section provides a general overview of the methodology used to identify the optimum PD configurations. Details specific to the two specimen types are provided in Section 4.5 for the SEN specimen, and Section 4.6 for the C(T) specimen.

For each specimen a selection of possible PD configurations have been identified based on the results of previous studies [56, 65, 71, 76, 84] and for each configuration a series of FE analyses have been performed to calculate the metrics discussed above. FE provides the precise control of crack length and the PD configuration necessary to perform this study. COMSOL [124] was used to perform these analyses because of its capability to automatically re-mesh geometry which makes it ideal for performing parametric studies looking at a growing crack and different PD configurations.

4.4.1 Influence of Specimen Size

Specimen size will influence the accuracy of the crack extension measurements however, to limit the number of variables in this study only a single, common size is considered for each specimen type. For the SEN specimen W = 25 mm and for the C(T) specimen W = 50 mm. Details of the exact geometries are provided in the individual specimen sections later in this chapter.

4.4.2 Influence of the Amount of Crack Growth

Some of the metrics used in this study depend on the magnitude of the measurement signal which is related to the amount of crack growth being measured; this may therefore influence the optimum PD configuration. For each specimen type the optimum configuration has been identified for significant crack growth and crack initiation separately. For crack growth, an arbitrary 10 mm of crack extension is considered in 0.5 mm increments. This is a significant amount of crack extension which is typical of fatigue crack growth tests although smaller crack extensions are often measured for other test types e.g. fracture toughness and creep crack growth. For each increment in crack extension, the metrics described earlier in this chapter have been calculated and the average value for all increments reported. For crack initiation, each metric is calculated for a single crack increment of 0.2 mm. This is the engineering definition of crack initiation implemented in many standards e.g. [3, 27].

4.4.3 Influence of Material

The magnitude of the measurement signal is also related to the resistivity of the specimen material which may also influence the optimum PD configuration. In this study two different materials are considered: Type 316H stainless steel at 550ºC and aluminium at 20ºC. They represent extremes in resistivity of typical structural metals.

The resistivity of these materials is provided in Table 4.1. The variation of resistivity with temperature is provided in Figure 4.4. The equations describing the second order polynomial fits in this figure are provided in Equations (4.13) and (4.14) for Type 316H and aluminium respectively where ρ is the material resistivity (in Ωm) and T is the temperature (in °C).

Material	Temperature [°C]	Resistivity [Ωm]	Reference
Type 316H Stainless Steel	550	1.05×10^{-6}	[125]
Aluminium	20	2.65×10^{-8}	[126]

Table 4.1: Resistivity and temperature of the materials considered in this study.

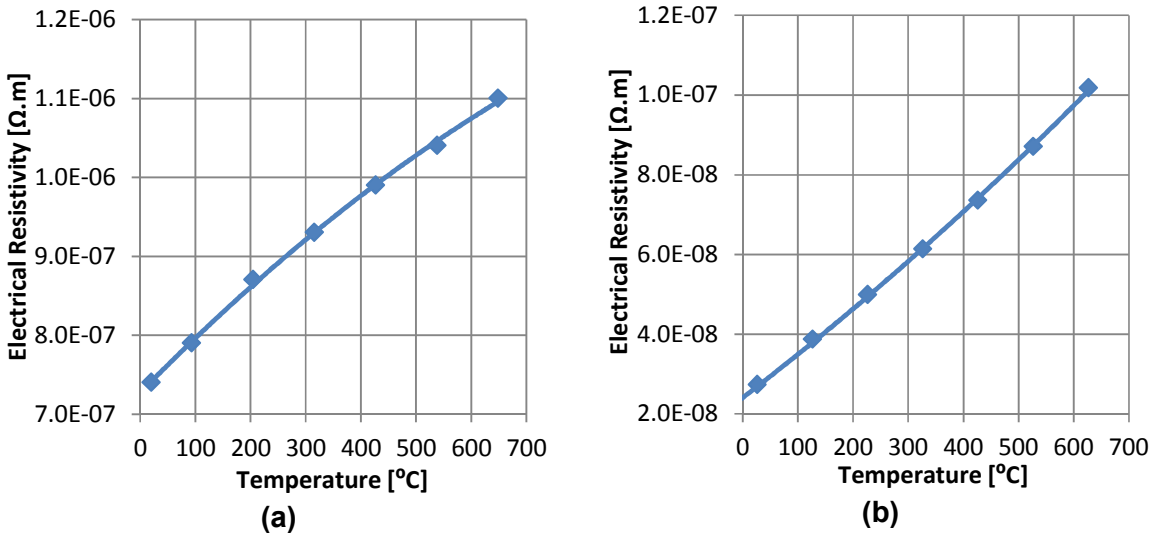

Figure 4.4: Variation of resistivity with temperature for (a) Type 316H stainless steel [125] and (b) Aluminium [126],

$$\rho_{316H} = 7.272\times10^{-07} + 7.134\times10^{-10}T - 2.237\times10^{-13}T^2 \quad \textbf{(4.13)}$$

$$\rho_{Al} = 2.409\times10^{-08} + 1.059\times10^{-10}T + 2.704\times10^{-14}T^2 \quad \textbf{(4.14)}$$

4.4.4 Influence of PD System

The resolution metric is dependent on the amplitude of the electrical noise, V_{noise}, which is a function of the PD system. The system used to obtain the measurements may therefore influence the optimum PD configuration. In this study two different systems have been considered: a typical DCPD system and a low frequency ACPD system. The DCPD system consists of a TDK Lambda ZUP 10-80 constant current source set to a typical value of 20 A, with a National Instruments USB-4065 digital multi-meter to measure the PD. This has been compared to the bespoke low frequency ACPD system, originally developed for measuring creep strain [54] with an applied constant current of 3 mA at a frequency of 2 Hz and a total gain of ~8000. Unlike the DCPD system, the ACPD system measures resistance rather than PD but for a constant current, the two are directly proportional. The calibration functions and metrics derived in this chapter, which are based on normalised PD, can therefore be implemented using normalised resistance for the ACPD system.

To measure the amplitude of the electrical noise for these two systems they were simultaneously connected to a C(T) specimen manufactured from Type 316H stainless steel at room temperature using the PD configuration recommended in ASTM E1457 [3]. An initial test was performed to confirm that the ACPD signal was not sensitive to small changes in frequency thus demonstrating that the skin effect was negligible and the current distribution

was quasi-DC. Consecutive measurements were then taken from the two systems at intervals of ~5 mins over a period of 80 hours. The typical noise amplitude and the signal-to-noise ratios are summarised in Table 4.2.

PD System	Noise Amplitude	Signal-to-Noise Ratio
Low frequency ACPD	25 μΩ	8900
DCPD	0.3 μV	1800

Table 4.2: Noise Amplitude used in the calculation of resolution for the different PD systems considered.

The signal-to-noise ratio for the low frequency ACPD system is much larger than the DCPD system. This was expected due to the lock-in amplifier which filters out noise at frequencies other than that of the applied current. In the following study, the noise amplitudes in Table 4.2 have been assumed to be constant for all signal amplitudes, i.e. they do not vary for different PD configurations or specimen geometries or materials. This simplified assumption is adequate for the purpose of this comparative study.

4.4.5 Method of Supressing Proportional Changes in PD

Two methods of suppressing proportional changes in PD due to, for example temperature fluctuations and/or amplifier drift, are discussed in Section 4.2.1. Both of these methods have been considered in this study. The optimum locations of the additional electrical connections required to implement these methods are identified.

4.5 SEN PD Configuration Optimisation

4.5.1 Specimen Geometry

The SEN specimen geometry and the co-ordinate system are shown in Figure 4.5. Only the gauge region is shown for clarity. The key dimensions are summarised in Table 4.3 which correspond to a typical SEN specimen as defined in ASTM E1457-13 [3]. Also shown in Figure 4.5 are the PD probe locations and the uniform current injection considered in this study.

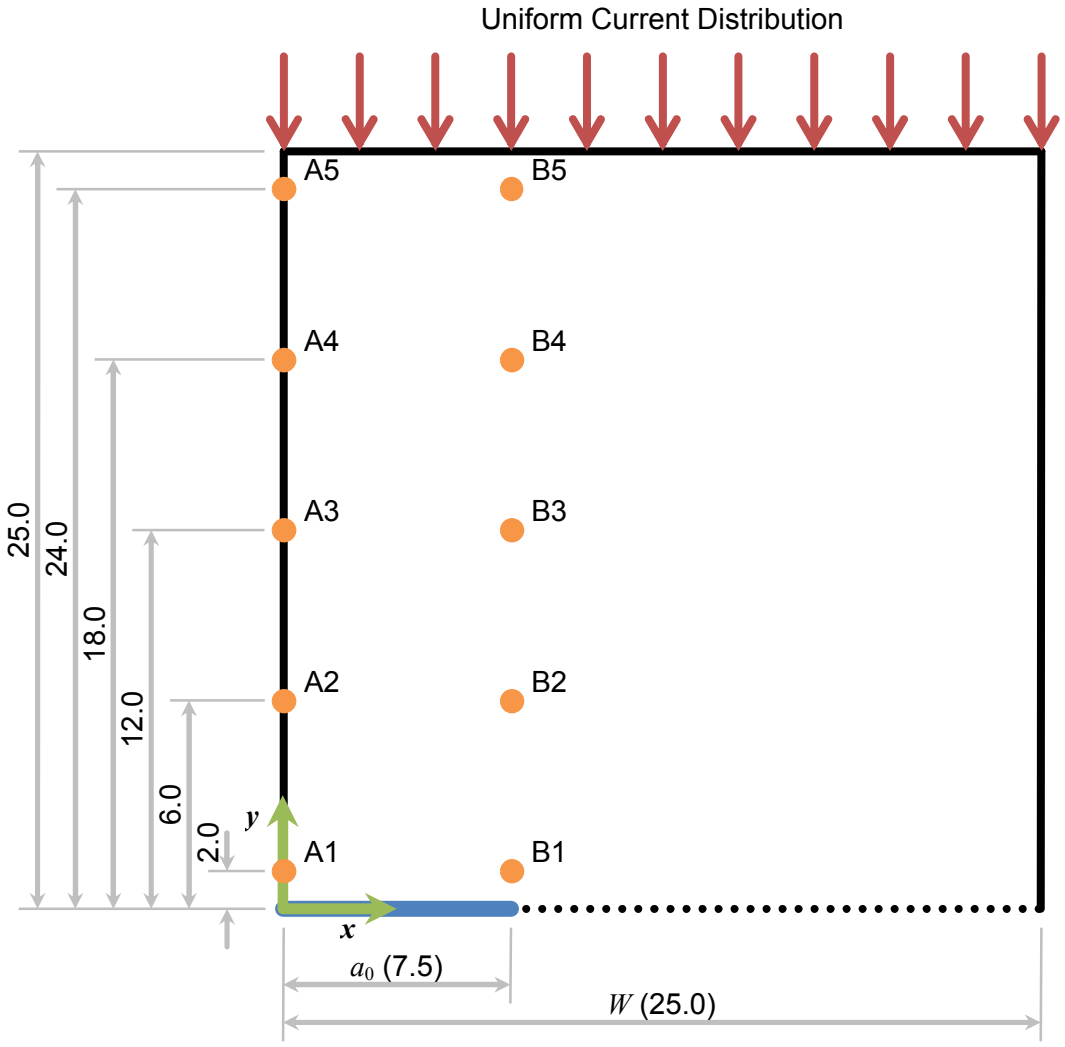

Figure 4.5: ½ SEN geometry and co-ordinate system, dimensions in mm. The crack is shown in blue and the remaining ligament is the dotted line. The current injection is shown in red and PD probe locations are shown in orange.

W [mm]	a_0 [mm]	$\frac{a_0}{W}$	a_f [mm]	$\frac{a_f}{W}$	B [mm]	$\frac{B}{W}$
25.0	7.5	0.30	17.5	0.70	12.5	0.50

Table 4.3: SEN specimen key dimensions.

4.5.2 PD Configurations

A uniform current distribution has been considered, as shown in Figure 4.5, based on the results from previous studies [65, 84]. This assumes that the current is injected at a location which is sufficiently remote from the gauge region that the calibration function is independent

of misplacement of the current injection points. The aspect ratio of a typical SEN specimen will usually facilitate this.

The PD probe locations considered in this study are also shown in Figure 4.5. The co-ordinates of these locations are provided in Table 4.4. Two lines of PD probes have been considered based on the results of previous studies [56, 76, 84]:

A. **Across the crack mouth:** A compromise between high sensitivity to crack extension and low sensitivity to probe misplacement. Often selected as the 'optimum' probe location.
B. **In-line with the initial crack tip:** Extremely sensitive to crack extension but also to probe misplacement.

Five distances from the crack plane were considered.

Probe Location	Co-ordinates			
	x/W	y/W	x (mm)	y (mm)
A1	0.00	0.08	0.0	2.0
A2	0.00	0.24	0.0	6.0
A3	0.00	0.48	0.0	12.0
A4	0.00	0.72	0.0	18.0
A5	0.00	0.96	0.0	24.0
B1	0.30	0.08	7.5	2.0
B2	0.30	0.24	7.5	6.0
B3	0.30	0.48	7.5	12.0
B4	0.30	0.72	7.5	18.0
B5	0.30	0.96	7.5	24.0

Table 4.4: Co-ordinates of the SEN PD probe locations.

4.5.3 Finite Element Model

A FE model of the gauge region was developed using COMSOL [124]. A 2D model was used which assumes that the current distribution is uniform through the thickness. Only half of the gauge region was modelled, taking advantage of the symmetry about the plane of the crack. The geometry, shown in Figure 4.5, was meshed using 10,000 quad elements with a uniform size of $0.01W$. A mesh refinement study was performed to confirm model convergence. Further validation was obtained by comparing the derived calibration functions for probe locations A1-A5 with Johnson's analytical solution [58] with excellent agreement.

A uniform current was distributed over the top surface. This assumes that the actual current injection point is sufficiently remote from the gauge region to produce this current distribution. A 0 V potential was applied to the ligament ahead of the crack (the dotted line in Figure 4.5). Crack growth was simulated by adjusting the length of the ligament in increments of $0.02W$ for $0.30 \leq a/W \leq 0.70$. This is equivalent to 10 mm of crack growth in increments of 0.5 mm. An initial crack increment of 0.2 mm was also performed to consider crack initiation. All other surfaces of the specimen were assumed perfectly insulated.

4.5.4 Results

The results presented here are split into three sections. The first two sections look at crack growth and crack initiation respectively. Crack growth considers 10 mm of crack extension in increments of 0.5 mm. The errors reported are the average of all increments. Crack initiation considers a single increment of 0.2 mm. Neither of these two sections considers the method of suppressing proportional changes in PD. This is considered separately in the third section.

4.5.4.1 Crack Growth

Figure 4.6 shows the average absolute errors (based on the metrics provided in Section 4.3) for the different PD configurations when measuring significant crack extension in a Type 316H SEN specimen at 550ºC. Figure 4.7 shows the results for an aluminium specimen at 20ºC.

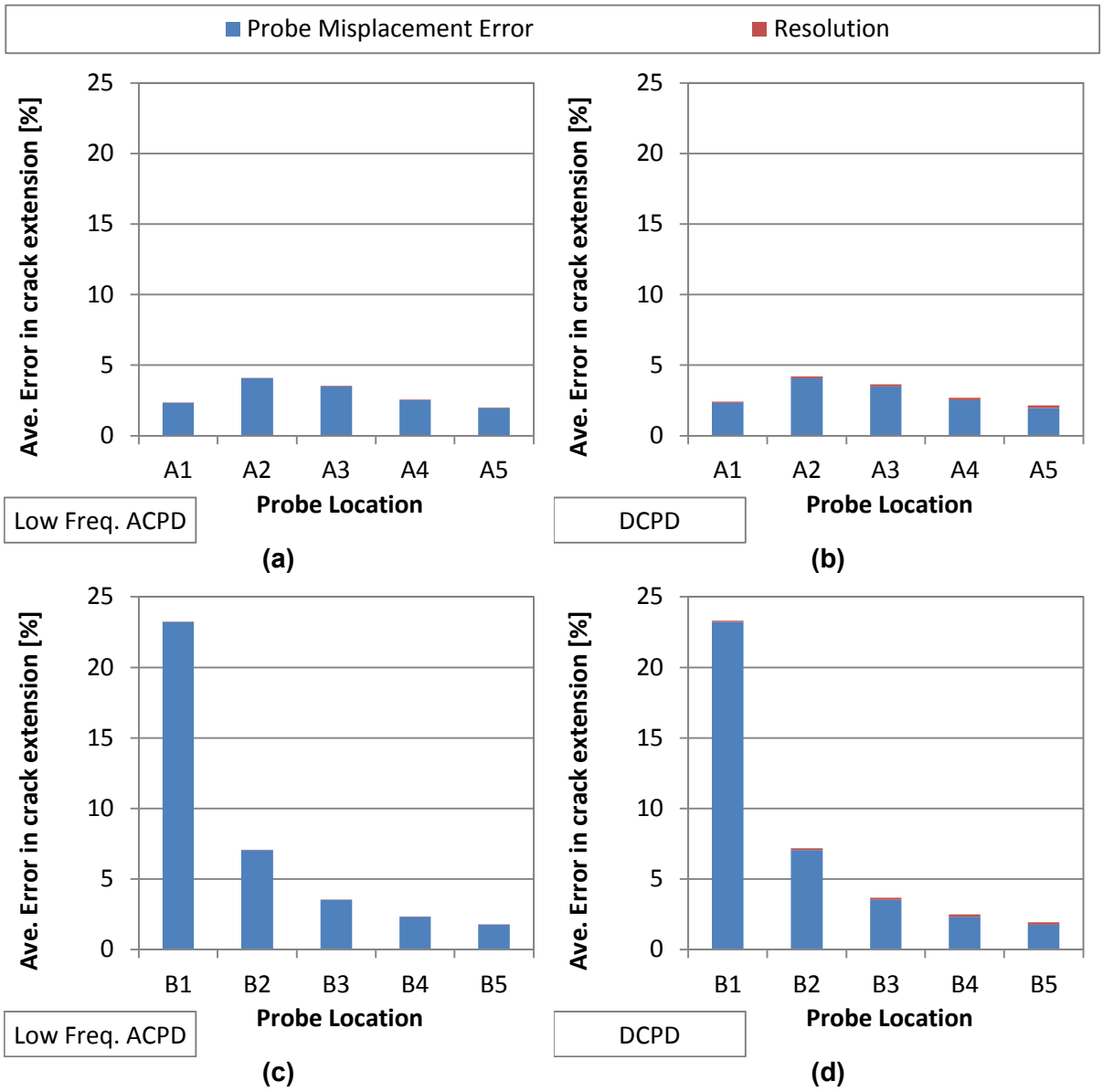

Figure 4.6: Average absolute error when measuring significant crack extension in a Type 316H SEN specimen at 550ºC with PD probes (a) across the crack mouth, using low frequency ACPD, (b) across the crack mouth, using DCPD, (c) in-line with the crack tip, using low frequency ACPD and (d) in-line with the crack tip, using DCPD.

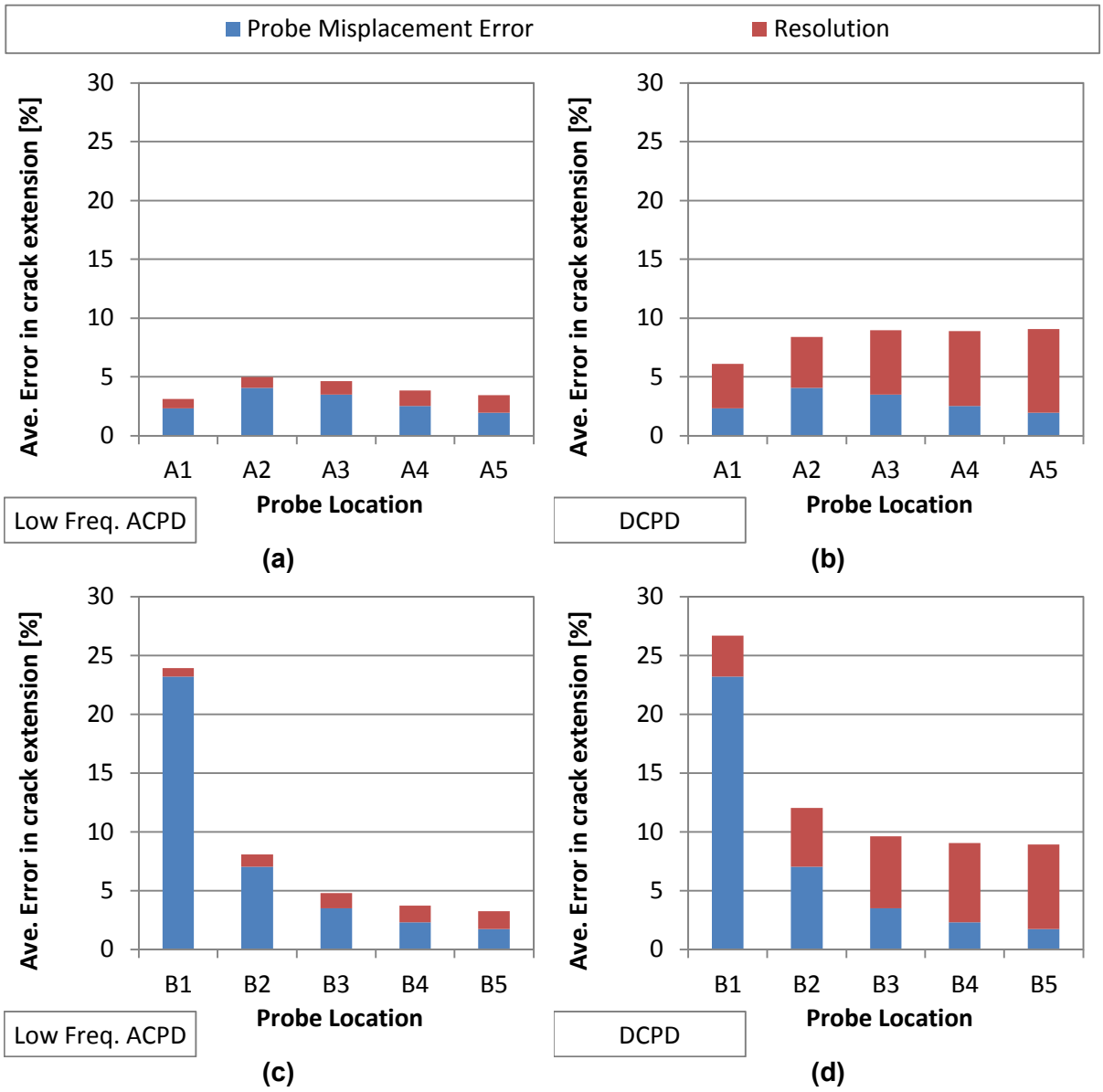

Figure 4.7: Absolute error when measuring significant crack extension in an aluminium SEN specimen at 20ºC with PD probes (a) across the crack mouth, using low frequency ACPD, (b) across the crack mouth, using DCPD, (c) in-line with the crack tip, using low frequency ACPD and (d) in-line with the crack tip, using DCPD.

When measuring significant crack growth, PD probes across the crack mouth (locations beginning with 'A') are generally less prone to errors than those in-line with the crack tip (locations beginning with 'B'). Probe location A1 consistently demonstrates the lowest average error. For a Type 316H specimen at 550ºC this error is 2.4% and is almost entirely due to probe misplacement. It is therefore independent of the type of PD system used to perform the measurement. For an aluminium specimen at 20ºC this error increases to 3.1% and 6.1% when using the low frequency ACPD system or the DCPD system respectively.

The type of system used is more important for materials with low resistivity because the signal-to-noise ratio reduces which increases the resolution. Only for the extreme case of an aluminium specimen and a DCPD system does the resolution become more significant than the probe misplacement error however, the optimum PD configuration remains A1.

4.5.4.2 Crack Initiation

Figure 4.8 shows the absolute errors (based on the metrics provided in Section 4.3) for different PD configurations when measuring 0.2 mm of crack extension in a Type 316H SEN specimen at 550ºC. Figure 4.9 shows the results for an aluminium specimen at 20ºC.

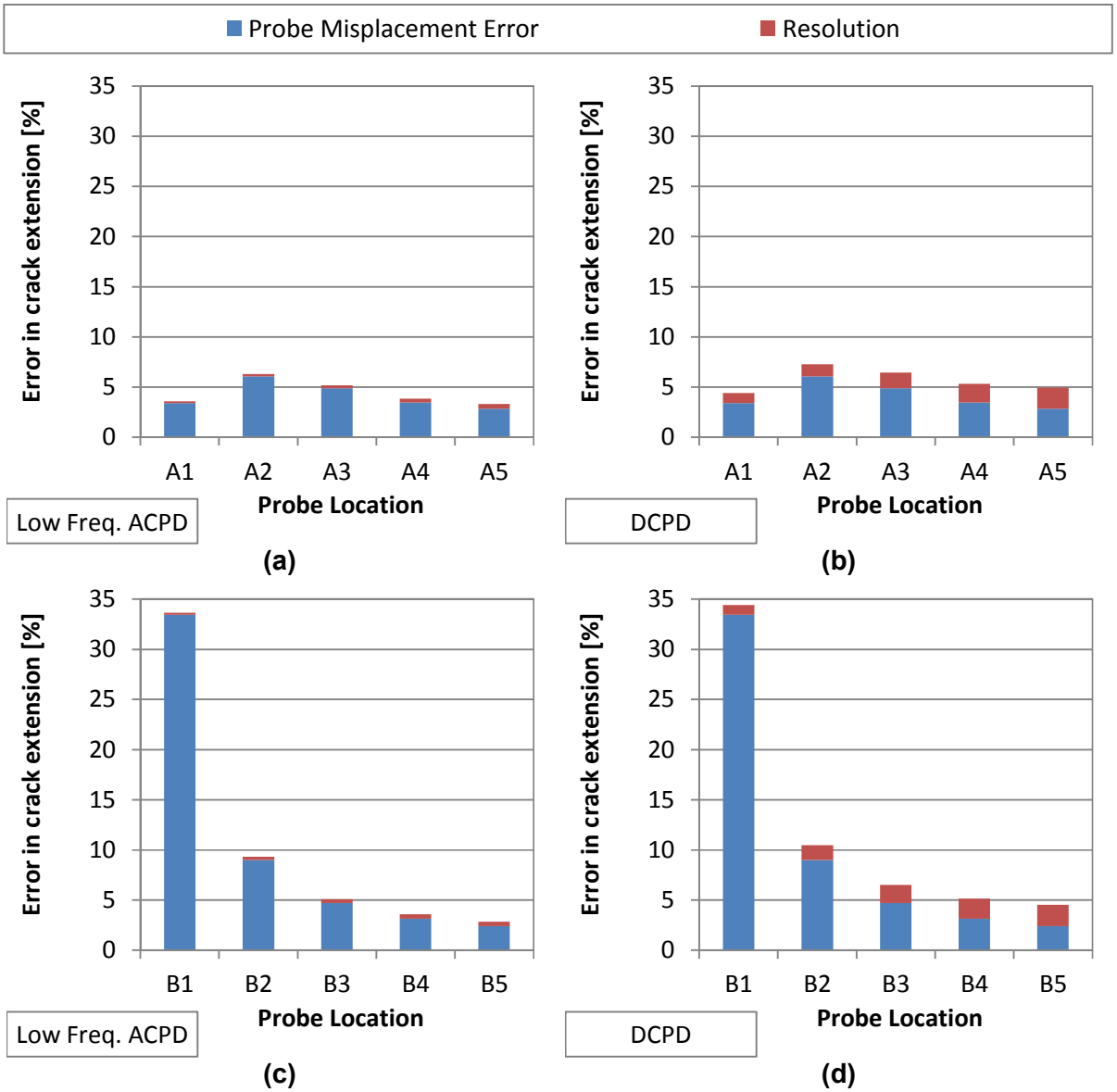

Figure 4.8: Absolute error when measuring 0.2 mm of crack extension in a Type 316H SEN specimen at 550ºC with PD probes (a) across the crack mouth, using low frequency ACPD, (b) across the crack mouth, using DCPD, (c) in-line with the crack tip, using low frequency ACPD and (d) in-line with the crack tip, using DCPD.

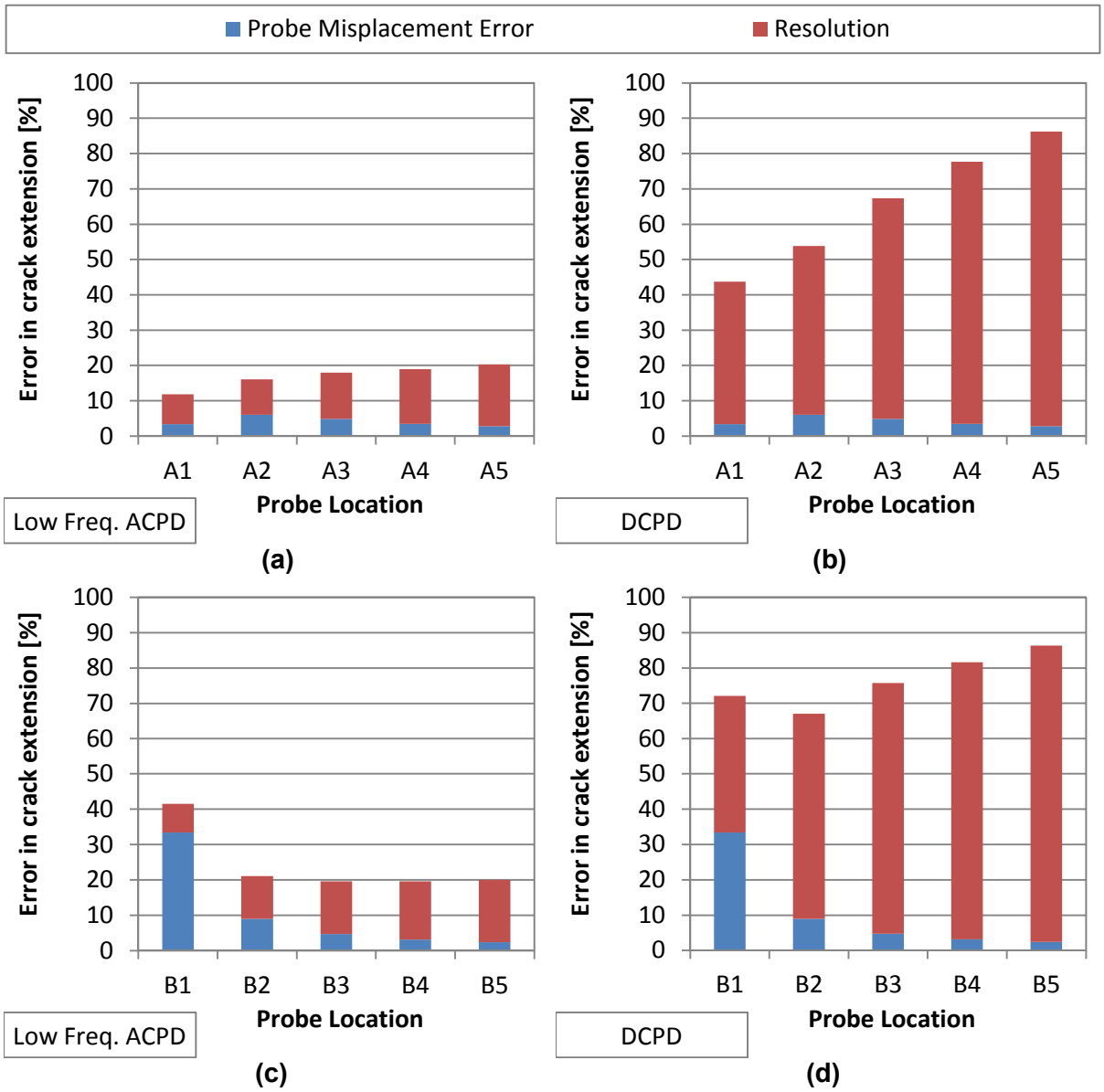

Figure 4.9: Absolute error when measuring 0.2 mm of crack extension in an aluminium SEN specimen at 20ºC with PD probes (a) across the crack mouth, using low frequency ACPD, (b) across the crack mouth, using DCPD, (c) in-line with the crack tip, using low frequency ACPD and (d) in-line with the crack tip, using DCPD.

When measuring 0.2 mm of crack extension, PD probes across the crack mouth (locations beginning with 'A') are again less prone to errors than those in-line with the crack tip (locations beginning with 'B') and probe location A1 again demonstrates the lowest total error. For a Type 316H specimen at 550ºC this error is 3.6% or 4.4% for the low frequency ACPD system and DCPD system respectively. For an aluminium specimen at 20ºC these errors increase to 11.8% and 43.7% for the respective PD systems.

The choice of PD system is more important when measuring small amounts of crack growth, particularly for specimens with low resistivity. This is again because the signal-to-noise ratio

is greatly reduced so the resolution becomes the dominant source of error. Despite this, A1 remains optimum because it is the probe location with the smallest resolution as well as the smallest probe misplacement error.

4.5.4.3 Method of Suppressing Proportional Changes in PD

When a reference measurement remote from the crack is used to suppress proportional changes in PD, the influence of crack growth on this measurement should be minimised to reduce the 'remote reference error' (see section 4.3.3). The magnitude of the reference signal should also be as large as possible to reduce the 'resolution' (see section 4.3.2). Suitable current injection and PD probe locations which fulfil these criteria have been identified for a SEN specimen. These are shown in Figure 4.10 where the current injection locations, shown in black, are labelled *Iref*, and the PD probes, shown in pink, are labelled *Sref*.

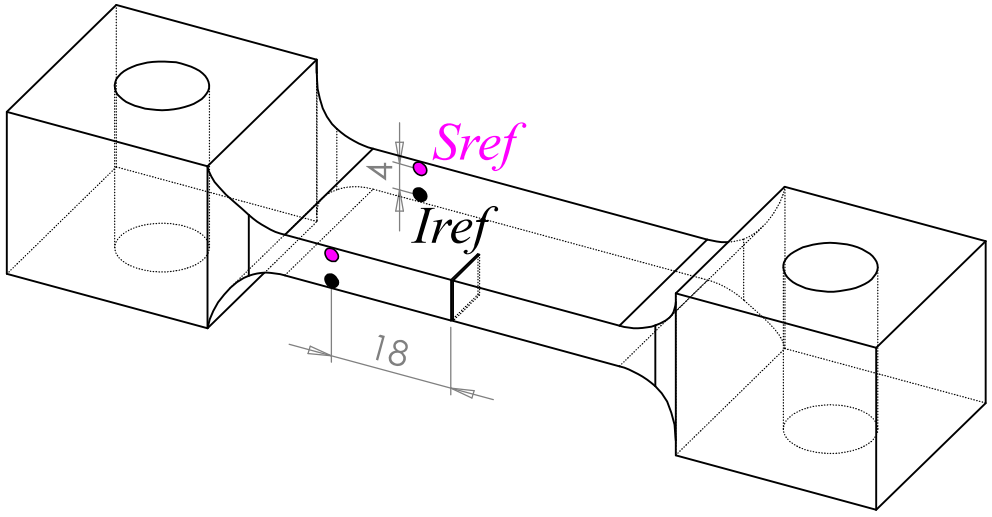

Figure 4.10: SEN remote reference PD configuration.

It has been identified that PD probes across the crack mouth (locations beginning with 'A') are generally less prone to errors than those in-line with the crack tip (locations beginning with 'B'). The reference configuration shown in Figure 4.10 has therefore only been considered in conjunction with PD probes across the crack mouth.

When using two measurements across the crack to suppress proportional changes in PD, again, only PD probes across the crack mouth have been. Only combinations including probe location A1 have been considered because this has been consistently identified as the optimum location. These combinations are:

- A1/A2: The ratio of A1 to A2,
- A1/A3: The ratio of A1 to A3,
- A1/A4: The ratio of A1 to A4,

- A1/A5: The ratio of A1 to A5.

Figure 4.11 shows the average absolute errors (based on the metrics provided in Section 4.3) in crack extension due to different methods of suppressing proportional changes in PD when measuring significant crack extension in a 316H SEN specimen at 550ºC. Figure 4.12 shows the results for an aluminium specimen at 20ºC. For some configurations where the errors are particularly high, the total extent of these errors are not shown because the scale of the axes has been selected to compare the PD configurations with the lowest errors.

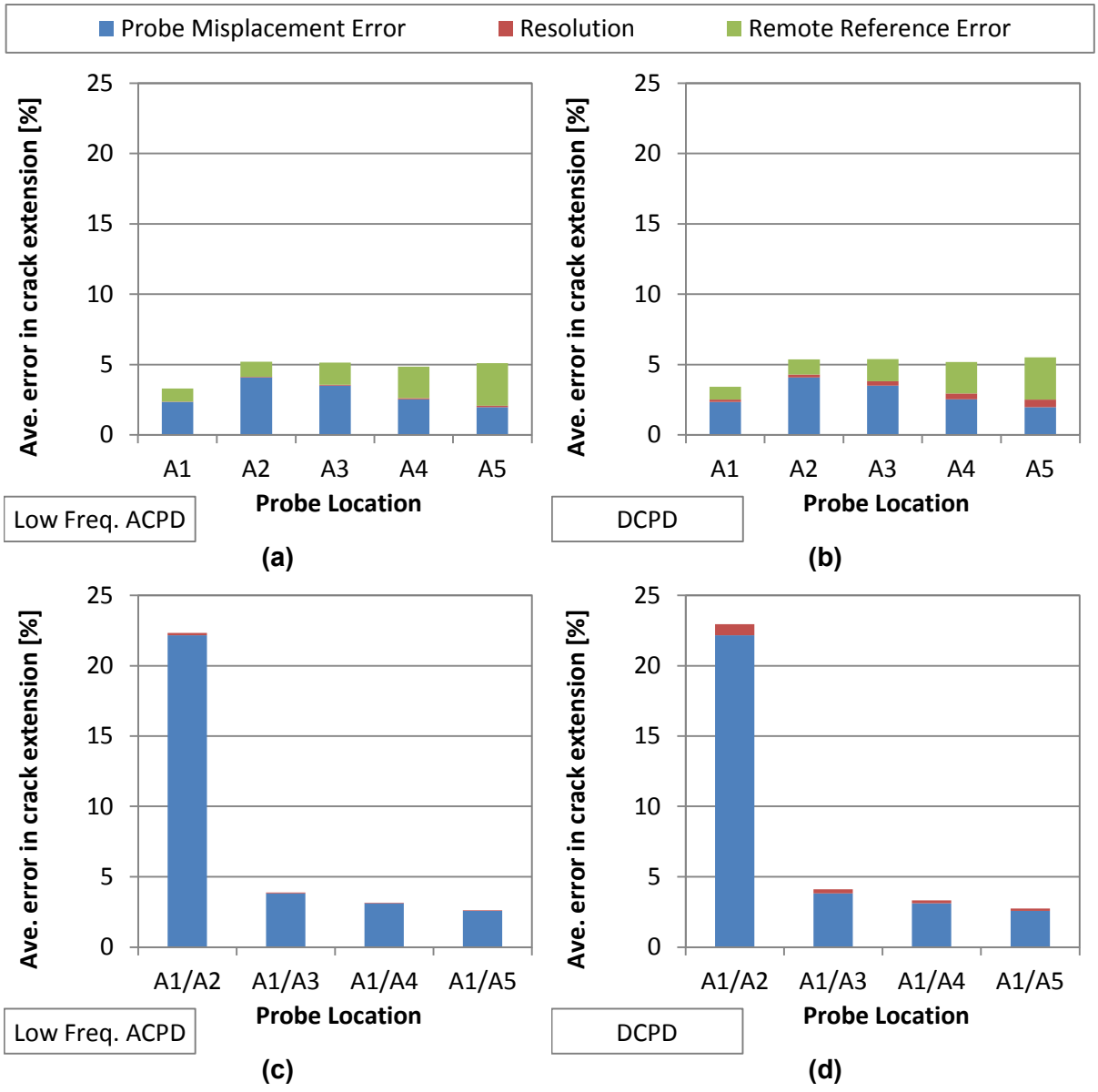

Figure 4.11: Average absolute error when measuring significant crack extension in a Type 316H SEN specimen at 550ºC for (a) a remote reference measurement, using low frequency ACPD, (b) a remote reference measurement, using DCPD, (c) two measurements across the crack, using low frequency ACPD, and (d) two measurements across the crack, using DCPD.

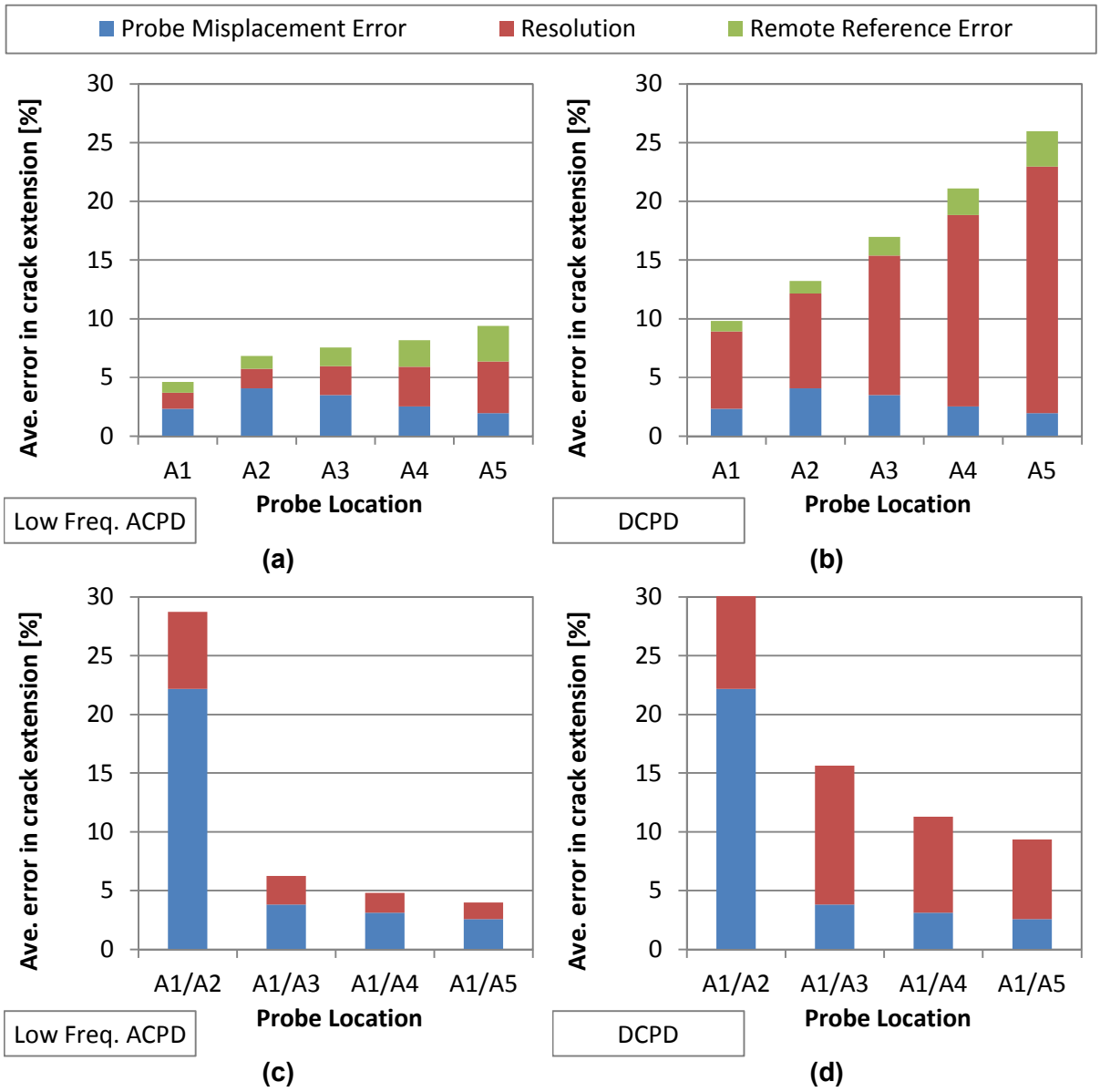

Figure 4.12: Average absolute error when measuring significant crack extension in an aluminium SEN specimen at 20ºC for (a) a remote reference measurement, using low frequency ACPD, (b) a remote reference measurement, using DCPD, (c) two measurements across the crack, using low frequency ACPD, and (d) two measurements across the crack, using DCPD.

When measuring significant crack growth the optimum PD configurations are A1 (when using a reference measurement remote from the crack) and A1/A5 (when using two measurements across the crack). Despite the dominant source of error depending on the type of PD system being used, the optimum PD configurations are the same for both systems.

The total average errors for PD configurations A1 and A1/A5 are similar. For a Type 316H specimen at 550ºC this error is ~3%, independent of the PD system. For an aluminium

specimen at 20ºC, this increases to ~4% for the low frequency ACPD system and ~10% for the DCPD system. These errors are larger than if no method of suppression is used because the additional measurements required to implement these suppression techniques are sources of error in themselves. This additional error must therefore be smaller than those which are being suppressed for the technique to be effective.

When using two measurements across the crack to supress proportional changes in PD, the errors reduce as the distance between the two measurement locations increases. When the two probes are very close together e.g. A1/A2, the errors are particularly large. This is because the calibration functions for these two probe locations are very similar so the normalised PD, V_{norm}, as calculated from Equation (4.4), remains close to unity for all crack lengths. The calibration is therefore relatively insensitive to crack extension so the resolution is large and small changes in the probe locations can significantly affect this sensitivity so the probe misplacement error is also large. When using this method to supress proportional changes in PD the two probe locations should be relatively far apart.

Figure 4.13 shows the absolute errors (based on the metrics provided in Section 4.3) when measuring 0.2 mm of crack growth in a Type 316H SEN specimen at 550ºC using different methods of supressing proportional changes in PD. Figure 4.14 shows the results for an aluminium specimen at 20ºC. For some configurations where the errors are particularly high, the total extent of these errors are not shown because the scale of the axes has been selected to compare the PD configurations with the lowest errors.

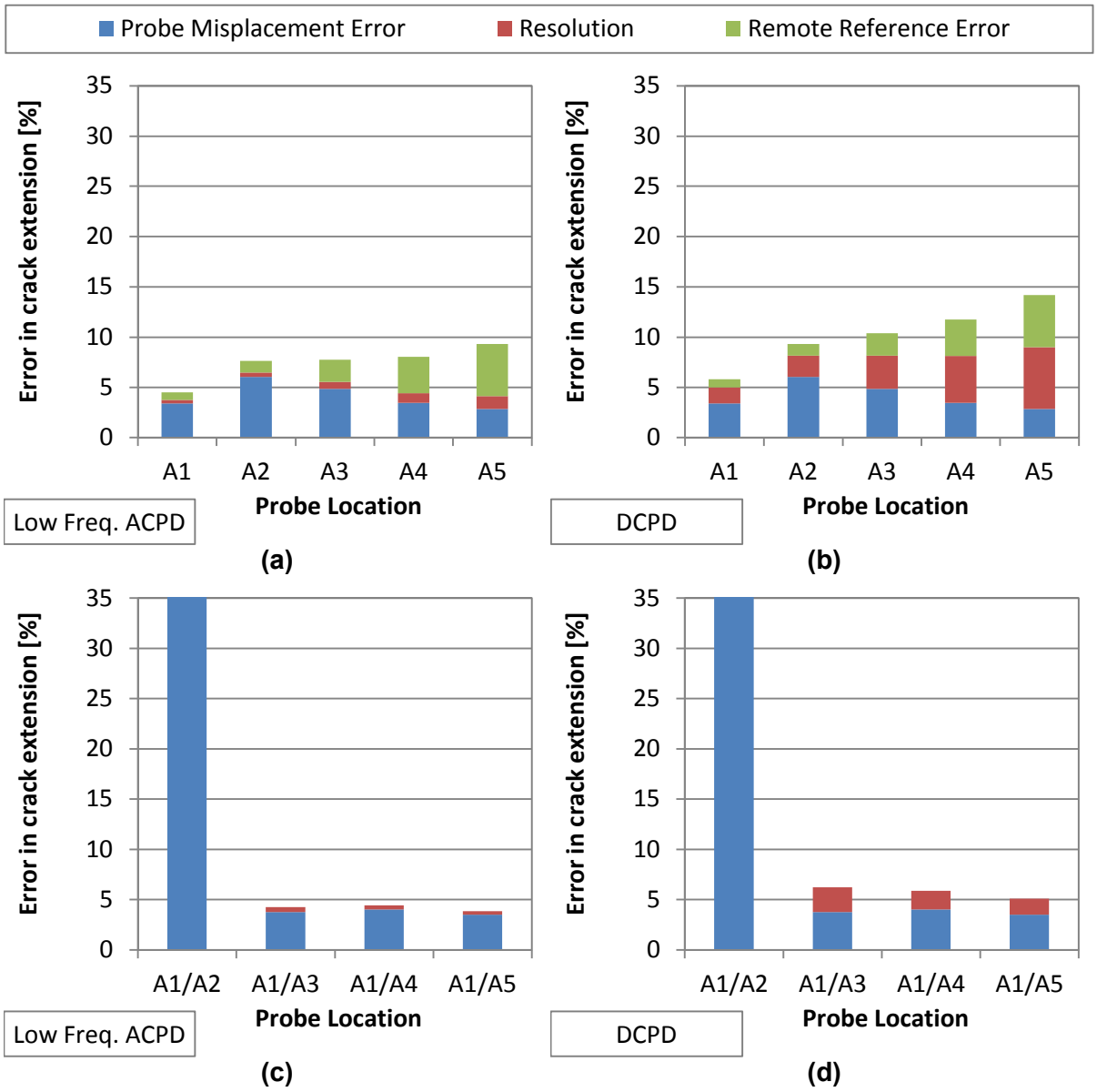

Figure 4.13: Absolute error when measuring 0.2 mm crack extension in a Type 316H SEN specimen at 550ºC for (a) a remote reference measurement, using low frequency ACPD, (b) a remote reference measurement, using DCPD, (c) two measurements across the crack, using low frequency ACPD, and (d) two measurements across the crack, using DCPD.

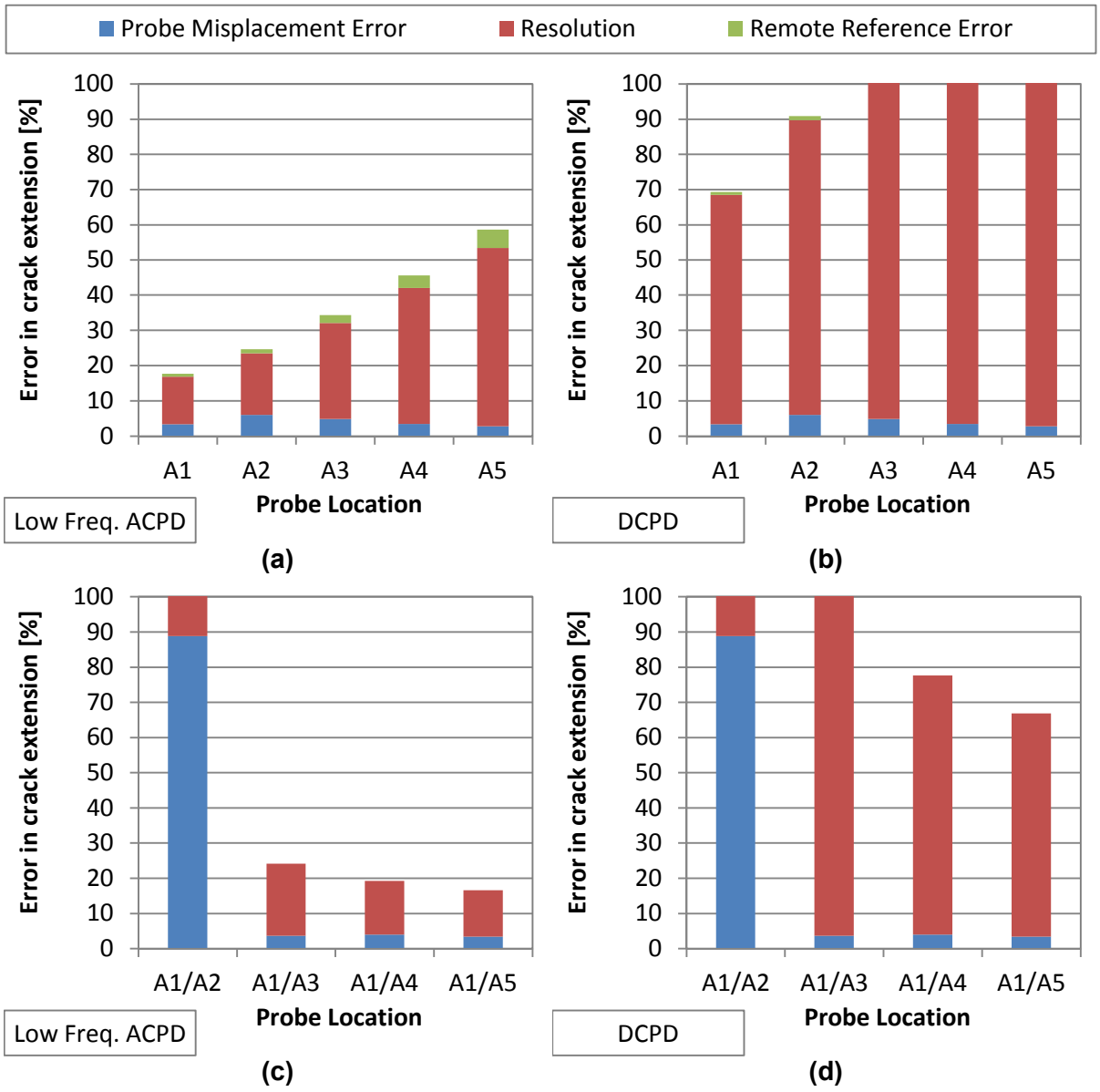

Figure 4.14: Absolute error when measuring 0.2 mm crack extension in an aluminium SEN specimen at 20ºC for (a) a remote reference measurement, using low frequency ACPD, (b) a remote reference measurement, using DCPD, (c) two measurements across the crack, using low frequency ACPD, and (d) two measurements across the crack, using DCPD.

When measuring 0.2 mm of crack growth the optimum PD configurations remain A1 (when using a remote reference measurement) and A1/A5 (when using two measurements across the crack). Both of these PD configurations again result in similar levels of error. For a Type 316H specimen at 550ºC this error is ~4% for the low frequency ACPD system and ~6% for the DCPD system. For an aluminium specimen at 20ºC, this increases to ~18% for the low frequency ACPD system and ~70% for the DCPD system. When measuring small amounts

of crack growth in an aluminium specimen the magnitude of the signal is particularly low, so the errors are very high, particularly when using DCPD.

4.6 C(T) PD Configuration Optimisation

4.6.1 Specimen Geometry

The C(T) specimen geometry and the co-ordinate system are shown in Figure 4.15 and the key dimensions are summarised in Table 4.5. Only half of the specimen is shown due to symmetry. The origin of the co-ordinate system is where the load-line intersects the plane of the crack. Figure 4.15 shows the two current injection locations, I_1 and I_2, and the five PD probe locations, A thru E, which are considered in this study. The process used to select these locations is discussed in the following section.

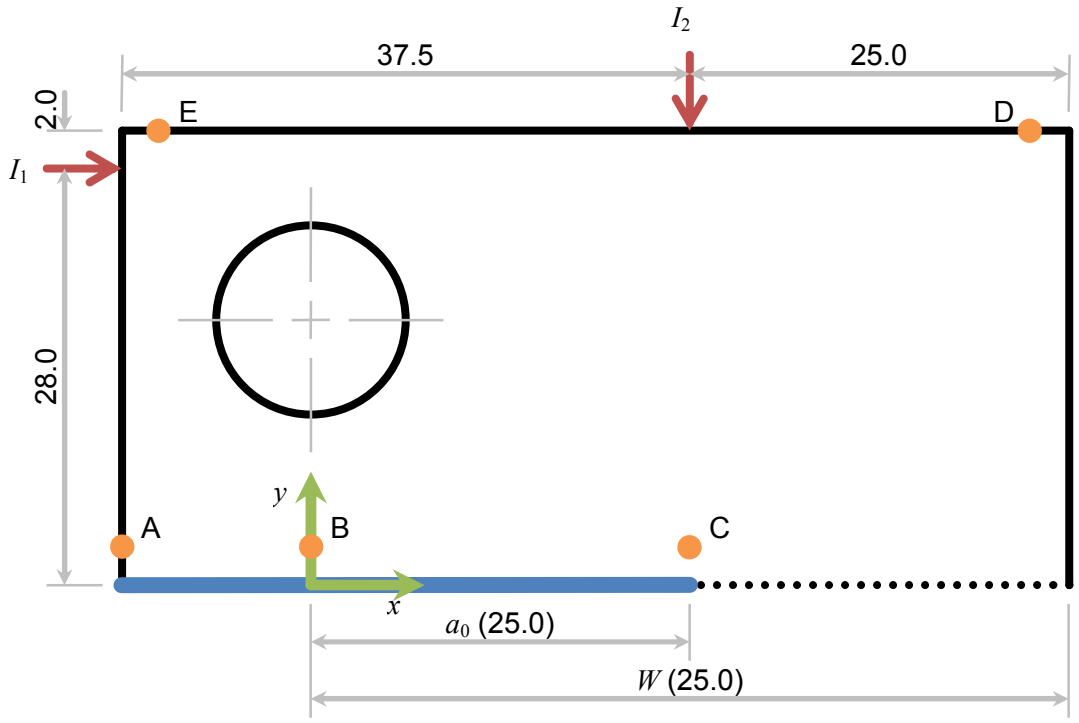

Figure 4.15: ½ C(T) geometry and co-ordinate system, dimensions in mm. The crack is shown in blue and the remaining ligament is the dotted line. The current injection locations are shown in red and PD probe locations are shown in orange.

W [mm]	a_0 [mm]	$\frac{a_0}{W}$	a_f [mm]	$\frac{a_f}{W}$	B [mm]
50.0	25.0	0.50	35.0	0.70	25.0

Table 4.5: C(T) specimen key dimensions.

4.6.2 PD Configurations

Two different current injection locations have been considered in this study as shown in Figure 4.15. Locations remote from the crack tip have been selected to provide a more uniform current distribution and reduce the sensitivity to misplacement. These current injection locations are consistent with previous optimisation studies [56, 71, 76, 84].

Five different PD probe locations have been considered which are also shown in Figure 4.15. Their co-ordinates are provided in Table 4.6. These locations were selected based on the results from the SEN specimen which demonstrated that the optimum probe locations tend to be those with a low sensitivity to probe misplacement. Locations A, B, D and E were identified in previous studies [56, 71] as having particularly low sensitivity to probe misplacement. Location C was included as an alternative which is the most sensitive to crack growth but is also sensitive to probe misplacement. All of the current injection and PD probe locations considered in this study are accessible when the specimen is gripped using a typical shackle assembly.

Probe Location	**Co-ordinates**			
	x/W	y/W	x **(mm)**	y **(mm)**
A	-0.25	0.04	-12.5	2.0
B	0.00	0.04	0.0	2.0
C	0.50	0.04	25.0	2.0
D	0.96	0.60	48.0	30.0
E	-0.21	0.60	-10.5	30.0

Table 4.6: Co-ordinates of the C(T) PD probe locations.

4.6.3 Finite Element Model

A FE model of the specimen was developed using COMSOL [124]. A 2D model was used which assumes that the PD probe locations are sufficiently far from the current injection locations such that the current is uniform through the thickness. Only half of the specimen was modelled taking advantage of the symmetry about the plane of the crack. The geometry in Figure 4.15 was meshed with ~31,000 linear quad elements with a maximum element size of $0.005W$. This mesh is shown in Figure 4.16. A mesh refinement study was performed to confirm model convergence.

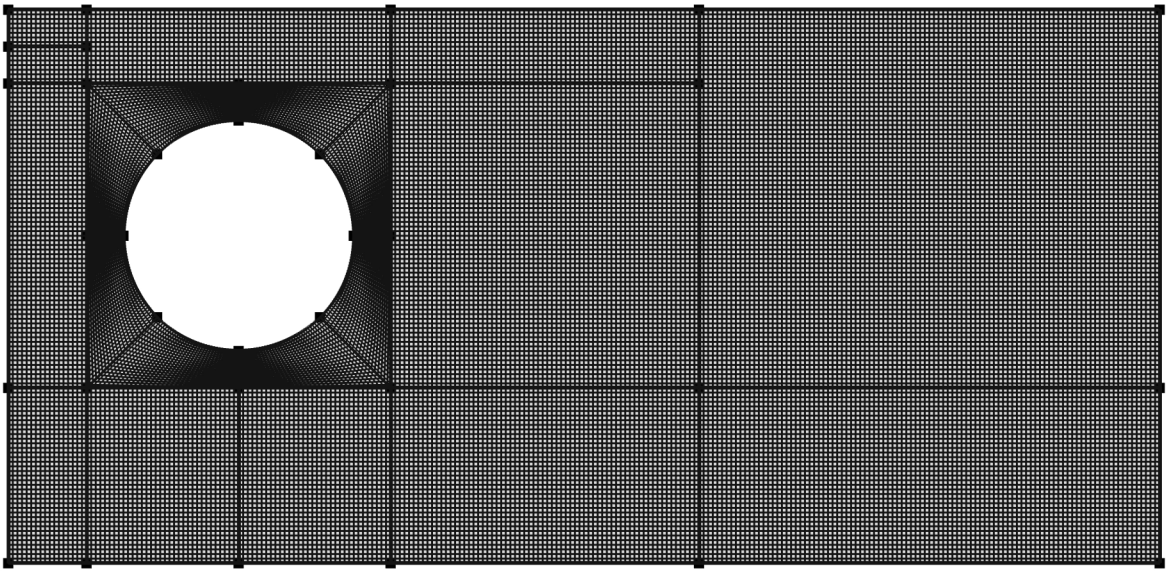

Figure 4.16: FE model of C(T) specimen

A 0V potential was applied to the ligament ahead of the crack (the dotted line in Figure 4.15). Crack growth was simulated by adjusting the length of the ligament in increments of $0.01W$ for $0.50 \leq a/W \leq 0.70$. This is equivalent to 10 mm of crack growth in increments of 0.5 mm. An initial crack increment of 0.2 mm was also performed to consider crack initiation. The current injection was modelled as a point source and separate analyses were performed to look at the two different current injection locations. All other surfaces were assumed perfectly insulated.

4.6.4 Results

Similar to the SEN specimen, the results are split into three sections. The first two sections look at crack growth and crack initiation respectively. Crack growth considers 10 mm of crack extension in increments of 0.5 mm. The errors reported are the average of all increments. Crack initiation considers a single increment of 0.2 mm. Neither of these two sections considers the method of suppressing proportional changes in PD. This is considered separately in the third section.

4.6.4.1 Crack Growth

Figure 4.17 shows the average absolute errors (based on the metrics provided in Section 4.3) for the different PD configurations when measuring significant crack extension in a Type 316H C(T) specimen at 550ºC. Figure 4.18 shows the results for an aluminium specimen at 20ºC.

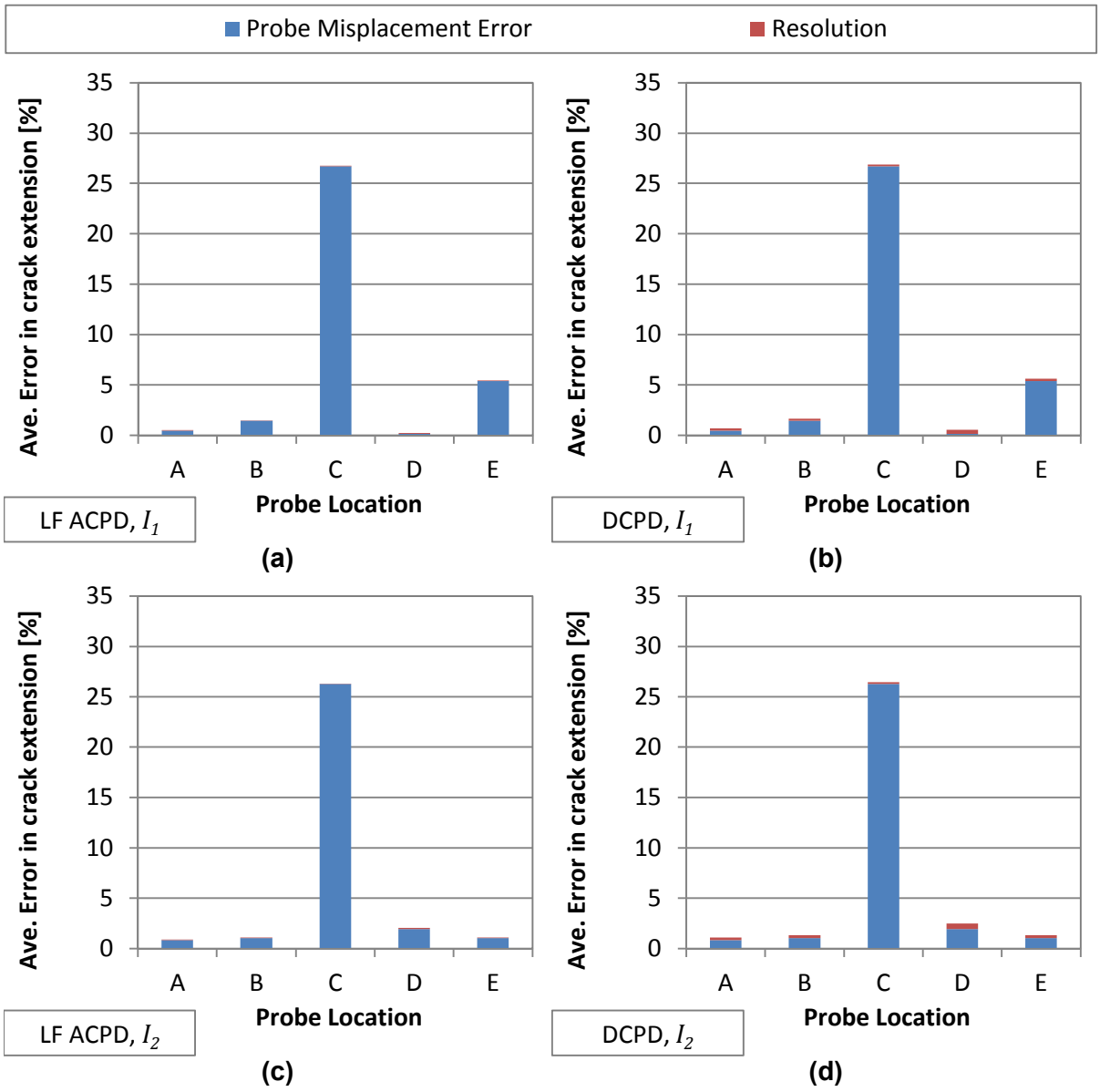

Figure 4.17: Average absolute error when measuring significant crack extension in a Type 316H C(T) specimen at 550ºC with (a) current injected at I_1, using low frequency ACPD, (b) current injected at I_1, using DCPD, (c) current injected at I_2, using low frequency ACPD and (d) current injected at I_2, using DCPD.

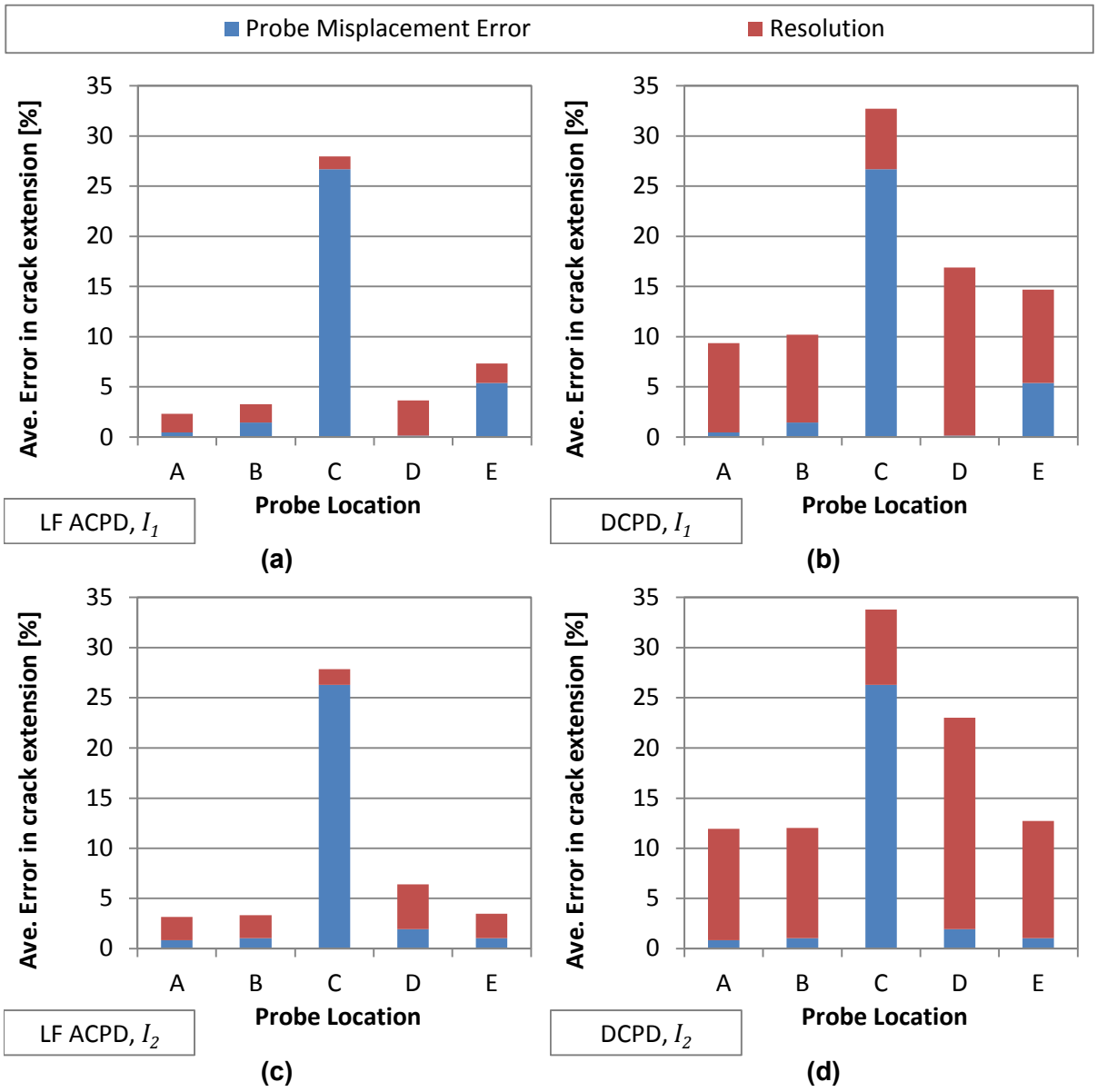

Figure 4.18: Average absolute error when measuring significant crack extension in an aluminium C(T) specimen at 20ºC with (a) current injected at I_1, using low frequency ACPD, (b) current injected at I_1, using DCPD, (c) current injected at I_2, using low frequency ACPD and (d) current injected at I_2, using DCPD.

When measuring significant crack growth, the lowest errors are typically at probe location A when the current is injected at I_1. For a Type 316H specimen at 550ºC this error is <1% for both PD systems and is almost entirely due to probe misplacement. For an aluminium specimen at 20ºC the resolution becomes more significant which increases the error to ~2% for the low frequency ACPD and ~9% for the DCPD.

Other suitable PD configurations where the error is similar, albeit slightly higher, are:

- Probe location A with the current injected at I_2
- Probe location B with the current injected at I_1 or I_2

- Probe location E with the current injected at I_2

The other PD configurations should generally be avoided. Probe location C, irrespective of the current injection location, is susceptible to very large probe misplacement errors because it is located close to the crack tip where the potential gradient is large [76, 84]. Probe location E with the current injected at I_1 is also susceptible to large probe misplacement errors. This is also due to a large potential gradient, but this time it is caused by the proximity of the PD probe to the current injection location [56]. Finally, probe location D, irrespective of the current injection location, is susceptible to high resolution because the probe is located ahead of the crack tip where the PD measurement is less sensitive to crack extension [76].

4.6.4.2 Crack Initiation

Figure 4.19 shows the absolute errors (based on the metrics provided in Section 4.3) for different PD configurations when measuring 0.2 mm of crack extension in a Type 316H C(T) specimen at 550ºC. Figure 4.20 shows the results for an aluminium specimen at 20ºC.

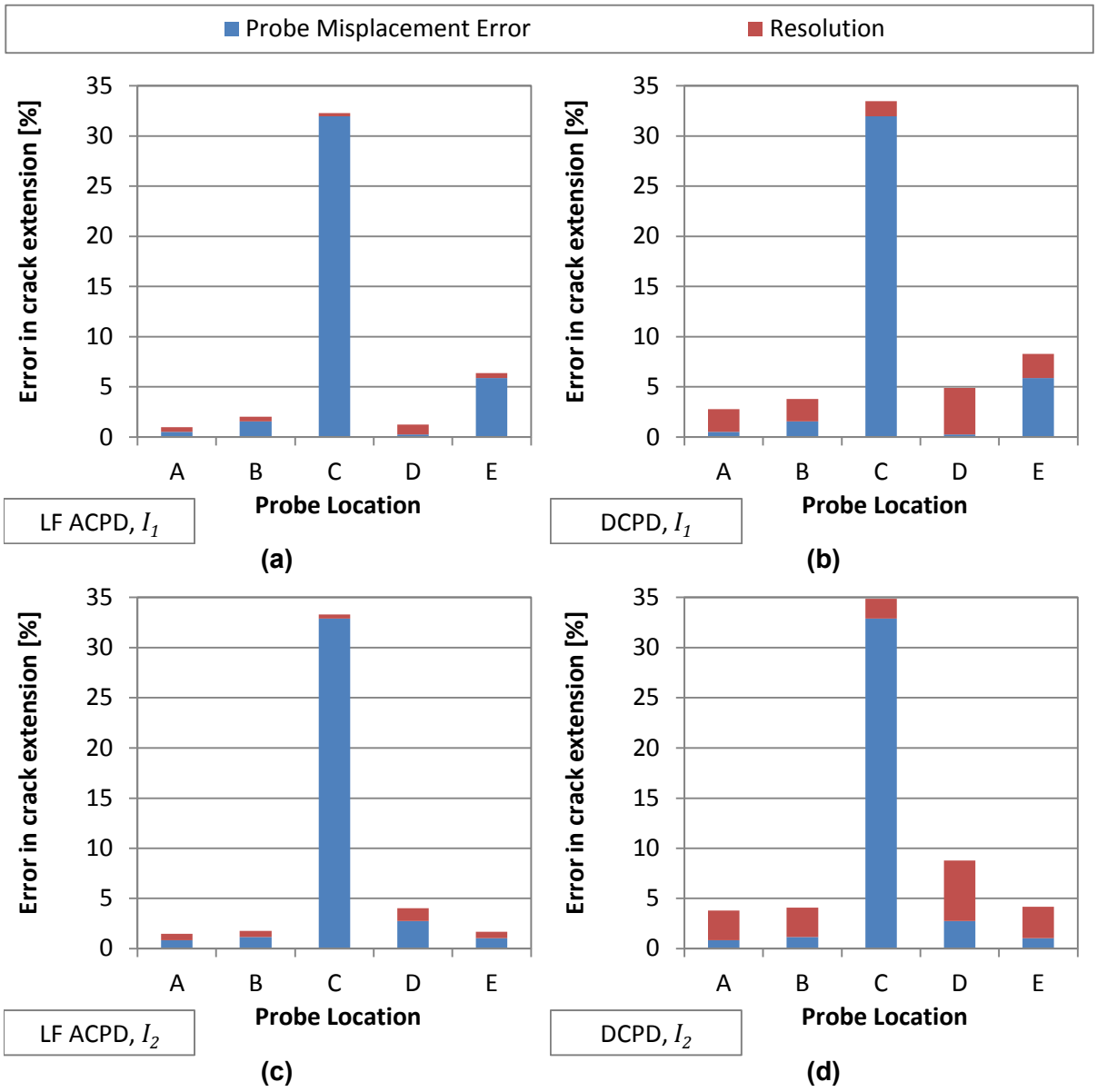

Figure 4.19: Absolute error when measuring 0.2 mm of crack extension in a Type 316H C(T) specimen at 550ºC with (a) current injected at I_1, using low frequency ACPD, (b) current injected at I_1, using DCPD, (c) current injected at I_2, using low frequency ACPD and (d) current injected at I_2, using DCPD.

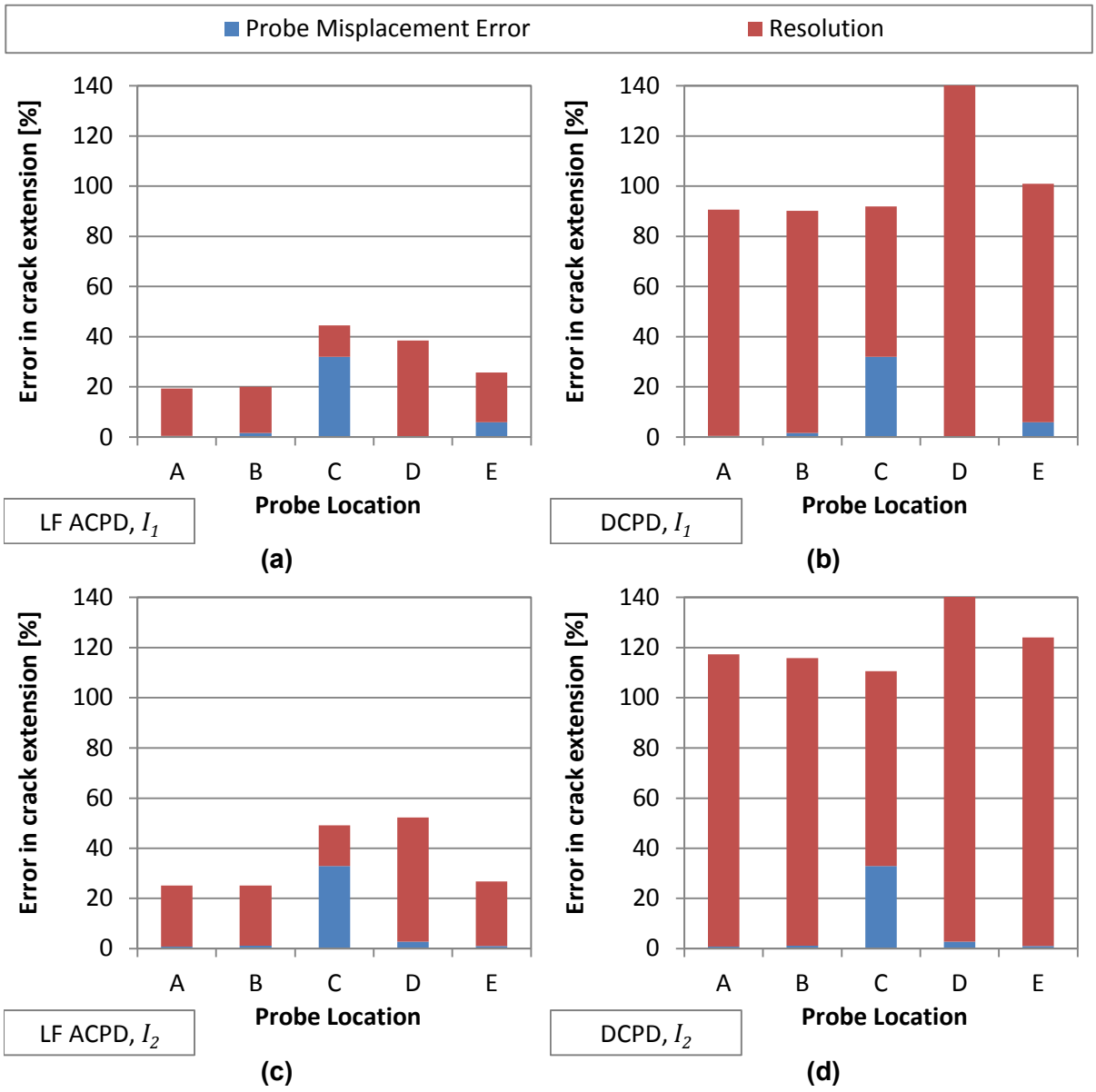

Figure 4.20: Absolute error when measuring 0.2 mm of crack extension in an aluminium C(T) specimen at 20ºC with (a) current injected at I_1, using low frequency ACPD, (b) current injected at I_1, using DCPD, (c) current injected at I_2, using low frequency ACPD and (d) current injected at I_2, using DCPD.

When measuring 0.2 mm of crack growth, the resolution is generally larger than the probe misplacement error, but despite this change in the dominant source of error, probe location A with the current injected at I_1 remains optimum. The total error for this configuration in a Type 316H specimen at 550ºC is ~1% and ~3% for the low frequency ACPD and DCPD systems respectively. For an aluminium specimen at 20ºC, this increases to ~19% and ~91% for the respective PD systems. When measuring small amounts of crack growth the choice of PD system is of vital importance, particularly for specimens with low resistivity.

Other PD configurations where the error is similar, albeit slightly higher, are:

- Probe location A with the current injected at I_2
- Probe location B with the current injected at I_1 or I_2
- Probe location E with the current injected at I_2

These are the same configurations identified when measuring significant crack growth.

In general, when measuring small amounts of crack growth, the errors for the C(T) specimen are larger than for the SEN specimen. This is because the dominant source of error is resolution which is inversely related to the magnitude of the signal. The C(T) specimen considered in this study is wider and thicker than the SEN specimen. It therefore has a lower resistance so the resolution is higher.

4.6.4.3 Method of Suppressing Proportional Changes in PD

A suitable remote reference PD configuration for the C(T) specimen has been identified in Figure 4.21 where the current injection locations, shown in black, are labelled *Iref*, and the PD probes, shown in pink, are labelled *Cref*. This configuration provides a large reference signal that is not significantly affected by crack growth. In the following section, this reference measurement has been considered in conjunction with the probe locations which produced the lowest errors in crack extension. These are: probe location A with the current injected at I_1 and I_2; Probe location B with the current injected at I_1 and I_2; and Probe location E with the current injected at I_2.

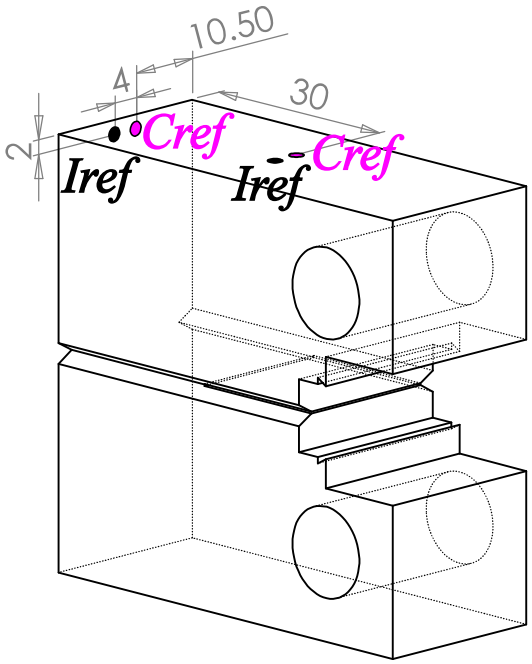

Figure 4.21: C(T) remote reference PD configuration.

From the SEN specimen, it was identified that when using two measurements across the crack to supress proportional changes in PD, the two probe locations should be located far from each other. Based on this observation configurations D/A (the ratio of D to A) and D/B (the ratio of D to B) have been considered here. The total error for probe location D is significantly higher if the current is injected at I_2, so only I_1 has been considered. These PD configurations are similar to those proposed by McCartney et al. [60].

Figure 4.22 shows the errors (based on the metrics provided in Section 4.3) in crack extension due to different methods of suppressing proportional changes in PD when measuring large amounts of crack extension in a 316H C(T) specimen at 550ºC. Figure 4.23 shows the results for an aluminium specimen at 20ºC.

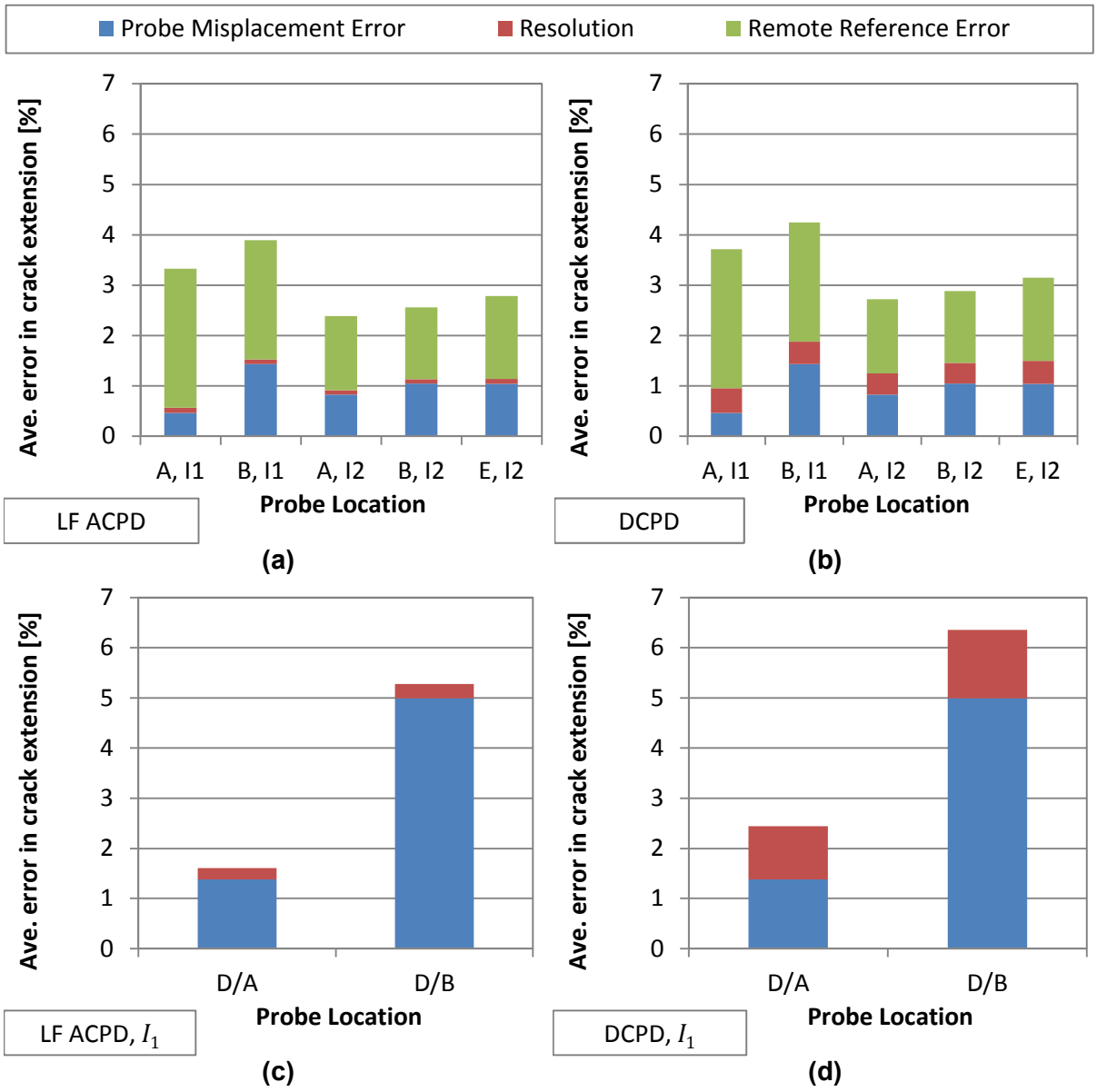

Figure 4.22: Average absolute error when measuring significant crack extension in a Type 316H C(T) specimen at 550ºC for (a) a remote reference measurement, using low frequency ACPD, (b) a remote reference measurement, using DCPD, (c) two measurements across the crack, using low frequency ACPD, and (d) two measurements across the crack, using DCPD.

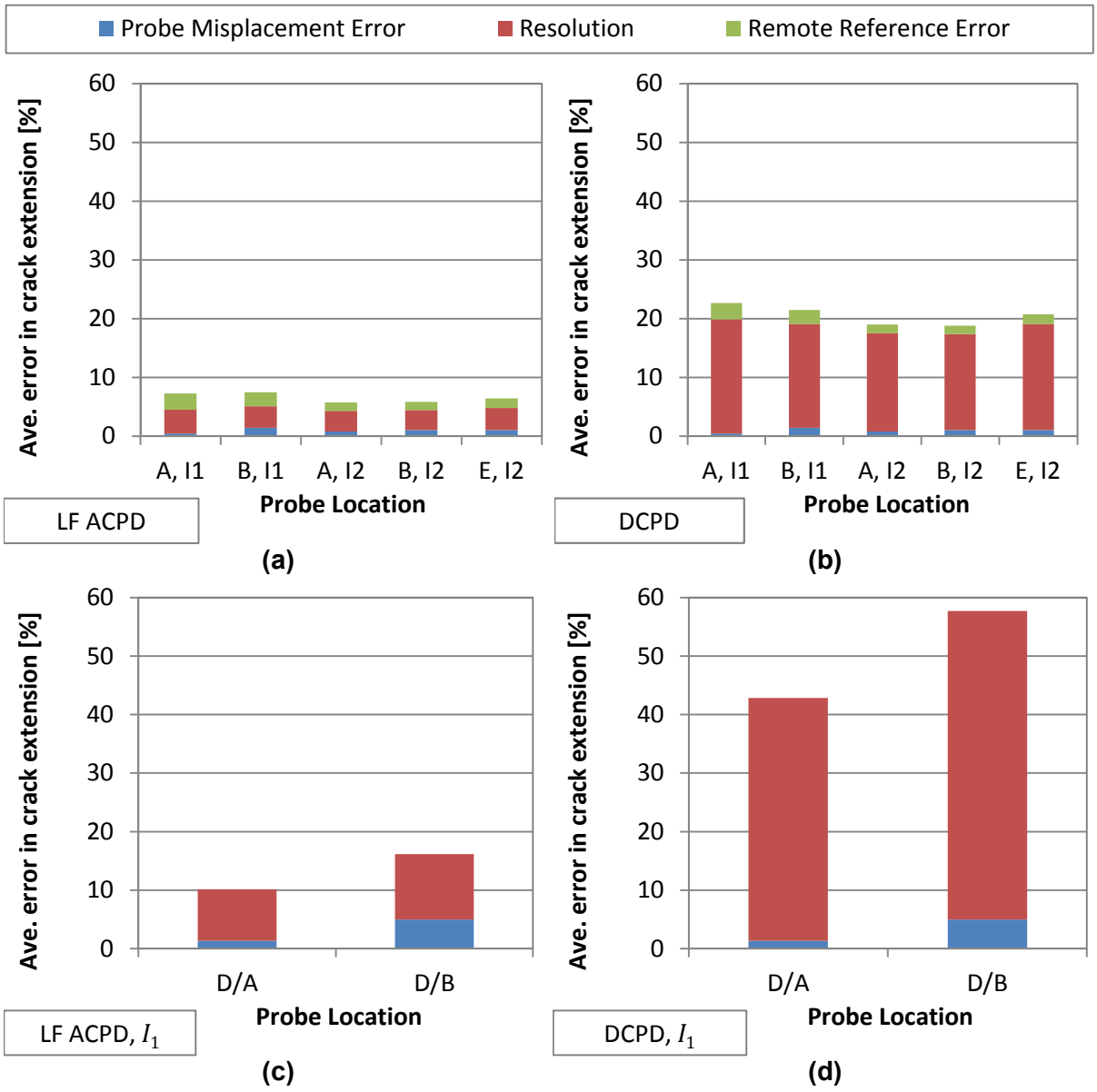

Figure 4.23: Average absolute error when measuring significant crack extension in an aluminium C(T) specimen at 20ºC for (a) a remote reference measurement, using low frequency ACPD, (b) a remote reference measurement, using DCPD, (c) two measurements across the crack, using low frequency ACPD, and (d) two measurements across the crack, using DCPD.

When measuring significant crack growth with a remote reference measurement the optimum PD configuration is probe A, with the current injected at I_2. For this configuration, the total error in a Type 316H specimen at 550ºC is 2.4% for the low frequency ACPD system and 2.7% for the DCPD system. For an aluminium specimen at 20ºC, this increases to 5.8% and 19.0% respectively. The optimum PD configuration is slightly different to when no method of suppression is implemented, where the optimum current injection location is I_1 but the errors for all of the other configurations considered in this study remain similar.

When two measurements are taken across the crack the optimum PD configuration is D/A, with the current injected at I_1. For a Type 316H specimen at 550ºC the total error is 1.6% for the low frequency ACPD system and 2.4% for the DCPD system. For an aluminium specimen at 20ºC, this increases to 10.1% and 42.3% respectively. The errors for configuration D/B are considerably higher.

When testing materials with a low resistivity the errors in the crack extension measurement are smaller when a remote reference measurement is used to supress proportional changes in PD rather than two measurements across the crack. When testing materials with a high resistivity the errors in the crack extension measurement reduce significantly such that either method may be implemented without a significant impact on the accuracy of the measurements.

Figure 4.24 shows the absolute errors (based on the metrics provided in Section 4.3) when measuring 0.2 mm of crack growth in a Type 316H C(T) specimen at 550ºC using different methods of supressing proportional changes in PD. Figure 4.25 shows the same results for an aluminium specimen at 20ºC. For some configurations where the errors are particularly high, the total extent of these errors are not shown because the scale of the axes has been selected to compare the PD configurations with the lowest errors.

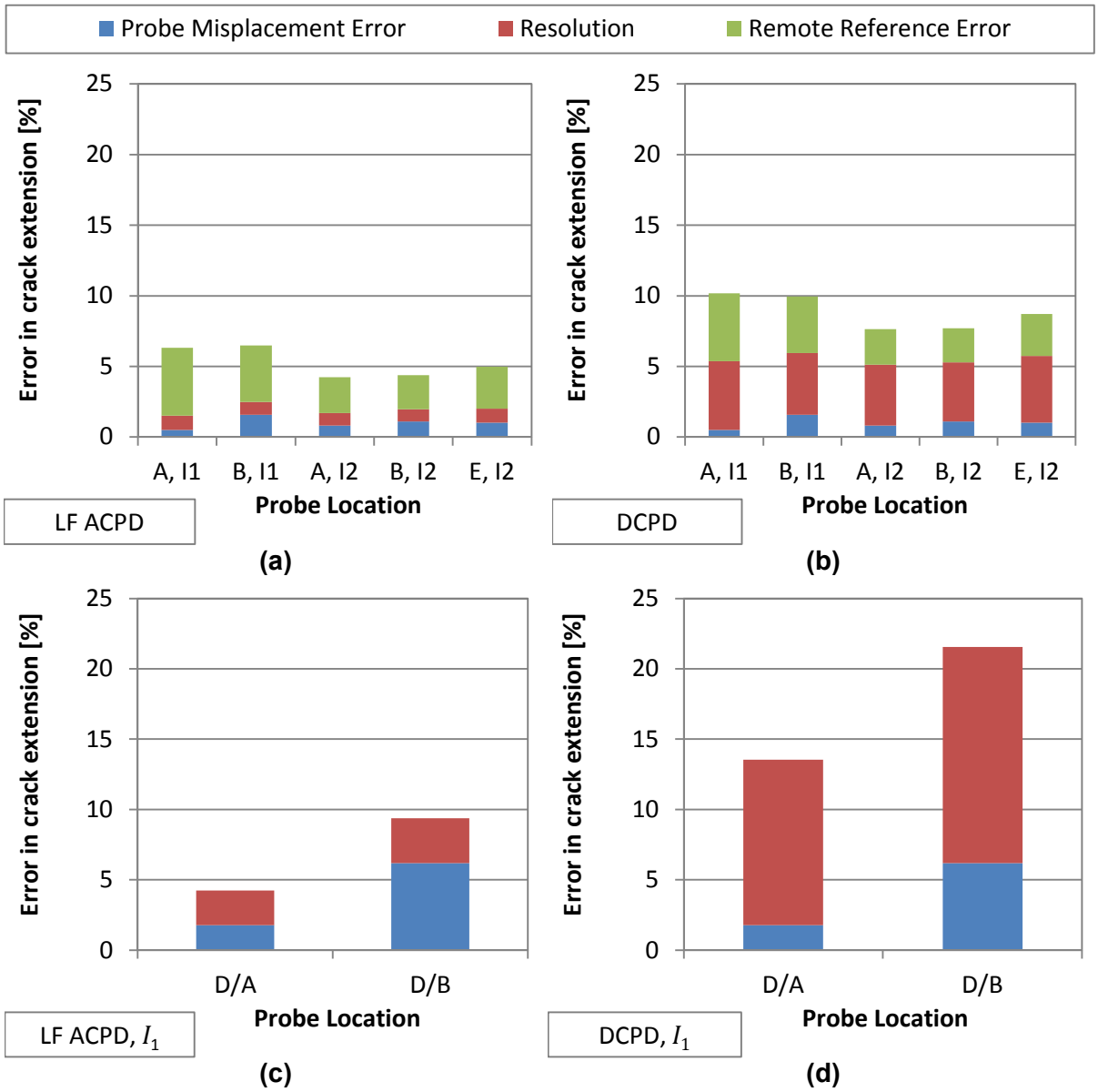

Figure 4.24: Absolute error when measuring 0.2 mm crack extension in a Type 316H C(T) specimen at 550ºC for (a) a remote reference measurement, using low frequency ACPD, (b) a remote reference measurement, using DCPD, (c) two measurements across the crack, using low frequency ACPD, and (d) two measurements across the crack, using DCPD.

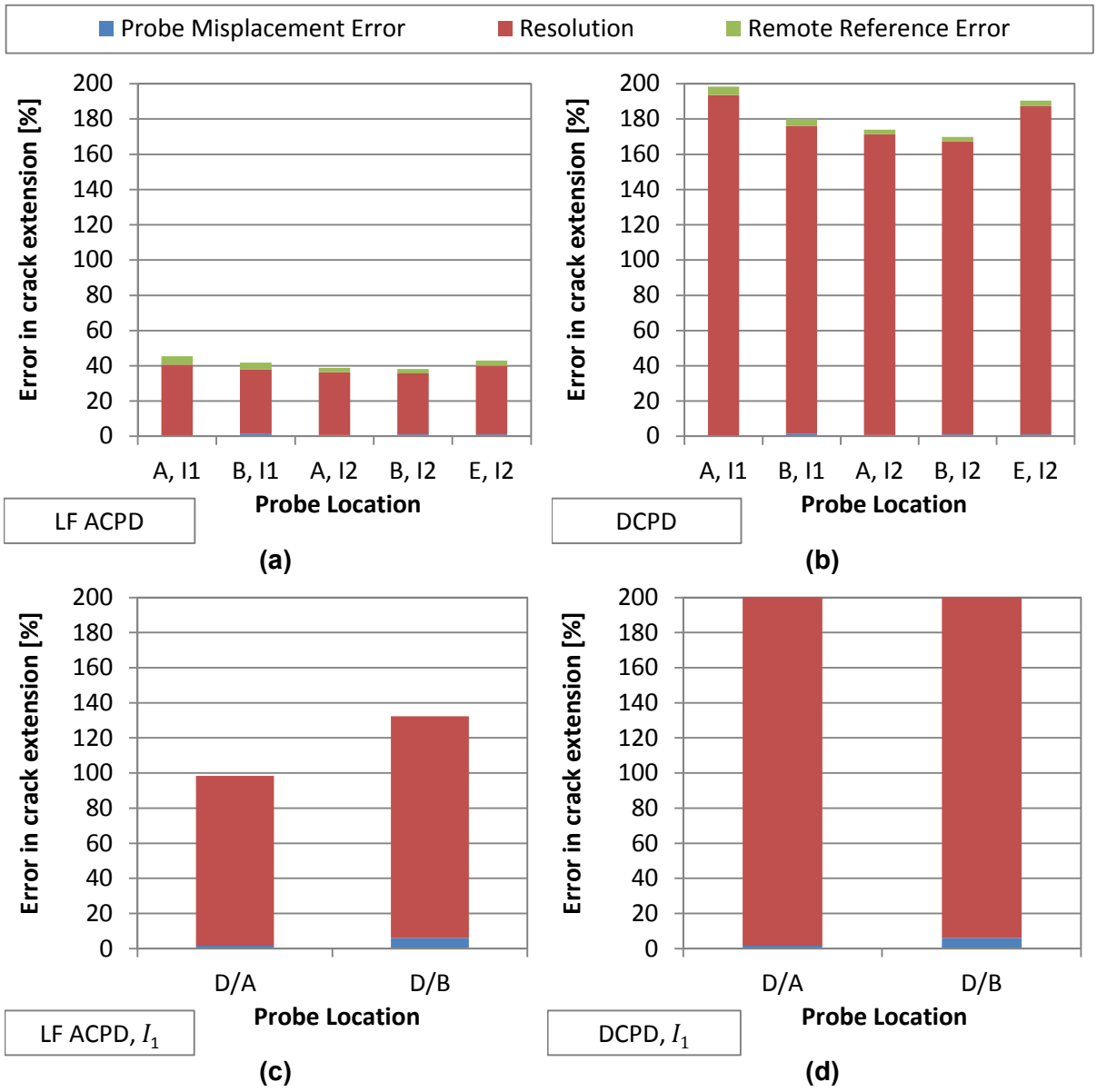

Figure 4.25: Absolute error when measuring 0.2 mm crack extension in an aluminium C(T) specimen at 20ºC for (a) a remote reference measurement, using low frequency ACPD, (b) a remote reference measurement, using DCPD, (c) two measurements across the crack, using low frequency ACPD, and (d) two measurements across the crack, using DCPD.

When measuring 0.2 mm of crack growth with a remote reference measurement the error for all the configurations considered in this study is similar. For PD probe A, with the current injected at I_2 (the optimum configuration when measuring significant crack growth) the total error in a Type 316H specimen at 550ºC is 4.2% for the low frequency ACPD system and 7.6% for the DCPD system. For an aluminium specimen at 20ºC, this increases to 38.9% and 173.9% respectively.

When two measurements are taken across the crack, the optimum configuration remains D/A with the current injected at I_1. For a Type 316H specimen at 550ºC the total error is 4.2% for the low frequency ACPD system and 13.5% for the DCPD system. For an aluminium specimen at 20ºC, this increases to 98.4% and 459% respectively. The errors for configuration D/B are considerably higher.

4.7 Discussion

When additional measurements are not implemented to suppress proportional changes in PD the optimum configuration for a SEN specimen, is probe location A1 with the current injected remote from the gauge region of the specimen. For a C(T) specimen the optimum configuration is probe location A with the current injected at I_1. These remain the optimum configurations when measuring small or large amounts of crack growth in specimens manufactured from a broad range of structural materials. For a C(T) specimen, a range of alternative configurations have been also been identified where the error is only slightly higher than the optimum configuration. These are:

- Probe location A with the current injected at I_2.
- Probe location B with the current injected at either I_1 or I_2.
- Probe location E with the current injected at I_2.

The errors in the measurement of crack extension for the optimum configurations are summarised in Table 4.7 and Table 4.8 for the SEN and C(T) specimens respectively.

Amount of Crack Growth	**Material**	**Error in crack extension measurement [%]**	
		DCPD	**Low Freq. ACPD**
Significant crack growth	Type 316H (550°C)	2.4	2.4
	Aluminium (20°C)	6.1	3.1
Crack Initiation	Type 316H (550°C)	4.4	3.6
	Aluminium (20°C)	43.7	11.8

Table 4.7: Summary of the errors associated with the optimum PD configuration for a SEN specimen.

For materials with high resistivity, the signal-to-noise ratio is high, so the resolution is small and probe misplacement is the dominant source of error. By implementing the optimum PD configurations identified above, the error in the crack extension measurement is <5% and the benefit of the reduced noise of the low frequency ACPD system is also small. For materials with low resistivity, the signal-to-noise ratio is reduced and the resolution becomes the dominant source of error. Despite this change, the optimum PD configurations remain

the same. For such materials, the total error in the crack extension measurement is much larger, and can be as high as 90%. It is therefore necessary, where possible, to increase the signal-to-noise ratio. The low frequency ACPD system is an effective way of achieving this.

Amount of Crack Growth	Material	Error in crack extension measurement [%]	
		DCPD	Low Freq. ACPD
Significant crack growth	Type 316H (550°C)	0.7	0.5
	Aluminium (20°C)	9.3	2.3
Crack Initiation	Type 316H (550°C)	2.8	1.0
	Aluminium (20°C)	90.6	19.3

Table 4.8: Summary of the errors associated with the optimum PD configuration for a C(T) specimen.

It should be noted that the errors calculated for aluminium specimens in this study are likely to be overestimated. For the DCPD system a constant current of 20 A has been assumed for simplicity, but for low resistivity materials, higher currents are sometimes used which would increase the signal-to-noise ratio. Also, the low frequency ACPD system incorporates a resistance bridge with a variable reference resistor which should be set to match the approximate resistance of the specimen. This reduces the signal noise when measuring smaller resistances. Although these changes would reduce the magnitude of the errors in Table 4.7 and Table 4.8, they will not change optimum PD configurations which, as has been demonstrated, remain unchanged for all conditions considered in this study.

Two methods of supressing proportional changes in PD have been considered in this study:

1. A reference measurement remote from the crack
2. Two parallel measurements across the crack

For a SEN specimen with a remote reference measurement, the optimum PD configuration remains probe location A1 with the current injected remote from the gauge region. When two measurements are taken across the crack, the optimum PD configuration is A1/A5 (the ratio of A1 to A5) with the current injected remote from the gauge region. For both of these configurations, the errors in the crack extension measurement are very similar. Typical values of these errors are summarised in Table 4.9.

Amount of Crack Growth	Material	Error in crack extension measurement [%]	
		DCPD	Low Freq. ACPD
Significant crack growth	Type 316H (550°C)	~3	~3
	Aluminium (20°C)	~10	~5
Crack Initiation	Type 316H (550°C)	~6	~5
	Aluminium (20°C)	~70	~18

Table 4.9: Typical errors associated with the optimum PD configurations for the SEN specimen when supressing proportional changes in PD.

For a C(T) specimen with a remote reference measurement, the optimum PD configuration is probe location A with the current injected at I_2. This current injection location is different to when no method of suppression is implemented but the difference between the two current injection locations is small. When two measurements are taken across the crack, the optimum PD configuration is D/A (the ratio of D to A) with the current injected at I_1. For a C(T) specimen, a remote reference measurement tends to result in smaller errors in the crack extension measurement than when two measurements are taken across the crack, particularly when the material resistivity is low. The errors in the measurement of crack extension for the optimum PD configuration, based on a remote reference measurement, are summarised in Table 4.10.

Amount of Crack Growth	Material	Error in crack extension measurement [%]	
		DCPD	Low Freq. ACPD
Significant crack growth	Type 316H (550°C)	2.7	2.4
	Aluminium (20°C)	19.0	5.8
Crack Initiation	Type 316H (550°C)	7.6	4.2
	Aluminium (20°C)	173.9	38.9

Table 4.10: Errors associated with the optimum PD configuration for the C(T) specimen when supressing proportional changes in PD.

By comparing Table 4.7 and Table 4.8 with Table 4.9 and Table 4.10 it is apparent that introducing additional measurements to supress proportional changes in PD increases other sources of error. For specimens with high resistivity, this additional error is relatively small (a few percent) so it is reasonable to implement these suppression techniques without significantly affecting the overall accuracy of the measurement. For specimens with low resistivity however, the total error is approximately doubled and can be extremely large,

especially when measuring crack initiation. If this additional error is larger than those which are being suppressed then these additional measurements should not be performed.

Where it is appropriate to supress proportional changes in PD, various factors should be considered when selecting which method of suppression to use. As well as the additional error in the measurement of crack extension consideration should also be given to the accuracy with which the initial crack length can be determined and the simplicity of implementing the chosen method.

When using a remote reference measurement, the initial crack length, a_0, is typically obtained from an independent optical measurement. This may be either from the side-face of the specimen or the post-test fracture surface. When two measurements are taken across the crack, the initial crack length is obtained directly from the PD. If the initial crack length can be measured optically with a high degree of accuracy, e.g. for specimens with an EDM pre-crack or if post-test measurements from the fracture surface are feasible, a remote reference measurement is likely to provide a more accurate initial crack length measurement compared to two PD measurements across the crack. If however a specimen with a fatigue pre-crack is used and the final fracture surface cannot be observed, the initial crack length may be more accurately determined from two PD measurements across the crack rather than a remote reference measurement.

Another consideration is the simplicity of implementing the chosen method of suppression. When two measurements are taken across the crack, it is often necessary to derive a calibration function specific for the PD configuration because very few calibration functions are available in the literature in this format. Implementing a remote reference measurement however is much simpler because the calibration function is the same as when no method of suppression is implemented. A calibration function can therefore be readily obtained from the literature. It should be noted however that small differences between the nominal geometry assumed in the derivation of the calibration function and the actual test geometry can introduce additional errors into the measurement of crack extension. The significance of these errors is assessed in the next chapter.

Chapter 5:

Errors Associated with PD Calibration Functions

5.1 Introduction

Calibration functions are provided in standards for various specimen geometries e.g. [3, 55]. When applying these calibration functions, the geometry of the specimen being tested is often different to the geometry for which the calibration was derived due to, for example, the addition of a notch to accommodate the necessary extensometry or side-grooves. Most calibration functions also assume uniform crack extension along the crack front whilst uneven crack extension, such as crack tunnelling, is often observed experimentally. Finally, for specimens containing two crack tips, calibration functions assume the same crack extension at each tip but some uneven crack growth is inevitable. These differences are all potential sources of error in the measurement of crack extension. In this chapter a finite element based investigation is presented which quantifies the significance of these sources of error. Consideration is given to the measurement of both crack initiation and significant crack growth. By quantifying these typical sources of error, the significance of the influence of large inelastic strains, considered in subsequent chapters, may be determined by comparison.

Most standards only provide calibration functions for a limited number of specimen types. This can preclude the use of other specimens which may be more representative of the structure for which the test is being performed. In this chapter, the possibility of a single unified calibration function for all geometries will also be investigated which would ensure that the specimen geometry was selected based on the test requirements rather than the availability of a suitable calibration function. The error in the measurement of crack extension based on a unified calibration function will be assessed and recommendations made with regards to its use. The seven specimen types considered in this study are:

- Middle Tension, M(T)
- Compact Tension, C(T),

- Single Edge-Notched Tension, SEN(T),
- Single Edge-Notched Bend, SEN(B),
- Double Edge-Notched Tension, DEN(T),
- Disc-shaped Compact Tension, DC(T),
- C-Shaped Tension, CS(T).

5.2 Influence of Notch Geometry

When performing crack growth tests on a C(T) specimen, either a capacitance gauge or a clip gauge are often used to measure load-line displacement and the size and shape of the notch required to accept the necessary extensometry can vary significantly. Conversely, when a load-line displacement measurement is not required, or is measured remotely, the specimen may only contain a thin EDM slot. Calibration functions are sensitive to these variations in notch geometry [58, 75] but are often derived based on a crack of infinitesimal width for simplicity [58, 60]. When applying these calibration functions to a specimen containing a substantial notch, this will introduce errors in the calculation of crack extension. The significance of these errors is investigated here.

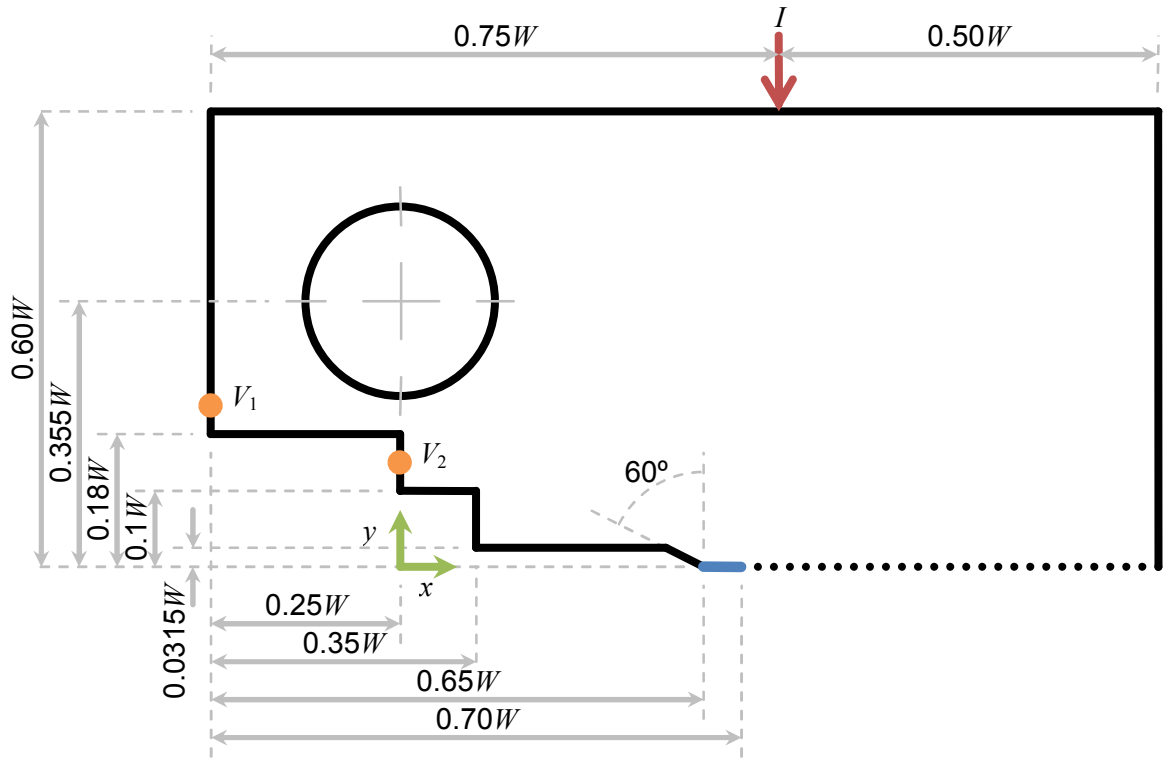

Figure 5.1: ½ C(T) specimen geometry, including the maximum allowable notch geometry from ASTM E1820-13 [27]. The fatigue pre-crack is highlighted blue, the current injection location is labelled I and the two likely PD probe locations are labelled V_1 and V_2.

ASTM E1820-13 [27] provides guidelines for the maximum allowable notch size in a C(T) specimen for fracture toughness testing. This notch geometry is shown in Figure 5.1. No guidance is provided for the size of opening at the crack mouth so $0.18W$ has been selected which is adequate to accommodate a typical clip gauge based on a specimen width, W, of 50 mm.

A similar modelling approach to the one outlined in the previous chapter was used to assess the influence of notch geometry. Two 2D ½ models of a C(T) specimen were developed using COMSOL [124]. One contained the minimum possible notch geometry (a crack of infinitesimal width) whilst the other contained the maximum allowable notch geometry shown in Figure 5.1. In each specimen, the crack was grown from $0.45W<a<0.90W$ and the change in PD was monitored at probe locations V_1 and V_2, also shown in Figure 5.1. The initial crack length, a_0, of $0.45W$ was based on the minimum requirement in ASTM E1820-13 [27]. For the model containing the maximum notch geometry, a $0.05W$ long fatigue pre-crack of infinitesimal width was assumed ahead of the notch which is another requirement of ASTM E1820-13 [27]. This standard does not provide a recommendation for the PD configuration, so the PD probe and current injection locations are based on recommendations in ASTM E1457-13 [3]. They also correspond to two of the preferred PD configurations identified in the previous chapter. The locations of the PD probes are provided in Table 5.1 based on the co-ordinate system shown in Figure 5.1.

PD Probe	Co-ordinates	
	x/W	y/W
V_1	-0.25	0.22
V_2	0.00	0.14

Table 5.1: Co-ordinates of the PD probes used to assess the influence of notch geometry on crack extension measurement

$$\frac{a}{W} = A_0 + A_1\left(\frac{V}{V_0}\right) + A_2\left(\frac{V}{V_0}\right)^2 + A_3\left(\frac{V}{V_0}\right)^3 \quad \textbf{(5.1)}$$

The initial crack increment was $0.004W$. This corresponds to 0.2 mm of crack extension for a standard C(T) specimen (W = 50 mm) which is often used as an engineering definition of crack initiation. Subsequent crack increments were $0.05W$. The results from the model with the minimum notch geometry were used to derive a third order polynomial calibration function in the form of Equation (5.1). This calibration function was used to predict crack extension from PD measurements obtained from the model containing the maximum

allowable notch geometry. The difference between the predicted crack extension and the modelled value is the error due to the notch geometry. This is shown schematically in Figure 5.2.

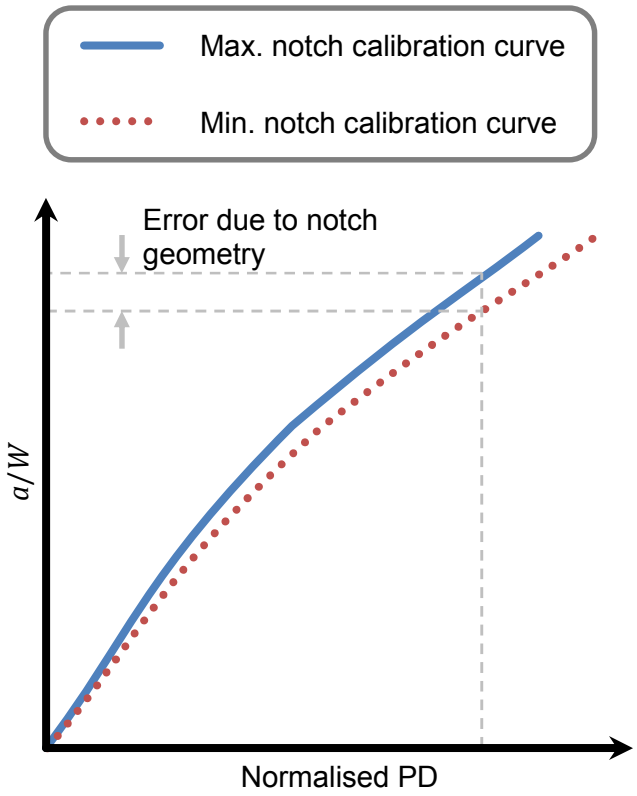

Figure 5.2: Schematic representation of the error due to notch geometry

The influence of notch geometry on the measurement of crack extension is illustrated in Figure 5.3. For both probe locations, the notch geometry has a significant influence on the crack extension measurement. The associated error is greatest when measuring small amounts of crack extension and is worse at probe location V_1. At this location, the initial error when measuring small amounts of crack extension is 21.9%. The mean error for all crack increments is much lower at 12.5%. At location V_2 the initial error is 13.6% and the mean is 6.4%.

The influence of the notch geometry is more significant for small crack extensions because the crack tip is closer to the notch. If a calibration function based on the minimum notch geometry was used to monitor crack extension when growing the $0.05W$ fatigue pre-crack the error would be even larger.

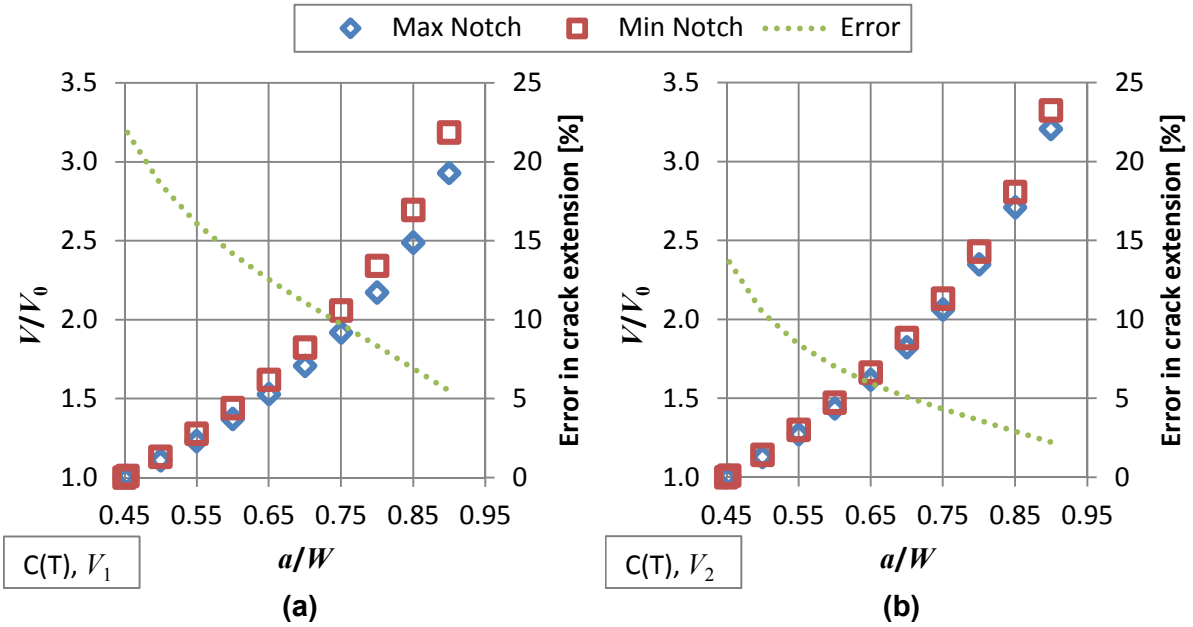

Figure 5.3: Influence of C(T) notch geometry on crack extension measurement for PD probe locations (a) V_1 and (b) V_2

5.3 Influence of Side Grooves

Calibration functions are often derived for plane sided geometry for simplicity however, crack growth tests performed on this type of specimen tend to exhibit crack tunnelling due to the reduced constraint associated with the plane stress conditions at the surface [127]. To avoid this, side grooves are often incorporated into the specimen however, these are likely to influence the calibration in a similar manner to the notch geometry.

The same approach used to investigate the influence of notch geometry has been used to investigate the influence of side grooves. Four 3D ¼ models of a C(T) specimen were developed using COMSOL [124] to model the effects of side grooves. A crack of infinitesimal width was assumed with no notch and a specimen thickness, B, of $W/2$. One of the models was plane sided whilst the others contained side grooves equal to 10%, 20% and 30% of the thickness (B_n = 0.9W, 0.8W and 0.7W respectively). The model with 30% side grooves is shown in Figure 5.4. The side grooves were modelled as perfectly sharp to simplify the mesh, with a root angle of 60º.

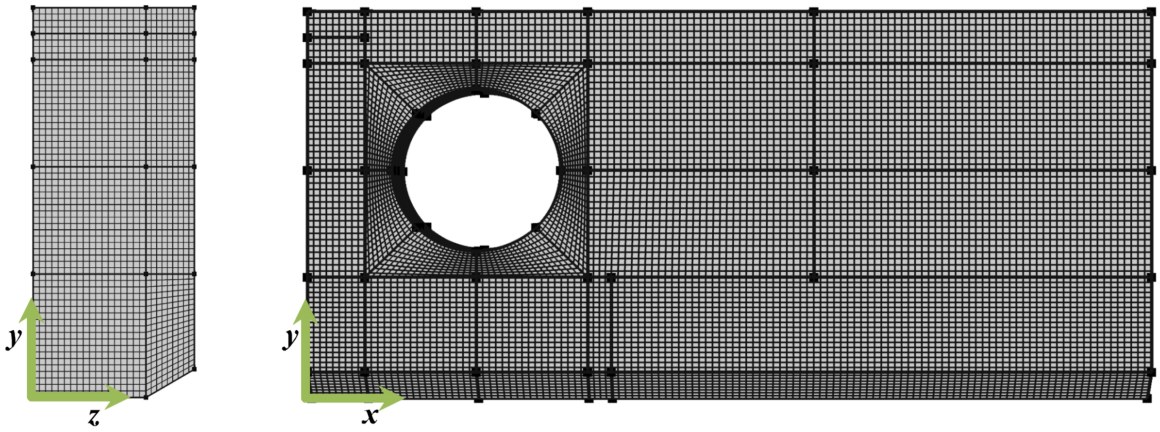

Figure 5.4: ¼ FE model of a C(T) specimen with 30% side-grooves.

Unlike the notch geometry study above, which was based on geometry from ASTM E1820-13, this and all subsequent studies are not specific to any standard and as such a wider range of crack lengths have been considered. For each model, the crack was grown from $0.20W<a<0.90W$ in increments of $0.05W$. An initial crack increment of $0.004W$ was also assessed to simulate initiation. The change in PD was monitored at two locations similar to those used in the notch geometry study. The location of the PD probes is provided in Table 5.2 based on the co-ordinate system shown in Figure 5.4. The results from the plane sided model were used to derive a third order polynomial calibration function in the form of Equation (5.1). This calibration function was used to predict crack extension from PD measurements obtained from the models containing the side grooves. The difference between the predicted crack extension and the modelled value is the error due to the side grooves.

PD Probe Location	Co-ordinates		
	x/W	y/W	z/W
V_1	-0.25	0.08	0.21
V_2	0.00	0.08	0.25

Table 5.2: Co-ordinates of the PD probes used to assess the influence of side-grooves on crack extension measurement

The influence of side-grooves on the measurement of crack extension is illustrated in Figure 5.5. Larger side-grooves result in a larger error, and these errors are greater at PD probe location V_2. For a C(T) specimen containing 20% side-grooves, which are suitable for most materials [3], the initial error when measuring small amounts of crack extension is 2.9% and 5.2% for probe locations V_1 and V_2 respectively. They increase to 5.8% and 10.0% for a

specimen with 30% side-grooves. These errors do not change significantly for the initial $0.3W$ of crack extension, but are much smaller when measuring large crack extensions.

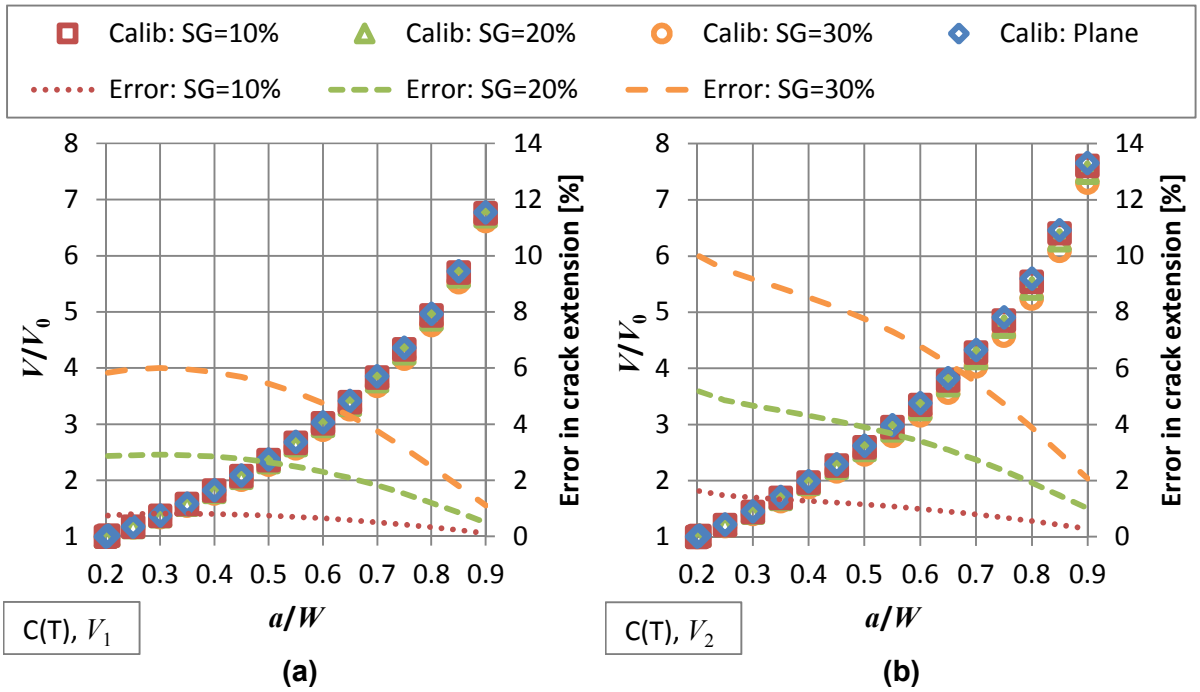

Figure 5.5: Influence of side grooves on crack extension measurement for PD probe locations (a) V_1 and (b) V_2

5.4 Influence of Crack Tunnelling

If a plane sided specimen is used, crack tunnelling tends to occur due to the reduced constraint at the free surface of the specimen but calibration functions are usually derived assuming uniform crack extension. Crack tunnelling will therefore influence the accuracy of the crack extension measurement. When using DCPD and low frequency ACPD the current distributes throughout the specimen. One of the often quoted advantages of this current distribution is that the measured PD will relate to some average crack length and will be less sensitive to uneven crack extension [105]. The accuracy of this statement and the significance of this source of error are investigated here.

A 3D model of a C(T) specimen was developed using COMSOL [124]. The crack was grown from $0.20W < a_{ave} < 0.90W$ in increments of $0.05W$, where a_{ave} is the mean crack length. This is calculated from Equation (5.2) where A_c is the crack area and B is the specimen thickness. An initial crack increment of $0.004W$ was also assessed to simulate initiation. The evolution of the crack tunnelling is shown in Figure 5.6 and is based on fracture surface observations from a creep crack growth test performed on a plane-sided C(T) specimen with no side-grooves [127]. A triangular rather than elliptical crack front was selected due to the ease of meshing this geometry. This simplification is considered adequate for the purposes

of this study. For each crack increment, the change in PD was monitored at the two probe locations in Table 5.2.

$$a_{ave} = \frac{A_c}{B} \tag{5.2}$$

The results from a model with a straight fronted crack were used to derive a third order polynomial calibration function in the form of Equation (5.1). This calibration function was used to predict crack extension from PD measurements obtained from the model including crack tunnelling. The difference between the predicted crack extension and the average modelled crack extension is the error due to crack tunnelling. The predicted crack extension has also been compared to the minimum and maximum crack extension where the minimum corresponds to the crack extension at the side face of the specimen and the maximum corresponds to the crack extension at the mid-plane.

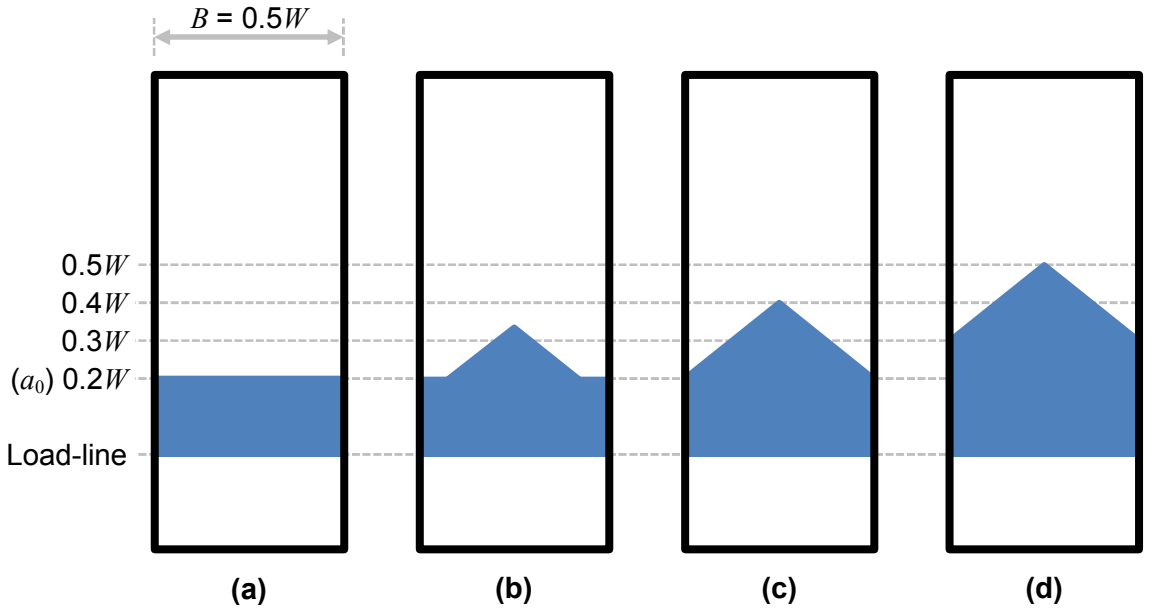

Figure 5.6: Section of a C(T) specimen showing the crack plane with the crack highlighted blue. The evolution of crack tunnelling is shown for (a) a_{ave} = 0.20W (a_0), (b) a_{ave} = 0.25 W, (c) a_{ave} = 0.30 W, (d) a_{ave} = 0.40 W.

The influence of crack tunnelling on the measurement of crack extension is illustrated in Figure 5.7. For both probe locations, the results are similar. The results based on uniform crack extension are in closer agreement with the mean extension of the tunnelling crack rather than the maximum or minimum but some significant errors still occur. For probe locations V_1 and V_2 these errors are 44.5% and 49.3% respectively. These errors reduce rapidly with crack extension and when measuring very large cracks they can be as low as 3%. In general the calibration function underestimates the mean crack extension of a tunnelling crack which is consistent with experimental observations [92]. This confirms that

DCPD measurements do indeed relate to some intermediate crack length, but not necessarily the arithmetic mean.

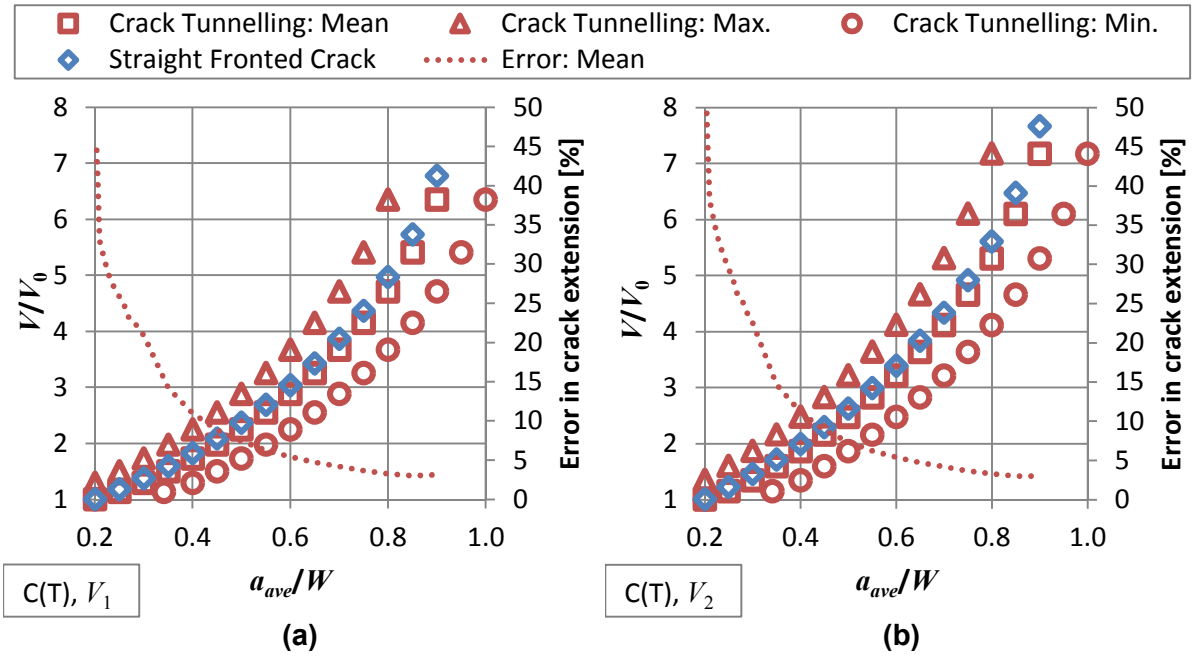

Figure 5.7: Influence of crack tunnelling on crack extension measurement for PD probe locations (a) V_1 and (b) V_2

This assessment of crack tunnelling is based on a specific crack front shape albeit based on experimental observations. In any one specific test, the error due to crack tunnelling may be smaller or larger depending on the shape of the crack front. Despite this, the results presented here are sufficient to conclude that the influence of crack tunnelling on DCPD measurements can be significant. This highlights the importance of applying appropriate side-grooves in order to obtain accurate measurements of crack extension and, in particular, crack initiation.

5.5 Uneven Crack Growth

DEN(T) and M(T) specimen geometries contain two crack tips. Calibration functions derived for these specimen geometries are based on the assumption that crack extension is identical at both crack tips however, in a physical test, crack growth is inevitably uneven. ASTM E647-13 [55] provides guidance for an M(T) specimen which limits the difference in distance from the centre-line of the specimen to each of the crack tips to $0.025W$ to avoid invalidating the SIF solution. This limit has been used in the following study to look at the influence of uneven crack growth on PD measurements for M(T) and DEN(T) specimens.

A 2D ½ model of an M(T) and a DEN(T) specimen was developed using COMSOL [124]. The specimen geometries, including the PD configuration are provided in Figure 5.8. A

uniform current distribution was assumed. In each specimen, the crack was grown from $0.20W<a_m<0.90W$ in increments of $0.05W$ where a_m is the mean of the two crack lengths, a_1 and a_2, defined in Figure 5.8. An initial crack increment of $0.008W$ was also assessed to simulate initiation. This corresponds to 0.2 mm of crack extension for a standard DEN(T) or M(T) specimen (W = 25 mm). The individual lengths of a_1 and a_2 were calculated from Equation (5.3) in accordance with the validity limit in ASTM E647-13. The change in PD was monitored at each crack increment.

$$\frac{a_1}{W} = \frac{a_2}{W} - 0.025 \tag{5.3}$$

The geometry of the M(T), shown in Figure 5.8(a), is identical to the geometry used by Johnson to derive his analytical calibration [58] (See Section 3.2.1.2). Due to the similarities in the geometry, the DEN(T) specimen, shown in Figure 5.8(b), will have an equivalent current distribution to that of the M(T), so the same analytical calibration is applicable [18]. Johnson's calibration function was therefore used to predict crack length from PD measurements obtained from the FE models with uneven crack extension. The difference between the predicted crack extension and the modelled value is the error due to uneven crack growth.

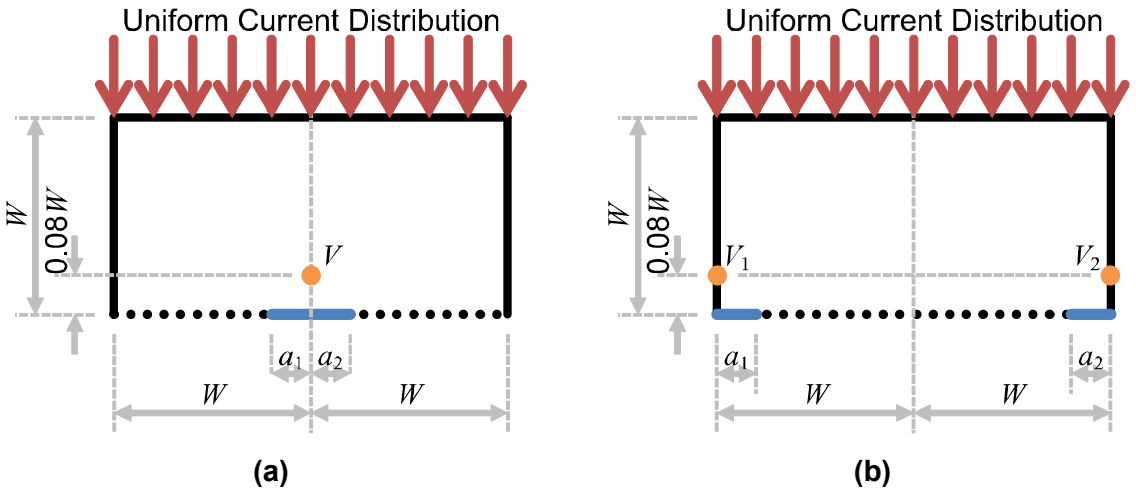

Figure 5.8: Geometry for (a) M(T) and (b) DEN(T) specimens

The influence of uneven crack growth on the measurement of crack extension in an M(T) and a DEN(T) specimen is shown in Figure 5.9. The FE results are in good agreement with the theoretical calibration derived by Johnson. For the M(T) specimen, the error is <0.5% for all crack extensions. For the DEN(T) specimen, the error is <1.5%. For the validity limits specified in ASTM E647-13, the influence of uneven crack growth is very small compared to the other sources of error considered in this study.

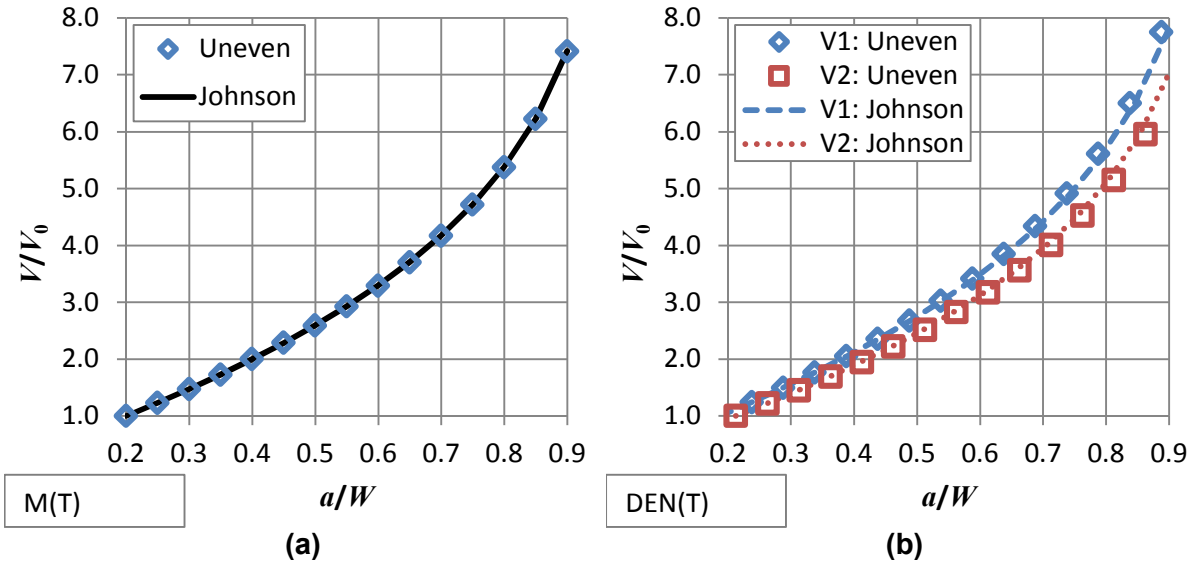

Figure 5.9: Influence of uneven crack growth in the measurement of crack extension for (a) an M(T) specimen and (b) a DEN(T) specimen

5.6 Unified Calibration Function

Calibration functions provided in standards are based on a set of assumptions about the geometry e.g. notch size and shape etc. When these are applied to a test specimen with slightly different geometry, the crack extension measurements will be subject to the sources of error discussed above. It is therefore preferable to derive a calibration function for the exact geometry being tested however, this is not always practical and the calibration functions provided in standards are often used.

Calibration functions are not available in the standards for the full range of specimen types. This can restrict the choice of specimen to the most common geometries which may not be representative of the structure for which the test is being performed. To avoid this restriction, the use of a single 'unified' calibration function has been considered for all the main specimen geometries. Whilst this will inevitably introduce some additional error into the calculation of crack extension, if this error is small relative to other typical sources of error, the availability of a unified calibration function would allow the specimen type to be selected based on the test requirements rather than the availability of a calibration function.

There are a wide range of specimen types available, the choice of which depends on the level of constraint required and material availability. The seven most common specimen types which will be considered in this investigation are:

- Compact Tension, C(T),
- Middle Tension, M(T),
- Single Edge-Notched Tension, SEN(T),

- Single Edge-Notched Bend, SEN(B),
- Double Edge-Notched Tension, DEN(T),
- C-Shaped Tension, CS(T),
- Disc-shaped Compact Tension, DC(T).

As discussed in Chapter 3, calibration functions can be derived analytically, numerically or empirically. Numerical and empirical calibration functions are derived by curve fitting to discrete data points. To ensure that they are independent of specimen material, thickness and in-plane size they are normalised with respect to a known defect size. This makes implementing these calibration functions more onerous since an additional calculation is required to identify the PD at this known defect size. Analytical calibration functions, such as the one derived by Johnson [58], are more general. This allows the user to select the normalising defect size to match the initial crack which simplifies the implementation of this form of calibration function. For this reason, the calibration curve derived by Johnson will be the focus of this study.

Johnson's calibration was originally derived for an M(T) specimen. Schwalbe and Hellman [66] identified that an M(T) specimen is geometrically equivalent to two mirrored SEN specimens and that the calibration should therefore be the same for the equivalent PD configuration. Similar to an M(T), a DEN(T) specimen is also equivalent to two mirrored SEN specimens so the calibration for this specimen should also the same [18]. Johnson's calibration is therefore an exact solution for four of the seven specimen types considered in this study, namely M(T), DEN(T), SEN(T) and SEN(B).

Schwalbe and Hellman [66] also observed that a C(T) is effectively a short SEN specimen so the calibration is similar although the non-uniform current distribution, due to the compact geometry, is a source of discrepancy. Of the remaining geometries, a DC(T) is geometrically similar to a C(T) specimen and a CS(T) is geometrically similar to an SEN specimen. It is therefore likely that the same calibration can also be applied to these geometries.

In this study, the work performed by Schwalbe and Hellman has been extended to include all of the geometries listed above. The error in crack extension associated with the use of Johnson's calibration function has been calculated for all seven specimen types listed above. For the three specimen types for which Johnson's calibration is not an exact solution, the PD configuration which results in the minimum error has been identified by trial and error.

For each specimen, a 2D finite element model was developed using COMSOL [124]. An infinitesimal crack width has been assumed, similar to Johnson's original derivation. The distance of the PD probes from the crack plane was set to $0.08W$ for all geometries. For a

specimen width, W, of 25 mm, this is a distance of 2.0 mm. This close proximity will reduce the errors due to probe misplacement based on the results of the previous chapter. Johnson's calibration also assumes a uniform current distribution so the current has been injected as remote from the crack as possible for each specimen. In the case of the M(T), SEN and DEN(T) specimens, which usually have a long thin aspect ratio, a uniform current distribution has been applied directly which assumes that the current can be injected at a location which is sufficiently remote from the crack. For the other, more compact geometries, the current injection location has been explicitly modelled.

For each model, the crack was grown from $0.20W<a<0.90W$ in increments of $0.05W$. For each increment the PD from the model was used to estimate crack extension using Johnson's calibration. The difference between the predicted and modelled crack extension is the error due to the applied calibration function.

The following sections focus on optimising the PD configurations for the C(T), CS(T) and DC(T) specimen types. This is followed by a comparison of Johnson's calibration with the FE results for each of the seven specimen types. The viability of using Johnson's calibration as a unified calibration function is then discussed.

5.6.1 C(T) Specimen

The C(T) specimen geometry and proposed PD configurations are shown in Figure 5.10(a). The current injection location is the one proposed by Schwalbe and Hellman [66]. Two PD probe locations, V_1 and V_2, have been considered. Schwalbe and Hellman used location V_1 but V_2 is more representative of the location used by Johnson. The results from the two PD probe locations are compared with Johnson's calibration function in Figure 5.10(b). The absolute errors in crack extension are also shown.

The calibration of PD probe location V_2 is in better agreement with Johnson's calibration function than V_1. The maximum absolute error in crack extension at this location is 7.9% when measuring small crack extensions compared with 24.9% at location V_1. At large crack extensions these errors are significantly reduced. Probe location V_2 will be considered for the unified calibration function.

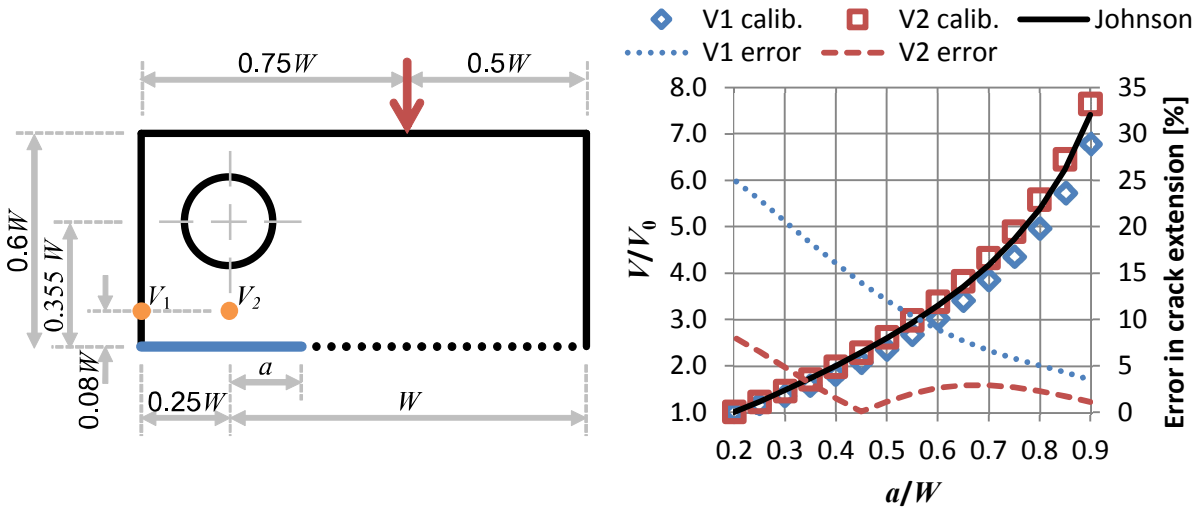

(a) (b)

Figure 5.10: C(T) Specimen (a) geometry and (b) influence of PD probe location on calibration

5.6.2 CS(T)

The CS(T) specimen geometry and proposed PD configuration is shown in Figure 5.11(a). The PD probe location is similar to that proposed by Schwalbe and Hellman for an SEN specimen. The current injection location has been varied to try and match Johnson's calibration. The influence of the angle, θ, on the calibration is shown in Figure 5.11(b). The absolute error in crack extension is only shown for the optimum PD configuration for clarity.

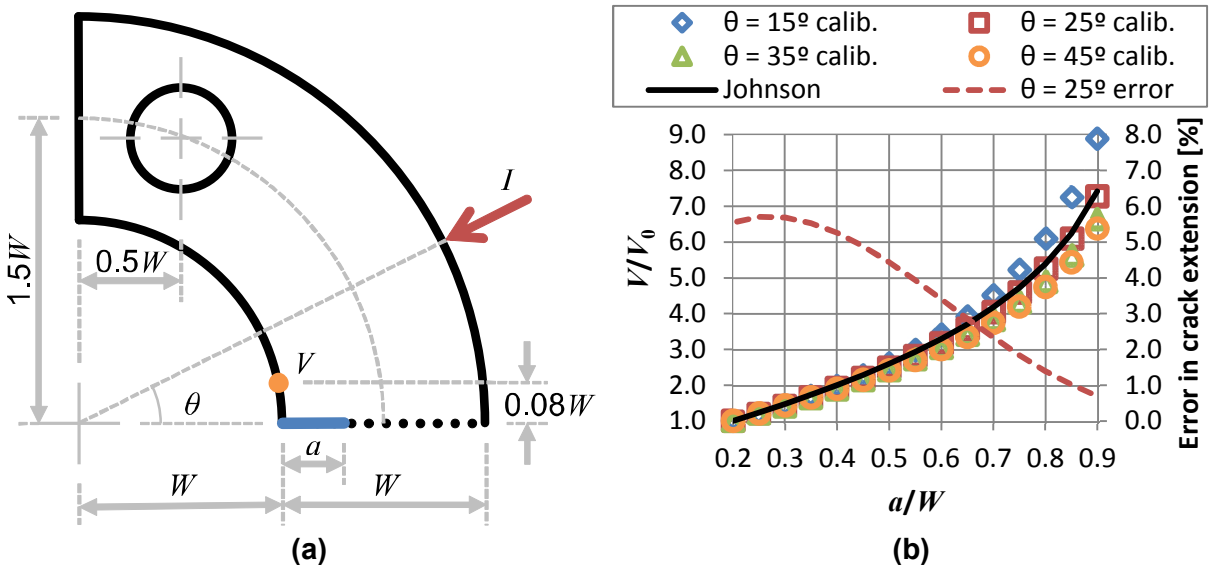

(a) (b)

Figure 5.11: CS(T) specimen (a) geometry and (b) influence of current injection location on calibration

The angle of the current injection, θ, which most accurately matches Johnson's calibration, is 25º. For this PD configuration, the maximum error in crack extension is 5.7% when

measuring small crack extensions. At large crack extensions, these errors reduce significantly. When the angle of the current injection is 45º, the worst case considered in this study, the maximum error increases to 9.8%.

5.6.3 DC(T)

The DC(T) specimen geometry and proposed PD configuration is shown in Figure 5.12(a). The PD probe location is similar to that used for a C(T) specimen. The current injection location has been varied to try and match Johnson's calibration. The influence of the angle, θ, on the calibration is shown in Figure 5.12(b). The absolute error in crack extension is only shown for the optimum PD configuration for clarity.

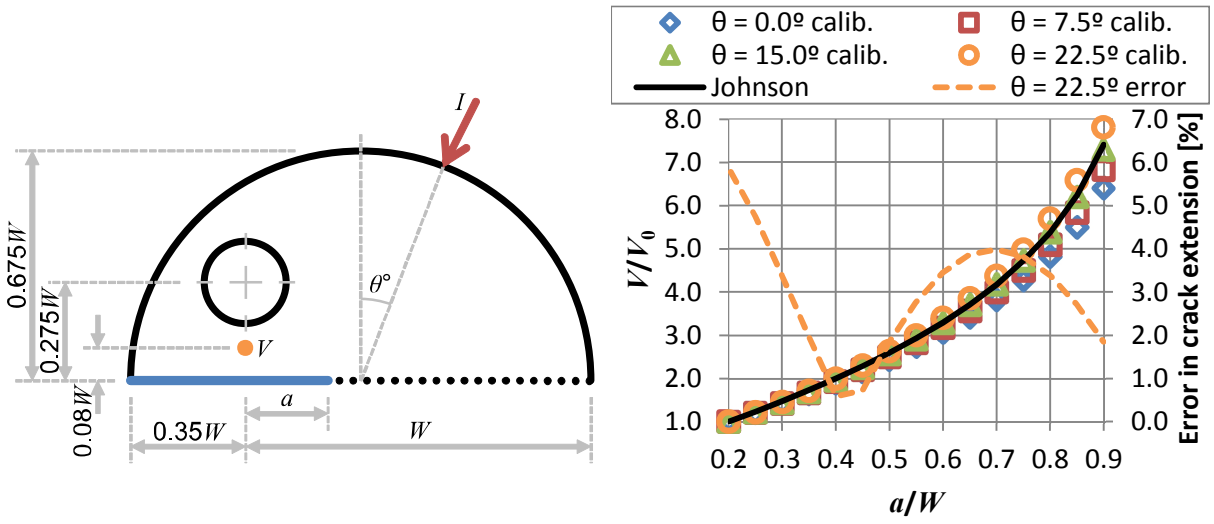

(a) **(b)**

Figure 5.12: DC(T) specimen (a) geometry and (b) influence of current injection location on calibration

The angle of the current injection, θ, which most accurately matches Johnson's calibration, is 22.5º. For this PD configuration, the maximum error in crack extension is 5.8% when measuring small crack extensions. When the angle of the current injection is 0º, the worst case considered in this study, the maximum error increases to 10.7%.

5.6.4 All Geometries

The selected PD configurations for the different specimen types are shown in Figure 5.13. The calibration functions for these geometries, obtained numerically, are compared with Johnson's calibration function in Figure 5.14. The errors in the measurement of crack extension based on Johnson's calibration function are provided in Table 5.3. The maximum and mean errors for all crack increments are provided along with the initiation error which corresponds to the initial 0.2 mm of crack extension.

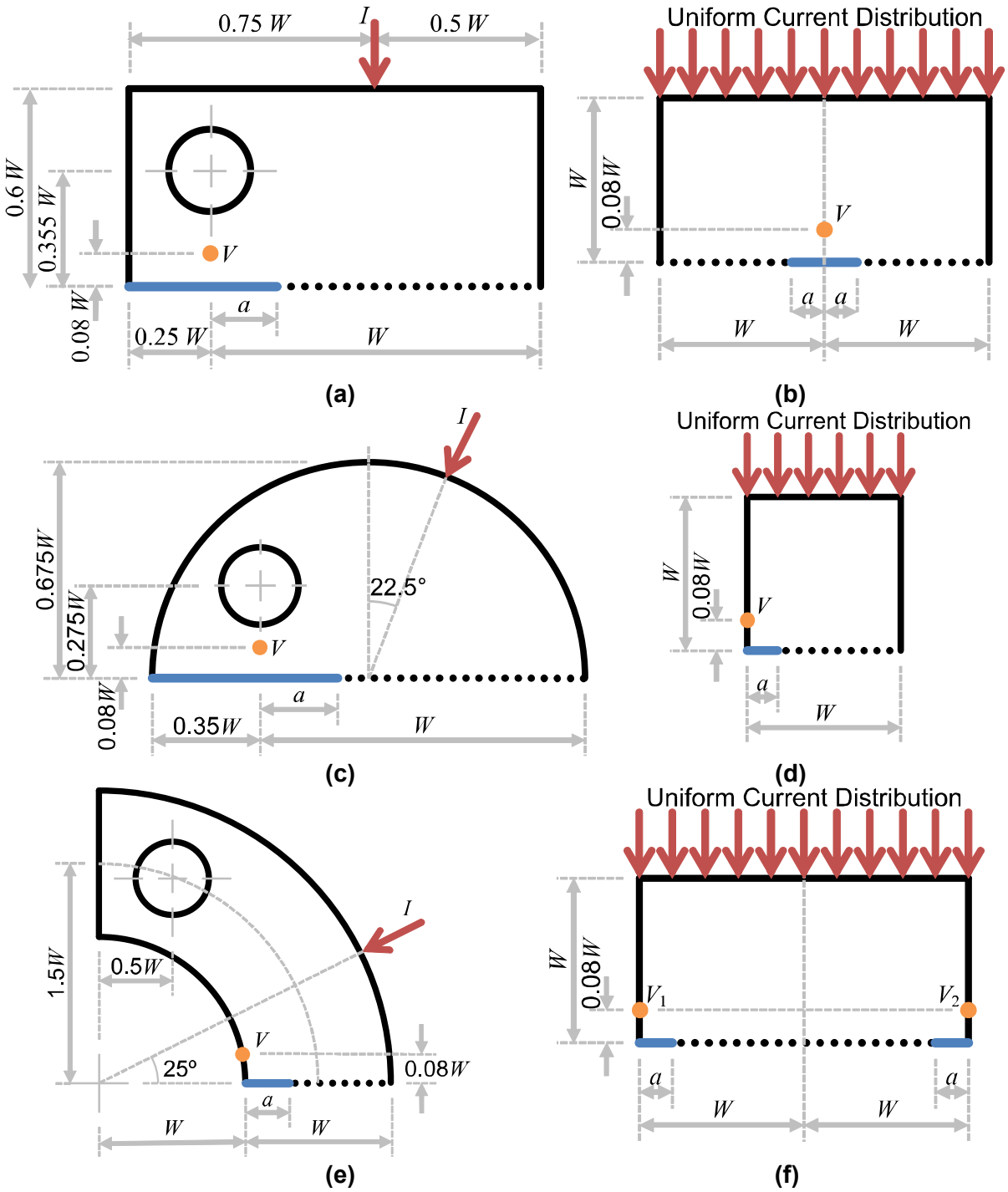

Figure 5.13: Geometry and PD configuration for (a) C(T), (b) M(T), (c) DC(T), (d) SEN, (e) CS(T) and (f) DEN(T) specimens.

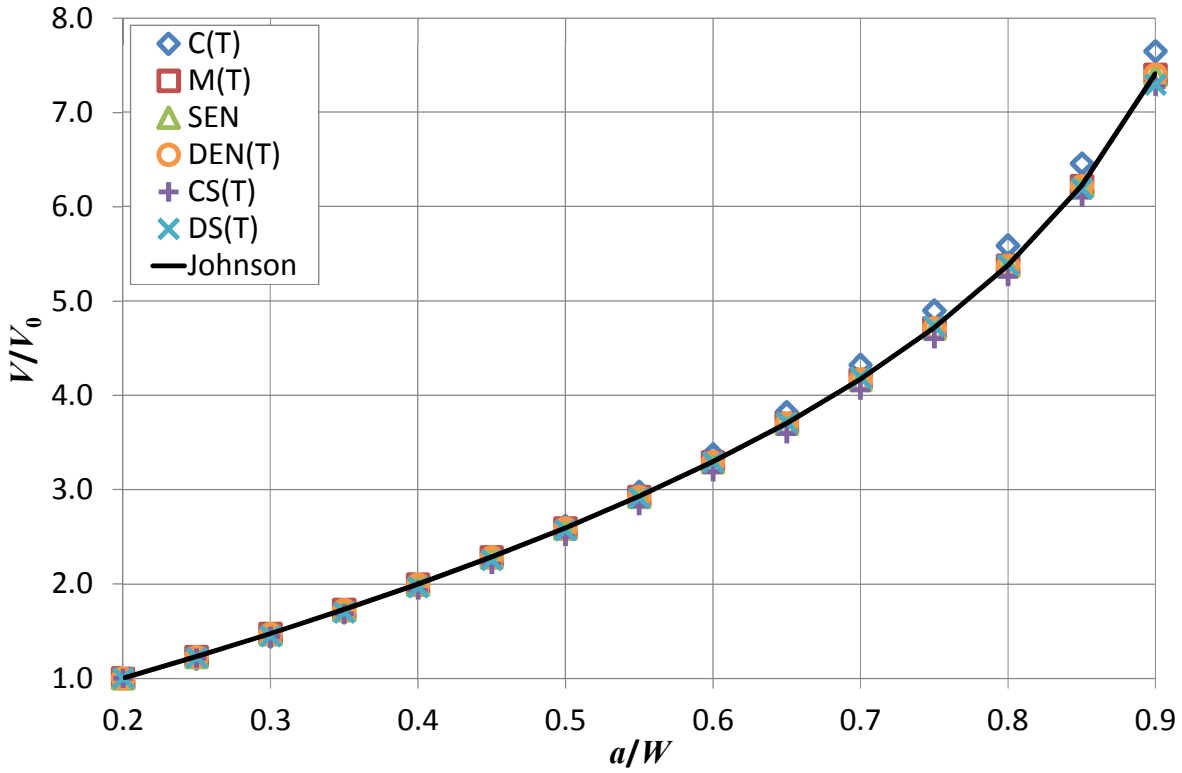

Figure 5.14: Comparison of the different geometries with Johnson's calibration function

For all geometries considered, Johnson's calibration function provides a reasonable approximation of the correlation between PD and crack length. As expected, the errors for the M(T), SEN and DEN(T) specimens, for which Johnson's calibration function is an exact solution, are negligible. The maximum errors for the other three specimen geometries are <8%. These errors are largest from small amounts of crack extension and tend to reduce with crack growth. The mean error is approximately half the maximum.

Geometry	Error in crack extension [%]		
	Maximum	Initiation	Mean
C(T)	7.9	7.9	2.9
M(T)	0.2	0.0	0.1
SEN	0.2	0.1	0.1
DEN(T)	0.2	0.0	0.1
DC(T)	5.8	5.8	3.0
CS(T)	5.7	5.6	3.6

Table 5.3: Error in crack extension associated with the application of Johnson's calibration to the main fracture specimen geometries.

The errors in Table 5.3 are relatively modest compared to some of the other sources of error identified in this and the previous chapter. Also, the largest errors corresponds to the C(T) specimen for which Johnson's calibration function is already applied in some standards e.g. [3]. It is therefore reasonable to extend the application of this calibration function to the other geometries considered here. It should be noted that the values in Table 5.3 would change for a different initial a/W, but any change is likely to be small.

5.7 Discussion

The various sources of error in the measurement of crack extension considered in this chapter are summarised in Table 5.4. The maximum and mean errors for all crack increments are provided along with the initiation error which corresponds to the initial 0.2 mm of crack extension. These are the typical errors which might be expected when applying a calibration function from the literature or standards for which the input assumptions are not known or don't exactly match the geometry being tested. It should be noted that the values in Table 5.4 would change for a different initial a/W, but any change is likely to be small.

Source of Error	Error in crack extension [%]		
	Maximum	Initiation	Mean
Notch geometry	13.6	13.6	6.4
20% side-grooves	5.2	5.2	3.4
Crack tunnelling	49.3	49.3	11.8
Uneven crack growth, DEN(T) specimen	1.5	0.5	1.1

Table 5.4: Errors associated with the measurement of crack initiation and small amounts of crack growth.

By far the most significant source of error considered here is crack tunnelling. Although DCPD measurements relate to some average crack length, it is apparent that this is not necessarily the mean value. To avoid this error, specimens should include appropriate side-grooves. Notch geometry is the other potentially significant source of error; however, this is often selected to accommodate the extensometry requirements of the test and cannot easily be avoided. The two other sources of error are relatively small although if very large side-grooves are implemented (>20%) this can become another significant source of error.

The errors in Table 5.4 are generally largest when measuring initiation (0.2 mm of crack extension) where the total error due to the two main sources (crack tunnelling and notch geometry) could potentially be as high as 63% based on the simplistic assumption that the

errors are additive. By introducing 20% side-grooves to the specimen and assuming the crack front remains flat, this reduces to 19%. When measuring significant crack extension the total mean error, due to crack tunnelling and notch geometry, is 18%. This reduces to 10% for a side-grooved specimen assuming a straight crack front. These errors are comparable to those identified in the previous chapter when testing specimens with low resistivity. When testing a specimen with a high resistivity, the errors identified in Table 5.4 will be the dominant sources of errors.

These results highlight the importance of applying appropriate side-grooves to the specimen to produce a straight-fronted crack in order to obtain accurate measurements of crack extension. Even with appropriate side-grooves, a calibration function should ideally be derived specifically for the geometry being tested. Where this is not possible and a suitable calibration function is not available in the literature, Johnson's formula may be used with the PD configurations shown in Figure 5.13. Although this will inevitably introduce some additional errors into the calculation of crack extension, this error should be relatively modest compared to the other sources of error identified here and in the previous chapter.

Chapter 6: Predicting the Influence of Strain on PD

6.1 Introduction

Large inelastic strains due to plasticity and creep influence the electrical response of fracture specimens which can erroneously be interpreted as crack growth [75, 78, 91]. For tests where the strain is constantly changing, for example monotonically loaded fracture toughness testing of tough materials or creep crack growth testing, it is difficult to experimentally decouple the effects of strain and crack extension on PD measurements. For this reason the influence of strain is not fully understood.

The influence of strain on PD measurements can be separated into geometric and material effects. For a material with significant plastic strains, the geometric effects dominate [85, 87, 88]. If the material effects are indeed small, a sequentially coupled structural-electrical FE analysis, which neglects them, should be capable of predicting the influence of strain on PD with a reasonable degree of accuracy. This would provide a powerful tool to help understand the influence of strain on PD. A similar approach has been applied to uniaxial tensile tests with some success [90] and has even been applied to cracked specimens [72, 83] although a detailed validation has not been performed.

In this chapter, the ability of a sequentially coupled structural-electrical FE analysis to predict the influence of strains on PD measurements is investigated by comparison with experimental data. For simplicity this chapter focuses on plasticity rather creep however, strains in a material undergoing power-law creep are driven by dislocations, similar to plasticity, so the conclusions should be applicable to both deformation mechanisms. Initially the simple case of a uniaxial tensile specimen is considered before applying the method to more complex fracture specimens to identify typical errors in the measurement of crack extension due to strain. Different specimen geometries and crack lengths are considered to investigate the influence of constraint. A range of different PD configurations are also considered to see if some are more susceptible to the influence of strain than others.

6.2 Uniaxial Tensile Tests

A series of nine uniaxial tensile tests were performed from specimens manufactured from ex-service Type 316H stainless steel. Five of these tests (Specimen IDs UTT_RB01 to UTT_RB05) were used to obtain the tensile material properties for use in the finite element models. The remaining four tests (Specimen IDs UTT_RB06 to UTT_RB09) were used to measure the influence of strain on the electrical resistance of the specimens for comparisons with predictions obtained from a finite element model. Independent validation of the finite element modelling approach was provided by comparison to a hand calculation based on strain gauge theory.

6.2.1 Experimental Methodology

6.2.1.1 Specimen Geometry

The uniaxial tensile specimen geometry is shown in Figure 6.1. This geometry is based on guidance in ASTM E8/E8M-13a [128].

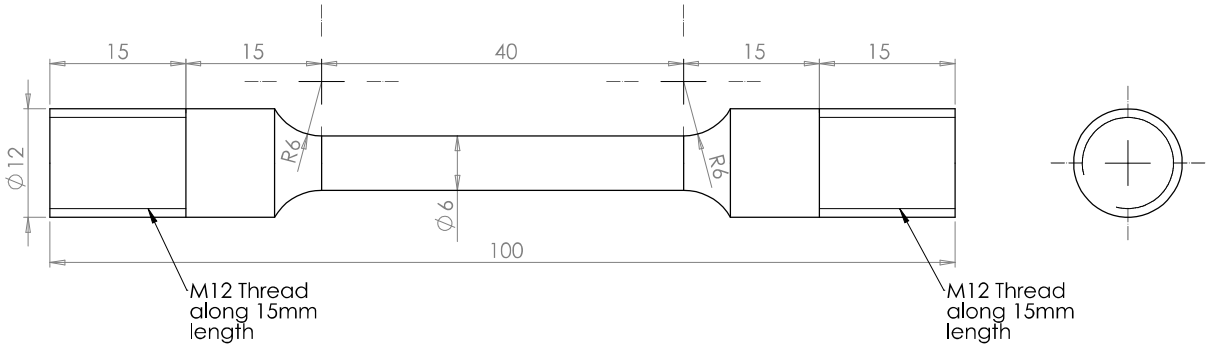

Figure 6.1: Uniaxial tensile specimen geometry

6.2.1.2 Loading

Each specimen was loaded in displacement control at a cross-head velocity of 2 mm/min. The applied load was recorded at a frequency of 10 Hz.

6.2.1.3 Extensometry

For all specimens, strain was monitored using an extensometer capable of measuring up to 100% strain and a gauge length of 25.0 mm. For specimens UTT_RB01 to UTT_RB05 an additional extensometer was located on the opposite side of the gauge region. The Young's modulus was calculated from the average of the two extensometers in accordance with ASTM E111-04 [129] which supresses any bending in the specimen due to misalignment of the cross-head. Strain measurements were recorded at a frequency of 10 Hz.

6.2.1.4 PD Measurements

A low frequency ACPD system was used to measure the resistance of the gauge region of specimens UTT_RB06 to UTT_RB09. A 3 mA constant current was passed through the specimen at a frequency of 2Hz. This frequency is low enough to produce negligible skin effect for this material and geometry such that the current behaves in a quasi-DC manner. This was confirmed by measuring the resistance of the undeformed specimen at a range of frequencies up to 30Hz and demonstrating that the measurement was not frequency dependent.

The current injection leads were attached to either end of the specimen on the unthreaded section of the grip region 2 mm from the threads. This is sufficiently remote to produce a uniform electrical field in the gauge region. The PD between two probes 25.0 mm apart on the central portion of the gauge length was recorded at a frequency of 10 Hz. This is the same region over which the axial strain was measured. The current injection and PD probe leads were 0.8 mm diameter Chromel wire which was spot welded to the specimen and twisted together to avoid electromagnetic interference. The grips were painted to isolate the specimen from the load frame and prevent alternative paths for the current. This experimental setup is shown in Figure 6.2.

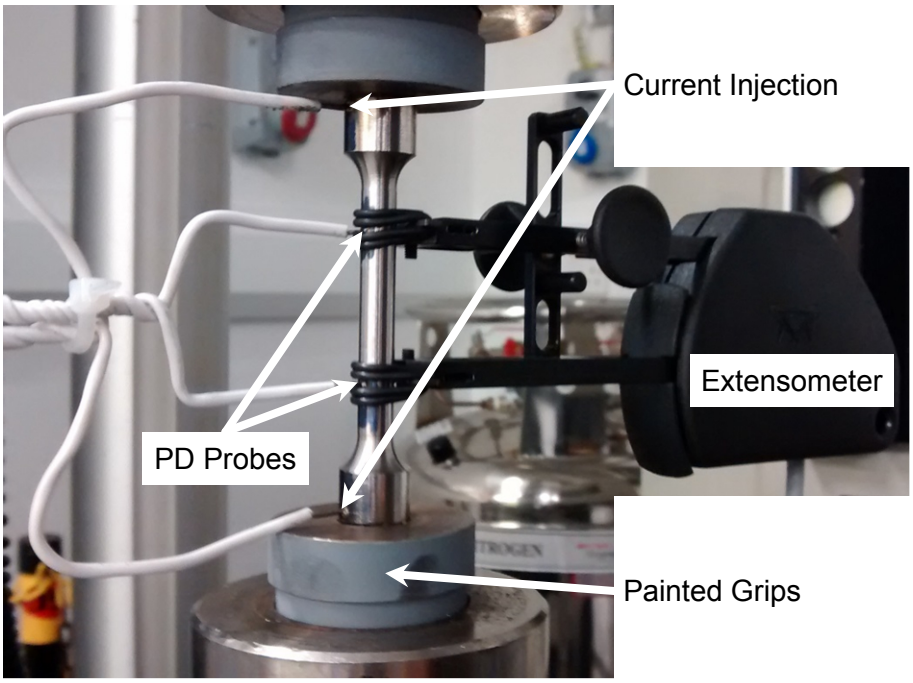

Figure 6.2: Uniaxial tensile test experimental setup.

6.2.2 Finite Element Analysis

A sequentially coupled structural-electrical analysis of the uniaxial tensile test has been performed using Abaqus v6.13-2 [130]. A structural analysis was used to obtain the deformed shape upon which an electrical analysis was performed. By comparing the results to an electrical analysis performed on the undeformed shape, the relative change in PD due to the geometric effects of strain was calculated. This approach assumes that the resistivity of the specimen remains constant throughout the test.

6.2.2.1 Geometry and Mesh

A 3D ¼ model of the specimen was produced shown in Figure 6.3. The current injection location, labelled '*I*', and the PD probe location, labelled '*PD*' are shown. The model includes the unthreaded portion of the larger diameter grip. This was included to explicitly model the current injection location, to confirm that a uniform current is generated in the gauge length as desired. The change in diameter in the model also promotes necking at the middle of the gauge length so the influence of necking on the PD response may be predicted. This approach is often implemented in FE investigations of the necking behaviour of uniaxial specimens [131]. Without this change in diameter, FE models do not neck due to the perfectly uniform stress distribution.

The mesh, shown in Figure 6.3, consisted of 11180 linear elements. The mesh is refined towards the middle of the gauge length where necking will occur. For the structural analysis, reduced integration 8-node brick elements (type C3D8R) were used. These were converted to 8-node thermal-electrical brick elements (type DC3D8E) for the electrical analysis. Large displacement formulation (NLGEOM) was applied to the structural analysis to accurately capture the large plastic deformation.

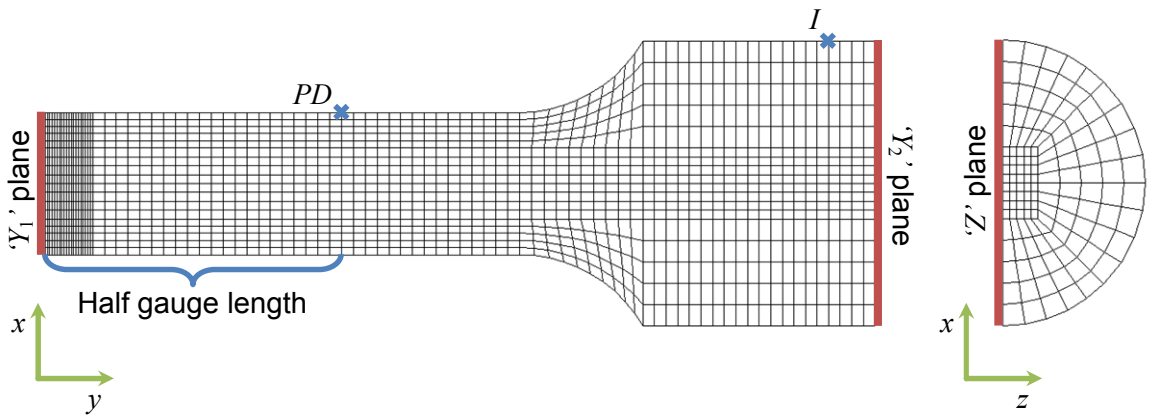

Figure 6.3: Uniaxial tensile specimen finite element mesh.

6.2.2.2 Material Properties

The Young's modulus, E, 0.2% proof stress, $\sigma_{0.2}$, ultimate tensile stress, σ_u, the strain at the ultimate tensile stress, ε_u, and failure strain, ε_f, for tests UTT_RB01 to UTT_RB05 are summarised in Table 6.1. The failure strain is the average engineering strain measured along the gauge length. The mean and standard deviations are also provided. The standard deviations are small, demonstrating a high level of repeatability.

Specimen ID	E [GPa]	$\sigma_{0.2}$ [MPa]	σ_u [MPa]	ε_u [%]	ε_f [%]
UTT_RB01	190.6	313.5	605.7	47.9	64.0
UTT_RB02	196.2	302.5	609.7	49.3	64.9
UTT_RB03	203.2	290.3	604.3	49.1	67.0
UTT_RB04	191.9	291.8	607.9	47.7	63.5
UTT_RB05	194.5	302.9	610.6	51.5	68.8
Mean:	**195.3**	**300.2**	**607.6**	**49.1**	**65.6**
Standard Deviation:	**4.9**	**9.4**	**2.6**	**1.5**	**2.2**

Table 6.1: Young's modulus, engineering 0.2% proof stress, ultimate tensile stress and failure strain for each uniaxial tensile test.

The true plastic stress-strain data for the same tests are provided in Figure 6.4. Again, the results are consistent for all five tests. The mean data used in the FE model are provided in Table 6.2 where ε^p_{true} is the true plastic strain and σ_{true} is the true stress.

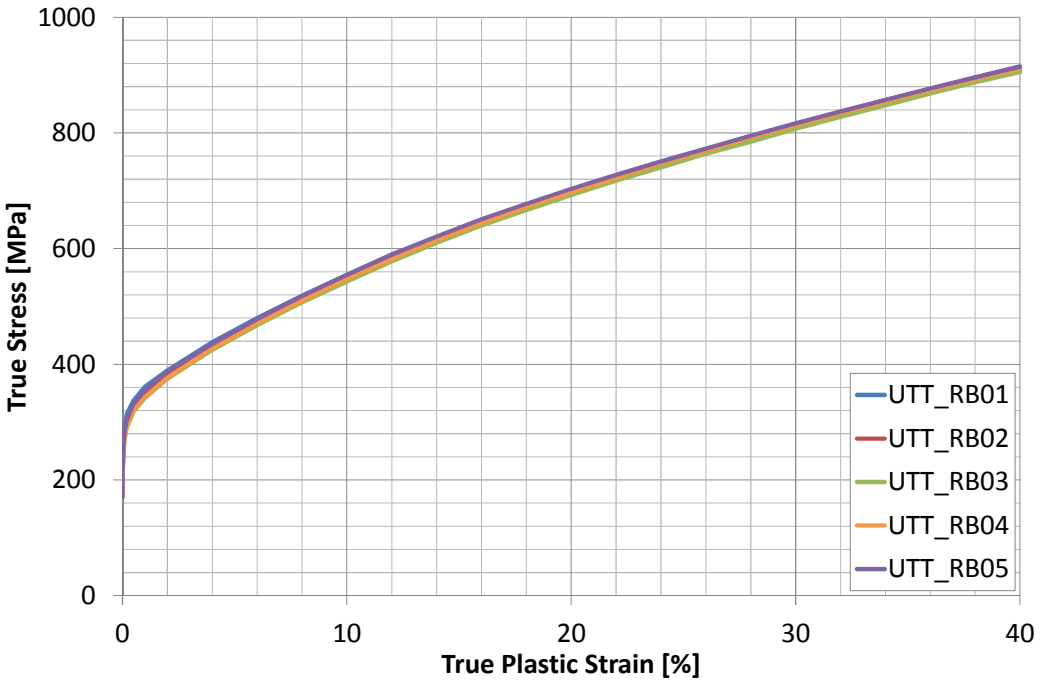

Figure 6.4: True plastic stress-strain data for UTT_RB01-05

ε^{p}_{true} [%]	σ_{true} [MPa]
0	170.0
0.01	213.7
0.02	233.1
0.05	260.3
0.10	280.8
0.20	301.4
0.50	327.9
1.00	350.8
2.00	382.5
5.00	453.5
10.00	550.8
20.00	698.8
30.00	812.6
40.00	910.3

Table 6.2: Mean true stress-plastic strain room temperature material from UTT_RB01 to UTT_RB05.

The mean properties, provided in Table 6.1 and Table 6.2, were applied to the finite element model. The properties in Table 6.2 are provided up to 40% strain which corresponds approximately to the true plastic strain at the ultimate tensile stress. Beyond this point material data cannot be easily obtained from a standard uniaxial tensile test so a power-law fit to the data between 10% and 40% plastic strain has been used to extrapolate this data for the FE model.

6.2.2.3 Boundary Conditions

For the structural analysis, symmetry boundary conditions were applied to the *'Y_1'* and *'Z'* planes, labelled in Figure 6.3. A displacement boundary condition was applied to all nodes on the *'Y_2' plane* in the positive y direction. This displacement was selected to produce an average strain, in the gauge region equal to the average failure strain, ε_f, provided in Table 6.1.

The deformed shape of the specimen was output from structural analysis at eight displacement increments. An electrical analysis was performed on each of these deformed geometries as well as the undeformed geometry. An electrical ground (0 V potential) boundary condition was applied to all nodes on the *'Y_1'* plane and a point source current was

applied to the node labelled *'I'*. All other surfaces were assumed to be perfectly insulated. The electrical potential was measured at the node, labelled 'PD'.

The low frequency ACPD system used in the experimental set-up provides a measurement of resistance rather than PD. The experimental results are therefore presented in terms of the relative change in resistance, $\Delta R/R_0$ (where ΔR is the change in resistance due to strain and R_0 is the resistance of the undeformed geometry) so they are independent of current and electrical resistivity. The finite element analysis will output a PD; however, for a constant current the two are directly proportional so the relative change in resistance from the FE model can be calculated from Equation (6.1) where V and V_0 are the measured electrical potential for the deformed and undeformed geometries respectively.

$$\frac{\Delta R}{R_0} = \frac{V - V_0}{V_0} \tag{6.1}$$

6.2.3 Hand Calculation

The change in resistance of a uniform bar due to strain can be calculated based on strain gauge theory. This has been used to validate the FE predictions. For consistency with the FE model, the influence of strain on the resistivity of the material has been ignored.

The geometric gauge factor of a strain gauge is calculated from Equation (6.2) [85] where ε is the engineering strain and v is the Poisson's ratio.

$$\frac{\Delta R}{R_0} = (1 + 2\nu)\varepsilon \tag{6.2}$$

This can be rewritten as Equation (6.3) where ΔL is the change in axial length due to strain and L_0 is the original length.

$$\frac{\Delta R}{R_0} = (1 + 2\nu)\frac{\Delta L}{L_0} \tag{6.3}$$

Equations (6.2) and (6.3) are valid for small strains only which is often a reasonable assumption because strain gauges typically do not exceed their elastic limit. To account for the large plastic strains which occur during a uniaxial tensile test, this must be rewritten as Equation (6.4):

$$\int_{R_0}^{R} \frac{dR}{R} = (1 + 2\nu)\int_{L_0}^{L} \frac{dL}{L} \tag{6.4}$$

Expanding these definite integrals gives Equation (6.5) which can be rearranged to give Equation (6.6).

$$ln\left(\frac{R}{R_0}\right)=(1+2\nu)ln\left(\frac{L}{L_0}\right) \quad \textbf{(6.5)}$$

$$\frac{R}{R_0}=\left(\frac{L}{L_0}\right)^{(1+2\nu)} \quad \textbf{(6.6)}$$

Therefore the relative change in resistance due to geometric changes for a uniaxial tensile specimen can be calculated from Equation (6.7) assuming the change in cross section is uniform along the gauge length of the material. This is a reasonable assumption up to the onset of necking.

$$\frac{\Delta R}{R_0}=(\varepsilon+1)^{(1+2\nu)}-1 \quad \textbf{(6.7)}$$

For elastic deformation the Poison's ratio is approximately 0.3 whilst for plastic deformation the material may be assumed to be incompressible, i.e. ν = 0.5. During a uniaxial tensile test elastic and plastic deformations occur simultaneously however, assuming that the plastic strains are much larger than the elastic strains (as they are for the majority of a test performed on Type 316H) a constant Poisson's ratio of 0.5 may be assumed such that the total relative change in resistance is estimated from Equation (6.8).

$$\frac{\Delta R}{R_0}=(\varepsilon+1)^{2.0}-1 \quad \textbf{(6.8)}$$

6.2.4 Results

For tests UTT_RB06 to UTT_RB09, necking and subsequent failure occurred within the 25.0 mm gauge length. No failures occurred at the PD probe spot weld so the welds did not influence the test results.

6.2.4.1 Influence of strain on PD

The true stress-strain data for tests UTT_RB06 to UTT_RB09 are compared to the mean data from tests UTT_RB01 to UTT_RB05 in Figure 6.5. Except for some small discrepancies with specimen UTT_RB06, the results are in excellent agreement. Test UTT_RB06 demonstrates slightly higher yield strength than the other tests which may be due to slight inhomogeneity of the ex-service material.

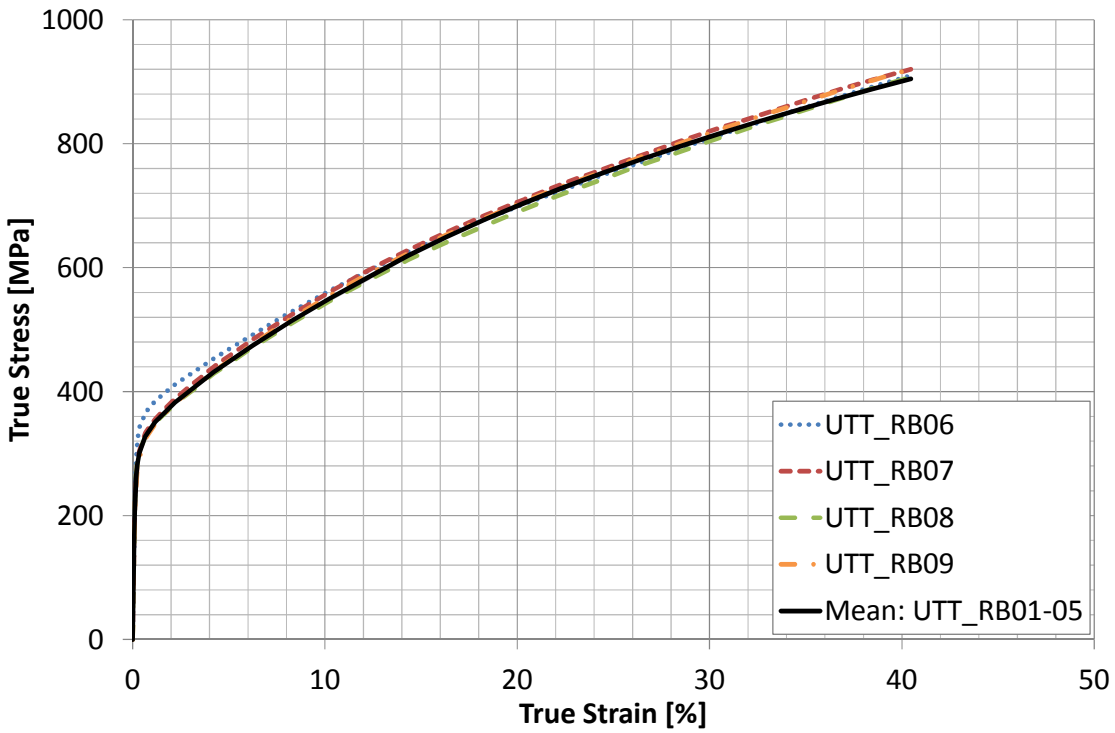

Figure 6.5: True stress-strain data for specimens UTT_RB06 to UTT_RB09 and the mean data from specimens UTT_RB01 to UTT_RB05.

The relative change in resistance due to strain for each specimen is compared with predictions based on Equation (6.8) in Figure 6.6.

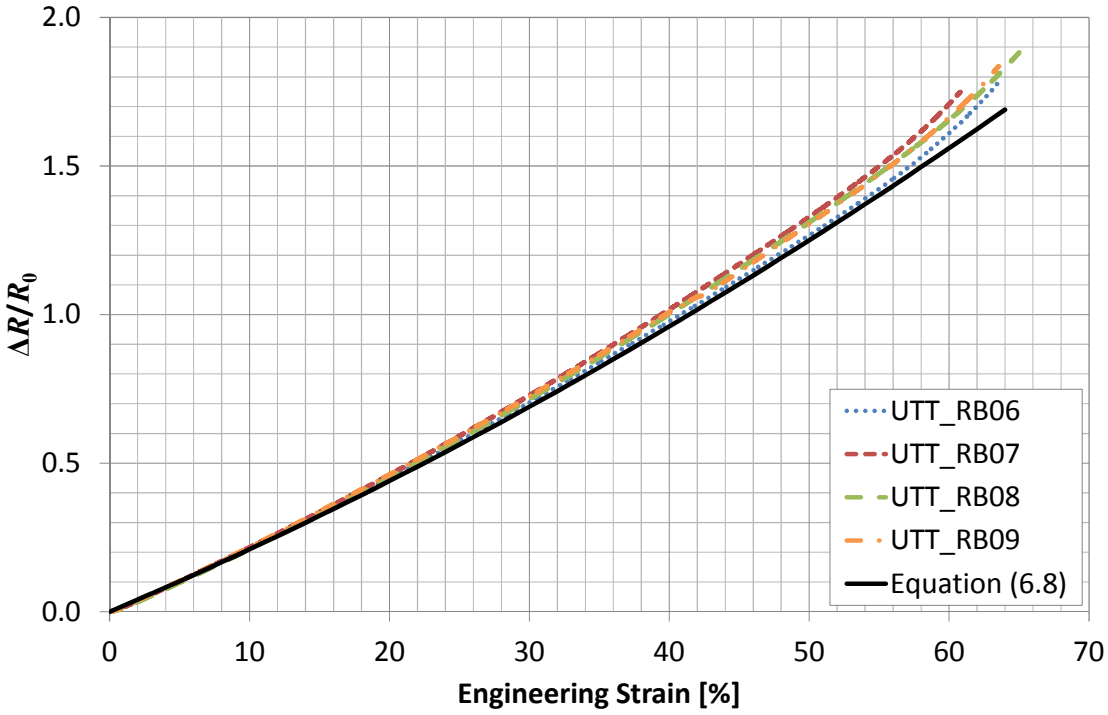

Figure 6.6: Measured relative change in resistance for specimens UTT_RB06 to UTT_RB09 compared with predictions based on Equation (6.8).

The engineering strain at the ultimate tensile stress, from Table 6.1, is approximately 50%. For strains below 50%, the hand calculation under-predicts the relative change in resistance by up to 6.6%. At higher strains this increases to as much as 10.5%. This increase is expected because Equation (6.8) assumes uniform strain along the gauge length, which is invalid after the onset of necking. These results are in good agreement with observations made by Ljustell [83] who performed similar tests on type 316L stainless steel.

The discrepancy between the experimental and theoretical results up to the onset of necking is probably due to changes in material resistivity which are not accounted for in Equation (6.8). The 6.6% discrepancy equates to a 3.5% change in resistivity. The likely causes of a change in resistivity are piezo-resistivity (the dependency of resistivity on stress) and an increase in temperature due to the strain rate. From the electrical material properties of Type 316H (provided in the previous chapter), a change in temperature of ~37°C is required to produce a 3.5% change in resistivity. Whilst the temperature of the specimen was not monitored, an increase of this magnitude would be noticeable and temperature fluctuations of a few degrees are considered more likely for the relatively slow strain rate. Piezo-resistivity is therefore the most likely cause of this discrepancy.

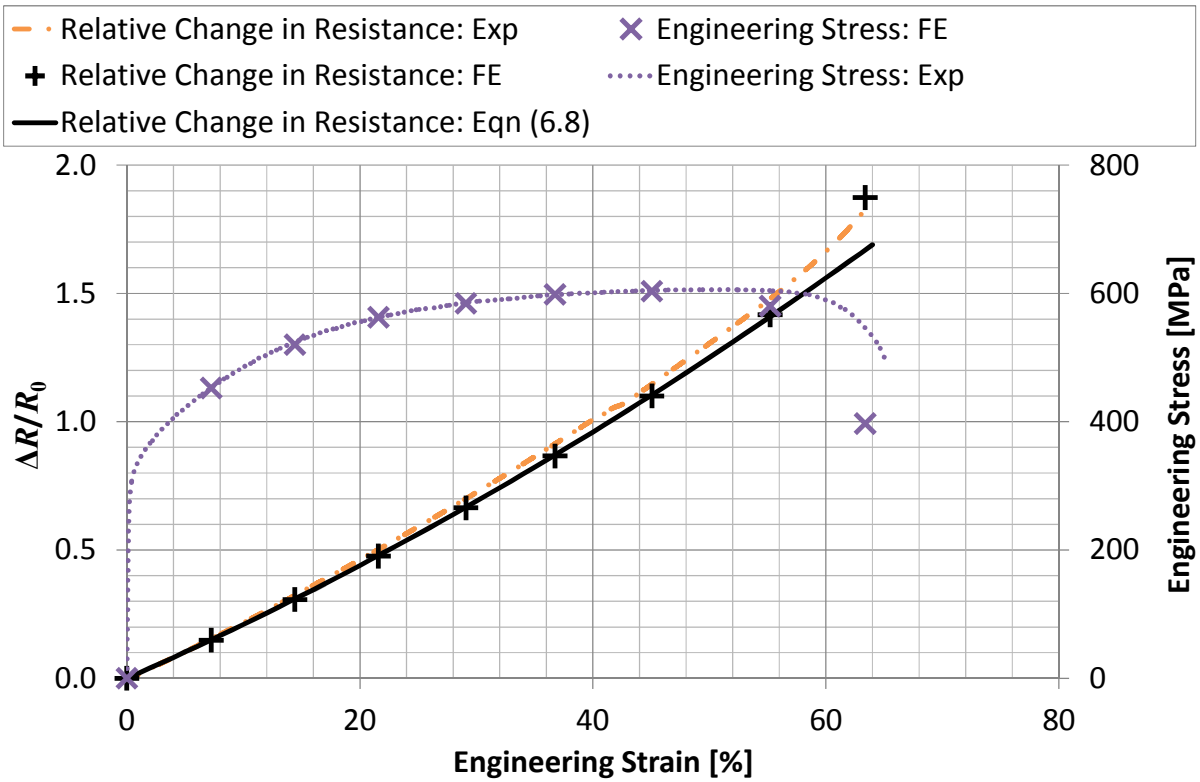

Figure 6.7: Comparison of experimentally observed relative change in resistance for specimen UTT_RB08 with predictions obtained from Equation (6.8) and FEA.

The results from the finite element model are compared to the experimental data and predictions based on Equation (6.8) in Figure 6.7. Only the experimental results of

UTT_RB08 are included for clarity. The engineering stress-strain data obtained from the FE are averaged over the 25.0 mm gauge length and so are directly comparable to the experimental data obtained from an extensometer over the same region. The final deformed shape and axial strain distribution predicted by FEA are provided in Figure 6.8.

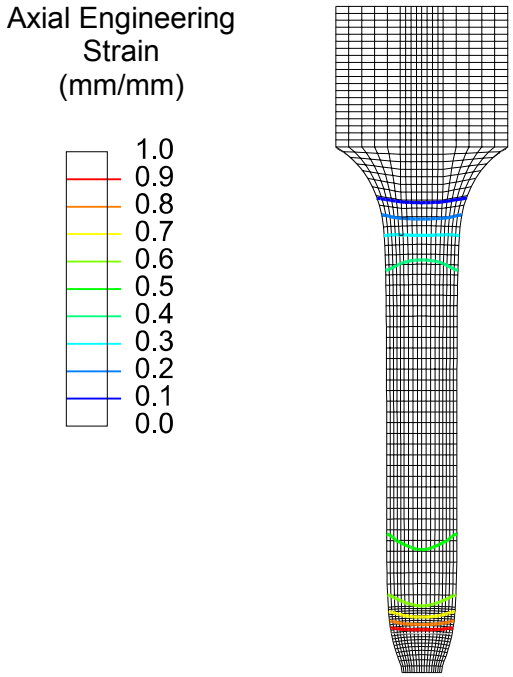

Figure 6.8: FEA predictions of the final deformed shape and the corresponding axial engineering strain.

Prior to necking the results from the FE model are in excellent agreement with Equation (6.8) which provides confidence in the modelling approach. After the onset of necking the FE diverges from Equation (6.8) similar to the experimental data. The influence of necking predicted by the FE is more significant than observed experimentally. This can be attributed to the extrapolation of the uniaxial tensile data beyond the ultimate tensile stress. The differences between the experimental and FE stress-strain data observed in Figure 6.7 suggest that the extrapolated material properties result in the FE over-predicting the extent of necking. This is consistent with the over-prediction of the relative change in resistance.

These results demonstrate that for a simple uniaxial tensile specimen manufactured from Type 316H stainless steel, the material effects of strain on resistance are small compared to the geometric effects. By neglecting any change in resistivity, a relatively simple sequentially coupled structural-electrical FE model may be used to predict the change in resistance (or PD) due to strain with a reasonable degree of accuracy. If the influence of any change in temperature is suppressed by the use of a suitable reference measurement, the accuracy of the predictions may be improved although, for the results presented here, this improvement is likely to be small.

6.3 Fracture Specimens

The same FE technique is applied to the more complex geometry and stress state of a standard fracture specimen here. Two specimen types have been considered to investigate the influence of constraint. These are a high constraint, thick C(T) specimen with side grooves and a relatively low constraint, thin, plane sided SEN(T) specimen. For each specimen type a range of PD configurations and crack lengths have also been considered. All specimens were manufactured from ex-service Type 316H stainless steel. This is a material with high resistivity so any errors associated with probe misplacement and signal noise should be small as identified in Chapter 4.

6.3.1 Experimental Methodology

The experimental setup for the SEN(T) and C(T) specimens is shown in Figure 6.9.

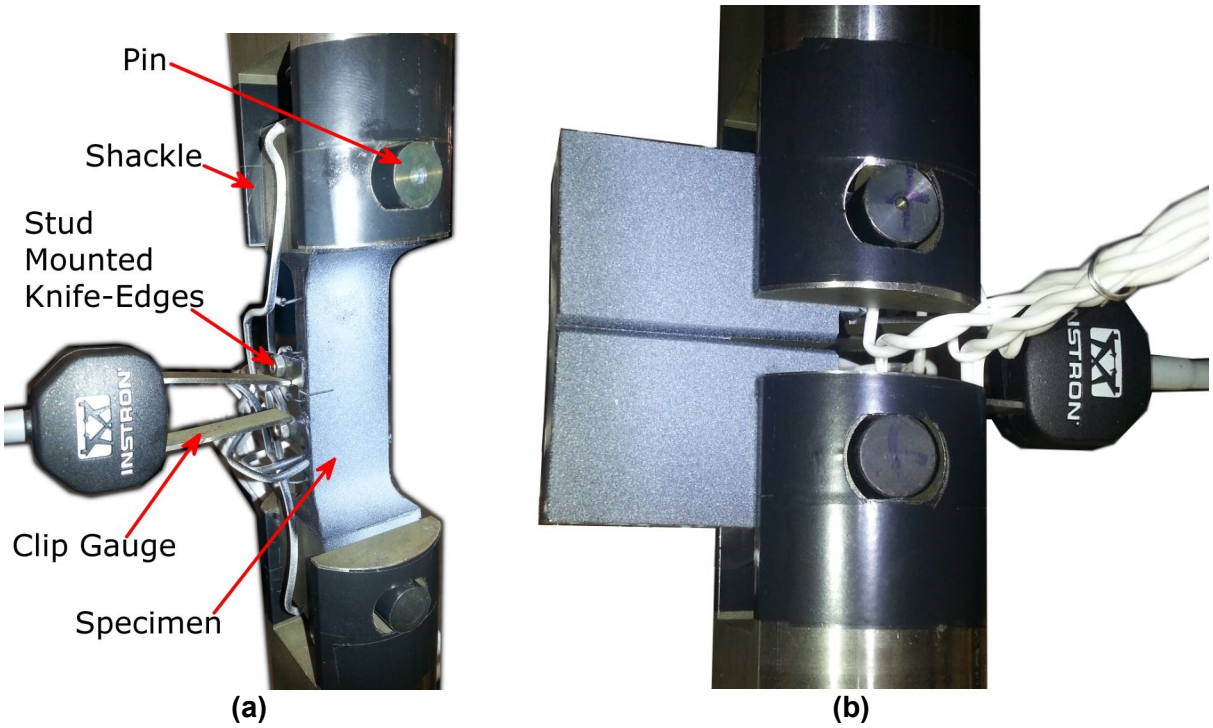

Figure 6.9: Experimental setup for (a) SEN(T) specimen and (b) C(T) specimen.

Each specimen was loaded in small increments in displacement control at a cross-head velocity of 2 mm/min. At each increment, with the load applied, the change in resistance relative to the undeformed specimen was measured. This was compared to predictions obtained from a sequentially coupled structural-electrical FE model of the specimen. Each test was stopped after significant plastic deformation had occurred, but before any crack extension was predicted so any change in resistance was primarily due to strain. After the test, the fracture surface was heat tinted and the specimen broken open to confirm that no crack extension had occurred.

6.3.1.1 Specimen Geometry

The geometry of the SEN(T) specimen is shown in Figure 6.10. Four specimens were tested with different crack lengths. The key dimensions of these specimens are summarised in Table 6.3. Studs were spot welded onto the front face of the specimen and 'knife edges' were firmly attached to accommodate a clip gauge for the measurement of Crack Mouth Opening Displacement (CMOD) as shown in Figure 6.9(a). The position of the knife edges was measured before each test so comparable CMOD measurements could be obtained from the FE models.

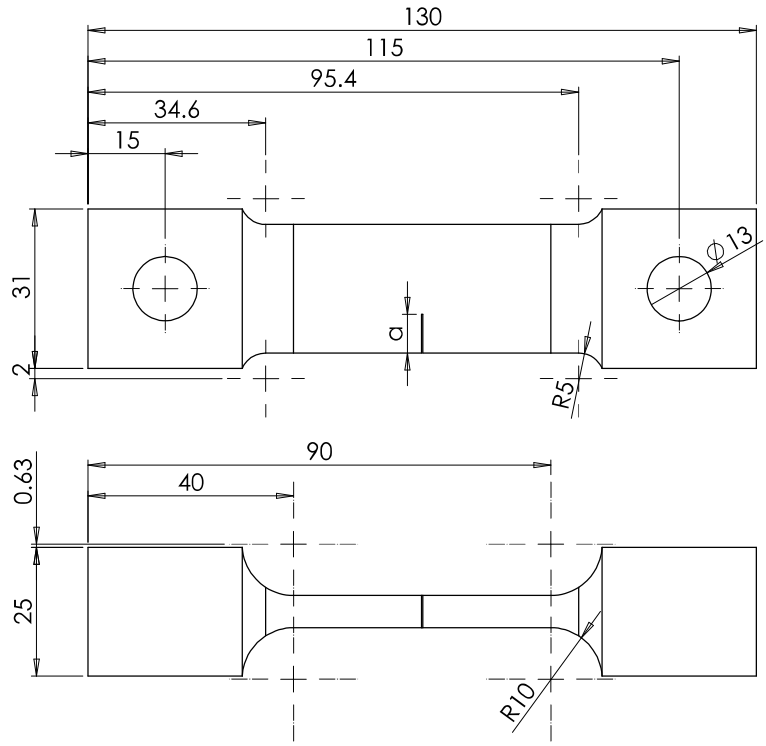

Figure 6.10: SEN(T) specimen geometry.

Specimen ID	a_0/W	a_0 [mm]	W [mm]	B [mm]	L [mm]
CTP_ST30	0.30	7.5	25.0	6.25	50.0
CTP_ST38	0.38	9.5	25.0	6.25	50.0
CTP_ST54	0.54	13.5	25.0	6.25	50.0
CTP_ST70	0.70	17.5	25.0	6.25	50.0

Table 6.3: SEN(T) specimen key dimensions.

The geometry of the C(T) specimen is shown in Figure 6.11. Two specimens were tested with different initial crack lengths. The key dimensions of these specimens are summarised in Table 6.4. The selected crack lengths are the extreme allowable initial values for creep

crack growth testing in accordance with ASTM E1457-13 [3] and are typical of fracture toughness tests performed in accordance with ASTM E1820-13 [27]. 'Knife edges' were machined into the specimen, as shown in Figure 6.11, to accommodate a clip gauge.

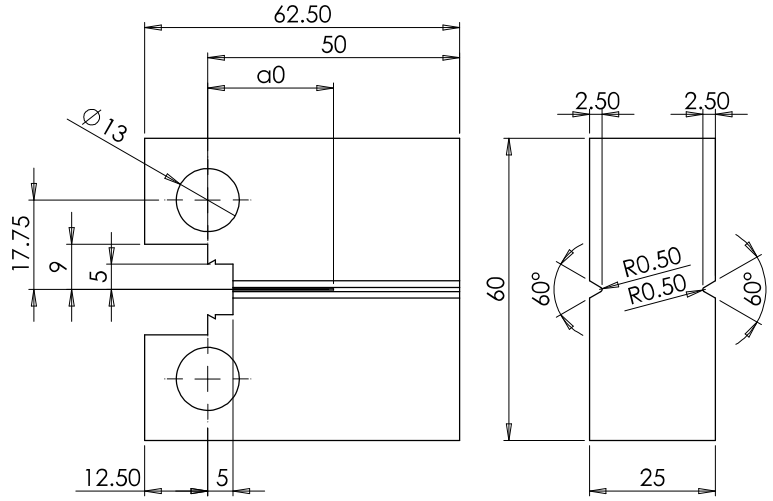

Figure 6.11: C(T) Specimen Geometry

Specimen ID	a_0/W	a_0 [mm]	W [mm]	B [mm]	B_n [mm]
CTP_CT45	0.45	22.5	50.0	25.0	20.0
CTP_CT55	0.55	27.5	50.0	25.0	20.0

Table 6.4: Key dimensions of the two C(T) specimens

An EDM slit of width 0.3 mm was used to simulate the crack for both the SEN(T) and C(T) specimens. This ensured a straight fronted crack of known dimensions which could be accurately modelled in FE. The specimen was electrically isolated from the loading pins and shackles using PVC insulation tape, as shown in Figure 6.9, to prevent alternative paths for the electrical current. To accommodate the insulation tape, the loading holes in all specimens were increased from the standard 12.5 mm diameter to 13.0 mm. The clip gauge was isolated from the specimen by painting the knife edges.

6.3.1.2 Digital Image Correlation

To validate the structural component of the FE model, the experimental surface strain fields were obtained using Digital Image Correlation (DIC) at each displacement increment and compared to the numerical results. 3D DIC was performed using a stereo camera system consisting of two 5 megapixel monochrome cameras with 100mm lenses. This set-up was capable of capturing the out-of-plane displacements such as necking at the crack tip. The surface of the specimen was painted using matt black paint and white speckles were applied using an airbrush to produce a high contrast speckle pattern.

The images were post-processed using GOM proprietary software Aramis v6.3.0 [132]. A facet size of 19 pixels with 4 pixel overlap was sufficient to capture the strain field without excessive noise. A single pass of a smoothing algorithm was applied to further reduce the noise. This algorithm averaged the strains over a 3x3 grid of facets. Multiple passes of the smoothing algorithm were avoided to ensure the high strain gradient close to the crack tip was captured.

6.3.1.3 PD Measurements

For both specimens, a range of PD configurations have been considered to identify if some are more susceptible to the influence of strain than others. The PD configurations for the SEN(T) specimens are shown in Figure 6.12. The PD probe locations are labelled with the suffix *'S'* and the current injection locations are labelled with the suffix *'I'*. Four configurations have been used to measure the PD across the crack as shown in Figure 6.12(a). These were selected based on the results of the optimisation study presented in Chapter 4. The optimum location identified in that study is *S1*. Locations *S2* and *S3* are included to investigate the influence of moving the PD probes away from the crack plane. Location *Stip* is included because it is the most sensitive to crack extension although it is also sensitive to probe misplacement errors. For each of the PD probe locations, the same current injection location was used which is sufficiently remote from the gauge region to produce a uniform current distribution.

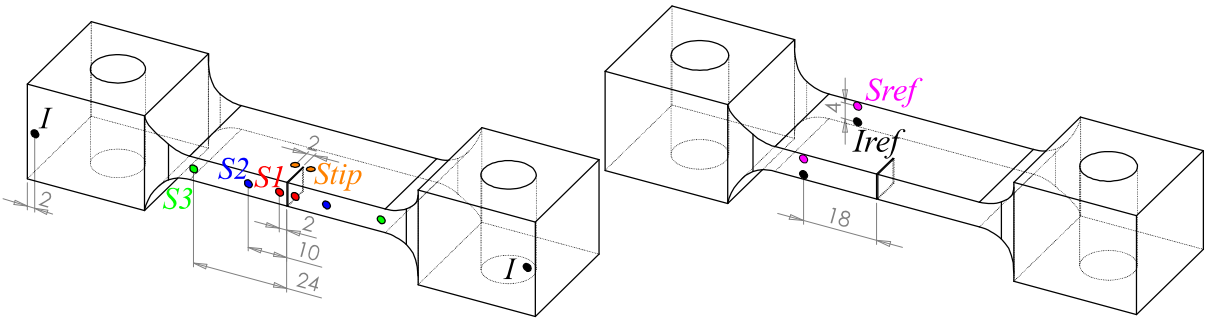

Figure 6.12: SEN(T) specimen PD configurations (dimensions in mm)

A reference measurement has also been used to supress any changes in ambient temperature. The PD probe and current injection locations, shown in Figure 6.12(b), are labelled *Sref* and *Iref* respectively. This configuration was also obtained from the optimisation study in Chapter 4.

The PD configurations for the C(T) specimens are shown in Figure 6.13. The current injection locations are labelled with the suffix *'I'* and the PD probes are labelled with the suffix *'C'*. The optimisation study presented in Chapter 4 identified a range of different suitable PD configurations with similarly low errors. A range of these configurations

incorporating different PD probe and current injection locations has been considered in this study. These are labelled *C1*, *C2* and *C3*. Configuration *Ctip* has also been included because it is the most sensitive to crack extension although it is also sensitive to probe misplacement. Figure 6.13(a) shows the PD configurations *C1*, *C3* and *Ctip* where the current is injected at *I1*. Figure 6.13(b) shows the PD configuration *C2* where the current is injected at *I2*. The reference PD configuration, also obtained from the optimisation study in Chapter 4, is shown in Figure 6.13(c).

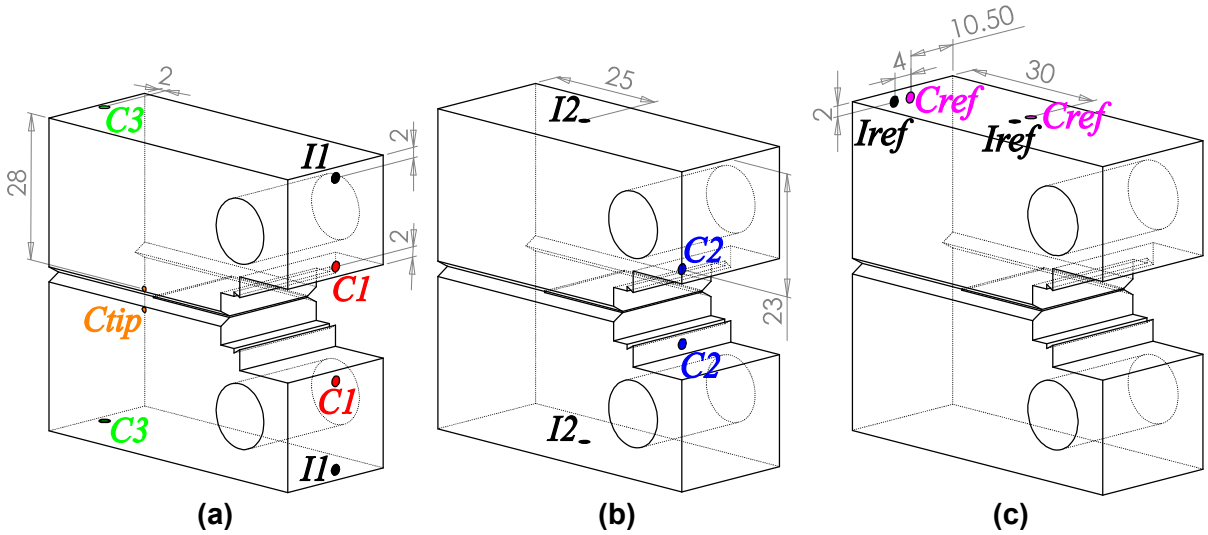

Figure 6.13: C(T) specimen PD configurations (dimensions in mm)

Resistance measurements were taken using the low frequency ACPD system. A multiplexor was used to switch between the different configurations discussed above. A 3 mA constant current was passed through the specimen at a frequency of 2Hz. This frequency is low enough to produce negligible skin effect for this material and geometry such that the current behaves in a quasi-DC manner. 0.8 mm diameter Chromel wire was spot welded to the specimen for the current injection and PD probes. Each pair of wires was twisted together to reduce electromagnetic interference.

6.3.1.4 Calibration Functions

Johnsons analytical calibration function is directly applicable to the SEN(T) PD configurations *S1*, *S2* and *S3* [18] and has therefore been used here. For all other PD configurations a calibration function in the form of Equation (6.9), was derived using COMSOL [124]. These calibration functions only consider the effects of crack growth and do not include the influence of strain.

$$\frac{a}{W} = A_3\left(\frac{R}{R_0}\right)^3 + A_2\left(\frac{R}{R_0}\right)^2 + A_1\left(\frac{R}{R_0}\right) + A_0 \qquad \textbf{(6.9)}$$

A separate calibration function has been derived for each combination of specimen type and initial crack length such that the normalising resistance, R_0, always corresponds to the initial crack length. The polynomial coefficients for the SEN(T) and C(T) calibration functions are provided in Table 6.5 and Table 6.6 respectively.

Specimen ID	$\frac{a_0}{W}$	PD Configuration	A_3	A_2	A_1	A_0
CTP_ST30	0.30	*Stip*	-0.000177	-0.005301	0.140327	0.165100
CTP_ST38	0.38	*Stip*	-0.000177	-0.006271	0.142426	0.243742
CTP_ST54	0.54	*Stip*	0.001699	-0.021944	0.171267	0.388128
CTP_ST70	0.70	*Stip*	0.023502	-0.127753	0.322516	0.481327

Table 6.5: SEN(T) Calibration function polynomial coefficients.

Specimen ID	$\frac{a_0}{W}$	PD Configuration	A_3	A_2	A_1	A_0
CTP_CT45	0.45	*C1*	-0.129087	-0.460516	2.586340	-1.546730
		C2	0.021744	-0.183473	0.675999	-0.064227
		C3	0.066542	-0.417092	1.046970	-0.246157
		Ctip	-0.000235	0.000005	0.113557	0.336937
04CTP_CT55	0.55	*C1*	-0.232736	-0.321649	2.570170	-1.465780
		C2	0.032998	-0.255912	0.813309	-0.040396
		C3	0.091550	-0.503110	1.117650	-0.156089
		Ctip	0.005043	-0.030741	0.164803	0.410759

Table 6.6: C(T) Calibration function polynomial coefficients.

6.3.1.5 Calibration Validation

Before implementing the calibration curves in Table 6.5 and Table 6.6, the method of deriving them using FE was validated experimentally. A C(T) specimen with the geometry shown in Figure 6.11 was manufactured. A 0.3 mm wide EDM slot was used to simulate the crack and was initially machined to a depth of $0.5W$ (25.0 mm). The EDM slot was then extended to $0.7W$ in increments of $0.02W$ (1.0 mm). At each increment the resistance was monitored at the PD configurations provided in Figure 6.13(a) and (b). The crack extension predicted from the PD measurement was compared to the value measured by the EDM machine. The results are presented in Figure 6.14.

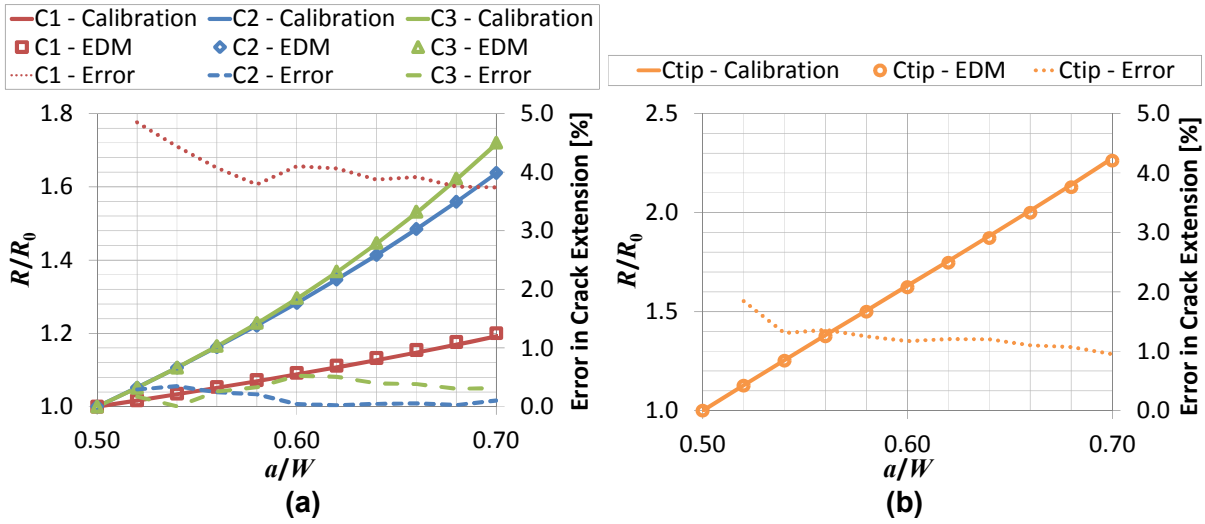

Figure 6.14: Calibration curve validation for PD configurations (a) *C1*, *C2* and *C3*, and (b) *Ctip*

The calibration curves for PD configurations *C2* and *C3* are in excellent agreement with the experimental measurements with errors in crack extension <<1%. The errors are larger for PD configuration *Ctip* but this is expected since it is more susceptible to probe misplacement error. The errors for these three PD configurations are generally within the errors predicted in Chapter 4 which provides confidence in the method used to derive the calibration functions. The agreement between the calibration curve and the experimental measurements for PD configuration *C1* is not as good where errors as high as 4.9% were observed. This is an order of magnitude larger than the error predicted in Chapter 4 (~0.5%).

The PD measurement at *C1* is dominated by the small section of material between the crack mouth cut-out for the clip gauge and the loading hole. This is demonstrated by the initial resistance measurement, a/W = 0.5, which is more than 3.5 times larger than the other three PD configurations. The calibration will therefore be particularly sensitive to small errors in the location of the loading holes. This is the likely cause of the discrepancy and highlights a possible issue with this PD configuration.

6.3.2 Finite Element Analyses

A 1/4 model of each SEN(T) specimen was developed using Abaqus v6.13-2 [130]. A 3D model was used to capture the out-of-plane strains, in particular the necking at the crack tip. The model for specimen CTP_ST30 (a/W = 0.3) is shown in Figure 6.15. It consists of ~12000 linear elements. The structural analysis was performed using reduced integration C3D8R elements and the electrical analysis used DC3D8E thermal-electric elements. Large displacement formulation (NLGEOM) was applied to the structural analysis and a focused

mesh was used at the crack tip to accurately capture the strain field in this region and extract J-Integral values from the model. The crack was modelled with a 0.3 mm tip diameter, consistent with the EDM pre-crack machined in the specimen. To reduce the computational expense of the analysis only the gauge region of the specimen was modelled. A displacement boundary condition was applied to a reference node located at the centre of the pin hole on the z plane of symmetry. This was transmitted to the gauge region via a kinematic coupling which effectively models the grip region as rigid. The reference node was fixed in the x and z directions and prevented from rotating about the x and y axes. It was free to rotate about the z axis to simulate the rotation of the pin on the flats in the holes of the shackles (see Figure 6.9).

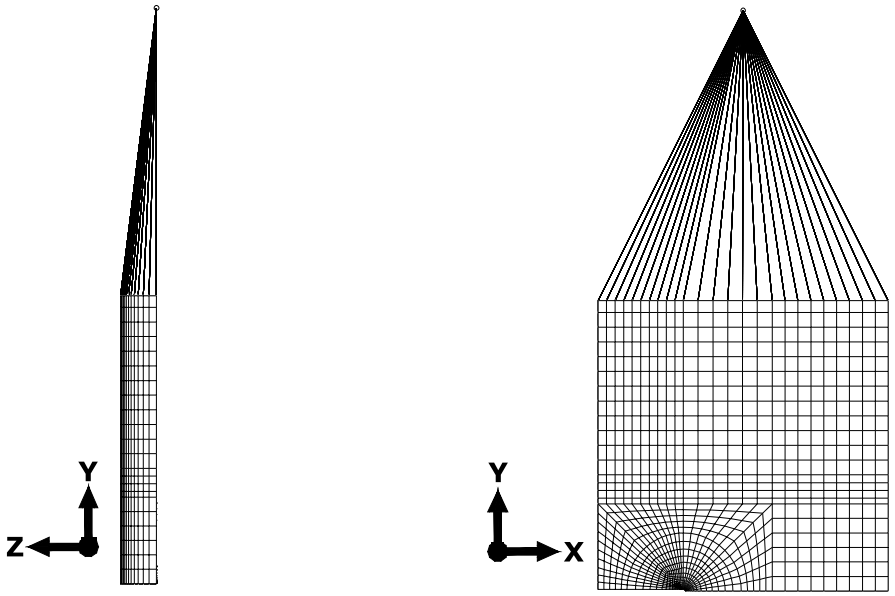

Figure 6.15: Finite element mesh for SENT(T) specimen CTP_ST30 (a/W = 0.30)

The applied displacement was chosen so the CMOD, measured at the location of the knife edges, matched the values measured experimentally. For each increment, the deformed shape of the specimen was used for an electrical analysis. An electrical ground (0 V potential) boundary condition was applied to the ligament ahead of the crack tip and a uniform unit current (1A) was applied to the top surface of the specimen. All other surfaces were assumed to be perfectly insulated. The electrical potential was measured at nodes located at the PD probe locations shown in Figure 6.12. For each of these locations the relative change in resistance due to deformation was compared to the experimentally measured values.

1/4 models of both C(T) specimens were also developed using Abaqus v6.13-2 [130]. The model for specimen CTP_CT45 (a/W = 0.45) is shown in Figure 6.16. It consists of ~45000 linear elements. The side-grooves were modelled as perfectly sharp to simplify the mesh. A sensitivity study was performed which demonstrated that this did not significantly influence

the results. The pin was explicitly modelled to capture the strain around the pin hole. It was modelled as rigid for simplicity. A displacement boundary condition was applied to the pin in the y direction and it was free to rotate about the z axis. It was fixed in the x and z directions and prevented from rotating about the x and y axes. Contact between the pin and the specimen was modelled as 'rough' for simplicity. To assist with model convergence, contact stabilization was included in the model. Checks were performed to confirm that the stabilization energy remained small compared to the total strain energy in the model.

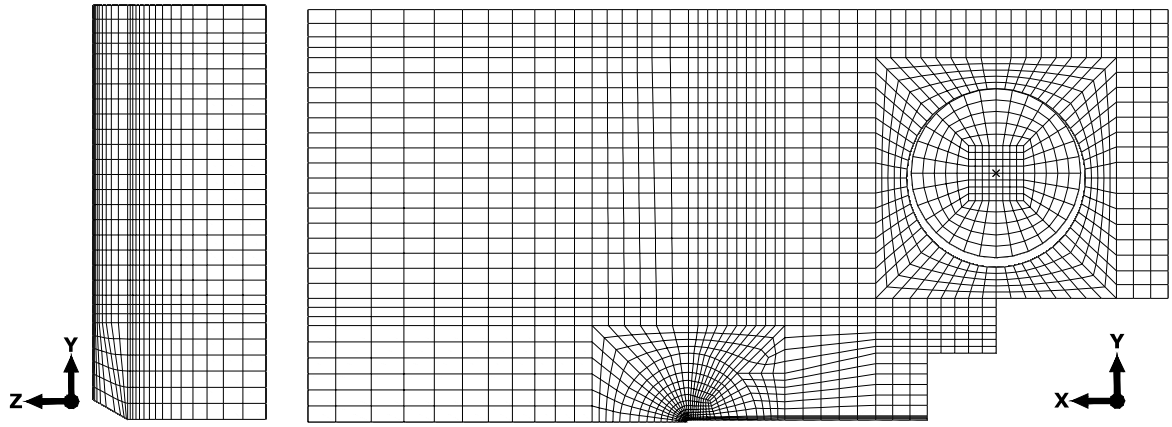

Figure 6.16: C(T) finite element mesh

The applied displacement was chosen so the CMOD, measured at the location of the knife edges, matched the values measured experimentally. For each increment the deformed shape was used to perform two separate electrical analyses, one for each of the current injection locations shown in Figure 6.13. In each analysis an electrical ground (0 V potential) boundary condition was applied to all nodes on the ligament ahead of the crack tip and a point source unit current (1A) was applied to a node at the relevant current injection location. All other surfaces were assumed to be perfectly insulated. The electrical potential was measured at nodes located at the PD probe locations shown in Figure 6.13. For each of these locations the relative change in resistance due to deformation was compared to the experimentally measured values.

6.3.3 Results

6.3.3.1 SEN(T) Specimen Results

In order to validate the structural finite element models, the experimental load-displacement curves were compared with the FE results. The surface strain fields from DIC were also compared to the models for the final displacement increment (CMOD = 0.556 mm). These comparisons are provided in Figure 6.17 for specimen CTP_ST30 (a/W = 0.30). There is excellent agreement between the experimental and finite element results which provides

confidence in the structural model and material data. Similar results were obtained for the other three SEN(T) specimens.

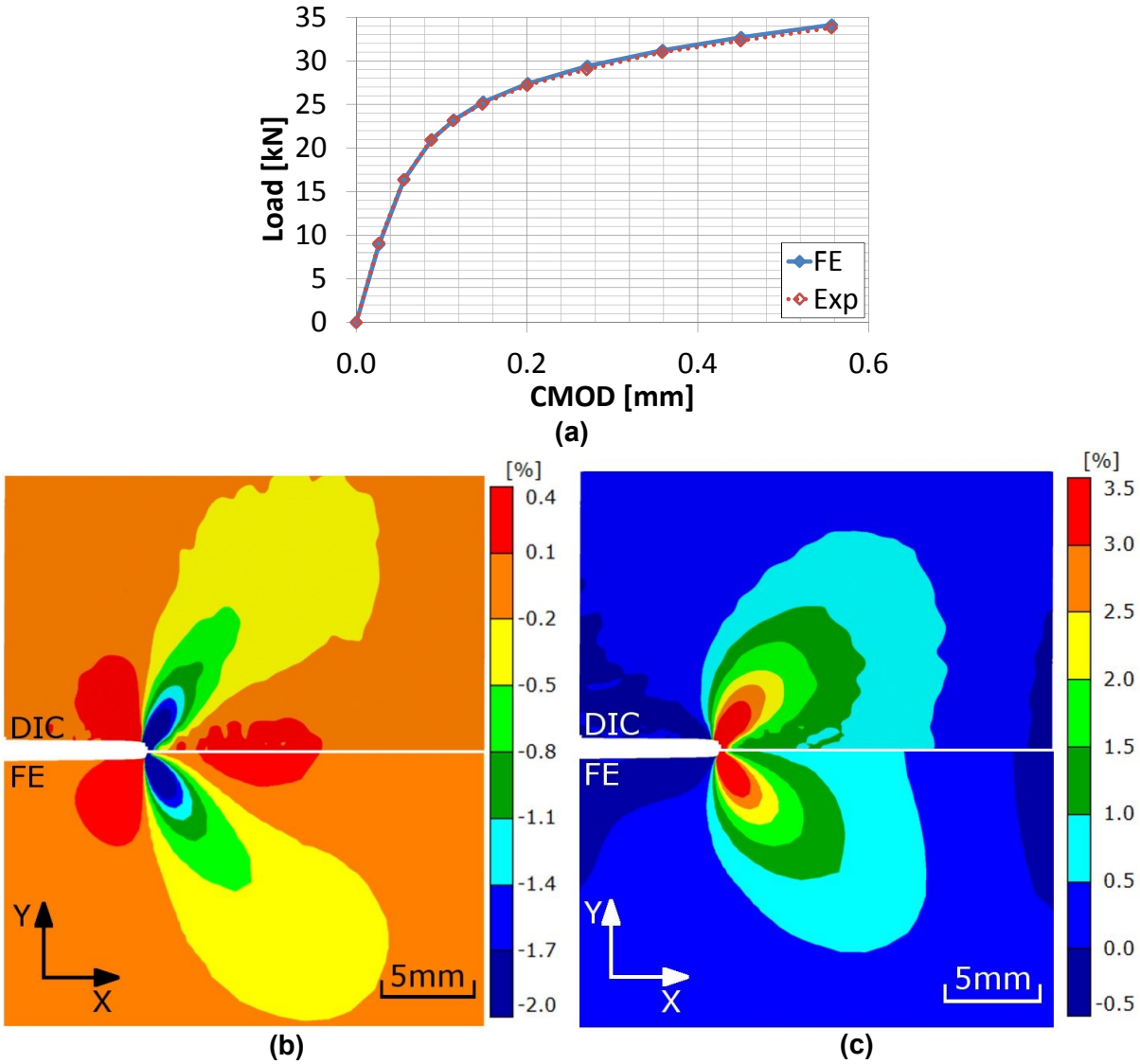

Figure 6.17: Validation of structural FE model CTP_ST30 (a/W = 0.3) by comparison with experimental data showing (a) load-displacement plot, (b) crack tip ε_{xx} field and (c) crack tip ε_{yy} field.

Figure 6.18 shows the relative change in resistance with CMOD for all four SEN(T) specimens. Experimental data, shown by the dashed lines and hollow symbols, is compared with FE predictions, shown by the solid lines and solid symbols. There is a strong correlation between the FE and the experimental data although the FE consistently under-predicts the relative change in resistance. The validation of the structural model, presented above, demonstrates excellent agreement between the FE model and experimental observations so the differences identified in Figure 6.18 are likely related to variations in the electrical material properties which are not captured in the model.

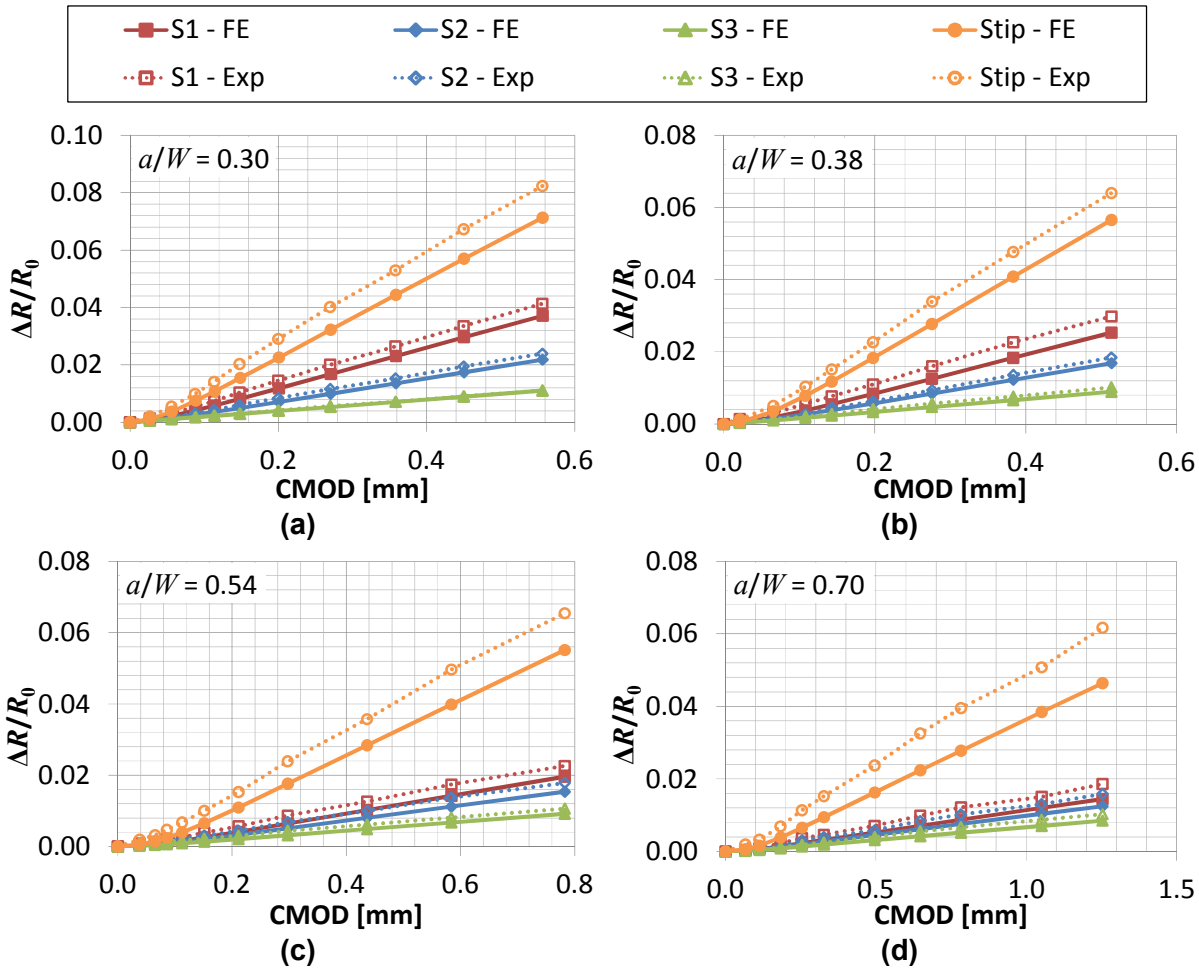

Figure 6.18: Relative change in resistance due to strain for a SEN(T) specimen with different PD configurations and (a) a/W = 0.30, (b) a/W = 0.38, (c) a/W = 0.54 and (d) a/W = 0.70.

Only a small change in material resistivity is required to account for the discrepancies between the experimental data and FE predictions and the necessary change increases with load which suggests it may be stress/strain related. For each PD configuration the required change in resistivity at maximum load is provided in Table 6.7. The ranges in this table are to cover all four specimens.

PD Configuration	$\Delta\rho$ [%]
Stip	0.97 - 1.44
S1	0.31 - 0.44
S2	0.15 - 0.33
S3	0.03 - 0.18

Table 6.7: Change in resistivity necessary to account for the discrepancies between the experimental data and FE predictions.

The values in Table 6.7 have been calculated assuming that any change in resistivity occurs across the entire specimen but a uniform change in resistivity would be suppressed by the reference measurement. The change must therefore be non-uniform across the specimen. The largest change in resistivity is required for configurations where the PD probes are closest to the crack tip. This is the region with the highest stresses and strains and is consistent with the suggestion that the change in resistivity may be stress/strain related. The current density at the crack tip is also highest, as shown in Figure 6.19, so the influence of any change in resistivity in this region will be magnified. The change in resistivity is therefore likely due to piezo-resistive effects and strain rate related local temperature changes at the crack tip.

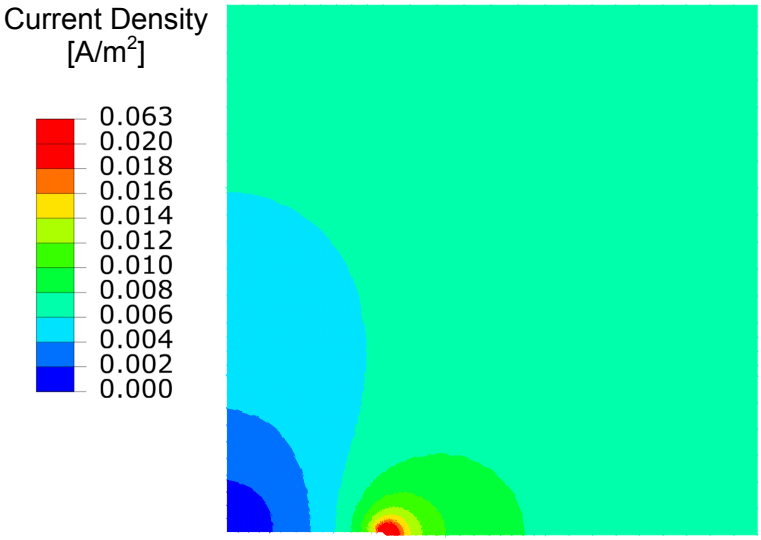

Figure 6.19: SEN(T) specimen current density based on a unit current, a/W=0.30

Figure 6.18 demonstrates that the relative change in resistance due to strain at the crack tip is larger when the PD probes are closest to the crack tip but these PD configurations are also more sensitive to crack extension. To investigate how the crack length measurement is influenced by strain, the relative change in resistance in Figure 6.18 has been converted into a 'spurious crack extension' due to strain using Johnson's calibration function for PD configurations $S1$, $S2$ and $S3$ and the calibration function provided in Table 6.5 for $Stip$.

Figure 6.20 shows the 'spurious crack extension' for all four SEN(T) specimens. For short crack lengths (a/W = 0.3) the influence of strain on the measurement of crack extension is strongly dependent on the PD configuration. The closer the PD probes are to the crack tip, the smaller the spurious crack extension. The spurious crack extension measured by configuration $S3$ is approximately double that of $Stip$ and also $S1$ which is the optimum configuration identified in Chapter 4. For larger crack lengths the influence of the PD

configuration is less significant. When a/W = 0.7, the spurious crack extension due to strain is almost identical for all configurations considered.

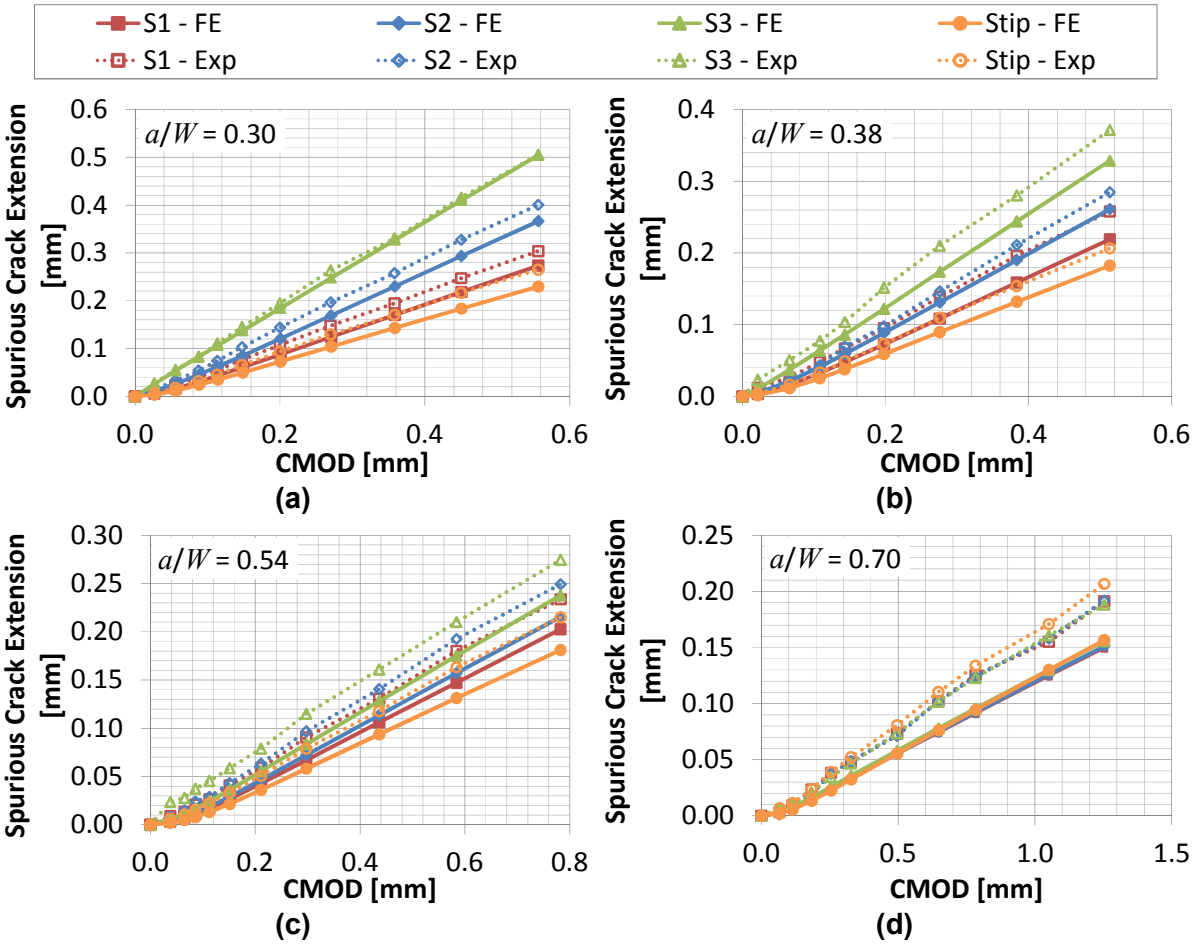

Figure 6.20: Spurious crack extension due to strain for a SEN(T) specimen with different PD configurations and (a) a/W = 0.30, (b) a/W = 0.38, (c) a/W = 0.54 and (d) a/W = 0.70.

The reason for this difference is the ratio of the nominal stress to the reference stress. When the crack length is large, a small load is required to attain a relatively large reference stress so the stresses in the gauge region, and therefore the strains, remain small. When the crack length is small, a large load is required to achieve the same reference stress, so the strains in the gauge region become significant. These strains are only sampled by the PD configurations where the PD probes are remote from the crack, so these configurations exhibit larger spurious crack extension measurements.

6.3.3.1.1 Influence of Crack Length

The influence of crack length on spurious crack extension due to strain is shown in Figure 6.21. The mode I stress intensity factor, K_I, has been used to compare the different specimens because, for a given material, this is related to the size of the plastic zone ahead

of the crack tip which is likely to influence the spurious crack extension. The experimental results are shown in Figure 6.21(a) and the FE predictions are shown in Figure 6.21(b). This comparison demonstrates the ability of the sequentially coupled structural-electrical FE models to predict similar trends to those observed experimentally.

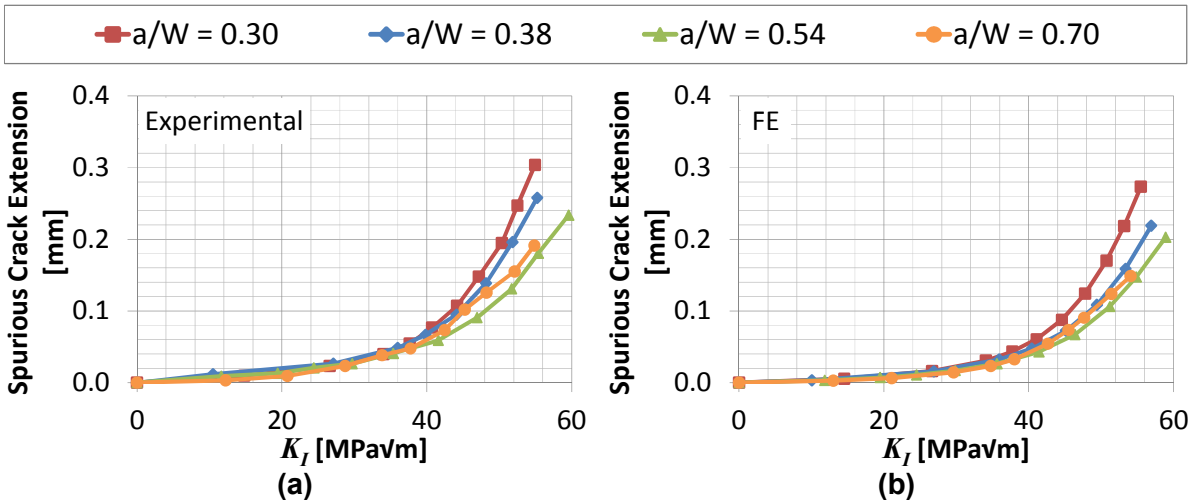

Figure 6.21: Influence of crack length on spurious crack extension due to strain derived for PD configuration *S1* from (a) Experimental data, and (b) FE predictions

For a strain hardening material, such as Type 316H, the size of the plastic zone, r_p, can be approximated from Equation (6.10) where σ_y is the yield strength, N is the stress exponent and β is a constant which depends on the level of constraint at the crack tip. For plane stress conditions β is 2 and for plane strain conditions β is 6.

$$r_p = \frac{2}{\beta\pi}\left(\frac{N-1}{N+1}\right)\left(\frac{K}{\sigma_y}\right)^2 \qquad \textbf{(6.10)}$$

Figure 6.21 shows that, for a given value of K_I, the spurious crack extension reduces as the crack length increases from $0.3W$ to $0.54W$. This suggests that the size of the plastic zone is reducing, so the value of β must be increasing due a higher level of constraint. This constraint is caused by the increase in bending associated with the larger a/W. At very large crack lengths ($0.70W$) the spurious crack extension starts to increase again. This is probably due to a loss of constraint associated with gross yielding of the remaining ligament. Similar trends could be expected for all specimen types.

6.3.3.2 C(T) Specimen Results

The experimental load-displacement curves are compared to the FE predictions in Figure 6.22. The FE consistently over-predicts the stiffness of the specimen compared to the experimental data for both specimens. A series of sensitivity studies were performed to investigate the source of this discrepancy. The results were relatively insensitive to mesh

size, pin flexibility, crack tip acuity and side-groove acuity. The results were sensitive to the method of modelling the pin/hole interaction however, the proposed boundary condition with a rough interface and a pin which is free to rotate is the most flexible. Preventing the pin from rotating and varying the coefficient of friction between the pin and the specimen increases the stiffness of the assembly and therefore the difference between the FE and experimental results. The source of the discrepancy in Figure 6.22 may therefore be due to inhomogeneity within the ex-service material.

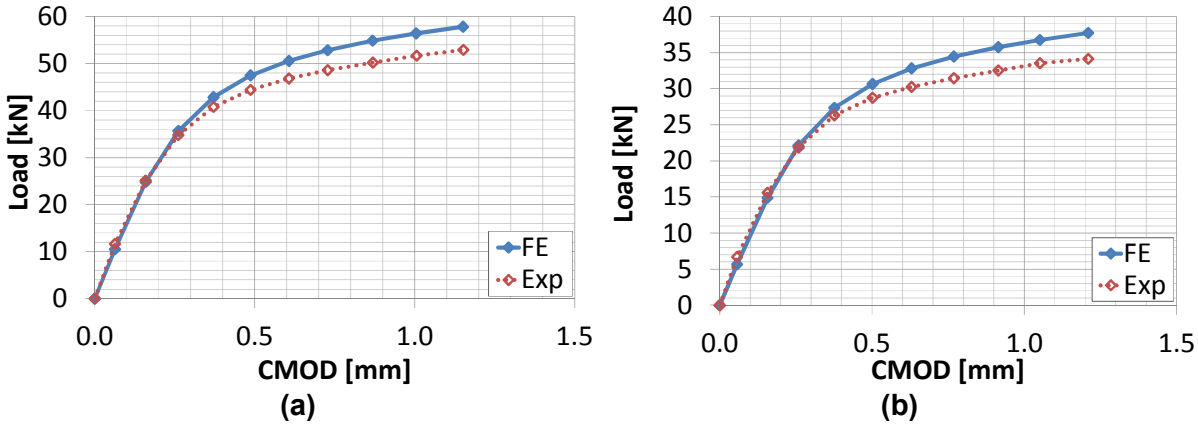

Figure 6.22: Load-displacement plot for C(T) specimens (a) a/W = 0.45 and (b) a/W = 0.55.

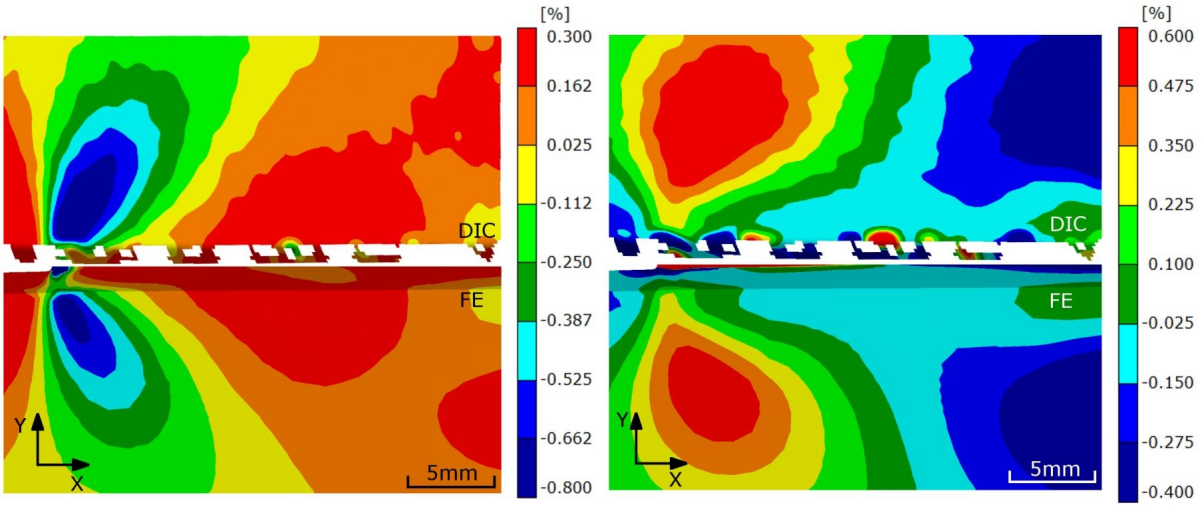

Figure 6.23: Comparison of the experimental and numerical surface strain field for the final displacement increment of specimen 04CTP_CT45 (a/W = 0.45) showing (a) crack tip ε_{xx} field and (b) crack tip ε_{yy} field.

Figure 6.23 compares the experimental and numerical surface strain fields for the final displacement increment of C(T) specimen CTP_CT45 (a/W = 0.45). The strains predicted by the FE are lower than those measured experimentally, although the difference is small. This is likely related to the discrepancy observed in Figure 6.22. The small difference in the crack tip strain field suggests that by matching the CMOD of the FE to the experimental data, it

should remain possible to predict the influence of strain on PD, despite the difference in stiffness identified in Figure 6.22. The FE predictions would change significantly if the load from the FE was matched to the experiment.

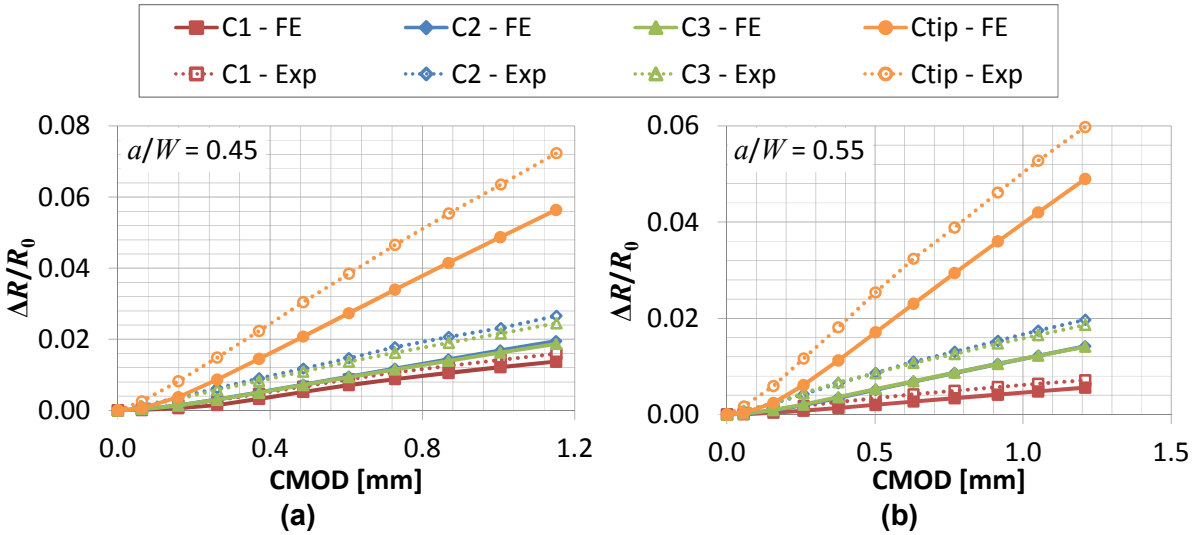

Figure 6.24: Relative change in resistance due to strain for a C(T) specimen with different PD configurations and (a) a/W = 0.45 and (b) a/W = 0.55.

Figure 6.24 shows the relative change in resistance with CMOD for both C(T) specimens. There is a strong correlation between the FE and the experimental data with the FE consistently under-predicting the relative change in resistance. The differences between the FE and experimental predictions are typically slightly larger than those predicted for the SEN(T) specimens. This is consistent with the discrepancies in the strain fields shown in Figure 6.23.

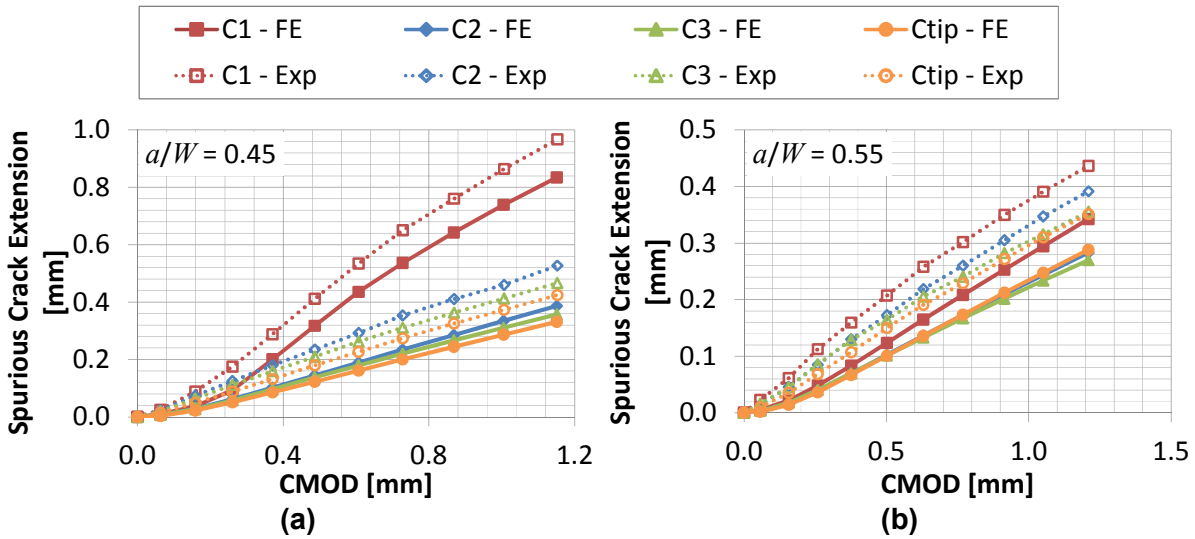

Figure 6.25: Spurious crack extension due to strain for a C(T) specimen with different PD configurations and (a) a/W = 0.45, and (b) a/W = 0.55.

The relative change in resistance from Figure 6.24 has been converted into a 'spurious crack extension' due to strain in Figure 6.25, using the calibration functions provided in Table 6.6. PD configurations $C2$, $C3$ and $Ctip$ all demonstrate similar spurious crack extensions but for a/W = 0.45 this is more than doubled at configuration $C1$. To investigate if this is related to strains around the pin hole the FE model was rerun with a modified boundary condition. The rigid pin was removed and the displacement boundary condition was applied to a node at the centre of the hole. This this was transferred to all of the nodes on the circumference of the loading hole via a kinematic coupling which prevented the hole from deforming. The node to which the displacement boundary condition was applied was free to rotate about the z axis to simulate pin rotation. The results for the original and modified FE models are shown in Figure 6.26(a) and (b) respectively.

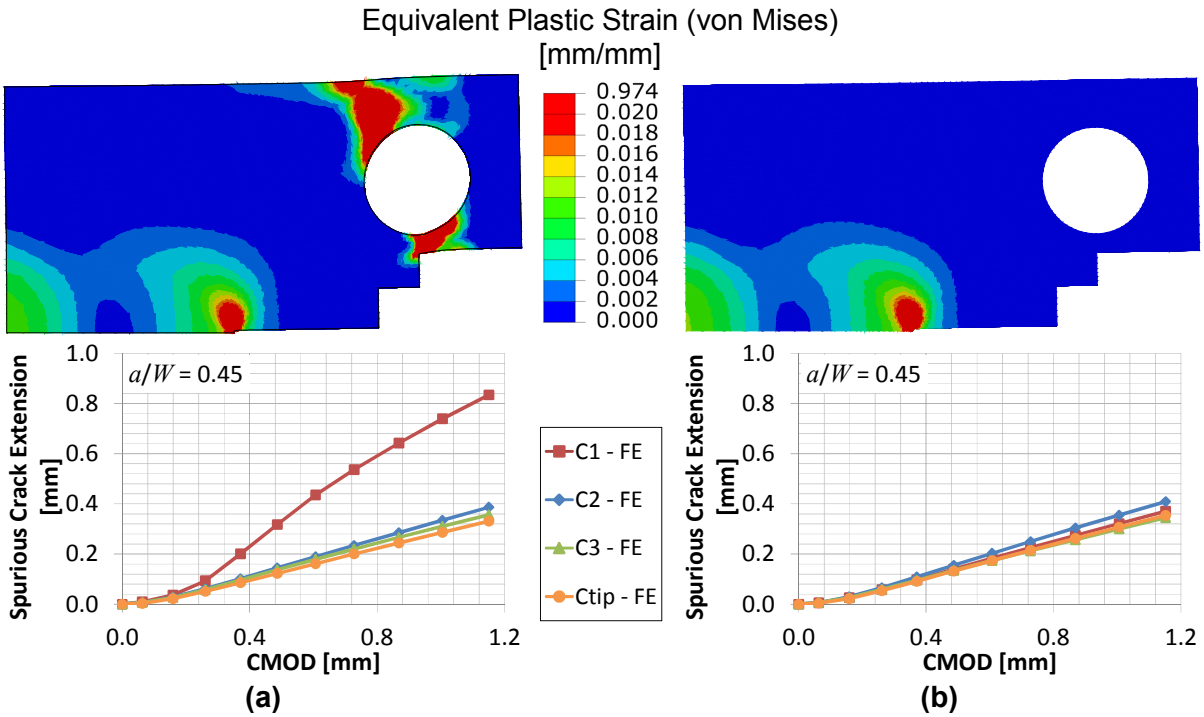

Figure 6.26: Equivalent plastic strain and distribution and spurious crack extension due to strain for (a) FE model with rigid pin, (b) FE model with kinematic coupling boundary condition.

The modified boundary condition removes the plastic strain around the hole whilst maintaining the strain field around the crack tip. This reduces the spurious crack extension for PD configuration $C1$ to a similar value to the other probe locations. The influence of the boundary condition modification on the other PD configurations is negligible. This confirms that the plastic deformation around the loading hole can have a significant influence on crack extension measurements performed using PD configuration $C1$. It should be noted that this is the configuration suggested in many standards [3, 27].

6.3.3.2.1 Influence of Specimen Geometry

The influence of specimen type on spurious crack extension due to strain is shown in Figure 6.27. The mode I stress intensity factor, K_I, has been used to compare the different geometries. Only PD configurations *Stip* and *Ctip* have been considered since these are the most comparable.

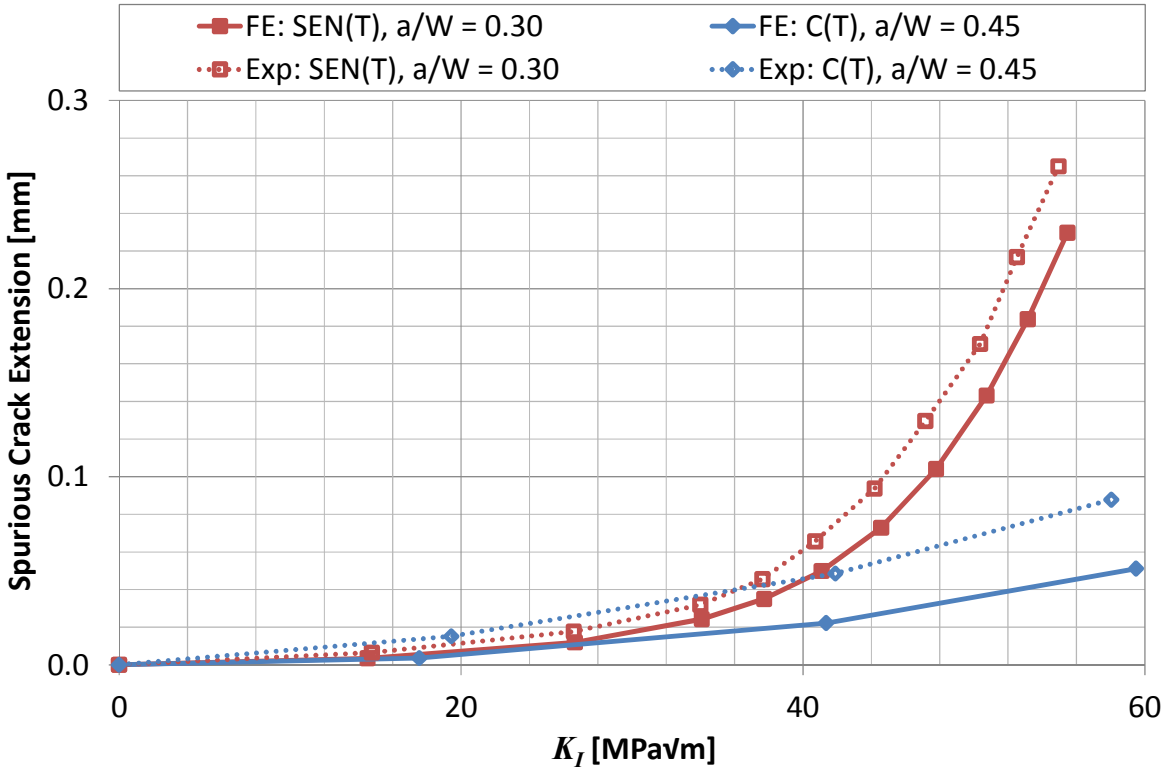

Figure 6.27: Influence of specimen geometry on spurious crack extension due to strain for PD configurations *Stip* and *Ctip*

For a given value of K_I, the spurious crack extension due to strain is much smaller for the C(T) specimen than the SEN(T) specimen. This is because the high constraint of the thick C(T) specimen with side grooves promotes stress tri-axiality at the crack tip, reducing the size of the plastic zone and the influence of strain on PD. Conversely, the relatively low constraint, thin SEN(T) has a large plastic zone for the same value of K_I, so the influence of strain on PD is larger.

6.4 Discussion

A sequentially coupled structural-electrical FE model is capable of predicting the influence of strain on PD measurements. It underestimates the magnitude of the change in PD because it neglects variations in electrical resistivity but it is capable of predicting the general trends because these variations tend to be secondary to the geometric effects of strain. The accuracy of the model could be improved by including strain dependent material properties

but this would significantly increase the necessary validation. Without this additional complexity, it provides a powerful tool which can be used to help understand the influence of strain on PD simply from the specimen geometry and the uniaxial tensile data.

The FE results and experimental data have confirmed that the influence of strain on PD measurements can be significant, particularly when testing low constraint geometries, such as SEN(T) specimens. In this study, spurious crack extension measurements significantly larger than the typical 0.2 mm engineering definition of crack initiation have been obtained prior to any physical crack growth. It is therefore of vital importance to mitigate the influence of strain in order to obtain accurate measurements of crack initiation and growth in ductile materials.

For SEN(T) specimens, PD configuration *S1* demonstrates the lowest spurious crack extension measurements, particularly for small initial crack lengths (a/W = 0.3) where moving the PD probes away from the plane of the crack increases the errors due strain. *Stip* also demonstrates relatively low spurious crack extension measurements, but this configuration is very sensitive to probe misplacement errors as identified in Chapter 4. *S1* is therefore considered the most suitable configuration for accurately measuring crack initiation and growth in the presence of large strains. Comparable configurations are likely to be appropriate for similar specimen geometries e.g. SEN(B), M(T), DEN(T) and CS(T).

For C(T) specimens, PD configuration *C1* should be avoided despite being recommended in many standards [3, 27]. Crack extension measurements using this configuration can be highly susceptible to spurious crack extension measurements due to strains around the loading holes. In general, configurations with the PD probes on the opposite side of the loading hole to the crack tip should be avoided. *C2* is a more suitable PD configuration. Comparable configurations are likely to be appropriate for similar specimen geometries e.g. DC(T).

Although the influence of strain may be reduced by selecting an appropriate PD configuration it cannot be avoided altogether. Even for the preferred PD configurations identified above, the spurious crack extension measurements due to strain remain large when compared to the 0.2 mm engineering definition of crack initiation. They are also large compared to the other sources of error identified in the previous two chapters. It is therefore important to develop experimental methods of supressing the influence of strain when measuring crack initiation and growth in the presence of large strains. Sequentially coupled structural-electrical FE models provide an ideal tool to help develop these methods and will be used to identify the most suitable approach for measuring crack extension during fracture toughness or creep crack growth testing in the following two chapters.

Chapter 7: Measuring Crack Extension during Fracture Toughness Testing

7.1 Introduction

During fracture toughness testing of ductile materials crack extension occurs prior to final failure in two ways: blunting and stable tearing. During such tests, the strains developed in the specimen can be very large, particularly during blunting where it is effectively the source of crack extension. If using the PD technique to measure crack extension it is of vital importance to ensure that only the crack extension is being measured.

When using DCPD (or low frequency ACPD) to measure this crack extension, two methods of interpreting the PD data are widely accepted and are included in some standards [1, 2]. Both of these methods are based on experimentally observed phenomena, and the underlying theory is not fully understood. In this chapter, both of these methods are reviewed using a combination of experimental techniques and the finite element based tool developed in the previous chapter. This combined approach allows the blunting and stable tearing phases to be considered separately. The limitations inherent in each of the two methods are discussed and recommendations provided with regards to the most appropriate method of measuring crack extension during fracture toughness testing.

7.2 Interpreting Fracture Toughness Test PD Data

The two methods of interpreting PD measurements during fracture toughness testing are the 'load' method and the 'COD' method. These methods are described in Chapter 2 but a recap is provided here for clarity. They are shown schematically in Figure 7.1. In this figure

the PD measurements are presented in terms of resistance for consistency with the low frequency ACPD system.

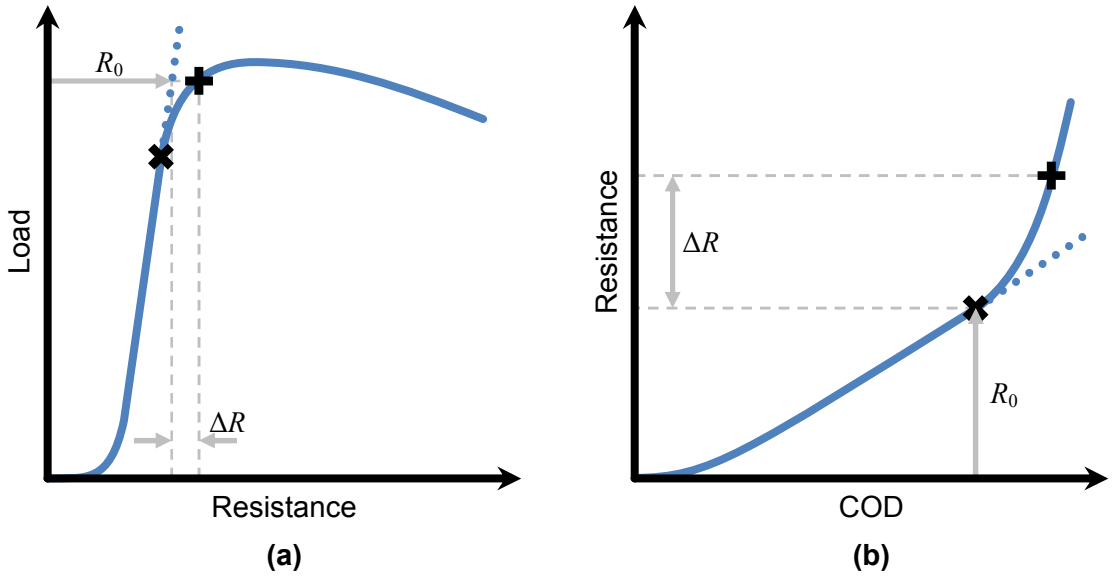

Figure 7.1: Interpretation of PD data during fracture toughness testing of ductile materials using (a) the 'load' method, and (b) the 'COD' method.

7.2.1 The 'Load' Method

The 'load' method is based on a linear regression applied to the initial steep portion of the load vs. PD plot. The onset of crack blunting is assumed to correspond to the point where the data deviates from this linear trend, labelled '×' in Figure 7.1(a). The subsequent crack extension is calculated using a standard calibration function, but the value of R_0 is assumed to be a function of the applied load, P. This function is the equation of the linear regression. The values of R_0 and ΔR used to calculate crack extension corresponding to the point labelled '+', are shown.

In this method, the PD is used to measure the both blunting and stable tearing. To calculate the initiation fracture toughness, J_{IC}, it is necessary to identify the onset of stable tearing. This is achieved by comparing a plot of J vs Δa, obtained experimentally, with a suitable blunting line. The onset of stable tearing is identified from the point where the two diverge.

7.2.2 The 'COD' Method

The 'COD' method was originally proposed by Lowes and Fearnehough [75]. Unlike the 'load' method, the PD is only used to measure stable tearing. A linear regression is applied to a plot of PD vs. COD where COD could be CMOD or LLD. The onset of stable tearing is assumed to correspond to the point where the data deviates from this linear trend. This is labelled '×' in Figure 7.1(b). The subsequent tearing is calculated using a standard

calibration function and a fixed value of R_0. The values of R_0 and ΔR used to calculate crack extension at the point labelled '+', are shown. The crack extension due to blunting is not obtained from the PD technique and is instead obtained from SEM images of the SZW or it is assumed to follow a suitable blunting line.

7.3 Measuring Blunting using the PD Technique

In the previous chapter, the influence of strain on PD in the absence of crack growth was measured for a series of monotonically loaded specimens. These experiments were essentially measuring the change in PD during the blunting phase of a fracture toughness test. The results were also compared with predictions obtained from a sequentially coupled structural-electrical FE model with good agreement. These FE results are reanalysed here to investigate the ability of the PD technique to accurately measure the crack extension due to blunting.

Six specimens were tested in total: four SEN(T) and two C(T) specimens. The key dimensions of each of the specimens are summarised in Table 7.1. The high constraint C(T) geometry is typical of most fracture toughness tests where high constraint, approximately plane strain, crack tip conditions are required. The SEN(T) specimens are typical of fracture toughness tests performed on pipeline steels where low constraint crack tip conditions are more representative.

Specimen ID	Specimen Type	a_0/W	W [mm]	B [mm]	B_N [mm]	L [mm]
CTP_ST30	SEN(T)	0.30	25.0	6.25	6.25	50.0
CTP_ST38	SEN(T)	0.38	25.0	6.25	6.25	50.0
CTP_ST54	SEN(T)	0.54	25.0	6.25	6.25	50.0
CTP_ST70	SEN(T)	0.70	25.0	6.25	6.25	50.0
CTP_CT45	C(T)	0.45	50.0	25.0	20.0	-
CTP_CT55	C(T)	0.55	50.0	25.0	20.0	-

Table 7.1: Specimen key dimensions.

The 'load' method assumes that the PD technique can be used to directly measure crack extension due to blunting. To investigate the validity of this assumption, the FE models from the previous chapter have been interrogated. For each model, the PD results were interpreted using the method shown in Figure 7.1(a) to predict the crack extension due to blunting. These predictions have been compared to measurements obtained directly from the FE displacement field and the blunting lines provided in ASTM E1820-13 [27], ISO 12135 [2], and ESIS P2-92 [1]. A detailed review of these blunting lines is provided in Section 2.3.2.6.

An example of the interpretation of the FE PD results for C(T) specimen CTP_CT45 (a/W = 0.45) is provided in Figure 7.2. A linear regression was fitted to the initial data points where the global response of the specimen is elastic. This linear regression was used to determine the equation for R_0. The subsequent blunting predicted from the PD data, $\Delta a_{b\_FE\_PD}$, was determined using the calibration functions provided in the previous chapter. PD configurations $C2$ and $S1$ were used for the C(T) and SEN(T) specimens respectively. These were identified in the previous chapter as suitable configurations for measuring crack initiation and growth in the presence of large strains.

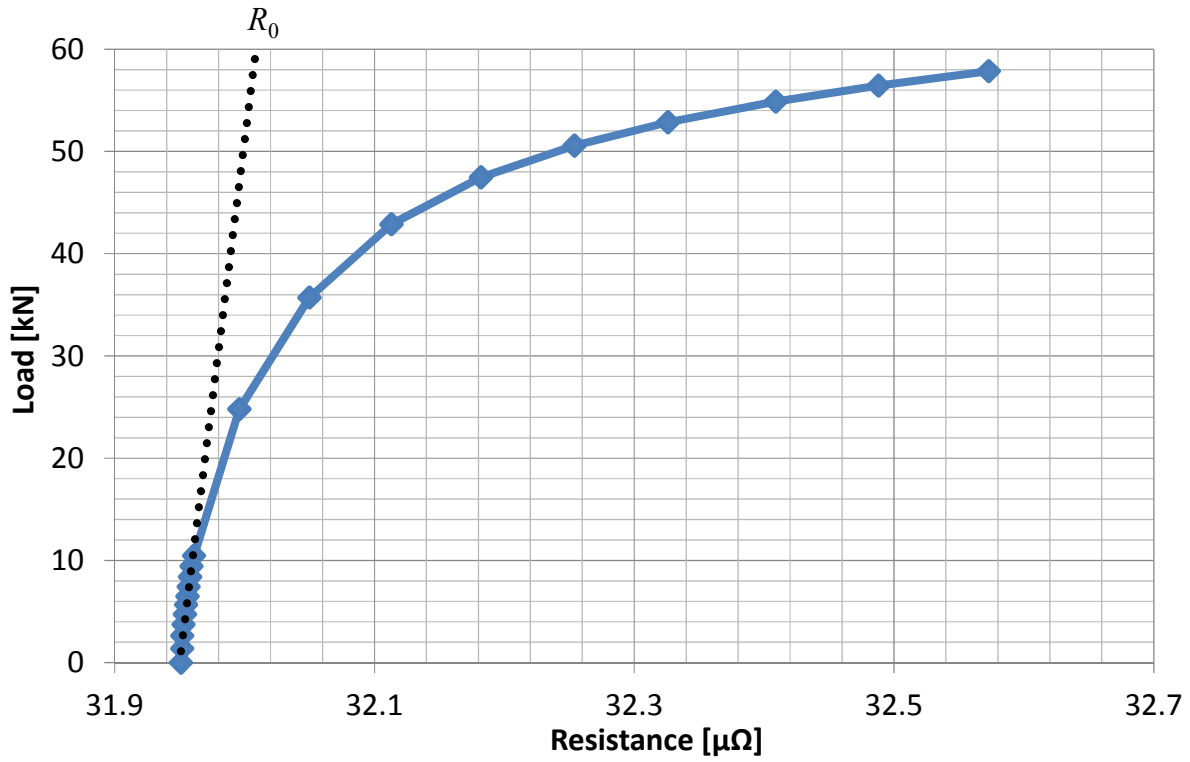

Figure 7.2: Linear regression used to calculate R_0 when assessing the PD data for specimen CTP_CT45 using the 'load' method.

The blunting predictions obtained from the PD data were compared to measurements from the FE displacement field, $\Delta a_{b\_FE\_disp}$, calculated from the difference in the x displacement at "*Node A*" and "*Node B*" shown in Figure 7.3. Due to the three dimensional nature of the FE model, this was performed for all pairs of "*Node A*" and "*Node B*" along the crack front and the mean value was calculated.

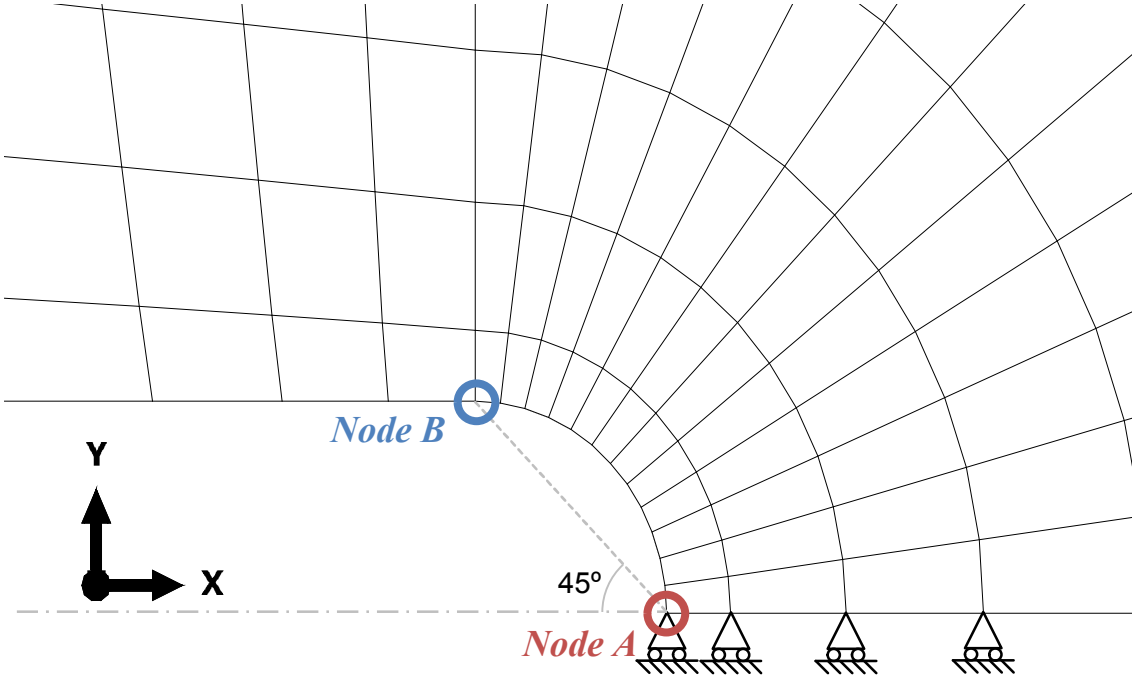

Figure 7.3: Example crack tip mesh, including the nodes used to calculate crack extension due to blunting from the displacement field. The crack tip is '*Node A*'.

The predictions based on the PD were also compared to the three different blunting lines implemented in fracture toughness standards ASTM E1820-13 [27], ISO 12135 [2] and ESIS P2-92 [1]. The crack extensions due to blunting calculated from these lines are denoted Δa_{b_ASTM}, Δa_{b_ISO} and Δa_{b_ESIS} respectively. These blunting lines calculate the crack extension from the J contour integral. This was obtained directly from the FE analysis using the focused mesh at the crack tip. In a 3D analysis Abaqus performs a volume integral of the region surrounding the crack tip to calculate a value of J at each element along the crack front. This calculation was based on a region which extended approximately 5 mm from the crack tip where it was demonstrated that the contour integral was approximately path independent and in good agreement with the EPRI handbook solutions [20].

The value of J varies along the crack front along with the stress state. This variation is shown in Figure 7.4 for a C(T) specimen CTP_CT45 (a/W = 0.45). The large spike at the free surface is caused by the tip of the side-groove and is enhanced because the side-grooves have been modelled as perfectly sharp to simplify the mesh. A 'characteristic' value of J, was used in the blunting line formulae. This value was taken from a node approximately mid-way between the mid-plane and the free surface as highlighted in Figure 7.4.

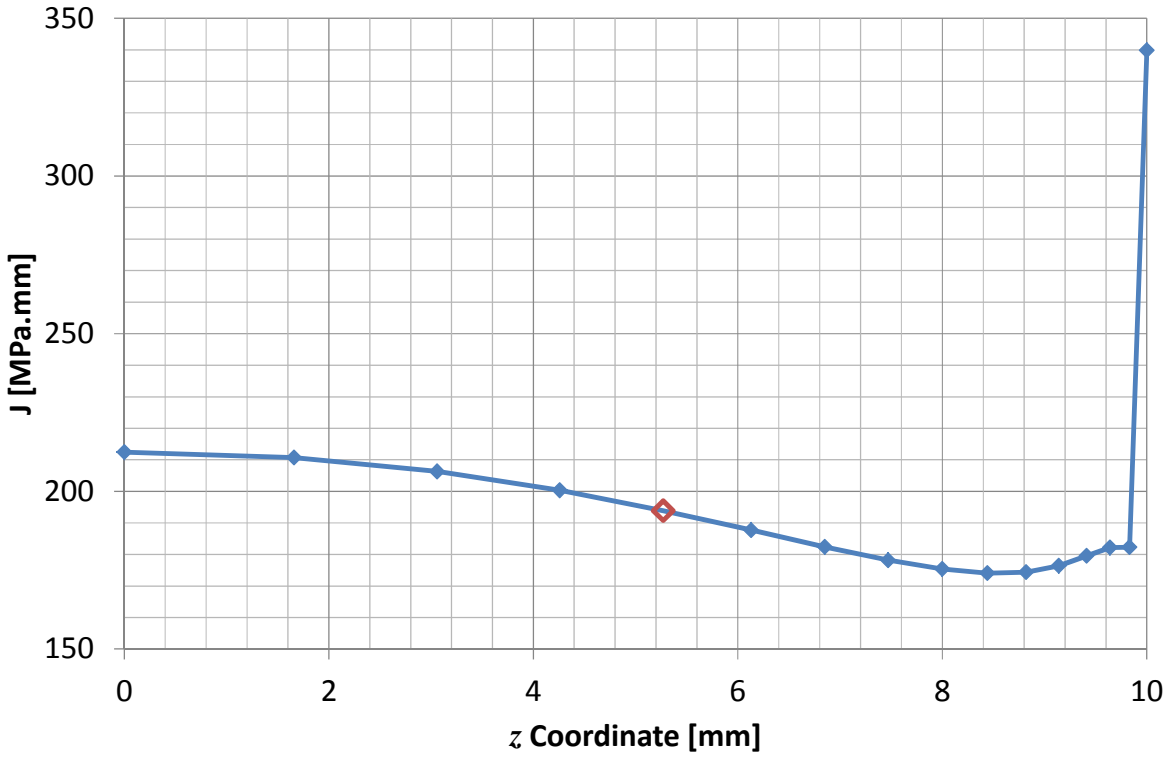

Figure 7.4: Variation of J along the crack front where z = 0 mm at the mid-plane of the specimen and z = 10 mm at the tip of the side-groove. The node used to provide a characteristic value of J is highlighted.

The different estimations of crack extension due to blunting at the maximum load are provided in Table 7.2 for the two C(T) specimens. Similar trends are identified for both specimens. The blunting estimated from the PD is significantly larger than the other predictions. The predictions based on the blunting line in ASTM E1820-13 are also relatively high whilst the measurements from the displacement field and the predictions from the blunting lines in ISO 12135 and ESIS P92-2 are much lower and in good agreement. These different estimations are compared in Figure 7.5 for C(T) specimen CTP_CT45 (a/W = 0.45).

Specimen ID	$\frac{a}{W}$	$\Delta a_{b\_FE\_PD}$ [mm]	$\Delta a_{b\_FE\_disp}$ [mm]	Δa_{b_ASTM} [mm]	Δa_{b_ISO} [mm]	Δa_{b_ESIS} [mm]
CTP_CT45	0.45	0.33	0.08	0.21	0.09	0.08
CTP_CT55	0.55	0.27	0.07	0.19	0.07	0.07

Table 7.2: Predictions of crack extension due to blunting for the C(T) specimens.

The blunting line in ASTM E1820-13 was derived for an elastic-perfectly-plastic material and assumes a semi-circular crack tip. It was modified to account for stain hardening materials by replacing the yield stress, σ_y, with the flow stress, σ_f, however, it has been demonstrated that it over-estimates blunting [28, 31], particularly for strain hardening materials such as

Type 316H stainless steel. A detailed review of fracture toughness data for Type 304 and Type 316 stainless steels based on a large number of tests from various sources has been performed by Mills [133]. It was identified that the ASTM procedure is not applicable to stainless steels because of their exceptionally high toughness, ductility and strain hardening capacity and as a result, the blunting is over-predicted by a factor of ~2. This is consistent with the other two blunting lines and the measurements from the crack tip displacement field measurements presented in Figure 7.5.

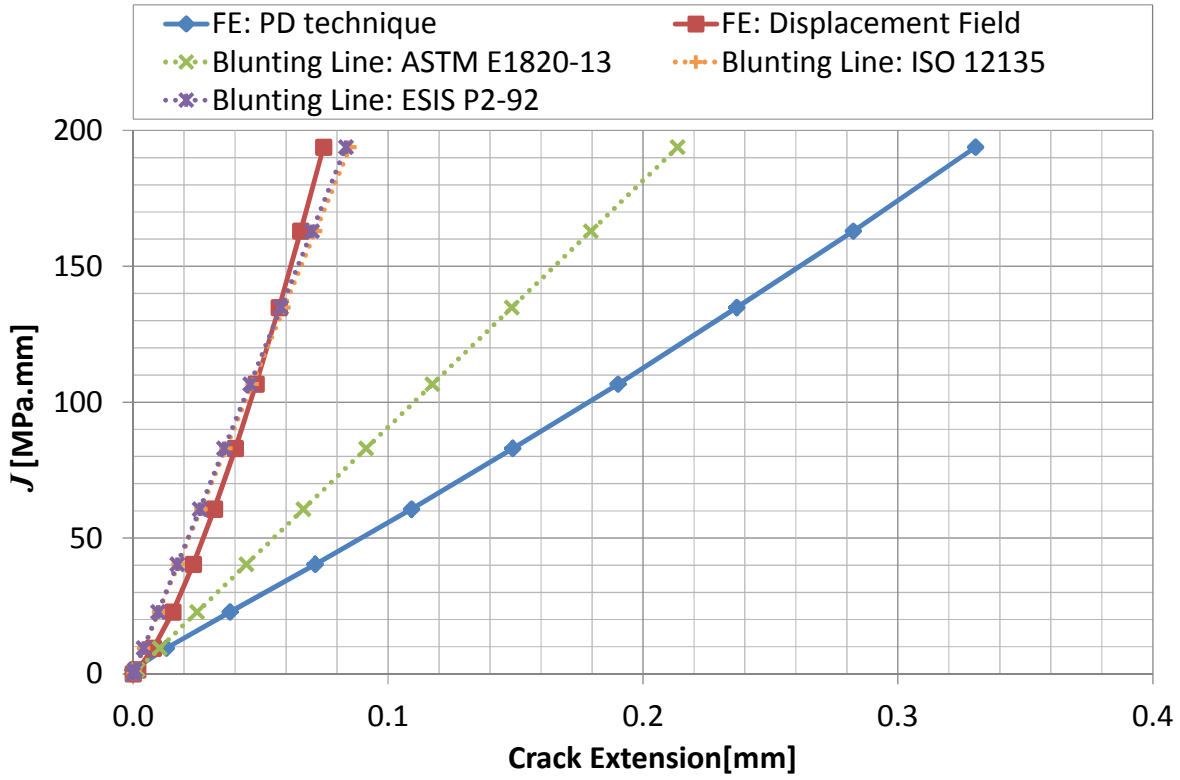

Figure 7.5: Predictions of crack extension due to blunting for C(T) specimen CTP_CT45 (a/W = 0.45).

The blunting line in ISO 12135 was developed as a simplified approximation of the more detailed approach presented in ESIS P2-92. They are both based on the HRR field for power-law strain hardening materials assuming plane strain conditions. This explains the good agreement between them and the measurements from the displacement field. The blunting predicted by the PD however is approximately four times larger. If used to measure the initiation fracture toughness, J_{IC}, this would result in extremely conservative results.

The different estimations of crack extension due to blunting at the maximum load are provided in Table 7.3 for the four SEN(T) specimens. The predictions for specimen CTP_ST30 (a/W = 0.30) are compared in Figure 7.6. The blunting estimated from the PD is again significantly larger than the other predictions and the discrepancy is even greater than

for the C(T) specimens. In Figure 7.6 the PD predictions are approximately 11 times larger than the values measured from the displacement field.

Specimen ID	$\frac{a}{W}$	$\Delta a_{b\_FE\_PD}$ [mm]	$\Delta a_{b\_FE\_disp}$ [mm]	Δa_{b_ASTM} [mm]	Δa_{b_ISO} [mm]	Δa_{b_ESIS} [mm]
CTP_ST30	0.30	0.25	0.02	0.13	0.05	0.05
CTP_ST38	0.38	0.20	0.02	0.10	0.04	0.04
CTP_ST54	0.54	0.19	0.02	0.11	0.04	0.04
CTP_ST70	0.70	0.14	0.02	0.10	0.04	0.04

Table 7.3: Predictions of crack extension due to blunting for the SEN(T) specimens.

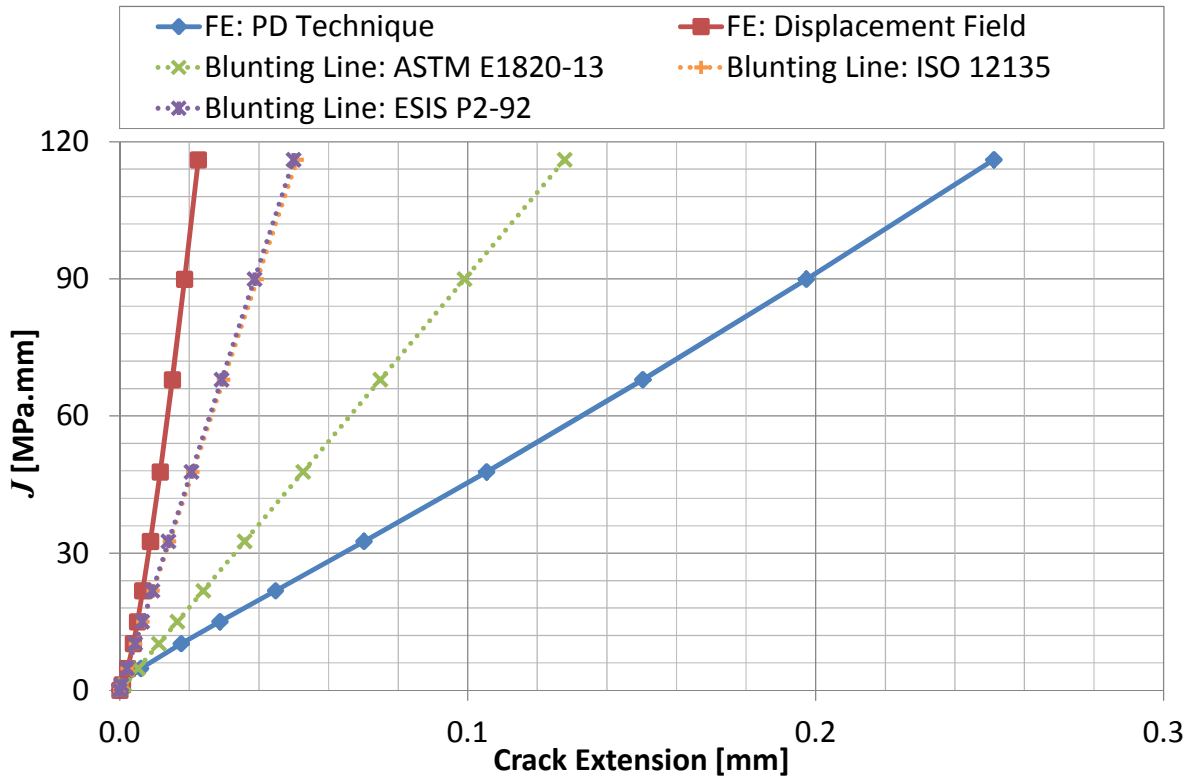

Figure 7.6: Predictions of crack extension due to blunting for SEN(T) specimen CTP_ST30 (a/W = 0.30).

The measurements from the displacement field are lower than the predictions based on the blunting lines. The discrepancy with the blunting line in ASTM E1820-13 is expected for the reasons discussed above, but there is also a discrepancy with the blunting lines in ISO 12135 and ESIS P92-2. This is because these blunting lines assume plane strain conditions at the crack tip. This is reasonable for the most common fracture toughness specimens, such as C(T) and SEN(B), which are high constraint geometries but for the relatively low constraint geometries, such as thin SEN(T) specimens, this is not a valid assumption.

To demonstrate that this discrepancy is related to the stress state at the crack tip and provide confidence in the measurements based on the displacement field, the blunting line in ESIS P2-92 has been modified for plane stress conditions. This blunting line is defined by Equation (7.1) where d_N is derived from the plane strain HRR field [29] and the coefficient of 0.4 is based on experimental observations of the stretch zone [31] where $SZW/2SZH \approx 0.4$ for high constraint fracture toughness specimens.

$$\Delta a = 0.4 d_N \frac{J}{\sigma_{p0}} \tag{7.1}$$

To modify this blunting line, d_N has been recalculated based on the plane stress HRR field [29] and a new coefficient has been estimated from a 2D FE model of a SEN(T) specimen (a/W = 0.30). The ratio $SZW/2SZH$ was estimated from the crack tip displacement field of the 2D model where the SZH is the y displacement of "*Node B*" in Figure 7.3, and the SZW is the difference in the x displacement of "*Node A*" and "*Node B*" (the same as $\Delta a_{b\_FE\_disp}$). The variation of the ratio $SZW/2SZH$ with J for plane strain and plane stress conditions is shown in Figure 7.7.

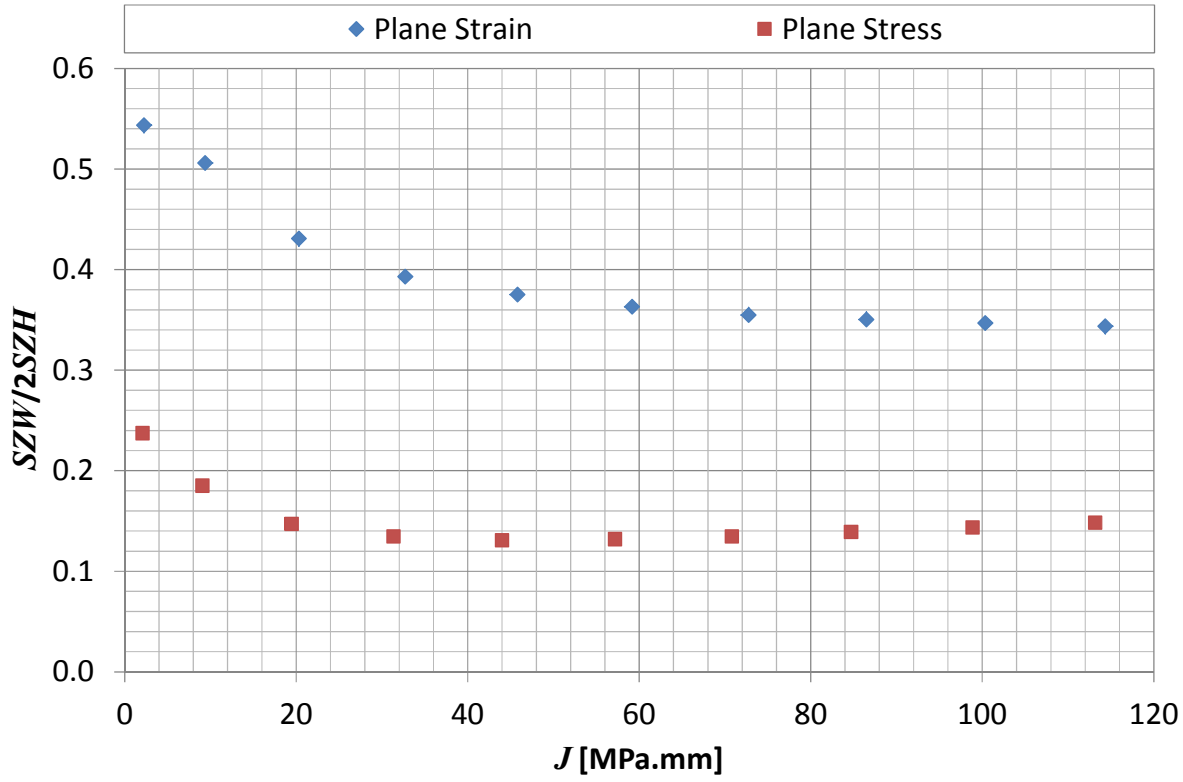

Figure 7.7: Variation of $SZW/2SZH$ obtained from a 2D FE model of a SEN(T) specimen for plane stress and plane strain conditions.

After an initial reduction at low loads the ratio $SZW/2SZH$ becomes approximately constant. For plane strain conditions this constant value is close to 0.4 which is the value used in

Equation (7.1). For plane stress this constant value is much lower at approximately 0.14. A coefficient of 0.14 is therefore considered more appropriate for the SEN(T) specimens.

The crack extension due to blunting obtained from the displacement field for specimen CTP_ST30 (a/W = 0.30) is compared to the original blunting line from ESIS P2-92 for plane strain conditions and a modified version based on plane stress conditions in Figure 7.8. The modified blunting line is in reasonable agreement with the from the displacement field. This provides confidence in the displacement field measurements provided in Figure 7.6 thus confirming that the PD can over-predict the crack extension due to blunting by more than an order of magnitude for low constraint geometry.

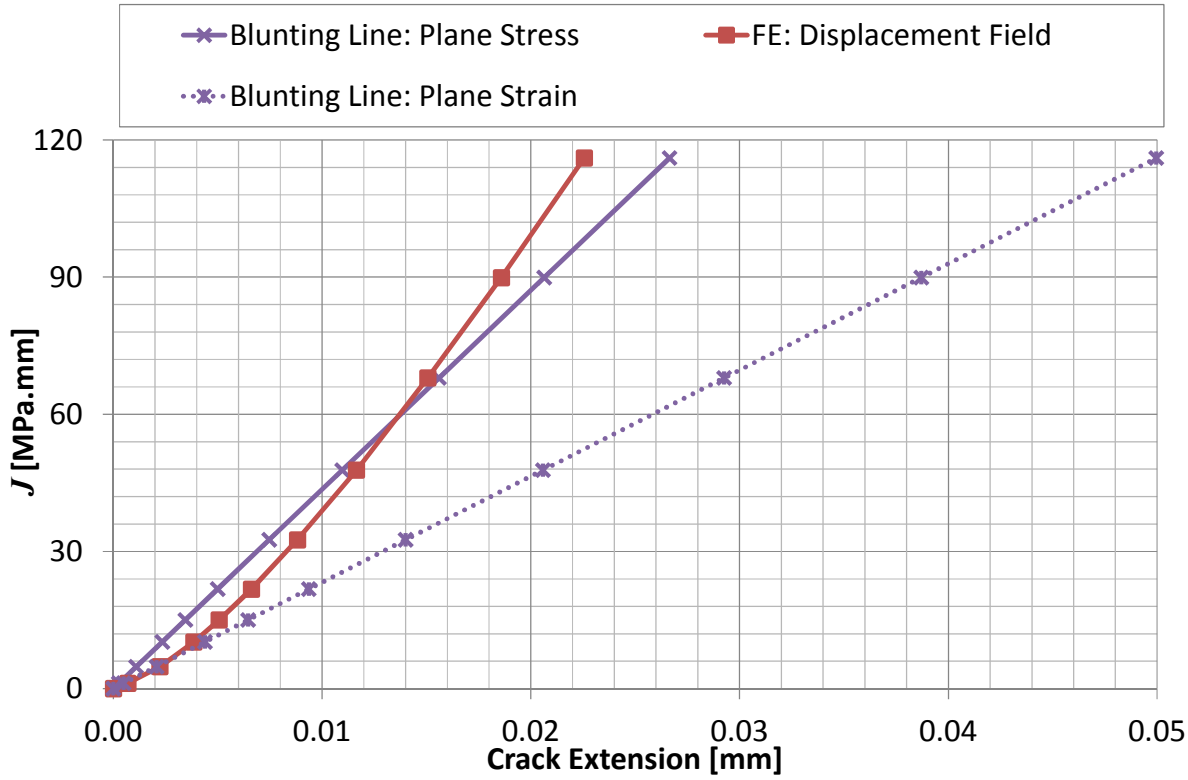

Figure 7.8: Predictions of crack extension due to blunting for SEN(T) specimen CTP_ST30 (a/W = 0.30)

In general it can be concluded that the PD technique significantly overestimates the crack extension due to blunting. The level to which it overestimates the blunting depends on the stress state and is also likely to depend on the degree of strain hardening exhibited by the material. For typical high constraint geometries such as C(T) specimens, manufactured from Type 316H stainless steel, the crack extension can be overestimated by a factor ~4. For lower constraint geometries which experience higher levels of plasticity, this factor can be significantly larger. This overestimation is probably because the PD response is related to the entire strain field and not just the geometry of the crack tip. It also explains why previous

studies have reported unexpectedly low values of J_{IC} when using the 'load' method to interpret PD data e.g. [82].

The discussion presented above is based entirely on FE analysis. It was demonstrated in the previous chapter that for Type 316H the FE under-estimates the change in PD compared with the experimental data because it does not include material effects such as piezo-resistivity which can be significant during the blunting phase. Including these material effects would increase the error in the PD measurement further still so the 'load' method of interpreting PD data is therefore not suitable for measuring crack blunting. The relationship between strain and resistivity is material specific. The error in the measurement of crack blunting based on the PD technique will therefore also be material specific thus making it difficult to quantify without a detailed understanding of the electrical material properties.

7.3.1 Measuring Blunting using the 'COD' Method

The 'COD' method uses SEM measurements of the SZW or a blunting line to predict crack extension prior to stable tearing. Significant scatter has been identified in SEM measurements [28] but extensive work is documented in the literature which demonstrates the suitability of the various blunting lines to different materials, e.g. [31]. As demonstrated above, it is important to ensure that the applied blunting line is applicable to the level of constraint provided by the specimen. As long as appropriate consideration is given to these factors, a good approximation of the crack extension due to blunting should be obtained.

7.4 Measuring Stable Tearing using the PD Technique

To investigate the use of the PD method for measuring stable tearing, a fracture toughness test was performed in accordance with ASTM E1820-13 [27]. The specimen was manufactured from the same ex-service Type 316H stainless steel used in the previous chapter. The crack extension was simultaneously monitored using the PD technique and the partial unloading compliance technique. The PD data was interpreted twice: once using the 'load' method and once using the 'COD' method. The J resistance curve and the initiation fracture toughness, J_{IC}, were determined using all three methods for comparison. Although the test was performed to ASTM E1820-13, the blunting line used in the post-processing of the data was taken from ISO 12135 [2] based on the findings of the previous section.

7.4.1 Methodology

7.4.1.1 Geometry

The test was performed on a standard, high constraint, C(T) specimen. The specimen geometry is shown in Figure 7.9 and the key dimensions summarised in Table 7.4. The specimen was loaded in displacement control at a cross-head speed of 2 mm/min.

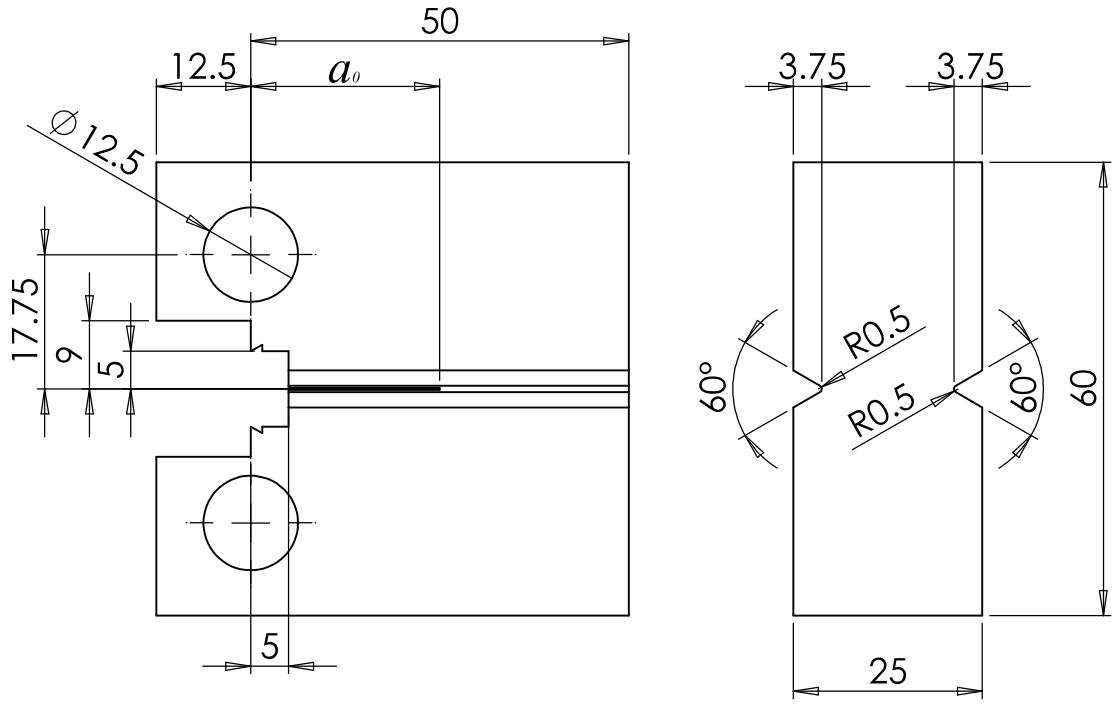

Figure 7.9: C(T) specimen geometry used for fracture toughness testing (dimensions in mm)

Specimen ID	a_0 [mm]	W [mm]	B [mm]	B_n [mm]
JIC_CT01	23.1	50.0	25.0	17.5

Table 7.4: C(T) specimen key dimensions

7.4.1.2 Crack Extension Measurement

Crack extension was monitored using the low frequency ACPD system and partial unloading compliance. Measurements were taken at increments of 0.15 mm of the cross head. A hold time was introduced prior to each unloading to record the PD. A total of 18 crack extension measurements were made throughout the test.

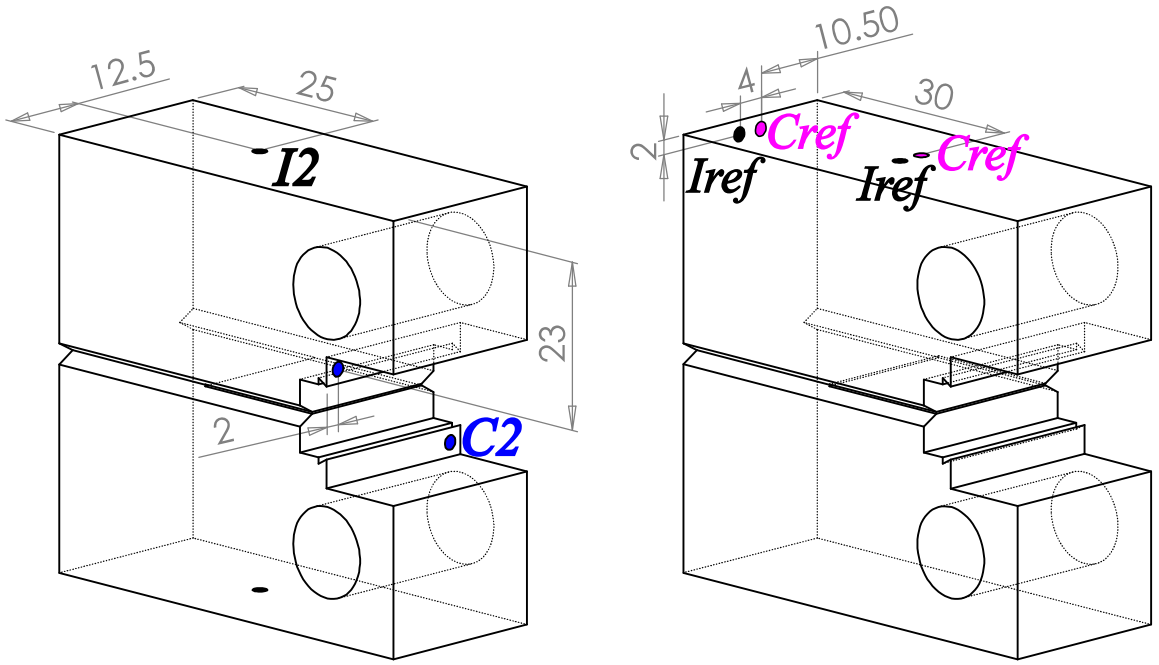

(a) (b)

Figure 7.10: PD configuration use to measure (a) crack extension measurement, and (b) reference measurement (dimensions in mm)

The PD configuration is shown in Figure 7.10. This configuration was selected based on the results of the previous chapter. The PD probes were located on opposite sides of the specimen to reduce the influence of any uneven crack growth. The corresponding calibration function was derived using COMSOL [124] and is provided in Equation (7.2), where R_0 is the resistance when a = a_0. The shackles and the loading pins were coated in PVC insulation tape to isolate the specimen from the load frame and prevent alternative paths for the electrical current. A reference measurement was taken to suppress any variations in temperature which occurred throughout the test.

$$\frac{a}{W} = 0.0230712\left(\frac{R}{R_0}\right)^3 - 0.194202\left(\frac{R}{R_0}\right)^2 + 0.701779\left(\frac{R}{R_0}\right) - 0.0806068 \qquad \textbf{(7.2)}$$

The unloading compliance was measured using a clip gauge mounted directly on the 'knife edges' machined into the specimen. These were painted to isolate the clip gauge from the specimen. For each measurement the specimen was unloaded to 50% of the applied load. The unloading compliance data was post-processed in accordance with ASTM E1820-13.

7.4.1.3 Fatigue Pre-cracking

The specimen was manufactured with a 20 mm long EDM slit (tip radius of 0.15 mm). This was extended approximately 3 mm by fatigue using a sinusoidal load with an R-ratio of 0.1

and a loading frequency of 25 Hz. The peak pre-cracking load was 12 kN which is small compared to the load at the onset of stable tearing of ~50kN.

Crack extension was monitored during fatigue pre-cracking using the same PD configuration described above. The pre-cracking was performed on a plane-sided specimen and the side faces were polished to observe the crack extension and confirm the PD measurements. After the fatigue pre-cracking, the side-grooves were machined into the specimen. The value of a_0, provided in Table 7.4, was measured from the post-test fracture surface.

7.4.1.4 Post-Test Measurements

After the test the specimen was cut in half to reveal the crack profile along the mid-plane of the specimen. One half of the specimen was sliced up to reveal the crack profile 2.5 mm and 5.0 mm from the mid-plane. The other half of the specimen was fatigued open to reveal the fracture surface whilst minimising further plastic deformation. The final crack length was obtained using an area average obtained from image processing software assuming the crack front was symmetrical about the mid-plane. The final crack length measurement was compared to the PD predictions.

7.4.2 The J Resistance Curve based on the 'Load' Method

The equation for the linear regression used to calculate R_0 (in μΩ), similar to Figure 7.2, is provided in Equation (7.3), where P is the applied load (in kN). Using this equation, the subsequent crack extension was calculated from the calibration function provided in Equation (7.2).

$$R_0 = 159.94P - 4395.8 \quad \textbf{(7.3)}$$

The resulting J resistance curve is provided in Figure 7.11. The data is separated into qualified and unqualified data for calculating J_{IC}, which is also shown. Data which exceeds the maximum crack extension, Δa_{limit}, have been omitted. The value of J_{IC} and the relevant validity limits from ASTM E1820-13 are summarised in Table 7.5.

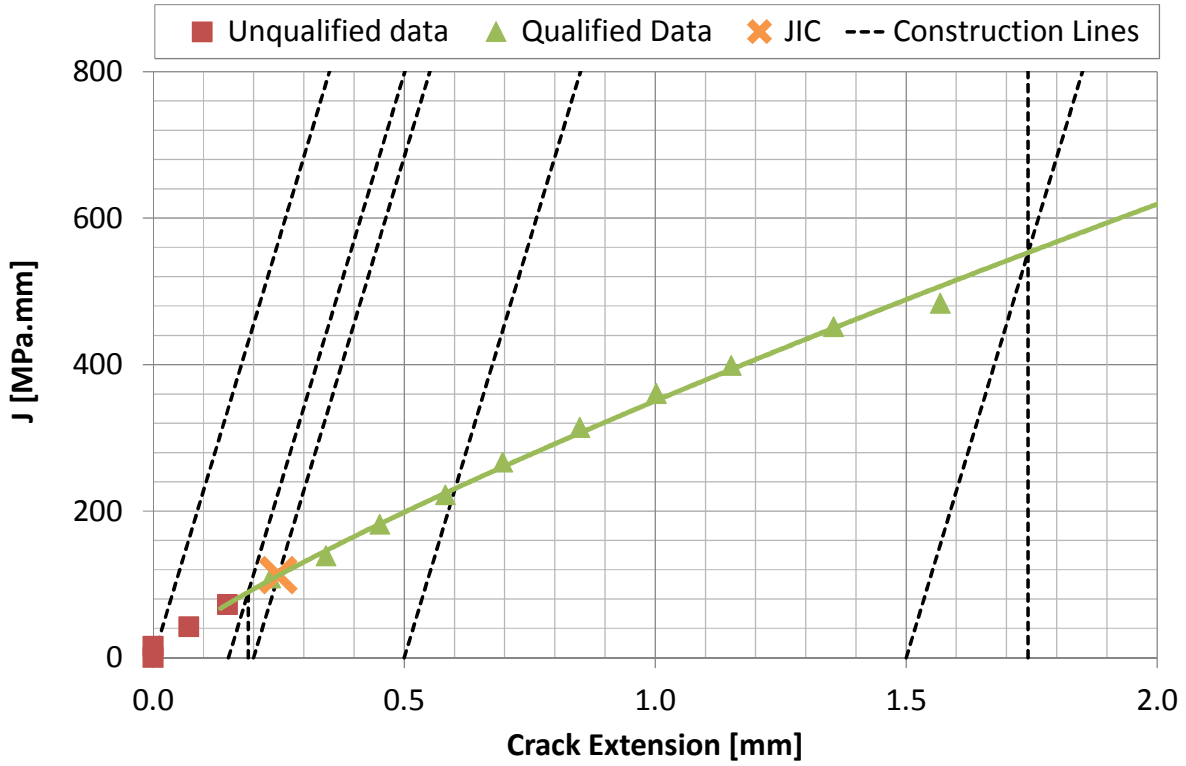

Figure 7.11: J resistance curve and J_{IC} for a fracture toughness test where the crack extension is measured using the PD technique, interpreted using the 'load' method.

The results do not show any appreciable blunting region. This is consistent with the results in the previous section which demonstrated that the PD over-predicts crack extension due to blunting. In accordance with ASTM E1820-13, this would be interpreted as almost instantaneous stable tearing and results in a value of J_{IC} of 112.4MPa.mm.

J_{IC} [MPa.mm]	J_{max} [MPa.mm]	J_{limit} [MPa.mm]	Δa_{min} [mm]	Δa_{limit} [mm]	Test Validity
112.4	1134.8	1691.5	0.19	1.74	Valid

Table 7.5: Summary of a fracture toughness test results where the crack extension is measured using the PD technique, interpreted using the 'load' Method.

7.4.3 The J Resistance Curve based on the 'COD' Method

Figure 7.12 shows the relationship between resistance and CMOD. An initial linear region is observed before the gradient gradually increases. A linear regression fit to the initial data is shown along with the point at which the data first deviates from this linear trend, labelled R_0.

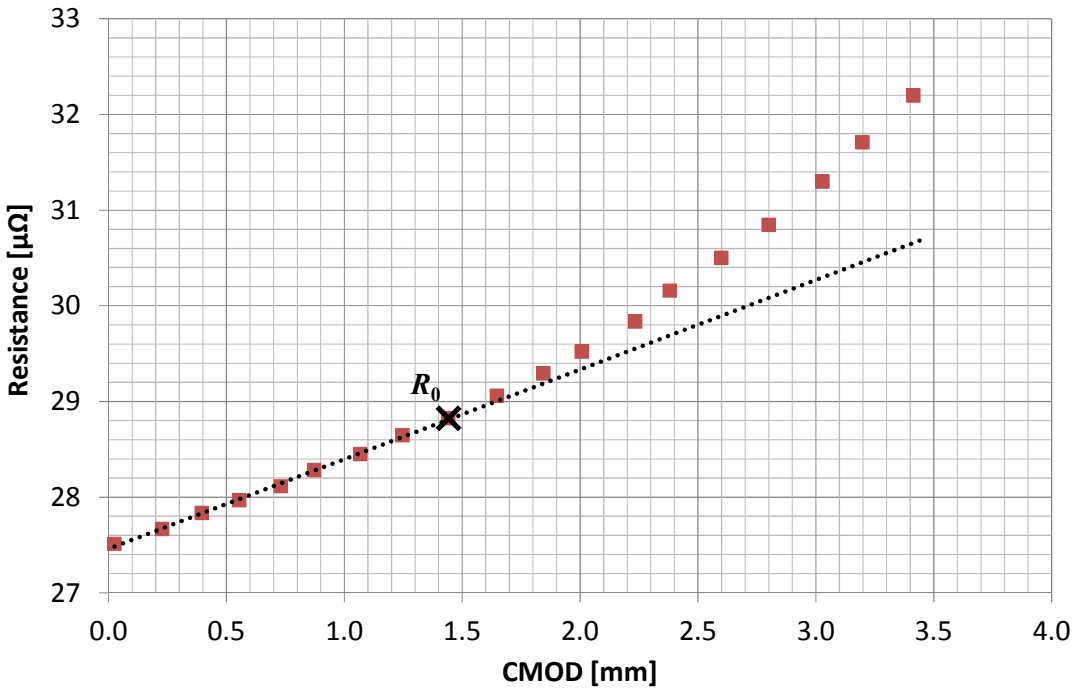

Figure 7.12: Estimation of R_0 from a plot of resistance vs. CMOD.

The value of R_0, obtained from Figure 7.12, is 28.82 μΩ. Using this value, the subsequent stable tearing was calculated from the calibration function provided in Equation (7.2). The resulting J resistance curve is provided in Figure 7.13. The test results, including the relevant limits are summarised in Table 7.6.

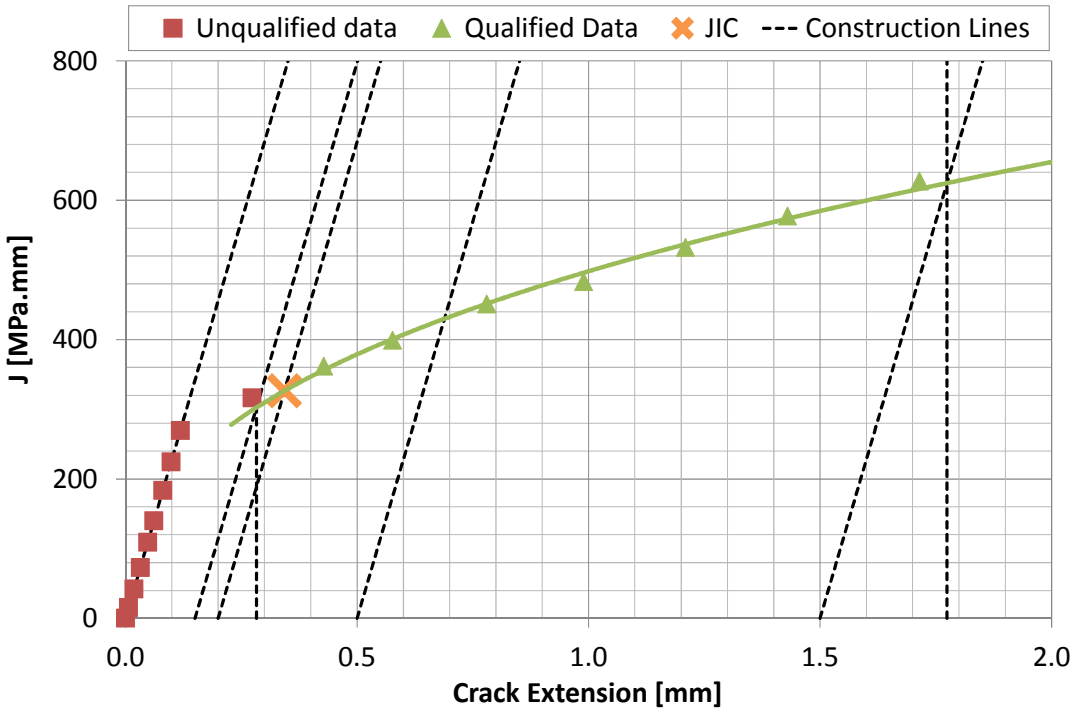

Figure 7.13: J resistance and J_{IC} for a fracture toughness test where the crack extension is measured using the PD technique, interpreted using the 'COD' method.

The shape of the J resistance curve is very different to the one derived based on the 'load' method. A distinct blunting phase is observed before the onset of stable tearing which results in a much larger value of J_{IC} of 326.7MPa.mm. It should be noted that the initial data points are perfectly linear because they are calculated from the blunting line formula in accordance with the 'COD' method. They are not experimental data points.

J_{IC} [MPa.mm]	J_{max} [MPa.mm]	J_{limit} [MPa.mm]	Δa_{min} [mm]	Δa_{limit} [mm]	Test Validity
326.7	1134.8	1691.5	0.28	1.77	Valid

Table 7.6: Summary of a fracture toughness test where the crack extension is measured using the PD technique, interpreted using the "COD Method".

7.4.4 The J Resistance Curve based on the Compliance Method

The J resistance curve calculated from the compliance method is provided in Figure 7.14. The test results, including the relevant limits are summarised in Table 7.7.

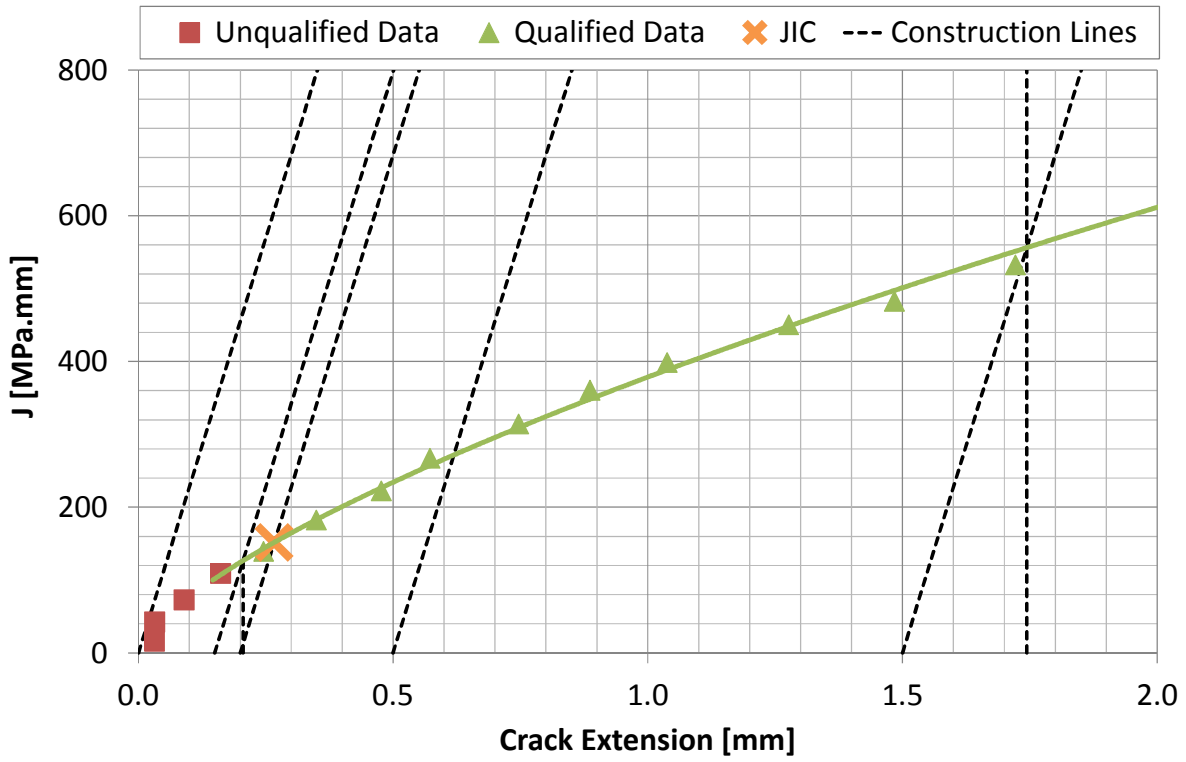

Figure 7.14: J resistance curve and J_{IC} for a fracture toughness test where the crack extension is measured using partial unloading compliance method.

There is an initial steep section in the J resistance curve which could be due to blunting however, the gradient reduces significantly very early in the test. This is interpreted as stable tearing and results in a value of J_{IC} of 151.7MPa.mm.

J_{IC} [MPa.mm]	J_{max} [MPa.mm]	J_{limit} [MPa.mm]	Δa_{min} [mm]	Δa_{limit} [mm]	Test Validity
151.7	1134.8	1691.5	0.21	1.74	Valid

Table 7.7: Summary of a fracture toughness test where the crack extension is measured using the compliance method.

7.4.5 Post-Test Measurements

The fracture surface of the specimen is shown in Figure 7.15 and the profile of the crack at various points though the thickness is shown in Figure 7.16. The crack extension is relatively uniform across the thickness with minimal crack tunnelling observed. The average crack extension due to stable tearing measured from the fracture surface is 2.4 mm.

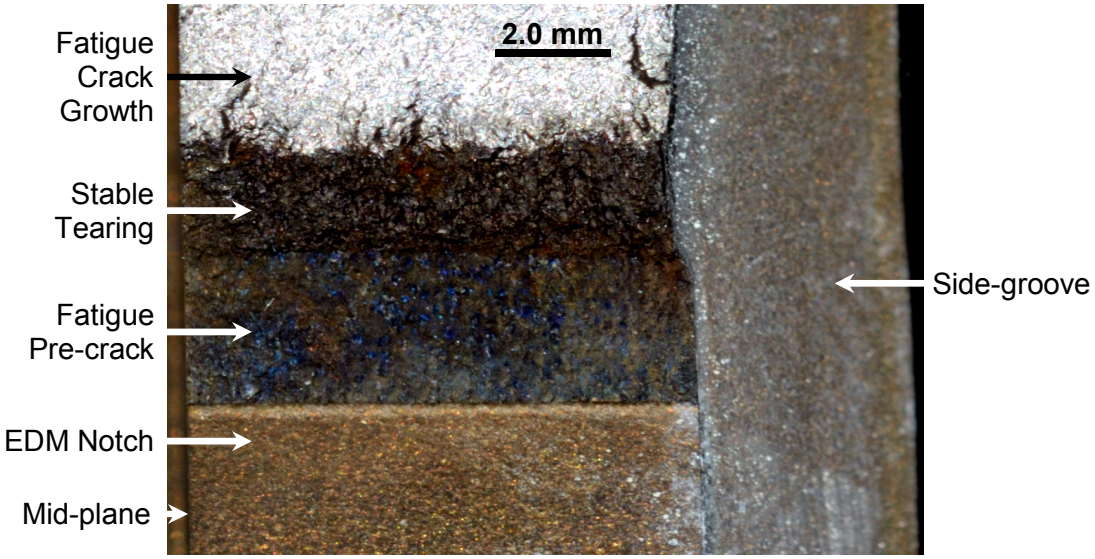

Figure 7.15: Post-test fracture surface.

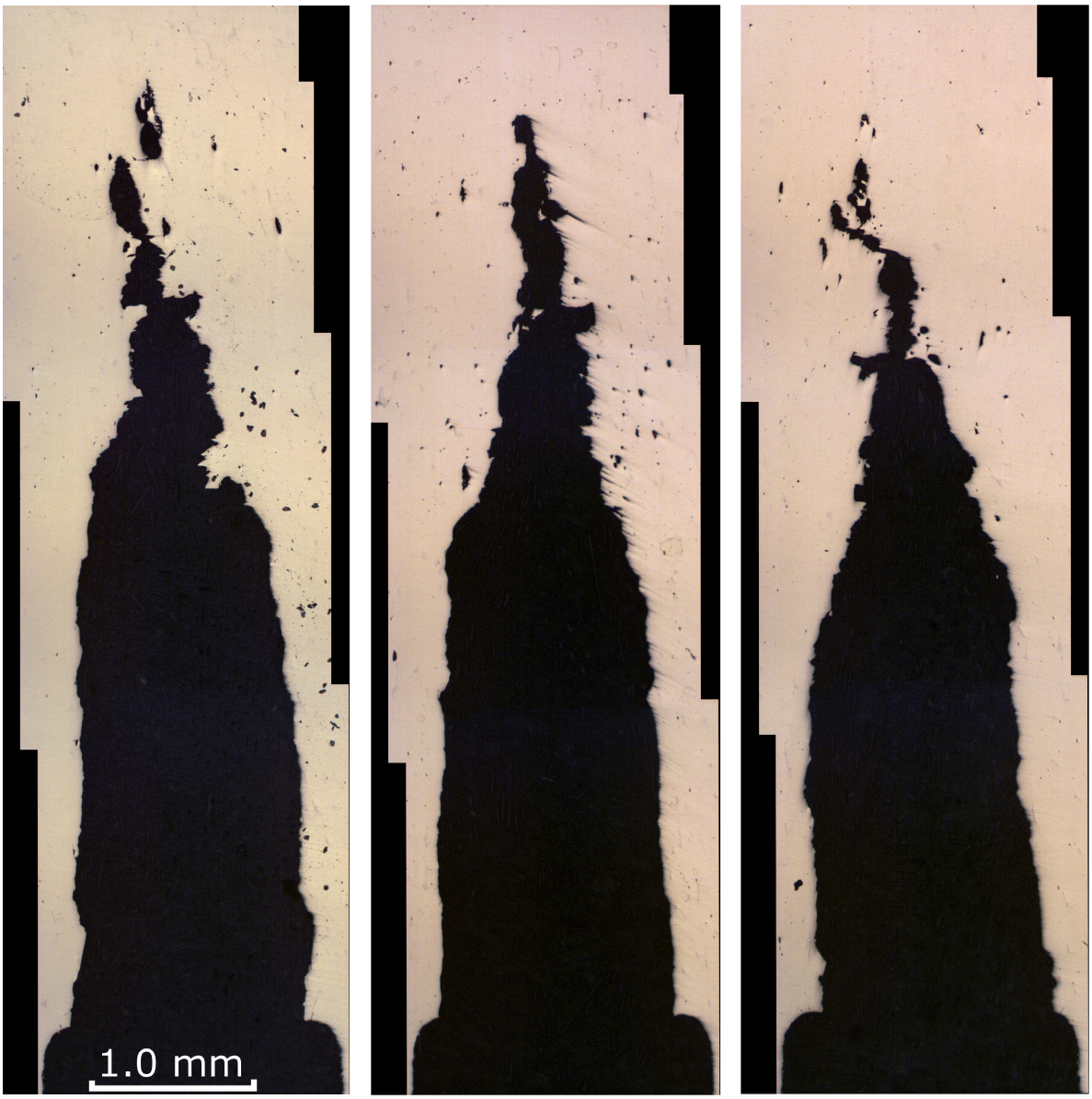

Figure 7.16:Crack profile at (a) the mid-plane, (b) 2.5 mm from the mid-plane, and (c) 5.0 mm from the mid-plane

7.4.6 Comparison of the Results

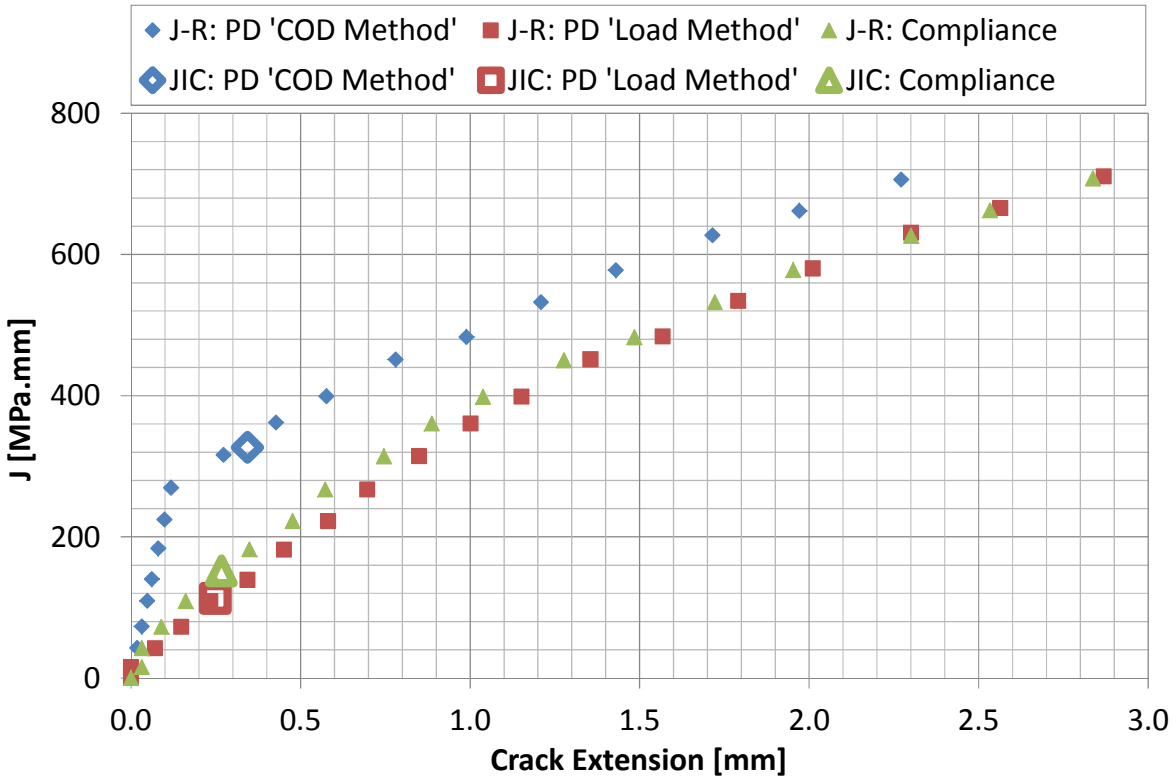

Figure 7.17: Comparison of the J-R curves derived using three different methods.

The three J resistance curves are compared in Figure 7.17 and the values of J_{IC} are summarised in Table 7.8. There are obvious similarities between the two curves derived from the 'load' method and the compliance method. Both diverge from the blunting line very early on in the test and a have a similar, shallow gradient which results in a relatively low value of J_{IC}. Conversely, the 'COD' method demonstrates a significant blunting phase and a value of J_{IC} which is more than double the other two methods.

Method	J_{IC} [MPa.mm]
PD technique: 'Load' method	112.4
PD technique: 'COD' method	316.7
Compliance method	151.7

Table 7.8: Values of J_{IC} predicted by the three different methods

Typical mean and lower bound values of the initiation fracture toughness of Type 316 stainless steel obtained from the literature are provided in Table 7.9. The values obtained by the 'load' method and the compliance method are equal to or below the lower bound values whilst the value predicted by the 'COD' method is comparable to the mean values and is therefore more likely to be correct.

Source	J_{IC} [MPa.mm]	
	Mean	Lower Bound
Mills [133]	672	215
Dixon [134]	312	152

Table 7.9: Typical values of J_{IC}

The blunting analysis performed at the start of this chapter demonstrated that the 'load' method over-estimates the crack extension due to blunting which leads to an underestimation of the value of J_{IC}. Given that the compliance method is consistent with the 'load' method this suggests that it too is over-estimating the crack extension due to blunting. The source of the error in the 'load' method is the relationship between strain and the resistance of the specimen which should not influence the results obtained from the compliance method. This suggests that the consistency between the 'load' method and the compliance method is probably coincidental.

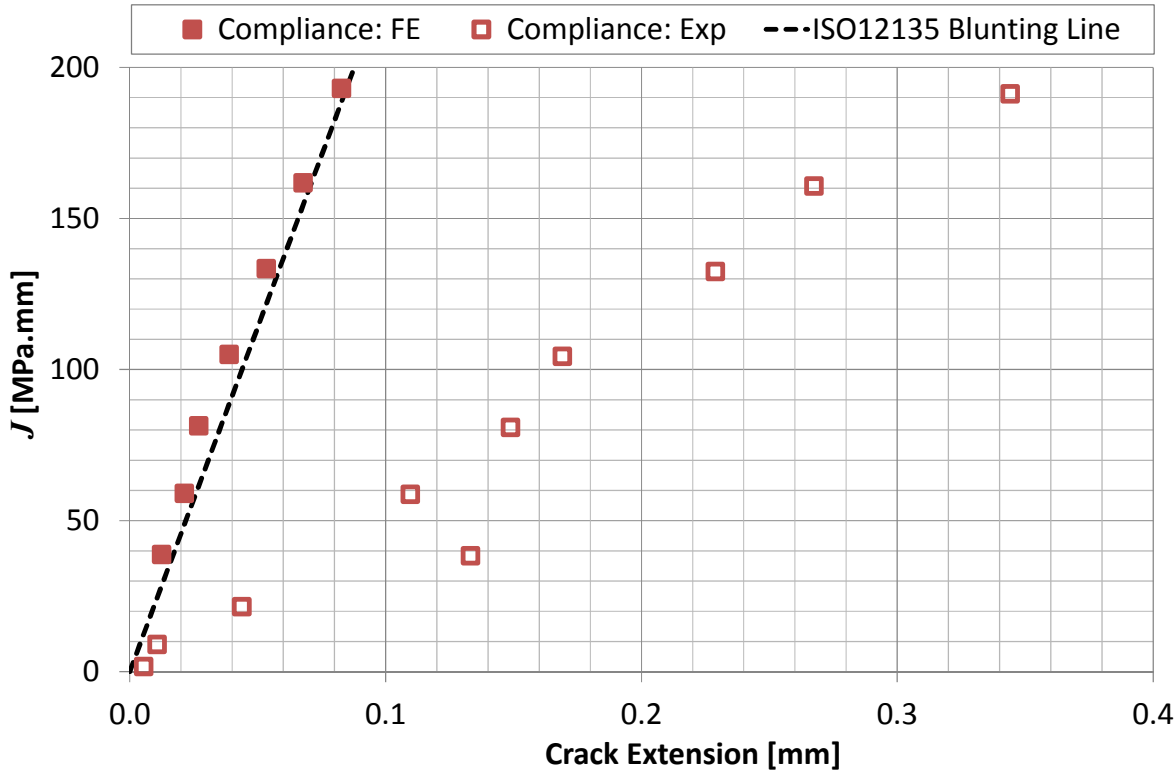

Figure 7.18: Comparison of experimental and numerical compliance measurements performed on a C(T) specimen (a/W = 0.45) with the blunting line from ISO 12135.

Compliance measurements obtained from C(T) specimen CTP_CT45 (a/W = 0.45) in the previous chapter are analysed here to investigate the source of these errors. The crack extension predicted from the compliance measurements is compared with the blunting line

from ISO 12135 in Figure 7.18. The FE model of this specimen was also rerun to include partial unloading cycles from which the compliance was calculated. Crack extension predictions obtained from the unloading compliance of the FE model are also included in Figure 7.18. Observations from the post-test fracture surface confirmed that no stable tearing occurred during the test, so any crack extension was due to blunting only.

The experimental measurements significantly over-predict the crack extension due to blunting compared with the FE measurements and the blunting line from ISO 12135. The FE measurements are in very good agreement with the blunting line which confirms that the compliance equations in ASTM E1820-13, used to calculate crack extension are suitable for this material. The large experimental crack extensions must therefore be related to the experimental setup. This may be due to the PVC insulation tape applied to the loading pins to electrically isolate the specimen from the load frame. It is well known that the compliance technique is very sensitive to the loading pin configuration [92, 106].

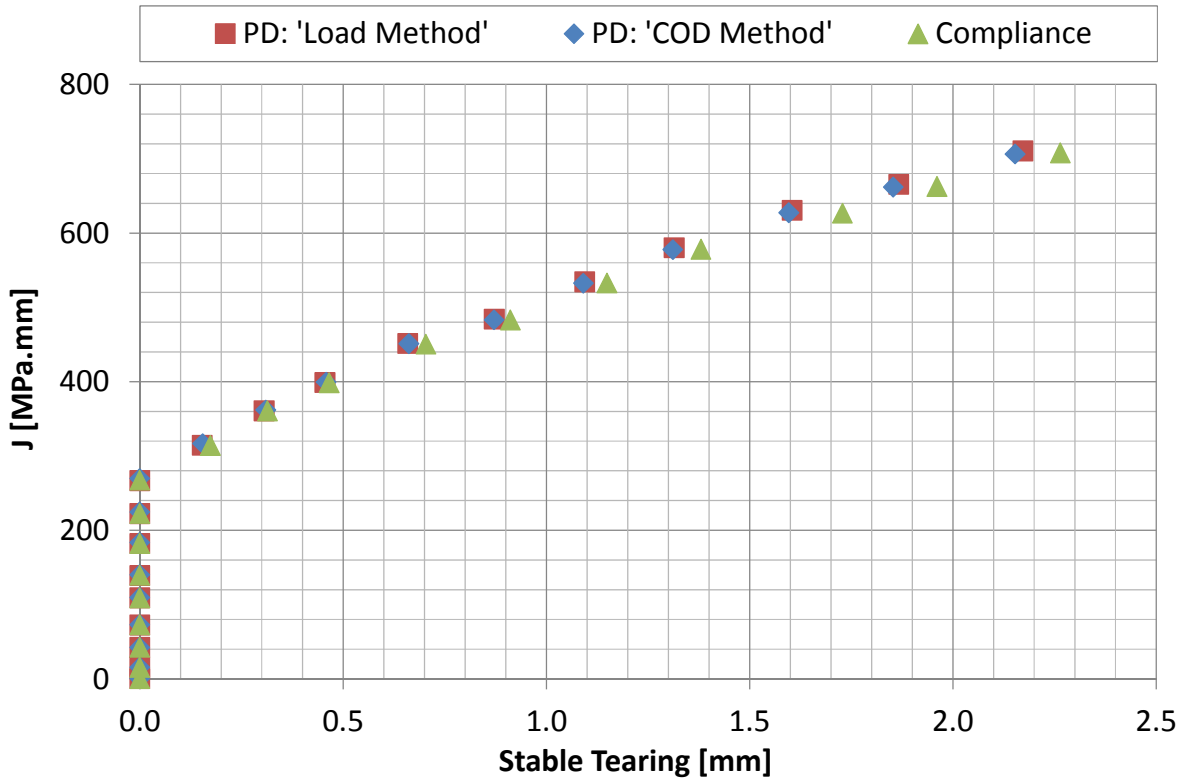

Figure 7.19: Comparison of the stable tearing predicted using three different methods.

Assuming that the 'COD' method is capable of accurately identifying the onset of stable tearing, it occurs at a value of J of ~270 MPa.mm, as identified in Figure 7.13 (the last point on the blunting line). Ignoring any crack extension prior to this point the three resistance curves have been re-plotted in Figure 7.19. The similarities are striking. The two PD methods are in excellent agreement although this is to be expected because they are both based on the same calibration function (albeit with different values of R_0) and the same PD

data; however, the compliance measurements are also in very good agreement. This provides confidence in the measurement of stable tearing and suggests that the differences between the three methods are limited to the blunting phase.

The stable tearing measurements from Figure 7.19 are compared to measurements from the post-test fracture surface in Table 7.10. All of the measurements are in good agreement. The measurements based on the PD technique assume that the influence of strain on PD is negligible during stable tearing. The close agreement between the PD and the post-test fracture surface measurements suggests that this is a reasonable assumption. This demonstrates that the 'COD' method can be used to accurately identify the onset of stable tearing and measure subsequent crack extension. The slight underestimation may be due to the small amount of discontinuous crack growth observed at the crack tip in Figure 7.16.

Method	Stable Tearing [mm]
PD technique: 'load' method	2.2
PD technique: 'COD' method	2.2
Compliance method	2.3
Post-test fracture surface	2.4

Table 7.10: Comparison of the stable tearing predicted by the different methods with measurements from the post-test fracture surface.

7.5 Limitations of the 'COD' Approach

It has been demonstrated that the PD technique can be used to accurately measure crack extension using the 'COD' method. One limitation of this technique is that the point of deviation from linear on a plot of PD (or resistance) against COD, necessary for identifying the onset of stable tearing, can be difficult to identify, particularly for high toughness, high strain hardening materials [82]. To investigate this limitation, a sequentially coupled structural-electrical FE model, similar to the one developed in the previous chapter was used. Here the analysis has been extended to include crack growth.

Initially the experimental results presented above were recreated to validate the modelling approach and demonstrate that the model was able to capture the PD behaviour for a growing crack. Then the analysis was used to look at the influence of material toughness on the ability to identify the onset of stable tearing.

7.5.1 Model Validation

7.5.1.1 Geometry and Mesh

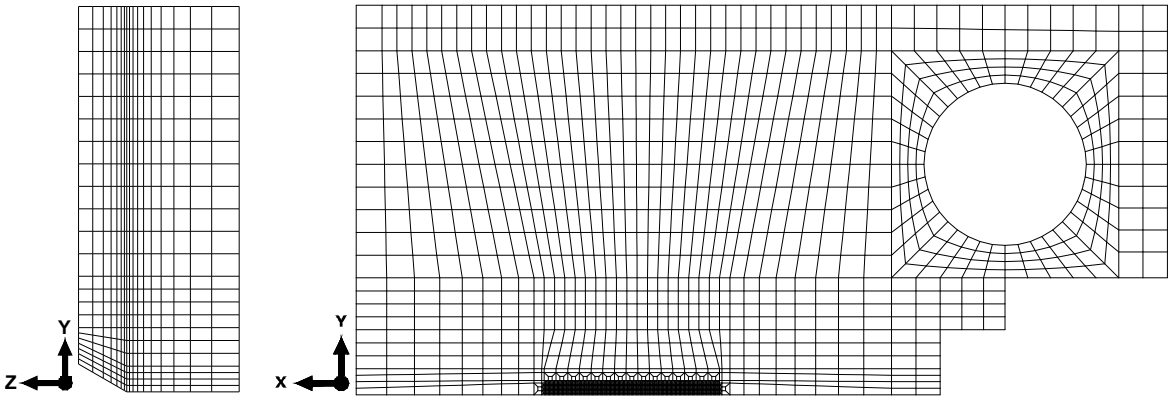

Figure 7.20: C(T) mesh for modelling fracture toughness testing including stable tearing.

A 3D ¼ model of the C(T) specimen was produced using Abaqus. The side-grooves were modelled as perfectly sharp to simplify the mesh. To allow small, uniform increments of crack extension, the mesh at the crack tip was refined to a uniform element size of 0.1 mm and the crack tip was modelled as infinitely sharp. The specimen mesh is shown in Figure 7.20 and the refined mesh at the crack tip is shown in Figure 7.21. The model consisted of 42,177 linear brick elements.

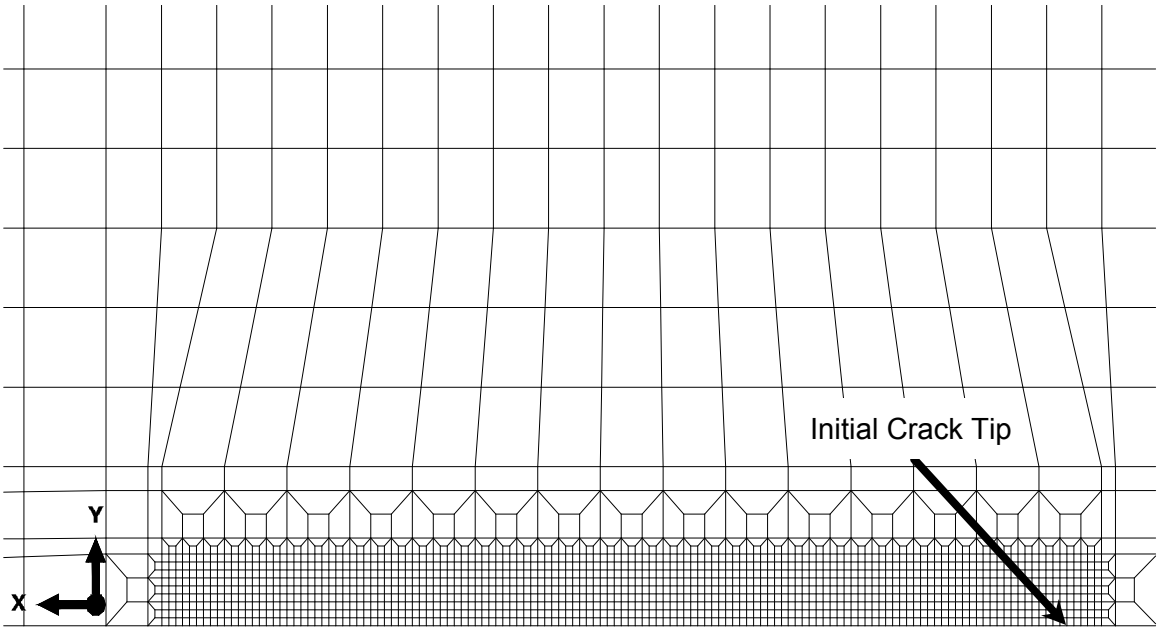

Figure 7.21: Refined crack tip mesh for modelling fracture toughness testing including stable tearing.

7.5.1.2 Material Properties

The material properties of Type 316H stainless steel provided in the previous chapter have been used in this model.

7.5.1.3 Boundary Conditions

A displacement boundary condition was applied to a node at the centre of the loading hole. This displacement was transmitted to the hole using a kinematic coupling. This avoids the computational expense of modelling contact between the loading pin and the hole and does not significantly influence the behaviour of the PD for the configuration shown in Figure 7.10. Validation of this approach is provided in the previous chapter.

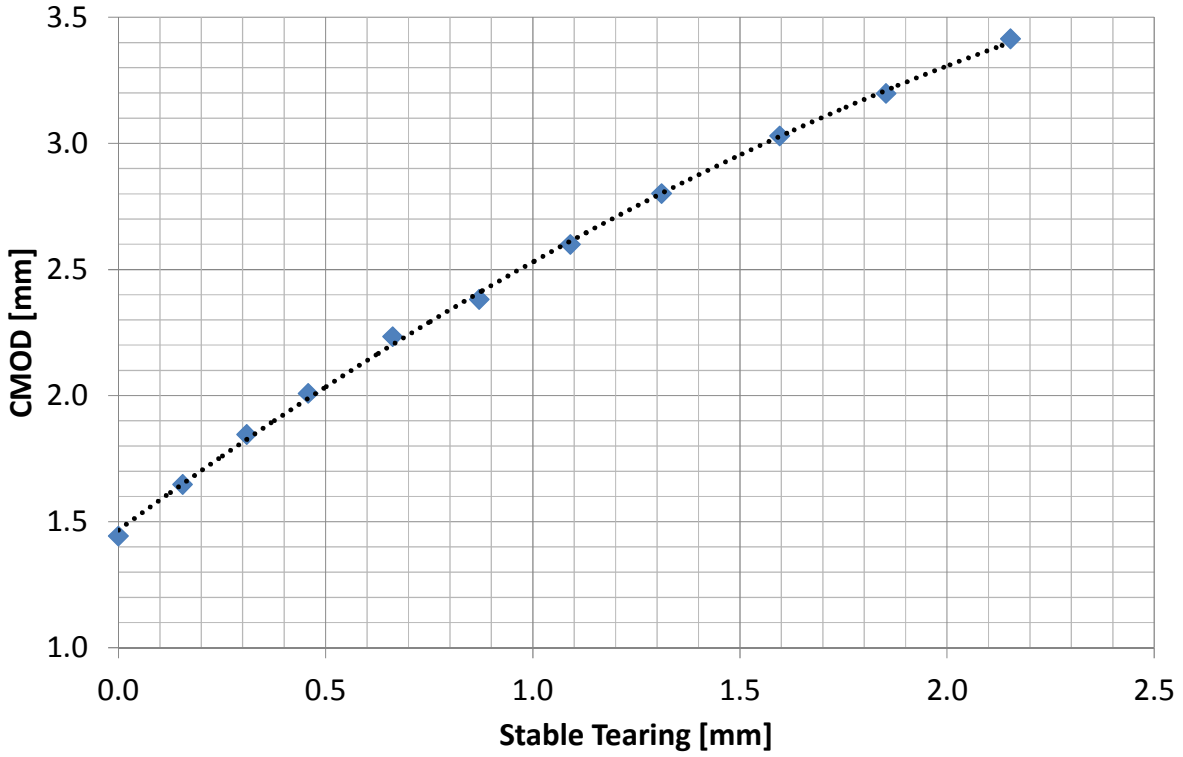

Figure 7.22: Variation of CMOD with stable tearing.

Appropriate boundary conditions were applied to the relevant planes of symmetry and crack growth was modelled simply by releasing nodes from the symmetry boundary condition applied to the remaining ligament ahead of the crack. The experimentally observed relationship between stable tearing, $\Delta a_{tearing}$, and CMOD was calculated from Figure 7.12 and is provided in Figure 7.22. A second order polynomial has been applied to this data and the equation for this line is provided in Equation (7.4) where CMOD and $\Delta a_{tearing}$ are in mm.

$$CMOD = -0.1429\Delta a_{tearing}{}^{2} + 1.206\Delta a_{tearing} + 1.4667 \quad \textbf{(7.4)}$$

This equation was used to define the crack extension in the model by modifying the symmetry boundary condition ahead of the crack accordingly. Each crack increment of 0.1 mm was modelled as a separate load step. In the initial step, a y displacement was applied to the node at the centre of the loading hole to produce a CMOD of 1.47 mm (corresponding to $\Delta a_{tearing}$ = 0.0 mm). In the subsequent step, a line of nodes parallel to the crack tip was released from the symmetry boundary condition and the y displacement increased to produce a CMOD of 1.59 mm (corresponding to $\Delta a_{tearing}$ = 0.1 mm). This process was repeated up to a CMOD of 3.37 mm ($\Delta a_{tearing}$ = 2.1 mm).

The electrical boundary conditions were similar to those used in the previous chapter, but only the PD configuration shown in Figure 7.10 was considered. The 0 V electrical potential applied to all nodes on the remaining ligament ahead of the crack was updated after each crack increment.

7.5.1.4 Results

The structural response of the FE model is provided in Figure 7.23. Consistent with the C(T) analyses presented in the previous chapter, the FE model slightly over-predicts the stiffness of the specimen.

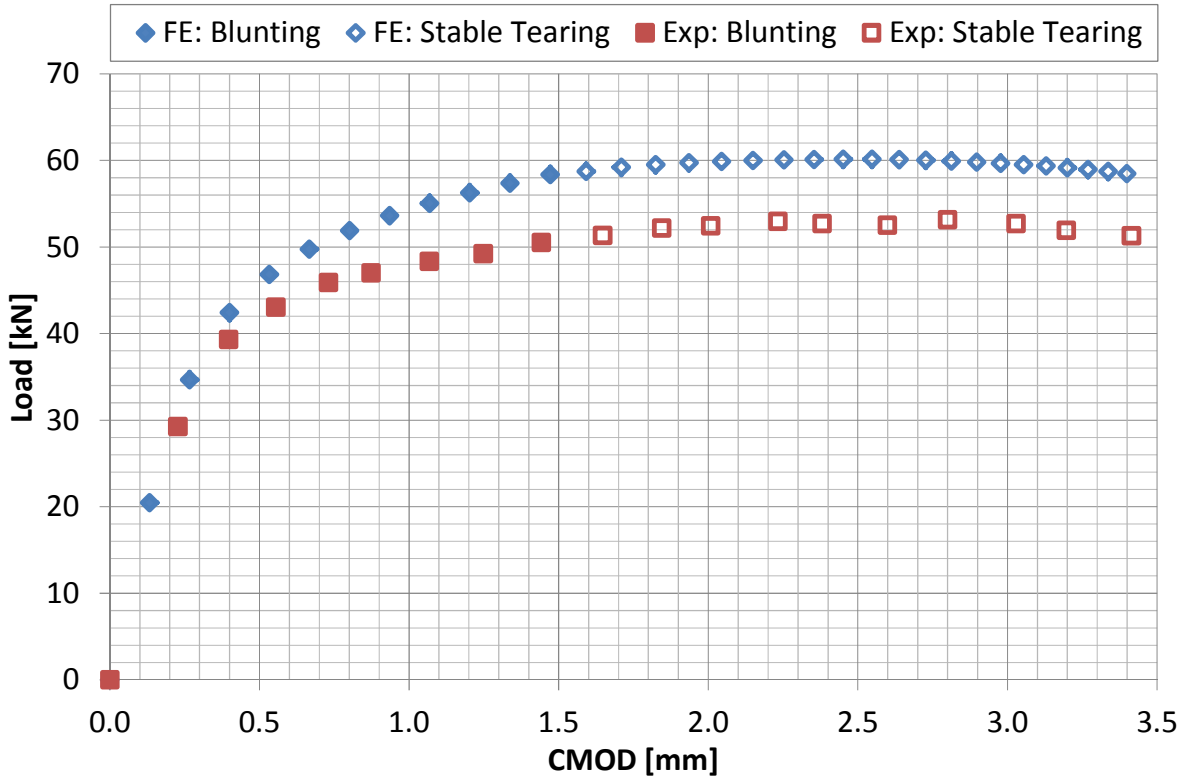

Figure 7.23: Comparison of the experimentally observed structural response of the specimen with the FE model.

The electrical response of the FE model is compared to the experimental data in Figure 7.24. Prior to stable tearing, the FE under predicts the influence of strain on PD. This is similar to the analyses of a stationary crack in the previous chapter and is because the changes in the resistivity of the material due to strain are not included in the model. Here the discrepancy is slightly larger which can be explained by the uniform mesh at the infinitely sharp crack tip which is unable to fully capture the deformed shape.

The change in PD after the onset of stable tearing predicted by the FE model is in excellent agreement with the experimental data as demonstrated by the almost constant offset between the two data sets. Given that the FE will inherently under predict any change in PD due to strain, Figure 7.24 confirms that after the onset of stable tearing, the PD response is dominated by crack growth and that subsequent changes due to strain are small. This is consistent with assumptions made in previous studies, e.g. [91].

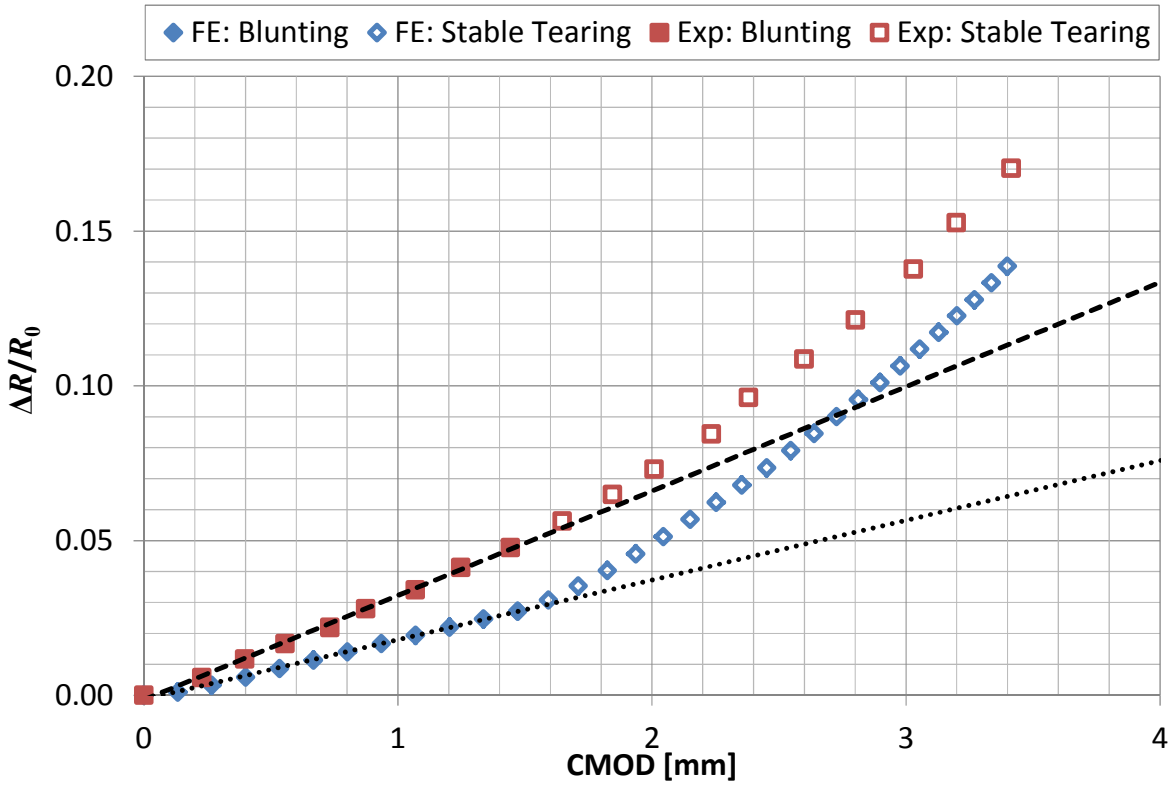

Figure 7.24: Comparison of the experimentally observed electrical response of the specimen with the FE model.

These results demonstrate that the FE is capable of capturing changes in PD for a growing crack and the change in slope at the onset of crack growth. A sensitivity study has also been performed which has shown that these results are not significantly sensitive to increasing the element size at the crack tip (and therefore the crack increments) to 0.3 mm.

7.5.2 Influence of Toughness

To investigate the influence of toughness on the increase in gradient on a plot of PD (or resistance) vs. CMOD, used to identify the onset of stable tearing, the FE model was rerun four times. The displacement boundary condition applied to the node at the centre pin hole was replaced with a concentrated load and the initial crack length was changed to 25.0 mm (a/W = 0.5). To simulate materials of different toughness, crack extension was assumed to occur at different loads. The loads considered were those which produced a reference stress, σ_{ref}, of 0.75, 1.00, 1.25 and 1.50 times the 0.2 % proof stress, $\sigma_{0.2}$. The reference stress was calculated assuming plane strain conditions. The applied loads are provided in Table 7.11. For each analysis, 0.2 mm of crack extension was modelled. For simplicity crack growth was assumed to occur at a constant load.

$\frac{\sigma_{ref}}{\sigma_{0.2}}$	σ_{ref} **[MPa]**	**Load [kN]**
0.75	225.3	25.4
1.00	299.8	33.8
1.25	375.2	42.3
1.50	449.7	50.7

Table 7.11: Loads at the onset of crack growth used to investigate the influence of toughness on a plot of PD (or resistance) vs. CMOD.

The results of the four analyses are provided in Figure 7.25. When crack initiation occurs at a reference stress below the 0.2% proof stress, the increase in gradient is easily observed. As the reference stress increases above the 0.2% proof stress, the increase in gradient becomes less well defined. This is because the crack extension is accompanied by a significant increase in CMOD associated with gross yielding of the remaining ligament. At very high loads the increase in gradient is very gradual and much more difficult to identify. In addition, for materials with a high tearing resistance, this increment in crack length would be accompanied by an increase in load which would further mask the increase in gradient. It is therefore the ability of a high toughness and high strain hardening material to sustain gross yielding of the remaining ligament without failing which makes it difficult to identify the onset of stable tearing using the 'COD' method. This is an inherent limitation of the 'COD' method for monitoring crack growth during fracture toughness tests.

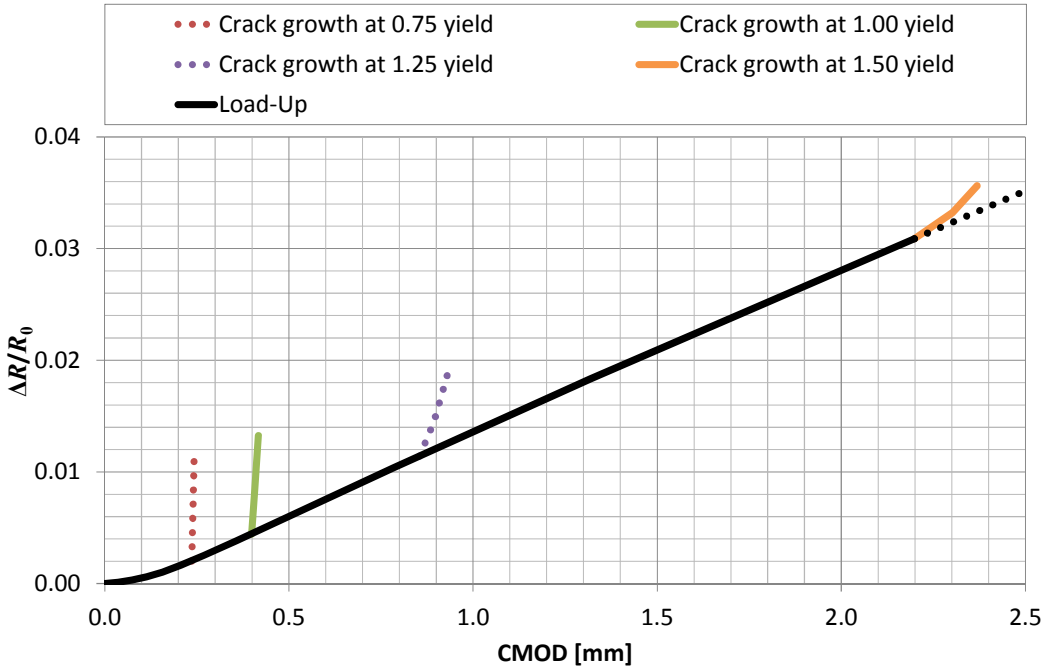

Figure 7.25: The influence of the onset of crack growth on a plot of relative change in resistance vs. CMOD at different values of $\sigma_{ref}/\sigma_{0.2}$

7.6 Discussion

The PD technique is not suitable for measuring crack blunting. This is because it is not just sensitive to the shape of the crack tip, but the entire strain field. The 'load' method of interpreting PD data from fracture toughness tests therefore overestimates the cack extension due to blunting and underestimates J_{IC} and is not fit for purpose. For high constraint geometries such as C(T) specimens manufactured from Type 316H stainless steel the crack extension predicted by this method is overestimated by at least a factor of 4. For lower constraint geometries which experience higher levels of plasticity, this factor can be significantly larger. In general, the extent of the error is likely related to the strain hardening and the strain dependence of the electrical properties of the material.

The PD technique is suitable for measuring stable tearing during which the influence of strain appears to be small. The onset of stable tearing may be identified from where a plot of PD vs COD deviates from linear. The 'COD' method is therefore suitable for interpreting PD data from fracture toughness tests. Experimental measurements based on this technique produce a value of J_{IC} which is consistent with the literature and the predicted stable tearing was also consistent with post-test fracture surface measurements and the compliance technique.

The implementation of the 'COD' method requires SEM images or a suitable blunting line to predict the crack extension prior to the onset of stable tearing. For Type 316H, the blunting

lines in ESIS P2-92 and ISO 12135 provide good approximations whilst the line in ASTM E1820-13 over-predicts the crack extension by approximately a factor of 2. This observation is consistent with the literature [28, 31, 133]. The use of a blunting line rather than experimental measurements appears prudent since in this study both the PD technique and the unloading compliance technique were both subject to errors when measuring blunting, for different reasons. Whilst the compliance technique has been successfully implemented in many previous studies, it is well known that the measurements are extremely sensitive to the configuration of the load train and the loading pins. This is believed to be the source of the error in the present study.

It has also been shown that the sequentially coupled structural-electrical FE tool developed in the previous chapter to predict the influence of strain on PD can be extended to include crack growth. FE results have been compared to experimental measurements from a fracture toughness test with good agreement. The FE confirms that a change in slope on a plot of PD vs. COD corresponds to the onset of crack growth and that the subsequent change in PD is almost entirely due to crack growth.

This FE tool has been used to investigate anecdotal observations from previous studies that the onset of stable tearing can be difficult to identify from a plot of PD vs COD when testing high toughness, high strain hardening materials. The analysis confirmed that the increase in gradient can be masked by gross plasticity in the remaining ligament for such materials. This is an inherent limitation of the ‘COD’ method which cannot be easily overcome. The compliance technique may therefore be more suitable when testing such materials.

Chapter 8: Measuring Creep Crack Initiation and Growth

8.1 Introduction

Creep Crack Initiation (CCI) can occupy a significant portion of a component's life when operating in a high temperature environment [42]. Despite this, it is currently not possible to accurately identify the onset of crack growth in laboratory tests. During a creep crack growth test, any change in PD which occurs after load-up is assumed to be associated with crack growth. Based on this interpretation of the data, the PD technique often predicts immediate crack extension; however, the initial change in PD is most likely due to creep strain rather than crack growth [6].

This chapter investigates whether an increase in gradient on a plot of PD vs. CMOD can be used to identify the onset of creep crack growth, similar to the method used to identify the onset of stable tearing during fracture toughness testing. A series of interrupted creep crack growth tests have been performed to determine the PD response before, at and after the onset of crack growth. These experimental observations are supported by predictions from a sequentially coupled FE analysis of a creep crack growth test. This FE based tool has also been used to investigate possible limitations of the proposed methodology.

8.2 Creep Crack Growth Testing Methodology

Two preliminary creep crack growth tests were performed. The first was an interrupted test performed on ferritic P91 steel to investigate the significance of strain on PD during the early stages of a test. The second was a test to failure on ex-service Type 316H stainless steel (cast 55882) to see if an abrupt increase in gradient exists on a plot of PD vs. CMOD. This test also compared the response of the low frequency ACPD system with a typical DCPD system. These preliminary tests were followed by a series of interrupted tests performed on the same cast of Type 316H stainless steel. With the exception of the interpretation of the

PD data, all of these tests have been performed in accordance with ASTM E1457-13 [3]. Details of the test methodology are provided here.

8.2.1 Specimen Geometry

The C(T) specimen geometry is shown in Figure 8.1 and the key dimensions are provided in Table 8.1. An EDM pre-crack with a tip radius of 0.15 mm was used. The specimen was not fatigue pre-cracked to ensure a straight crack front which could be easily modelled using FE. It has been demonstrated that the method of introducing the pre-crack does not significantly influence the steady-state creep crack growth behaviour [135]. It may influence the initiation time, but it is unlikely to change the increase in gradient on a plot of PD vs. CMOD.

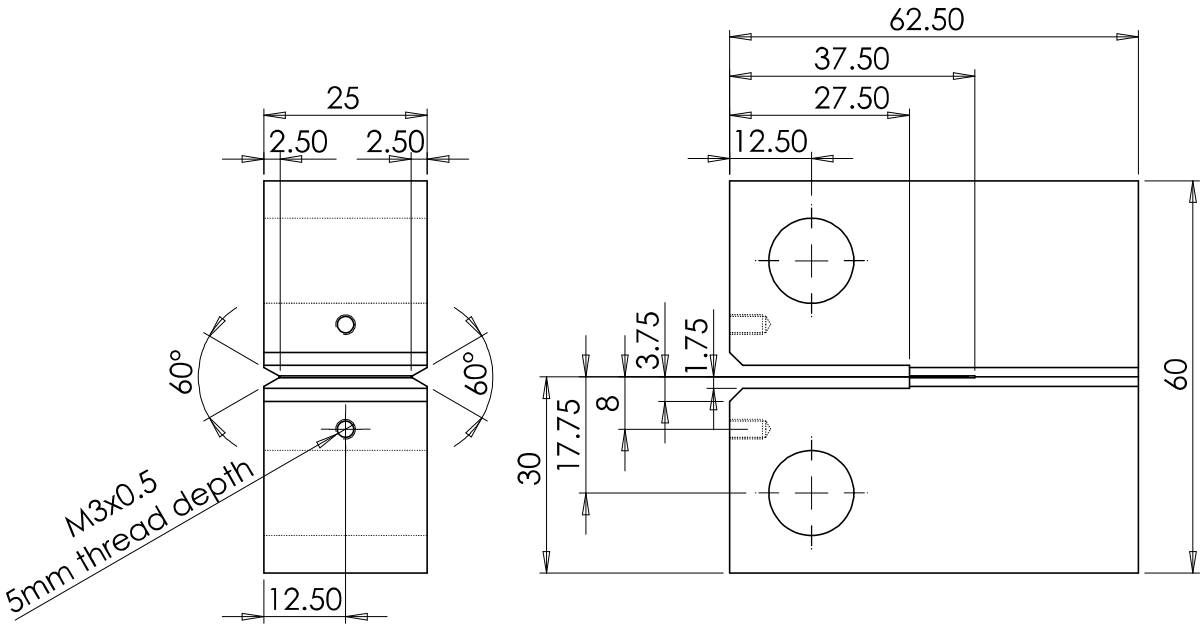

Figure 8.1: Geometry of C(T) specimens used for CCG testing (dimensions in mm)

a_0 [mm]	W [mm]	B [mm]	B_N [mm]
25.0	50.0	25.0	20.0

Table 8.1: Key dimensions of C(T) specimens used for CCG testing.

8.2.2 Materials

CCG tests have been performed on two materials. A preliminary test has been performed on ferritic type P91 steel at 620 ºC and the rest of the tests were performed on ex-service Type 316H stainless steel (cast 55882) at 550 ºC. These are two steels of specific interest to the power generation industry.

8.2.3 Extensometry

For the Type 316H specimens the CMOD was monitored using a single capacitance gauge located in the crack mouth cut-out and the opposite face of the cut-out was used as the target for the gauge. For the test performed on ferritic P91 steel the opposite face of the cut-out could not be used as the target due to significant oxidation so the fixture shown in Figure 8.2 was developed. It was manufactured from Nimonic 80A which is a creep resistant nickel-based superalloy that does not experience significant oxidation at the test temperature of 620 ºC. The gauge fixture was attached to one side of the crack mouth cut-out and the target fixture attached to the other side using the M3 holes shown in Figure 8.1. Two capacitance gauges were mounted on the gauge fixture either side of the specimen. The average measurement from the two gauges was used as the CMOD.

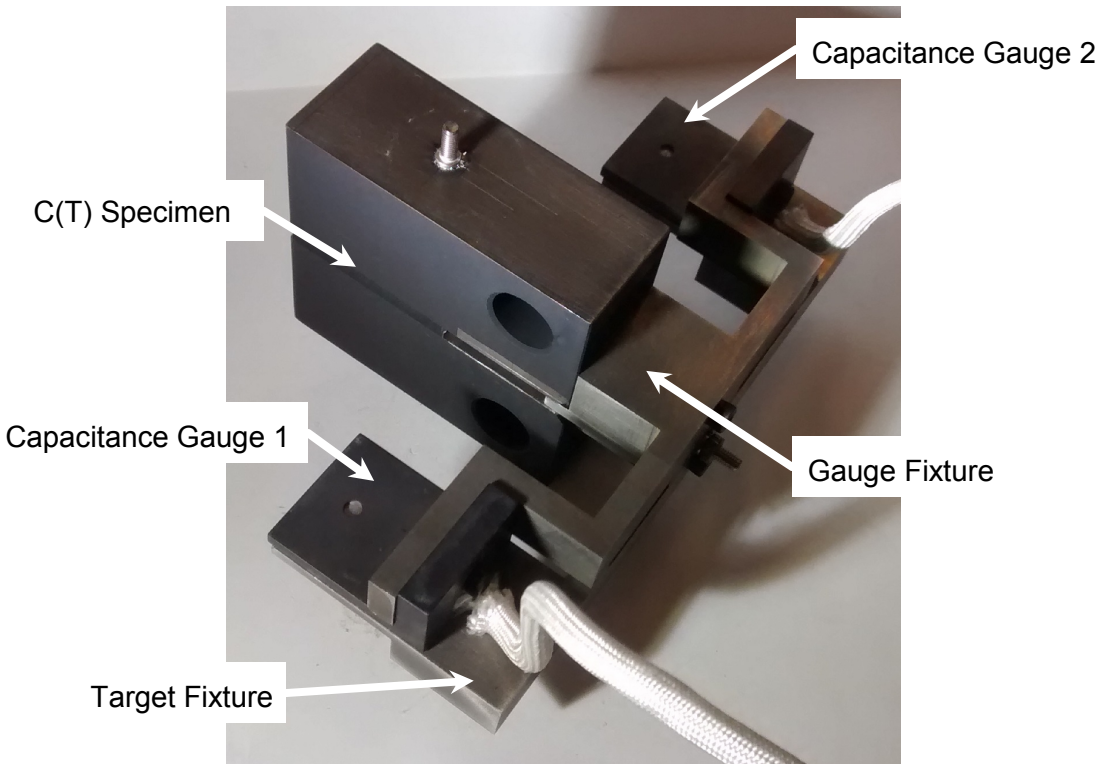

Figure 8.2: Fixture used to measure CMOD for P91 specimen.

8.2.4 Crack Length Monitoring

Crack length was monitored using the PD technique. The PD configuration, selected based on the results of Chapter 4, is shown Figure 8.3. The loading pins and the specimen were coated with high temperature exhaust paint to electrically isolate the specimen from the testing machine and avoid any alternative current paths.

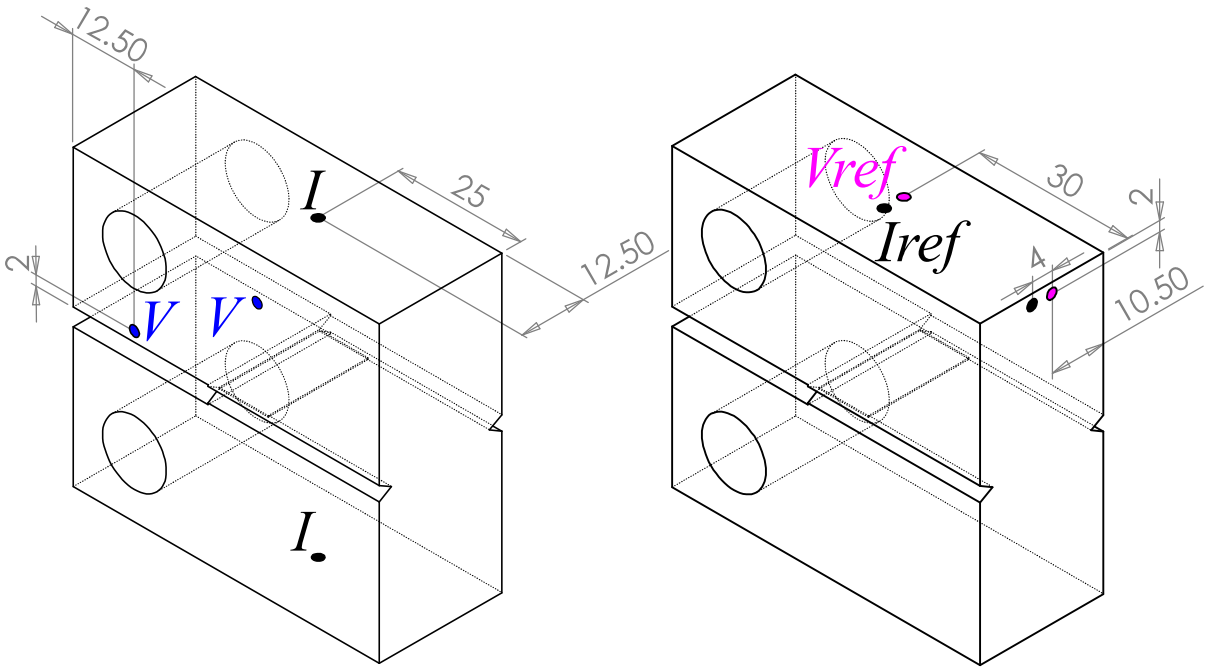

Figure 8.3: PD Configuration for (a) crack length measurement, and (b) reference measurement (dimensions in mm)

A third order polynomial calibration function was derived specifically for this specimen geometry and PD configuration using COMSOL [124] and is provided in Equation (8.1).

$$\frac{a}{W} = 0.034096\left(\frac{R}{R_0}\right)^3 - 0.252180\left(\frac{R}{R_0}\right)^2 + 0.801959\left(\frac{R}{R_0}\right) - 0.083862 \qquad \textbf{(8.1)}$$

The low frequency ACPD system was not suitable for the preliminary test performed on ferritic P91 steel. Although the initial current distribution at the lowest available frequency (2 Hz) was quasi-DC, the application of the initial load increased the magnetic permeability which resulted in a reduction in the signal. This response is typical to high frequency ACPD tests e.g. [79, 99] and is symptomatic of the skin effect. In order to implement the calibration function in Equation (8.1) crack extension was monitored using a DCPD system with a constant current of 20A. For the Type 316H specimens the skin effect is negligible at a frequency of 2Hz so the low frequency ACPD system was used with a constant current of 3mA.

8.2.5 Post-Test Sectioning

After each test the specimen was cut in half to reveal the crack profile along the mid-plane of the specimen. One half of the specimen was sliced up to reveal the profile at 2.5 mm, 5.0 mm and 7.5 mm from the mid-plane. The other half of the specimen was fatigued open to reveal the fracture surface whilst minimising further deformation.

8.3 Preliminary CCG Tests

8.3.1 Preliminary Test 1: Ferritic P91 Interrupted CCG Test

The preliminary CCG test on P91 steel was to investigate the significance of creep strain on the PD measurement in the absence of crack extension. The test was performed at 620 ºC. P91 has relatively high creep ductility of ~32% (mean of four tests performed at 625ºC [136]) so the influence of creep strain is more likely to be significant. The load applied to the specimen was 12.0kN. This results in a reference stress of 93.2MPa, assuming plane strain conditions, which is 39% of the 0.2% proof stress at 620 ºC (240MPa [136]). The influence of plastic strain should therefore be small. The DCPD system used only had a single input channel, so a reference measurement was not taken.

Microstructural evolution of P91 steel at high temperature is a well-documented phenomenon e.g. [137, 138], so the specimen was thermally soaked for 570 hours before the load was applied. This was enough time for the PD signal to stabilise. The load was applied for 1660 hours before the test was interrupted. A plot of relative change in PD against CMOD is provided in Figure 8.4(a). It demonstrates an approximately linear trend with no increase in gradient. The slight reduction in the PD signal corresponding to a CMOD of 0.8 mm corresponds with a small drop in the furnace temperature of ~0.5 °C. The PD measurements have been interpreted according to ASTM E1457-13 [3] and the predicted crack extension is plotted against time in Figure 8.4(b). At the termination of the test, the PD predicts a crack extension of 0.34 mm.

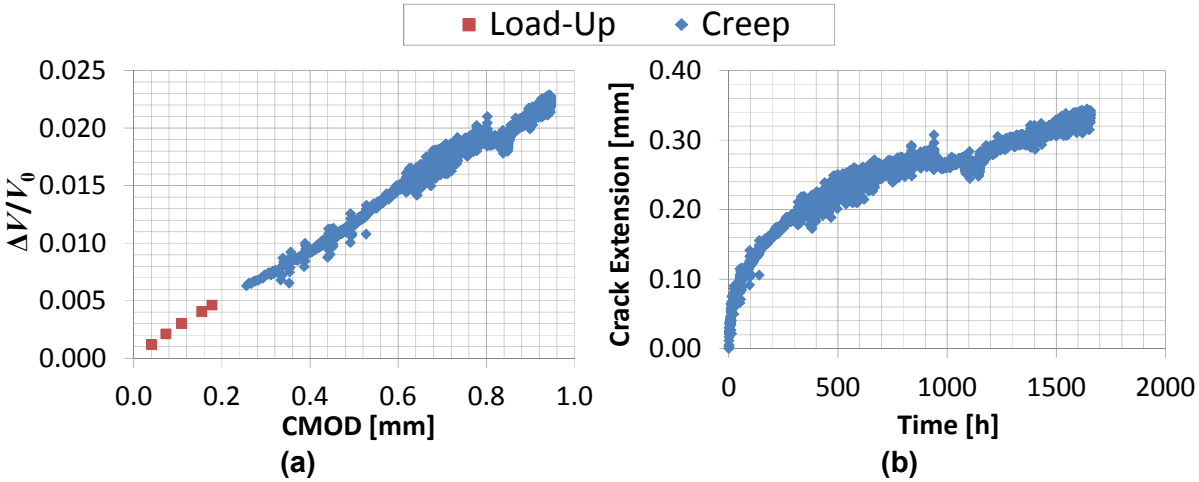

Figure 8.4: Results from an interrupted test performed on a P91 Steel C(T) specimen showing (a) the relative change in PD vs. CMOD, and (b) the crack extension vs. time inferred from this change in PD.

Following the test, the specimen was sectioned as described in Section 8.2.5. The crack profiles at the various points through the thickness are shown in Figure 8.5. There is little evidence of crack extension. The small indications at the crack tip observed in Figure 8.5(b) and (d) are most likely an artefact of the original EDM pre-crack or due to oxidation.

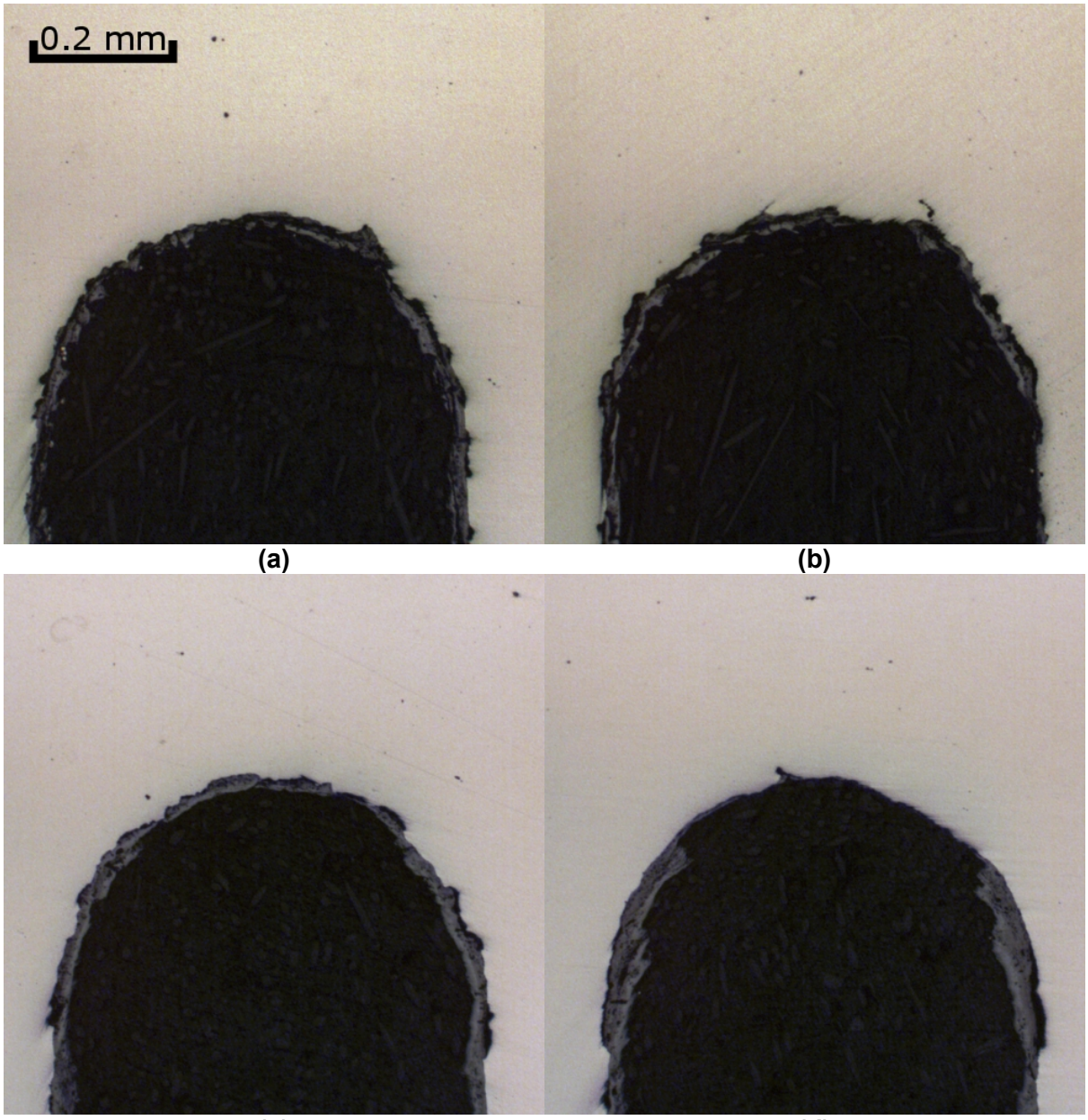

Figure 8.5: Post-test crack profile from the preliminary test performed on P91 steel showing (a) the mid-plane, (b) 2.5 mm from the mid-plane, (c) 5.0 mm from the mid-plane, and (d) 7.5 mm from the mid-plane.

The 0.34 mm crack extension predicted by the PD is much larger than the 0.2 mm used in ASTM E1457-13 as an engineering definition of crack initiation, but Figure 8.5 demonstrates no such crack growth. This demonstrates that the PD technique, as defined in ASTM

E1457-13, can significantly overestimate the early stages of crack growth and underestimate the time to initiate crack growth.

The likely source of this spurious crack extension is creep strain. It is apparent from Figure 8.5 that significant strains have occurred. The diameter of the notch tip is ~0.6 mm which is double that of the original EDM pre-crack. Given that the reference stress is small compared to the 0.2% proof stress, the plastic strain will be small and the majority of this deformation will be due to creep. These results highlight the need for an alternative method of interpreting PD measurements obtained from CCG tests.

8.3.2 Preliminary Test 2: Type 316H CCG Test to Failure

This test was performed to see if an increase in gradient exists on a plot of PD against CMOD which may indicate the onset of crack growth. Crack growth was monitored using DCPD and low frequency ACPD simultaneously to confirm that any change in slope was observed by both systems. The test was continued until final failure to confirm that the AC current distribution remained quasi-DC for the full duration of a test.

The test was performed on Type 316H stainless steel at 550 °C with a load, P, of 24.5 kN. This corresponds to a reference stress of 190 MPa, assuming plane strain conditions, which is approximately equal to the 0.2% proof stress of this cast of material at 550 °C (191.9 MPa [35]). Significant plasticity is therefore expected.

The PD configuration shown in Figure 8.3 was used for the AC and DC systems with the same current injection and PD probe locations used for both. To avoid the need for complex electronics, both current sources were constantly running for the duration of the test. This avoided any temperature fluctuations associated with switching the DC on and off. The lock-in amplifier of the ACPD system filtered out the DC component of the signal. The DCPD system was sensitive to the alternating current however; the 3mA AC was ~4 orders of magnitude smaller than the 20A DC so the effect was small. To further reduce this effect, each DC data point was averaged from 200 measurements taken over a period of ~10 seconds to remove the AC fluctuations.

The relative change in resistance is plotted against CMOD for both PD systems in Figure 8.6. Figure 8.6(a) shows the data for the entire test, and Figure 8.6(b) focuses on load-up and the initial part of the creep phase of the test. Some data is missing due to power failures. The agreement between the low frequency ACPD system and the DCPD system is good. The measurements based on the low frequency AC are slightly lower than the DC, but the difference is small. These results provide confidence that the ACPD system is behaving in a quasi-DC manner for the duration of the test.

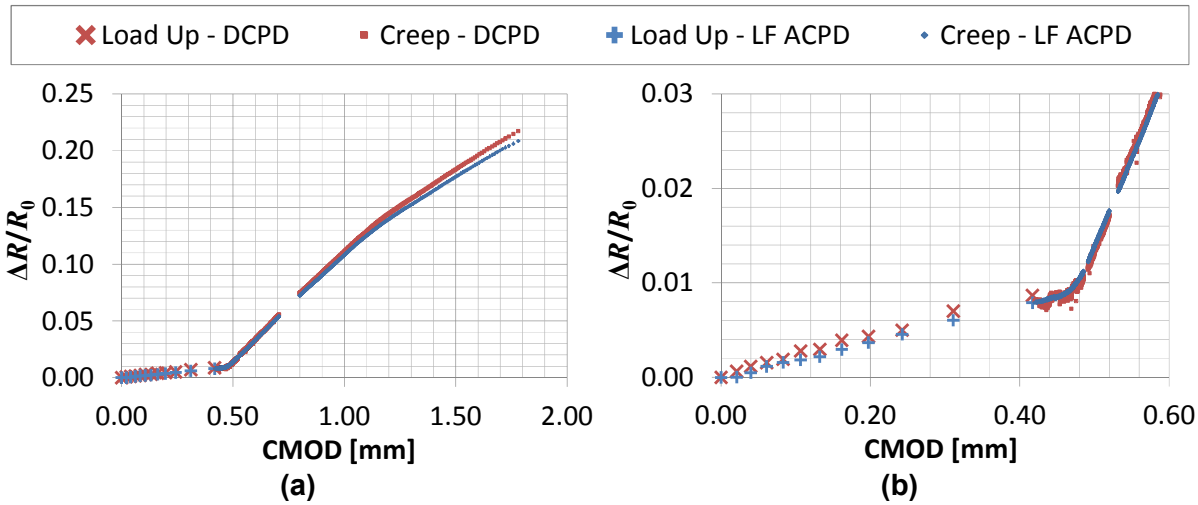

Figure 8.6: Relative change in resistance vs. CMOD measured using DCPD and low frequency ACPD showing (a) all data up to failure, and (b) load-up and the initial part of the creep phase of the test.

During load-up the relationship between the relative change in resistance and CMOD is approximately linear, similar to the trend observed in the previous chapters. This linear trend continues into the creep phase of the experiment until an abrupt increase in gradient is observed at a CMOD of ~0.48 mm. This occurs after ~240hrs and may indicate crack initiation. The increase in gradient is much easier to identify from the low frequency ACPD data because of the increased signal-to-noise ratio.

8.4 Interrupted CCG Tests

To investigate if the increase in gradient observed in the preliminary tests corresponds to the onset of crack growth, a series of interrupted creep crack growth tests have been performed using the low frequency ACPD system to monitor crack extension. These tests were performed on specimens manufactured from ex-service Type 316H (cast 55882) at 550 °C with a load, P, of 24.5 kN. These conditions are nominally identical to the specimen used in the second preliminary test. The tests were interrupted at different stages as detailed in Table 8.2.

Specimen ID	Point of Interruption
CCG316_CT01	Stopped after significant crack growth, prior to final failure.
CCG316_CT02	Stopped after 0.2 mm crack extension predicted by the PD.
CCG316_CT03	Stopped immediately after the increase in gradient on a PD vs. CMOD plot.
CCG316_CT04	Stopped prior the increase in gradient on a PD vs. CMOD plot.

Table 8.2: Point of interruption for each CCG specimen.

8.4.1 Results

Figure 8.7(a) shows the global response of each specimen during the load-up phase of the test and Figure 8.7(b) shows the time dependent response during the creep phase of the test. During load-up, the response of each specimen is very similar which suggests homogenous tensile properties throughout the ex-service material. The response remains similar during the creep phase of the test, within the scatter normally observed during CCG testing.

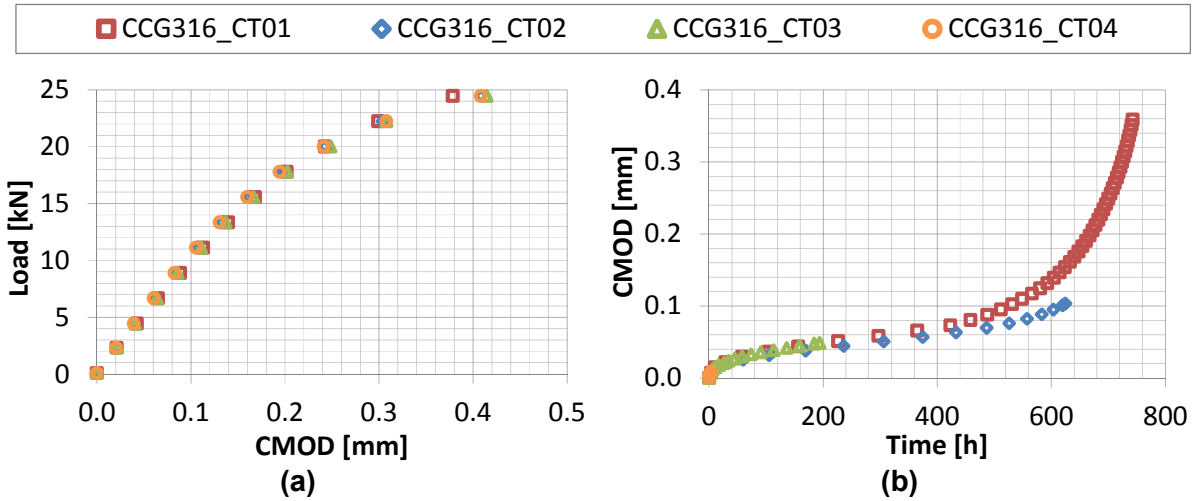

Figure 8.7: Structural response of each specimen during (a) the load-up phase, and (b) the creep phase.

Figure 8.8 shows the relative change in resistance with CMOD for all specimens. Figure 8.8(a) shows all the data whilst Figure 8.8(b) focuses on the initial part of the creep phase.

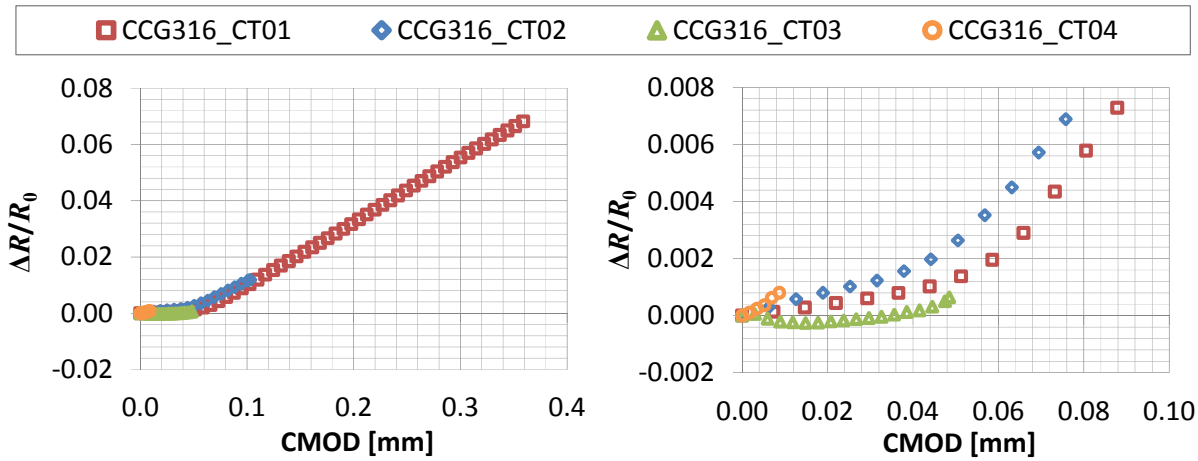

Figure 8.8: Relative change in resistance vs. CMOD during the creep phase of the test for each specimen showing (a) all data, and (b) the early stages of each test.

The data for specimens CCG316_CT01 and CCG316_CT02 are linear either side of the abrupt increase in gradient which occurs at a CMOD ~0.05 mm. The data for specimen CCG316_CT03 is slightly different with a small initial drop in resistance which occurs over the initial 10 hours of the test. This behaviour is not uncommon during creep crack growth testing and is commented on in ASTM E1457 [3] although the cause is not fully understood. After this initial drop the behaviour is similar to specimens CCG316_CT01 and CCG316_CT02 with an approximately linear region before the gradient increases and the test was interrupted.

The initial gradient in Figure 8.8 for all four specimens is different. This is despite very similar structural responses. The gradient for specimen CCG316_CT04 is steepest and is similar to the gradient observed after the change in slope for the other tests. Based on this observation, this test was stopped very early on to see if crack growth had already initiated.

The crack profiles at various points through the thickness are provided for each of these specimens in Figure 8.9, Figure 8.10, Figure 8.11 and Figure 8.12. Significant crack growth was observed for specimens CCG316_CT01 and CCG316_CT02. Due to the inter-granular nature of creep crack growth, the fracture surface for these specimens is not planar. The crack growth is also severely discontinuous, particularly for specimen CCG316_CT02, which is also typical of creep and despite the 20% side grooves some crack tunnelling has occurred. Significant damage ahead of the EDM pre-crack is observed for specimen CCG316_CT03 but this is only connected to the pre-crack at the mid-plane of the specimen. No crack growth and very little damage were observed for specimen CCG316_CT04 despite the notable steeper gradient in Figure 8.8.

The cause of the initial steep gradient observed for specimen CCG316_CT04 is not known. One possibility is that the unknown mechanism which sometimes causes the reduction in PD in the early stages of creep may also, in some instances cause an increase in PD. This would normally go unnoticed when the PD data is interpreted using the standard method in ASTM 1457-13 and would simply be interpreted as additional crack extension.

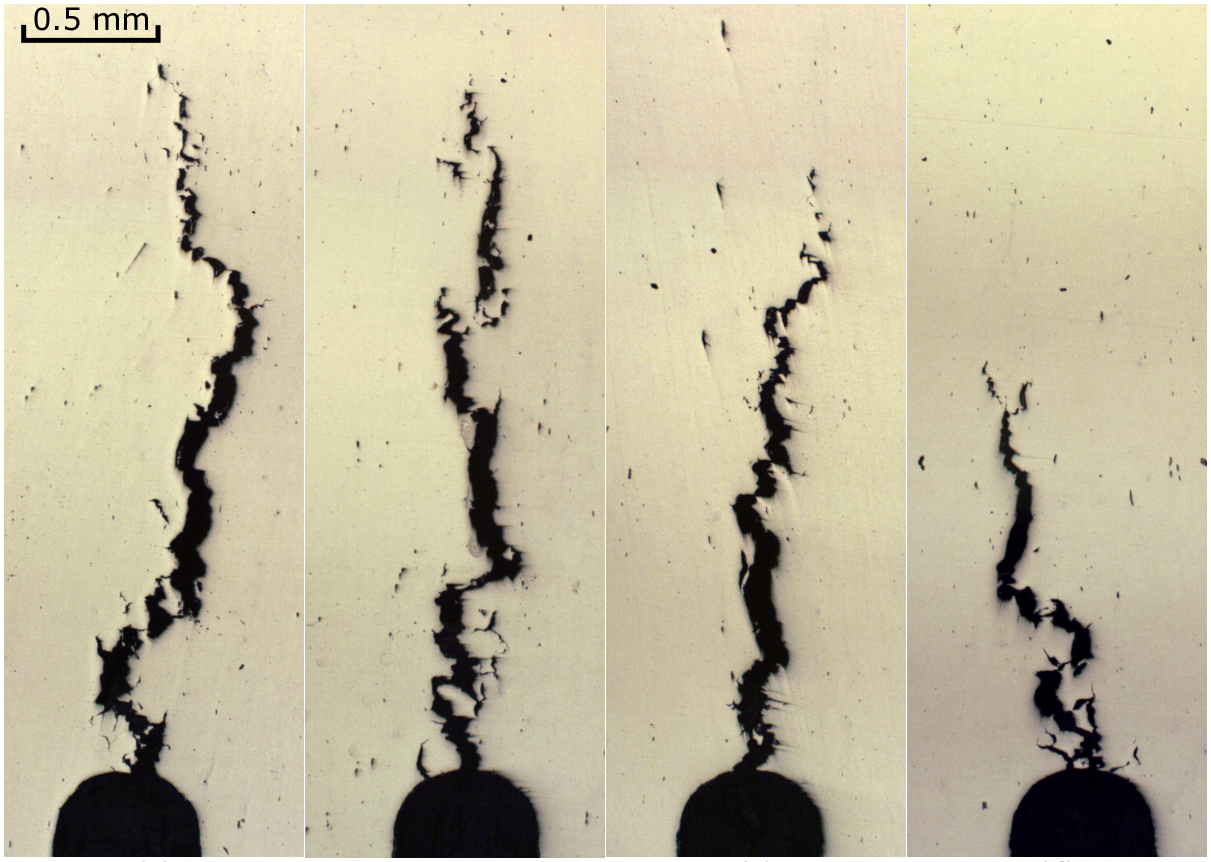

(a) (b) (c) (d)

Figure 8.9: Crack profile of specimen CCG316_CT01 at (a) the mid-plane, (b) 2.5 mm from the mid-plane, (c) 5.0 mm from the mid-plane, and (d) 7.5 mm from the mid-plane.

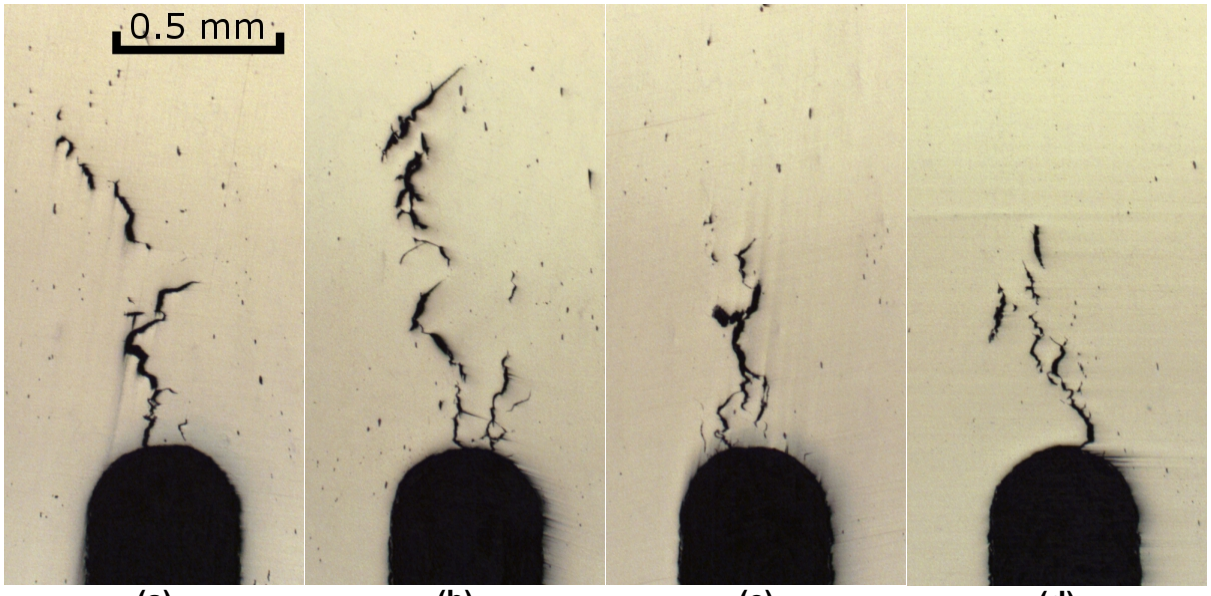

(a) (b) (c) (d)

Figure 8.10: Crack profile of specimen CCG316_CT02 at (a) the mid-plane, (b) 2.5 mm from the mid-plane, (c) 5.0 mm from the mid-plane, and (d) 7.5 mm from the mid-plane.

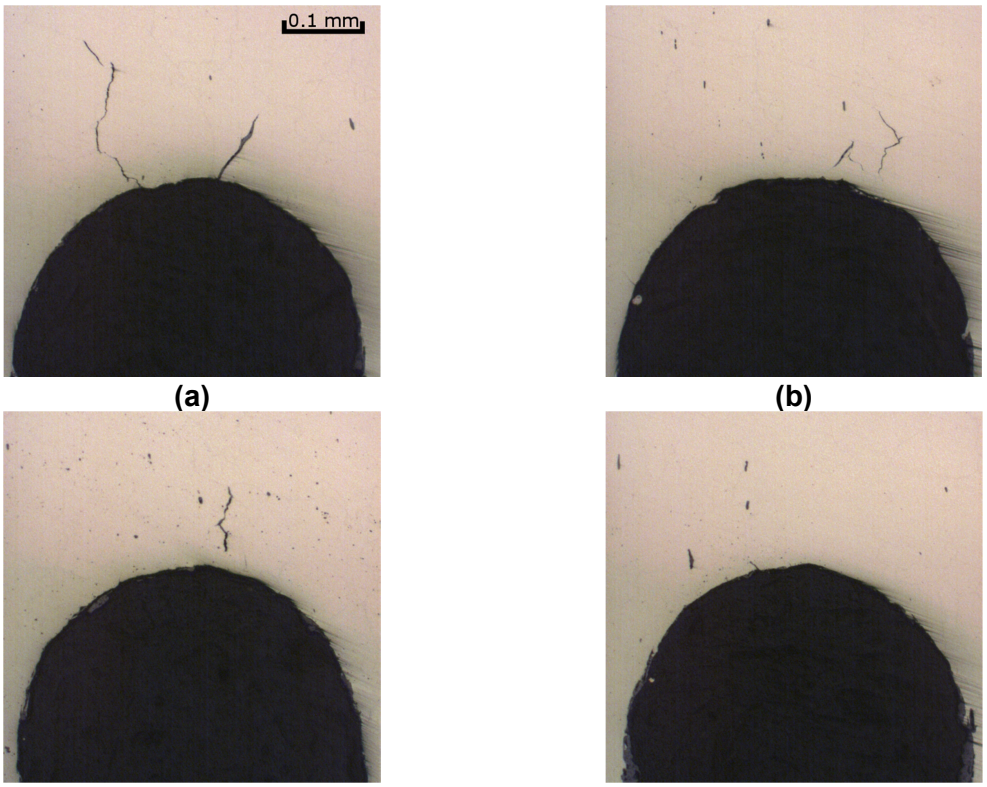

Figure 8.11: Crack profile of specimen CCG316_CT03 at (a) the mid-plane, (b) 2.5 mm from the mid-plane, (c) 5.0 mm from the mid-plane, and (d) 7.5 mm from the mid-plane.

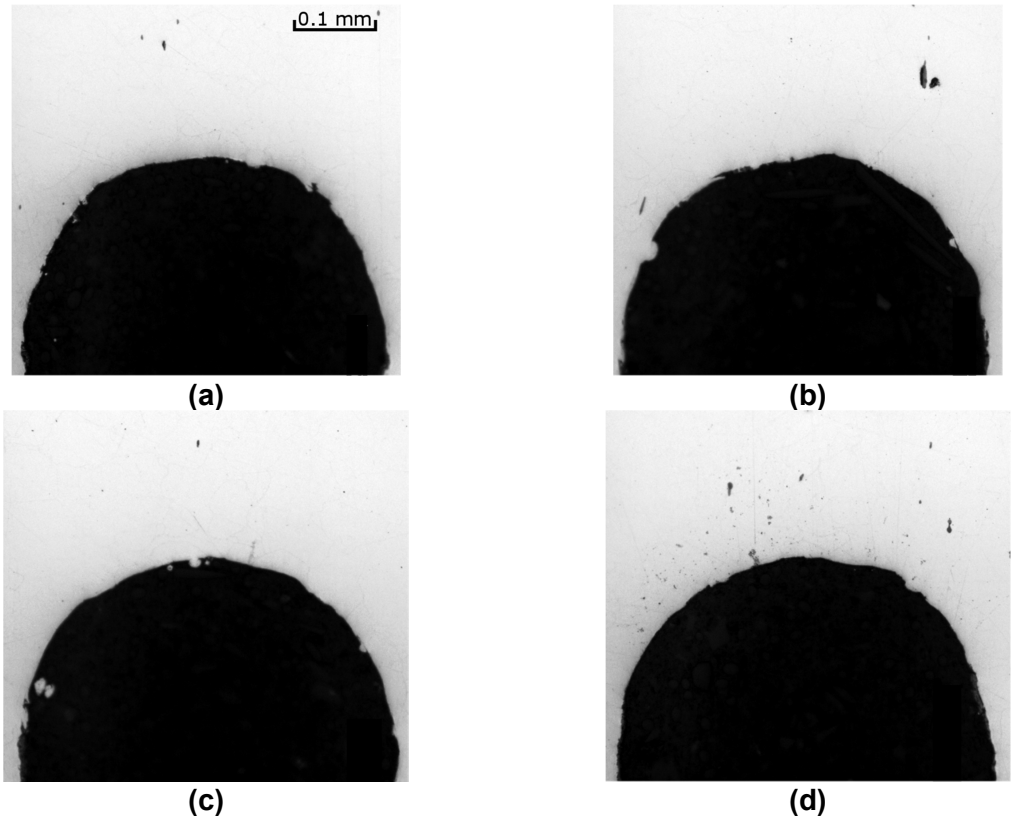

Figure 8.12: Crack profile of specimen CCG316_CT04 at (a) the mid-plane, (b) 2.5 mm from the mid-plane, (c) 5.0 mm from the mid-plane, and (d) 7.5 mm from the mid-plane.

Figure 8.13 shows the fracture surface for specimens CCG316_CT01, CCG316_CT02 and CCG316_CT03. The fracture surface of specimen CCG316_CT04 is not shown because no crack growth was observed. The mid-plane of the specimen is on the right-hand side of each image, and the side-groove is on the left. The dark, oxidised region ahead of the EDM pre-crack is the region of creep crack growth. This region contains small areas which are not heat tinted. They are most prevalent on specimen CCG316_CT02 which is the specimen most significantly affected by discontinuous cracking (see Figure 8.10) and are likely to correspond to islands of uncracked material which did not oxidise during the test. It is possible that some of the areas which are not heat tinted are due to contact with the opposing face when fatiguing open the specimens after the test but a positive R-ratio (0.1) was used in the fatigue process in an attempt to minimise this.

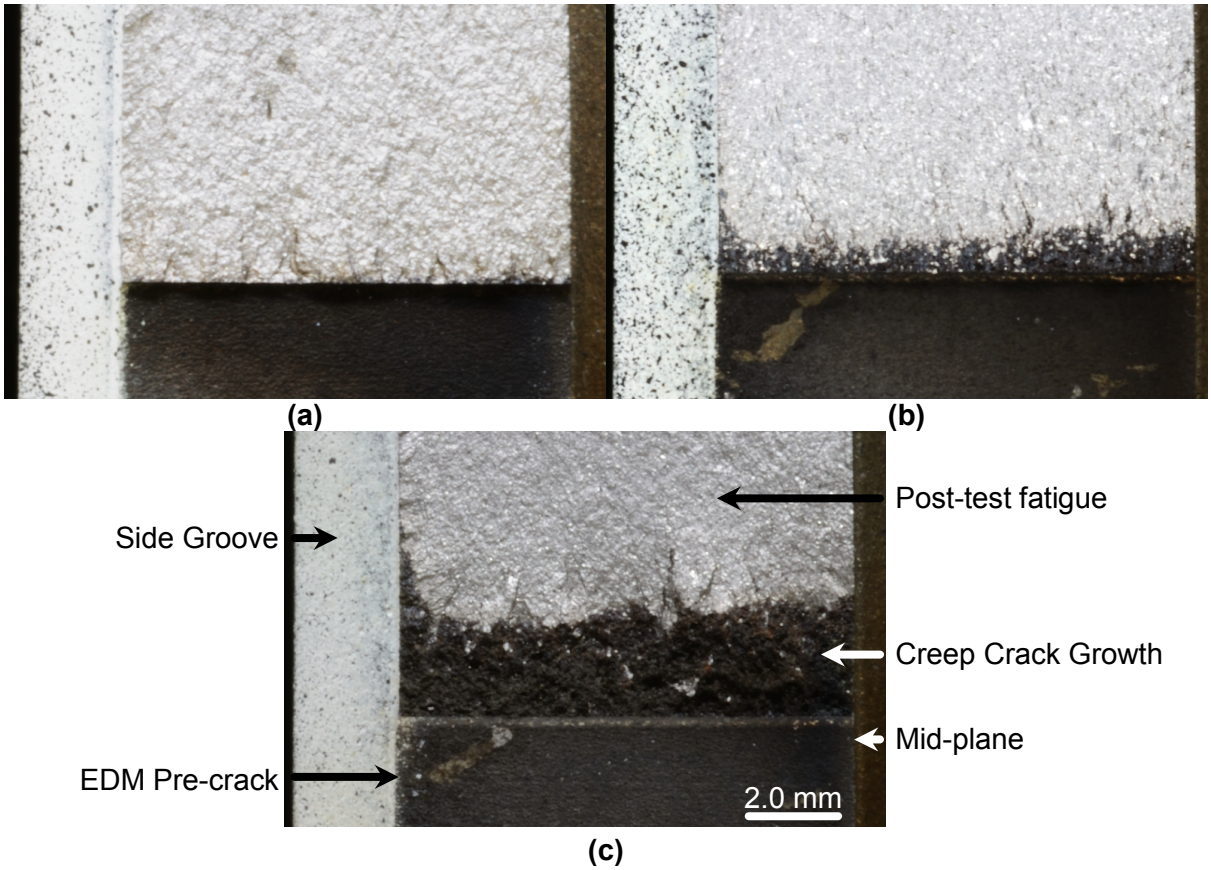

Figure 8.13: Fracture surface of specimens (a) CCG316_CT03, (b) CCG316_CT02, and (c) CCG316_CT01.

The average final crack extension, Δa_f, measured from the fracture surface using image processing software [139], is provided in Table 8.3. The crack extension for specimen CCG316_CT03 is from a small, localised region of creep crack growth close to the mid-plane

of the specimen which is consistent with observations from the crack profiles in Figure 8.11. Also provided in the same table are the crack extensions at the mid-plane, measured from the fracture surface, $\Delta a_{f\_mid\_fract}$, and the length of the crack at the mid-plane measured from the crack profiles in Figure 8.9(a), Figure 8.10(a) and Figure 8.11(a), $\Delta a_{f\_mid\_profile}$. The crack extensions determined from the crack profiles include the discontinuities ahead of the main crack tip. The two measurements of crack length at the mid-plane are in good agreement which suggests that whilst the crack appears discontinuous from the profile, these discontinuities are linked to the main crack in other planes which allows the apparent discontinuities to oxidise.

Specimen	Δa_f [mm]	$\Delta a_{f\_mid\_profile}$ [mm]	$\Delta a_{f\_mid\_fract}$ [mm]
CCG316_CT01	2.44	2.64	2.69
CCG316_CT02	0.62	0.99	0.96
CCG316_CT03	0.01	0.20	0.17
CCG316_CT04	0.00	0.00	0.00

Table 8.3: Post-test crack length measurements.

8.4.2 Interpretation of the PD Data

An abrupt increase in gradient on a plot of resistance (or PD) against CMOD appears to correspond to crack initiation as demonstrated by the fracture surface and crack profile observations of specimen CCG316_CT03. This test was interrupted immediately after the increase in gradient and significant damage, in the form of micro-cracks, is observed, but they are only linked to the EDM pre-crack at the mid-plane. This is the location of highest constraint and the most likely location for crack initiation to occur. This suggests that the test was interrupted shortly after the onset of crack growth as defined by the point at which damage first links up with the pre-crack. Conversely, no crack growth was observed for specimen CCG316_CT04 which did not demonstrate an increase in gradient, despite a notable increase in PD. This is consistent with the preliminary test performed on P91.

To determine crack extension, from the PD data a value of the normalising resistance, R_0, must be determined for the calibration function. Assuming that the increase in gradient corresponds to the onset of crack growth, it is proposed that the resistance at this point is the most appropriate value. This will remove any change in resistance due to strain which occurs prior to crack initiation from the calculation of crack growth. This includes plastic strains which occur during load-up and creep strains which occur during the incubation period. This approach is analogous to the 'COD' method used to measure stable tearing

during fracture toughness testing and assumes that after the onset of crack growth the influence of any additional strain is negligible. To determine how this method of interpreting the PD data will influence the results of a creep crack growth test, the data from the three tests for which crack growth occurred has been interpreted twice. Once using the current method in ASTM E1457-13 and once using the proposed modified method.

Where the value of R_0 has been derived based on the modified method it is denoted R_{0_MOD} and is determined from the intersection of two linear regressions applied to the data either side of the change in slope as shown in Figure 8.14. For specimen CCG316_CT03, the initial drop in resistance was ignored and the linear regression was applied to the data after this drop as shown in Figure 8.14(c).

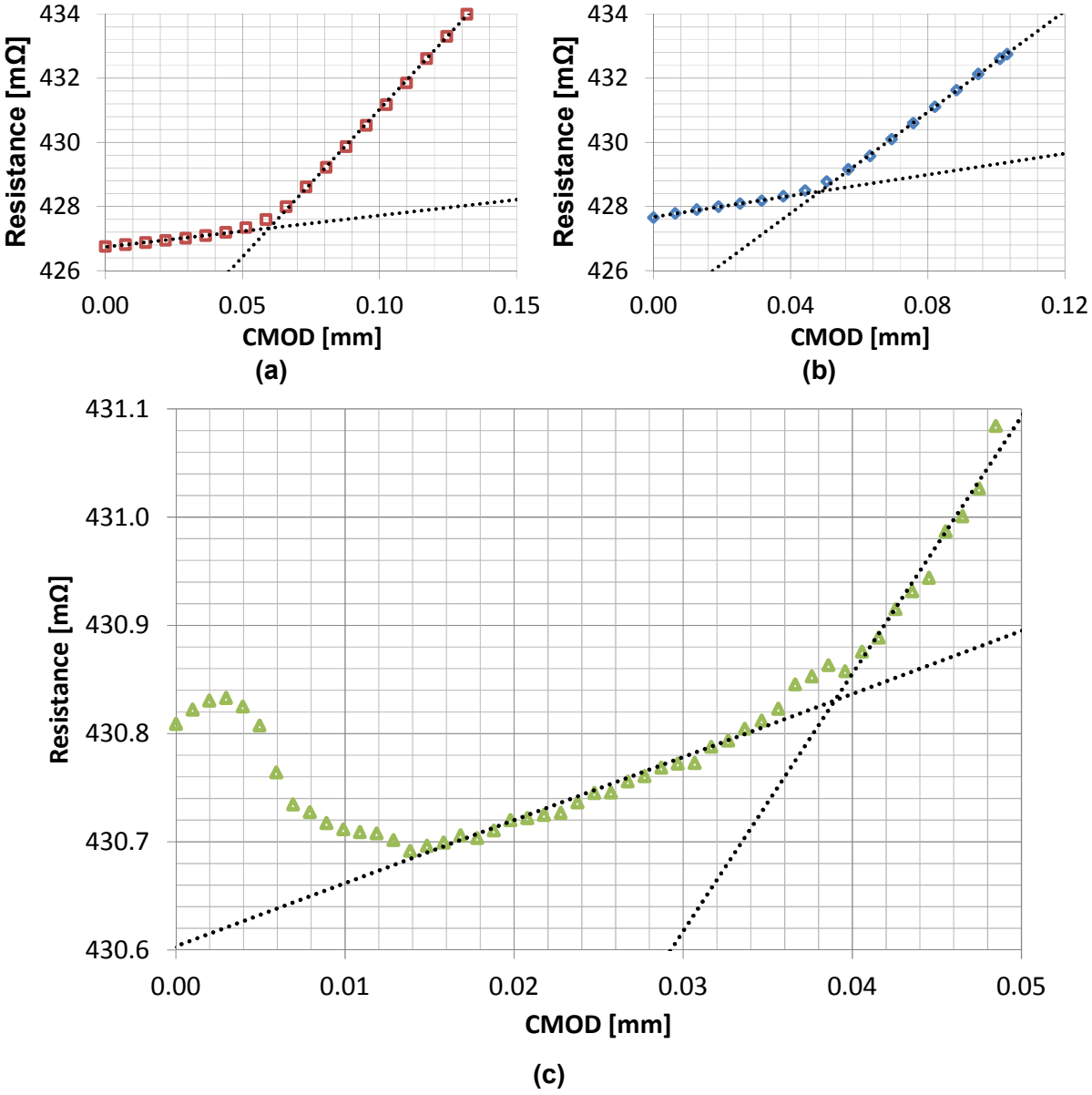

Figure 8.14: Identification of R_{0_MOD} for specimens (a) CCG316_CT01, (b) CCG316_CT02, and (c) CCG316_CT03.

Where the value of R_0 has been derived based on the method in ASTM E1457-13 it is denoted R_{0_ASTM}. According to this standard, R_0 should be taken as the resistance at the start of the creep phase of the test unless an initial drop in resistance is observed in which case the minimum value should be "extrapolated back to zero time". For specimen CCG316_CT03 this has been interpreted as setting R_{0_ASTM} equal to the minimum resistance in Figure 8.14(c).

The values of R_{0_ASTM} and R_{0_MOD} for each of the specimens are summarised in Table 8.4 along with the final resistance measurement, R_f. Also included in this table, are the predicted final crack extensions based on these resistances, Δa_{pf_ASTM} and Δa_{pf_MOD}, and the average crack extension measured from the fracture surface, Δa_f.

Specimen ID	R_{0_ASTM} [mΩ]	R_{0_MOD} [mΩ]	R_f [mΩ]	Δa_{pf_ASTM} [mm]	Δa_{pf_MOD} [mm]	Δa_f [mm]
CCG316_CT01	426.76	427.36	455.85	1.33	1.30	2.44
CCG316_CT02	427.65	428.47	432.74	0.24	0.20	0.62
CCG316_CT03	430.69	430.83	431.08	0.02	0.01	0.01

Table 8.4: Inputs to crack length calculations

For specimens CCG316_CT01 and CCG316_CT02, the crack growth predicted from the PD is significantly less than the value measured from the fracture surface, independent of the method of interpreting the PD data. For specimen CCG316_CT01 the PD predicts approximately half of the crack extension measured from the fracture surface and for specimen CCG316_CT02 this reduces to a third. According to ASTM E1457-13, which allows a maximum discrepancy of 15% between the predicted crack length and the fracture surface measurements, these tests are invalid. The most likely causes of these discrepancies are discontinuous cracking and asperities on the fracture surface, both of which can be observed from the crack profiles. These prevent clean separation of the crack faces and provide alternative paths for the current which will reduce the measured resistance and the predicted crack length [76, 78]. This crack morphology is typical of creep, which suggests that many tests will be rendered invalid in accordance with ASTM E1457-13.

The main output from a CCG test is a correlation between some parameter which characterises the crack tip conditions and the crack growth rate. The analytical models used to calculate the crack tip parameter assume a sharp, straight fronted, continuous crack which is very different from the crack profiles shown in Figure 8.9 and Figure 8.10. The interaction of the main crack and the discontinuities ahead of it will be extremely complex so the accurate determination of an 'effective' crack size is not practical. A conservative interpretation of the test data is therefore required.

The crack extension is typically small compared with the overall crack length, so the calculated crack growth rate is significantly more sensitive to the crack extension measurement than the parameter which characterises the crack tip. A conservative correlation should therefore be obtained by overestimating the crack extension. The length of the heat tinted region at the mid-plane of the specimen is in good agreement with the distance from the EDM pre-crack to the tip of the discontinuous crack measured from the crack profile at the same location. This suggests that the average crack length measured from the fracture surface, Δa_f, includes most of the discontinuities ahead of the crack tip and is effectively an upper-bound envelope of the crack size. ASTM E1457-13 provides a linear correction for the PD data based on measurements from the fracture surface. If the errors in the PD measurement vary approximately linearly with crack extension, this linear correction should produce conservative results for all intermediate crack lengths. This approach has been demonstrated to accurately suppress errors due to electrical bridging across the crack faces for stress corrosion cracking [76].

The subsequent analysis of the results is based on crack extensions which have been corrected based on the fracture surface measurements. Figure 8.15 compares the corrected crack extension for the ASTM and modified methods of interpreting the PD data for specimens CCG316_CT01 and CCG316_CT02. For both specimens, the ASTM method predicts immediate crack growth whilst the modified method demonstrates a period of incubation. At the point of initiation, as predicted by the modified method, the ASTM method predicts 0.05 mm and 0.10 mm of crack extension in specimens CCG316_CT01 and CCG316_CT02 respectively. This is most likely spurious crack growth caused by the accumulation of creep strains during incubation.

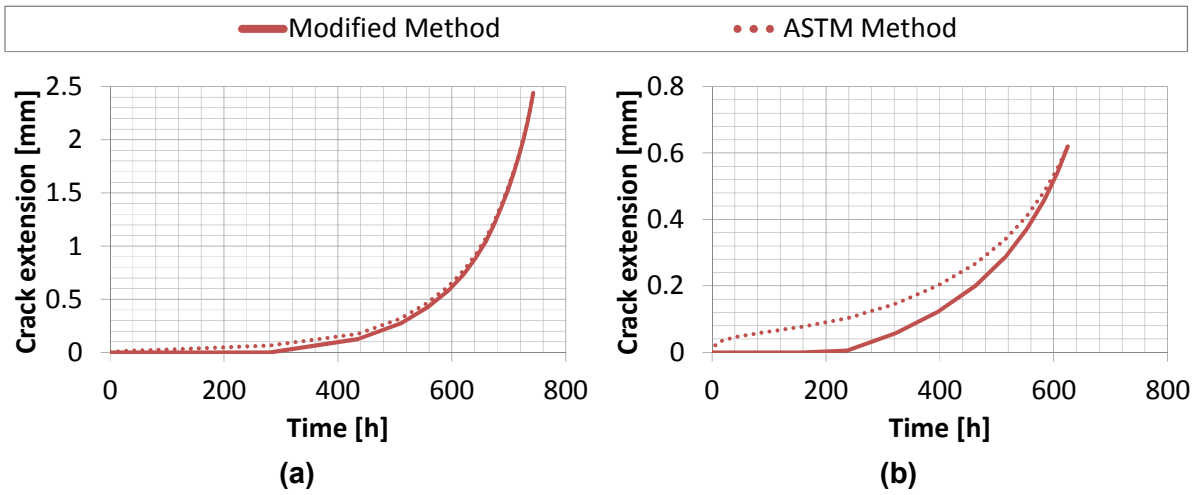

Figure 8.15: Corrected crack extension for (a) specimen CCG316_CT01, and (b) specimen CCG316_CT02

The initiation times for both methods of interpreting the PD data are summarised in Table 8.5 along with the experimental transition times, t_T. The onset of crack growth is denoted t_0^{ASTM} and t_0^{MOD} for the ASTM and modified methods respectively. The corresponding times for 0.2 mm of crack growth are denoted $t_{0.2}^{ASTM}$ and $t_{0.2}^{MOD}$.

Specimen ID	t_T [h]	t_0^{ASTM} [h]	t_0^{MOD} [h]	$t_{0.2}^{ASTM}$ [h]	$t_{0.2}^{MOD}$ [h]
CCG316_CT01	141	0	237	450	478
CCG316_CT02	192	0	226	396	463
CCG316_CT03	N/A	8	94	N/A	N/A

Table 8.5: Comparison of incubation times

There is a significant difference in the times corresponding to the onset of crack growth measured by the two methods. This is because the ASTM method assumes the onset of crack growth occurs at the start of the test unless there is an initial drop in PD in which case initiation corresponds to the time of the minimum PD value. The modified method predicts the onset of crack growth after ~230 hours for tests CCG316_CT01 and CCG316_CT02. For test CCG316_CT03, it is predicted to occur after approximately half this time. This difference is typical of the scatter often seen in creep crack initiation data.

Despite this difference in the onset of crack growth, the times for 0.2 mm of crack extension to occur, as measured by the two methods, are very similar as a result of the rapidly increasing crack growth rate shown in Figure 8.15. The modified method predicts it takes 6% longer than the ASTM method in specimen CCG316_CT01 and 17% longer for specimen CCG316_CT02. Although these differences are relatively small, the preliminary test performed on P91 steel has demonstrated that this is not always the case. The ASTM method predicted 0.2 mm of crack extension after ~350 hours whilst the test was interrupted after 1660 hours with no apparent crack growth which is almost a factor of 5 different.

The difference in behaviour between the two materials is because Type 316H stainless steel at 550 ºC has a creep ductility of ~11% [8] whilst P91 at 620 ºC has a much higher creep ductility of ~32% [136]. Assuming crack initiation occurs when this ductility is exhausted the PD system will measure larger spurious crack extensions due to creep in a P91 specimen. The difference in creep strain between the two specimens can be observed qualitatively by comparing the final diameter of the EDM pre-crack measured from the post-test crack profiles. For the Type 316H specimen it is ~0.45 mm, as measured from Figure 8.11, and for the P91 specimen it is ~0.60 mm, as measured from Figure 8.5. Both specimens initially had nominally identical ~0.30 mm EDM pre-cracks. The total strain at the crack tip is

therefore much larger in the P91 specimen despite larger plastic strains in the Type 316H specimen.

The crack growth rates for specimens CCG_CT01 and CCG_CT02, have been correlated with the crack tip parameter C* in Figure 8.16(a) and Figure 8.16(b) respectively. Both methods of analysing the PD data are shown. For both specimens the method of interpreting the PD data has a minimal influence on the steady state crack growth rates with both data sets lying approximately on top of each other. The main difference is in the so-called "tail" region with only the ASTM method predicting a sizable tail. This demonstrates that, for this material, the tail is mainly due to strain effects rather than crack growth. The difference in the steady-state crack growth rates would be more significant for materials with higher creep ductility.

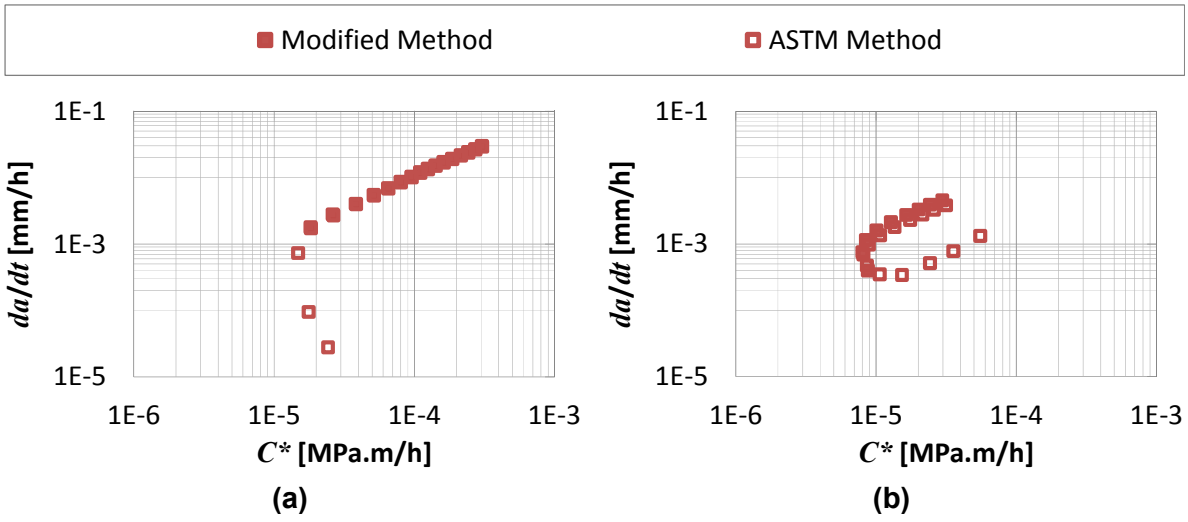

Figure 8.16: Correlation between crack growth rate and C^* for (a) specimen CCG316_CT01, and (b) specimen CCG316_CT02

8.5 Finite Element Investigations

A modified method of interpreting the PD data from a creep crack growth test has been proposed. To investigate possible limitations associated with this approach, a sequentially coupled structural-electrical FE model will be used. This FE based approach was developed in Chapter 6 for a stationary crack and extended to include crack extension in Chapter 7. In this chapter it will be extended further to include creep and validated against the experimental measurements obtained from specimen CCG316_CT01. It will then be used to investigate possible limitations the proposed method.

It was confirmed in the previous chapter that the increase in gradient on a plot of resistance (or PD) against COD can be difficult to identify during fracture toughness testing of high toughness, high strain hardening materials. This is because the additional load which

accompanies an increment in crack length produces a large change in COD which can mask the increase in gradient. This is analogous to a creep crack growth test performed on a material with very high creep ductility where the large creep strains which accompany crack growth may act in a similar manner. The influence of creep ductility on the ability to observe an increase in gradient will therefore be investigated.

An additional complication associated with creep crack growth testing is stress redistribution which occurs prior to attaining steady-state conditions. This stress redistribution is likely to influence the PD response and could also obscure the change in slope. The influence of stress redistribution on the PD response will also be investigated.

8.5.1 Model Validation

8.5.1.1 Geometry and Mesh

Two 3D ¼ models of the C(T) specimen were produced using Abaqus [11]. Model 'CCG_CI' was used to assess the influence of strain on resistance up to the point of crack initiation. Model 'CCG_CG' was used to assess the entire creep crack growth test, including crack growth. The two models are shown in Figure 8.17 and Figure 8.18 respectively. Model 'CCG_CI' includes the 0.15 mm radius EDM pre-crack and a focused mesh to accurately capture the strain field at the crack tip. Model 'CCG_CG' has a uniform mesh at the crack tip to allow 0.1 mm increments of crack growth to be modelled. Due to the increased computational expense of modelling crack growth, a coarser mesh was applied to this model. This mesh was validated by comparing the results of the two models up to the onset of crack growth. Both models used linear brick elements with a summary of the meshes provided in Table 8.6.

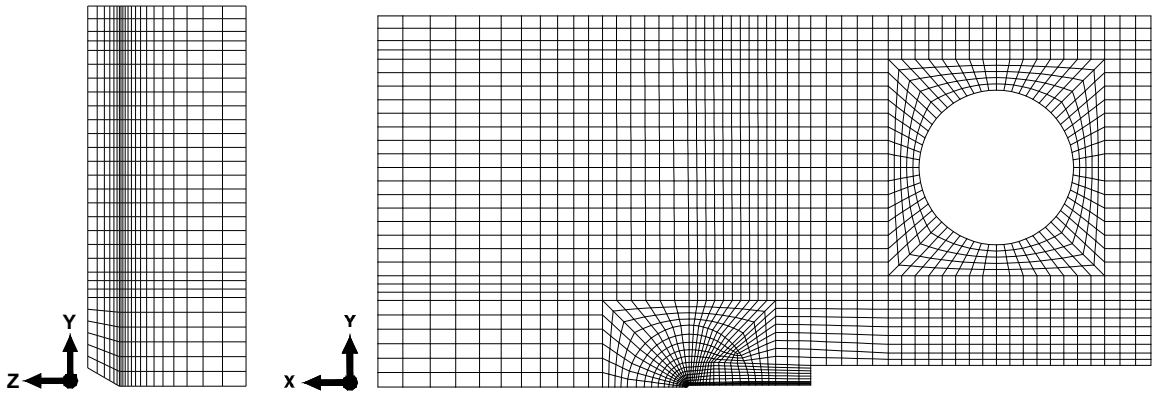

Figure 8.17: FE model 'CCG_CI' used to predict the change in PD up to crack initiation.

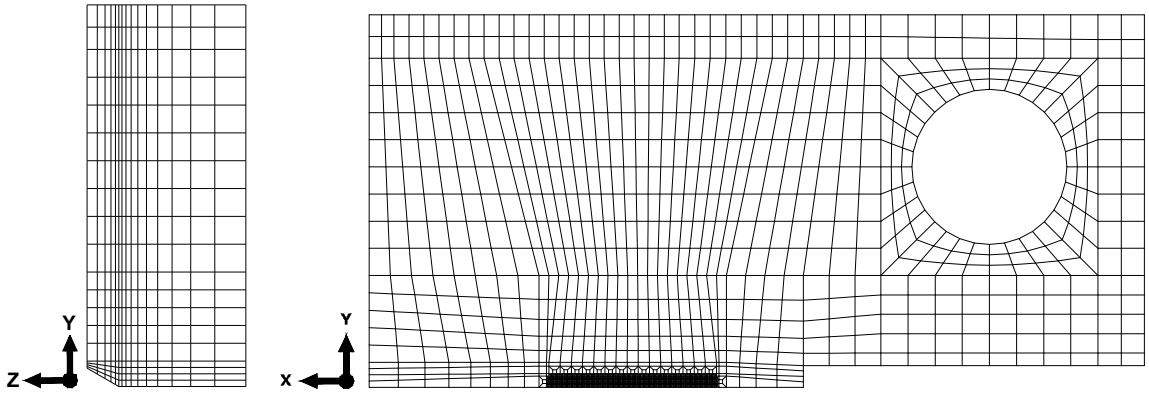

Figure 8.18: FE model 'CCG_CG' used to predict the change in PD including crack growth.

FE Model	Number of Elements	Structural Element Type	Electrical Element Type
CCG_CI	45,300	C3D8R	DC3D8E
CCG_CG	33,810	C3D8R	DC3D8E

Table 8.6: Finite element mesh details

8.5.1.2 Boundary Conditions

8.5.1.2.1 Model 'CCG_CI'

Appropriate boundary conditions were applied to the planes of symmetry. A concentrated force was applied to a node at the centre of the pin hole. This node was free to move in the y direction (the direction of the applied force) and free to rotate about the z axis to simulate pin rotation in the shackles. All other degrees of freedom were constrained. The motion of this node was transmitted to the inside surface of the pin hole in all degrees of freedom via a kinematic coupling. This prevented the hole from deforming. The loading pin was not explicitly modelled to reduce computational expense. It has been shown that the strain around the pin hole has a negligible impact on the resistance measurement obtained for a similar PD configuration to the one shown in Figure 8.3. A 12.25kN force was applied to the FE model. This is equivalent to the 24.5kN force applied in the experiments due to symmetry. The structural analysis consisted of two load steps: "load-up" and "creep". It has been assumed that no creep occurs during load-up.

For the electrical analyses a 0 V electrical potential was applied to all nodes on the remaining ligament ahead of the crack (the y plane of symmetry). A point current source

was applied to a node at the current injection location and the electrical potential was measured at a node at the PD probe location. All electrical results are presented in terms of relative change in resistance so they are independent of the magnitude of the applied current and the material resistivity.

8.5.1.2.2 Model 'CCG_CG'

For the structural analysis the method of applying the load and the initial symmetry boundary conditions were the same as for model 'CCG_CI'. The initial two load steps were also the same, but for every 0.1 mm increment of crack growth an additional two steps were included. The first of these was to release a line of nodes parallel to the crack front from the symmetry boundary condition applied to the ligament ahead of the crack. The second was to allow creep to occur before the next 0.1 mm increment in crack length. The rate of crack growth was determined from the experimental data for specimen CCG316_CT01. A comparison of the experimental and FE crack length vs. time is shown in Figure 8.19. The experimental crack length data is corrected based on the post-test fracture surface measurements. This method of simulating crack growth is extremely simplified. It assumes a straight crack front and a continuous, perfectly sharp crack tip.

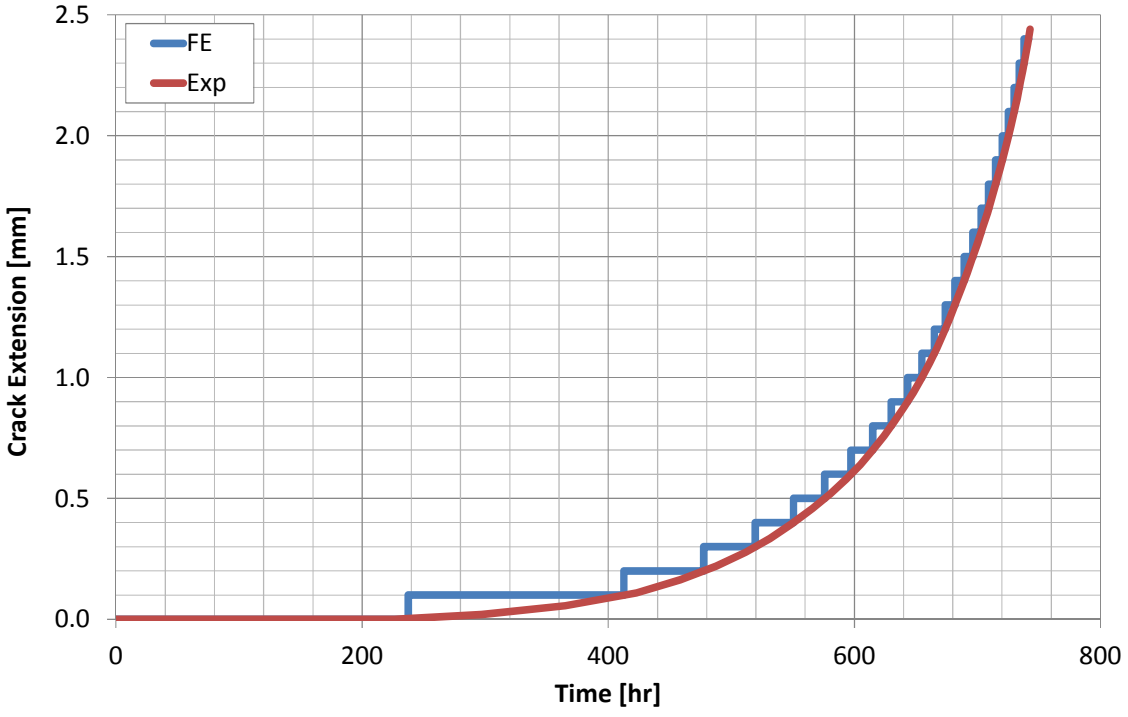

Figure 8.19: Comparison of experimental crack growth with the incremental crack growth applied to FE model 'CCG_CG'.

For the electrical analyses the boundary conditions were similar to those applied to model 'CCG_CI'. The 0V electrical potential applied to all nodes on the remaining ligament ahead of the crack was updated after each crack increment.

8.5.1.3 Material Properties

An elastic modulus, E, of 159.75 GPa and a Poisson's ratio, v, of 0.294 were applied to the structural model. The true plastic stress-strain data is provided in Table 8.7. This tensile data is specifically for cast 55882 of Type 316H and is obtained from the validation section of R6 [35].

True Stress [MPa]	True Strain [mm/mm]
116.2	0.000
191.9	0.002
228.7	0.010
257.2	0.020
332.9	0.050
425.7	0.100
530.8	0.200
606.1	0.300

Table 8.7: True plastic stress-strain data for Type 316H stainless steel (cast 55882).

A primary + secondary creep law, originally derived from Type 316LN creep data, is provided in RCC-MR [7]. The form of this creep law is shown in Equation (8.2):

$$\varepsilon^c = \begin{cases} C_1 t^{C_2} \sigma^{n_1}, & t \le t_{fp} \\ C_1 t_{fp}{}^{C_2} \sigma^{n_1} + C\sigma^n \left(t - t_{fp}\right), & t > t_{fp} \end{cases} \quad \textbf{(8.2)}$$

In this creep law, ε^c is the total creep strain (in mm/mm), C_1, C_2, C, n_1 and n are material constants and t is time (in h). The transition from primary to secondary creep occurs at time t_{fp}. This corresponds to the time at which the primary creep rate is equal to the secondary creep rate and can be calculated from Equation (8.3):

$$t_{fp} = C_3 \sigma^{n_3} \quad \textbf{(8.3)}$$

where:

$$C_3 = \left(\frac{C}{C_1 C_2} \right)^{\frac{1}{C_2 - 1}} \tag{8.4}$$

$$n_3 = \frac{n - n_1}{C_2 - 1} \tag{8.5}$$

At times less than t_{fp} the total creep strain is due to primary creep only, $\varepsilon^c{}_p$. After this the total creep strain is equal to the primary creep strain at the transition time plus a secondary creep component, $\varepsilon^c{}_s$.

The material constants for Equation (8.2) have been derived for Type 316H stainless steel from the uniaxial creep tests listed in Table 8.8.

Test ID	Header	Cast	Stress [MPa]	t_{fp} [h]	$\dot{\varepsilon}_s^c$ [h^{-1}]	Reference
G9	1C2/3	55882	318	300	5.42×10^{-6}	Bettinson [135]
G12	1C2/3	55882	359	120	6.10×10^{-5}	Bettinson [135]
G14	2D2/2	55882	349	160	4.18×10^{-5}	Bettinson [135]
G16	2D2/2	55882	366	100	7.11×10^{-5}	Bettinson [135]
CBB	2D2/2	55882	290	290	5.74×10^{-6}	Bettinson [135]
CBC	2D2/2	55882	308	308	1.02×10^{-5}	Bettinson [135]
A1-1	1B1/1	53415	335	82	1.95×10^{-4}	Mehmanparast [140]
A1-2	1B1/1	53415	300	198	4.43×10^{-5}	Mehmanparast [140]
A1-3	1B1/1	53415	290	N/A	1.19×10^{-5}	Mehmanparast [140]
A1-4	1B1/1	53415	280	598	1.26×10^{-5}	Mehmanparast [140]
A1-5	1B1/1	53415	257	602	8.50×10^{-6}	Mehmanparast [140]
2-2	unknown	55882	290	745	1.16×10^{-5}	Davies [141]
2-3	unknown	55882	335	38	1.22×10^{-4}	Davies [141]

Table 8.8: Uniaxial creep tests performed on austenitic type 316H stainless steel at 550ºC.

For each test, the data corresponding to the primary and secondary creep regimes was identified from a plot of creep strain vs. time. The transition time for each test is provided in Table 8.8. For each plot of creep strain vs. time the secondary creep rate was obtained from a linear regression fit to the secondary creep data. These secondary creep rates are also provided in Table 8.8. A plot of secondary creep strain rates against nominal stress was used to obtain values for the material constants, C and n in Equation (8.2). This plot is provided in Figure 8.20.

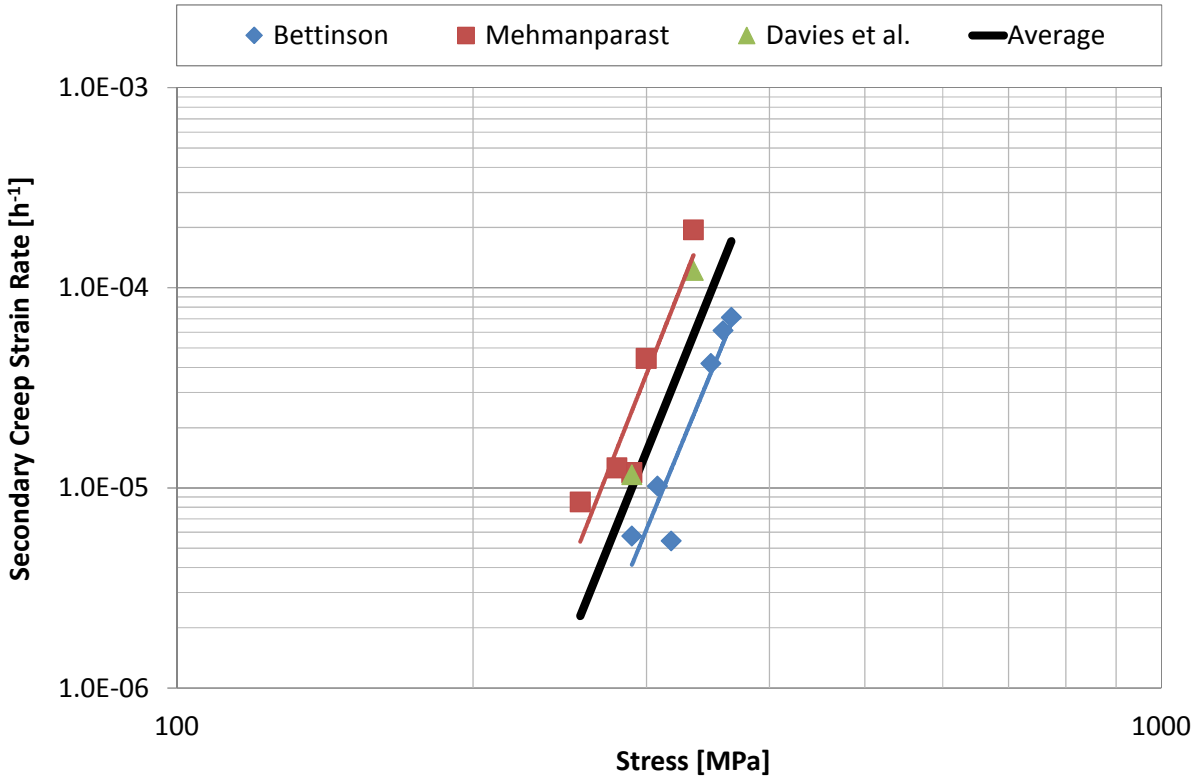

Figure 8.20: Calculation of average secondary creep strain rate for austenitic type 316H stainless steel based on the tests listed in Table 8.8

It is apparent from Figure 8.20 that all three data sets have a similar stress exponent, n, but a different coefficient, C. Due to the different stress ranges for each data set, a power-law regression fit to all the data results in a stress exponent which is much lower than would be predicted by each individual data set and a coefficient which is much higher. To avoid this, separate power-law regression fits were applied to the data from Bettinson [135] and Mehmanparast [140] and an average of these two fits was used. The values of C and n were calculated from Equations (8.6) and (8.7) respectively. A power-law regression fit was not applied to the data from Davies et al. [141] due to the limited number of data points however, it can be seen that this data is in good agreement with the average power law derived from the other two data sets.

$$C = \sqrt{\left(C_{Bettinson} C_{Mehmanparast}\right)} \tag{8.6}$$

$$n = \frac{n_{Bettinson} + n_{Mehmanparast}}{2} \tag{8.7}$$

A similar approach was used to derive the primary creep constants C_1, C_2 and n_1 in Equation (8.2). For each test listed in Table 8.8, the primary creep data was reduced to 10 evenly spaced data points to apply an even weighting to each test. For all tests performed by

Bettinson [135], a surface in the form of the primary component of Equation (8.2) was fitted to the data using the method of least squares. This process was repeated for the tests performed by Mehmanparast [140], and the average values of C_1, C_2 and n_1 were calculated from Equations (8.8), (8.9) and (8.10) respectively.

$$C_1 = \sqrt{\left(C_{1\_Bettinson} C_{1\_Mehmanparast}\right)} \quad \textbf{(8.8)}$$

$$C_2 = \frac{C_{2\_Bettinson} + C_{2\_Mehmanparast}}{2} \quad \textbf{(8.9)}$$

$$n_1 = \frac{n_{1\_Bettinson} + n_{1\_Mehmanparast}}{2} \quad \textbf{(8.10)}$$

The average material constants derived for Type 316H stainless steel at 550 °C are provided in Table 8.9. These material constants were applied to the FE model via a user subroutine which assumed strain hardening conditions. A sensitivity study was used to demonstrate that the difference between strain hardening and time hardening was negligible. When these material properties are applied to a multi-axial stress state, a flow rule similar to that used for plasticity is used to define the deformation.

Parameter	Value
C_1	2.42×10^{-17}
C_2	0.527
n_1	5.374
C	9.05×10^{-36}
n	12.202

Table 8.9: Average creep law coefficients for Type 316H at 550°C. Stress in MPa, time in h.

8.5.1.4 Results

Figure 8.21 compares the structural response of the finite element models with the experimental data for specimen CCG316_CT01 during the load-up phase of the test. The static response of both FE models during load-up is in very good agreement with the experimental data. This provides confidence in the tensile material properties and structural modelling assumptions. It also demonstrates that the differences between the two models (the crack tip acuity and mesh density) do not significantly influence the global response of the specimen during load-up.

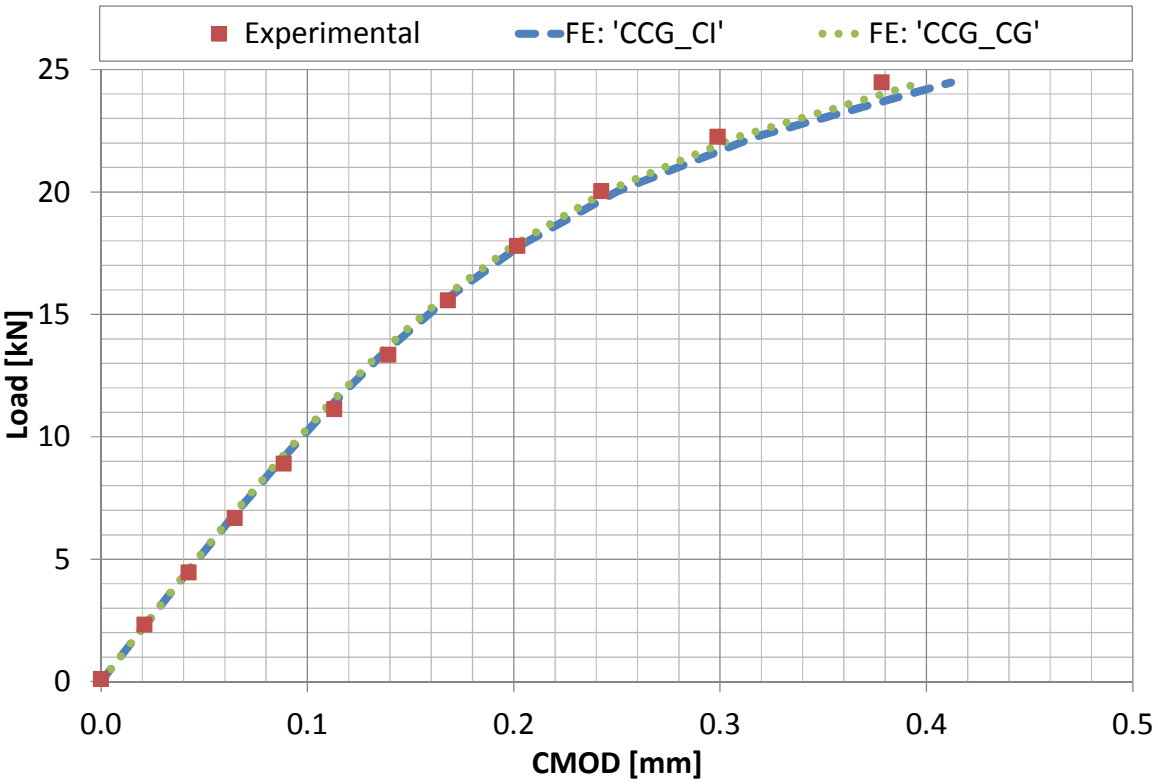

Figure 8.21: Comparison of the structural response of the FE models and the experimental data during load-up.

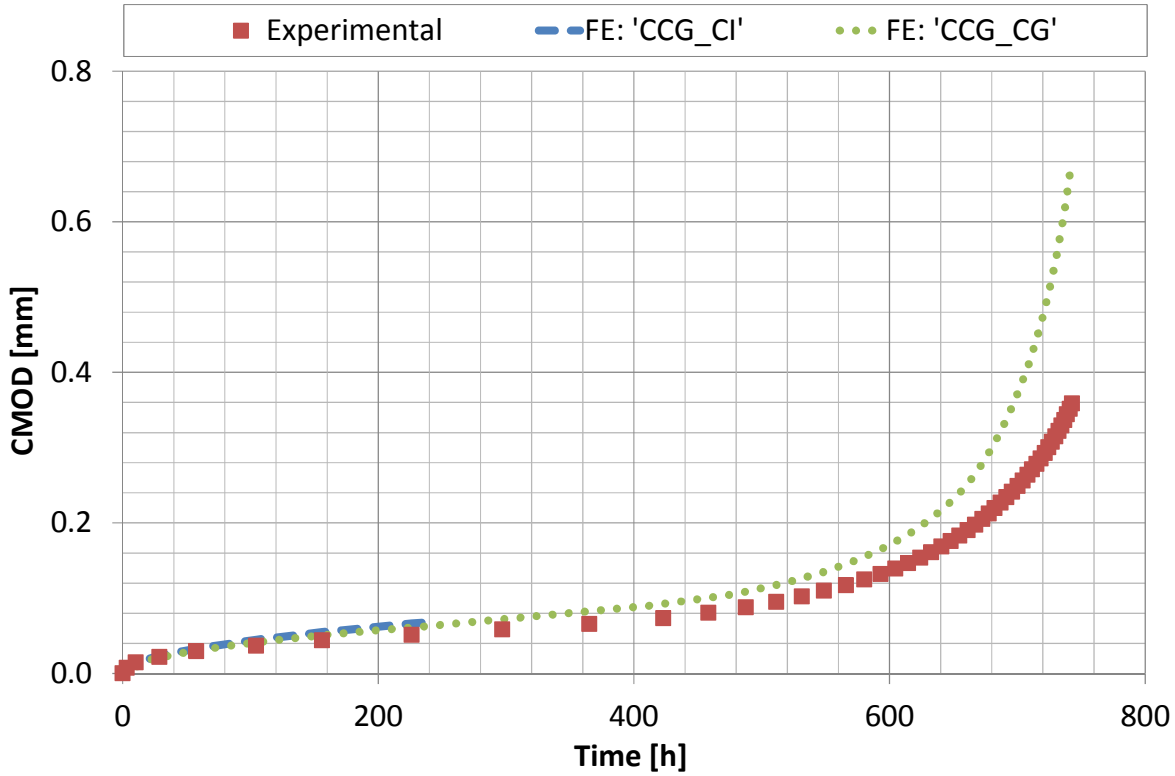

Figure 8.22: Comparison of the structural response of the FE models and the experimental data during load-up.

Figure 8.22 compares the time dependent response of the finite element models with the experimental data during the creep phase of the test. Both FE models are in good agreement with the experimental data up to the onset of crack growth at ~240hrs. This provides confidence in the creep properties derived above and demonstrates that the mesh and geometry differences between the two models do not significantly influence the global time dependent response. A sensitivity study was performed using the creep properties in RCC-MR [7] derived for Type 316LN which resulted in an increase in CMOD over the initial 200hours of ~50%. This difference is small compared to typical scatter observed in creep data thus providing further confidence in the creep properties derived above.

After crack initiation, the CMOD is over-estimated by model 'CCG_CG' compared to the experimental data. The most likely source of this discrepancy is the simplified modelling assumptions with respect to the crack morphology. Uneven crack extension and discontinuous cracking will both reduce the CMOD compared to the continuous, straight fronted crack which is modelled and both of these phenomena have been observed in specimen CCG316_CT01.

This discrepancy could also be due to the interaction between creep and plasticity. In the FE model, they are assumed to be independent, but they are both driven by dislocations. The introduction of dislocations by either of these mechanisms will therefore influence the

subsequent deformation by strain hardening the material [142]. This interaction will be most significant when the crack is growing due to the evolution of the stress and strain fields ahead of the crack however, it is likely to be a secondary effect compared to the significant discontinuous cracking observed experimentally. Scatter in the secondary creep data is unlikely to account for the discrepancy observed in Figure 8.22 because the value of t_{fp}, calculated from Equation (8.3) using the reference stress of 190 MPa, is much greater than the test time.

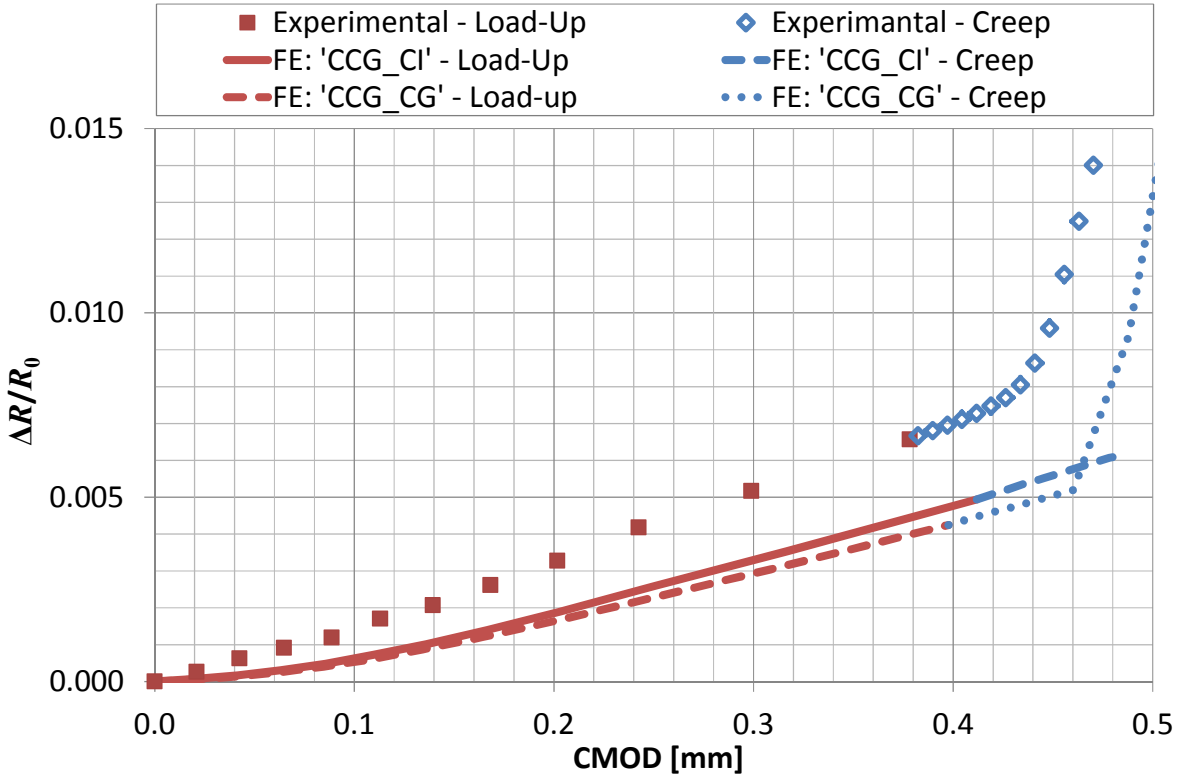

Figure 8.23: Comparison of the electrical response of the FE models and the experimental data during the load-up and early part of the creep phase, including crack initiation.

Figure 8.23 compares the electrical response of both models with the experimental data. It includes load-up and the early stages of creep until just after the onset of crack growth. Prior to any crack growth, the response of both models is similar which confirms that the differences between them (the crack tip acuity and mesh density) do not significantly influence the model behaviour. At the onset of crack growth, model 'CCG_CG' predicts an increase in gradient, similar to the one observed experimentally which supports the proposed interpretation of the PD data. Consistent with previous chapters both models under predict the relative change in resistance due to strain. This is because they do not include the influence of strain on the resistivity of the material.

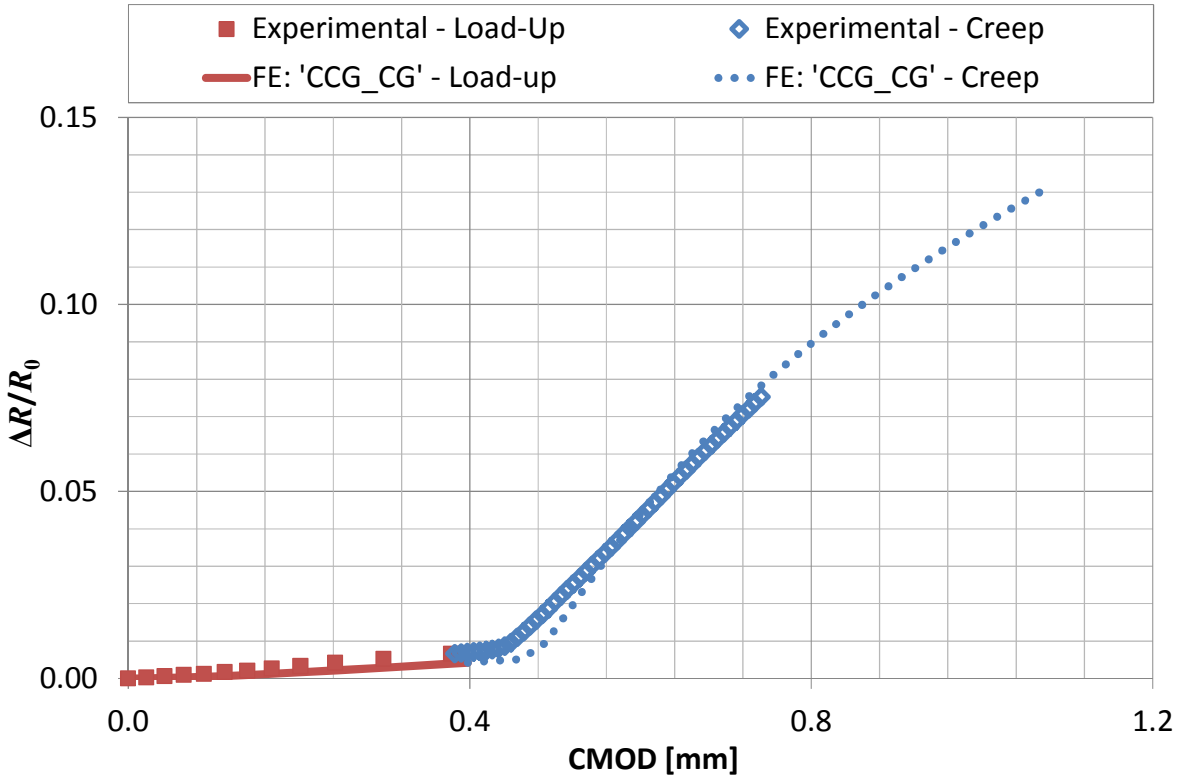

Figure 8.24: Comparison of the electrical response of FE model 'CCG_CG' and the experimental data for the entire creep crack growth test.

Figure 8.24 compares the electrical response of model 'CCG_CG' with the experimental data for the entire creep crack growth test. After the onset of crack growth, the FE over-predicts both the relative change in resistance and the CMOD. The differences in CMOD are primarily due to the simplified crack morphology as discussed above. The differences in resistance are likely to be for the same reason. Discontinuous cracking and asperities on the fracture surfaces observed experimentally will allow the current to short across the crack faces. This will reduce the measured resistance compared to the FE model. Crack tunnelling will also influence the experimental PD measurements as demonstrated in Chapter 5 although this is likely to be a secondary effect compared to the discontinuous cracking. These results are in contrast to the simpler crack morphology observed in the previous chapter for stable tearing where the correlation between the FE and the experimental data was extremely good.

These results demonstrate that a sequentially coupled structural-electrical FE model can be used to predict the influence of strain and crack initiation on the resistance of a specimen during a high temperature creep crack growth test. Similar to the room temperature predictions from previous chapters, the FE does not capture the magnitude of the changes in resistance because it does not include the influence of strain on resistivity, but it does capture the general behaviour, including the abrupt increase in gradient on a plot of

resistance vs. CMOD which corresponds to the onset of crack growth. A limitation of this FE technique is that it is not suitable for modelling complex crack morphology such as discontinuous cracking which is typical of creep crack growth. The following studies into possible limitations of the proposed method of interpreting the PD data from creep crack growth tests will therefore focus on small amounts of crack extension such as those associated with initiation. These studies will investigate the influence of creep ductility and stress redistribution on the increase in gradient used to identify the onset of crack growth.

8.5.2 The Influence of Creep Ductility

In the previous chapter it was identified that the increase in gradient on a plot of resistance (or PD) against COD for a high toughness, high strain-hardening material can be difficult to identify. This is because the additional load which accompanies stable tearing also produces a large change in COD which can obscure the change in slope. This is analogous to a material with very high creep ductility undergoing a creep crack growth test where the creep strain which accompanies crack growth will increase the COD and could obscure the change in slope in a similar manner.

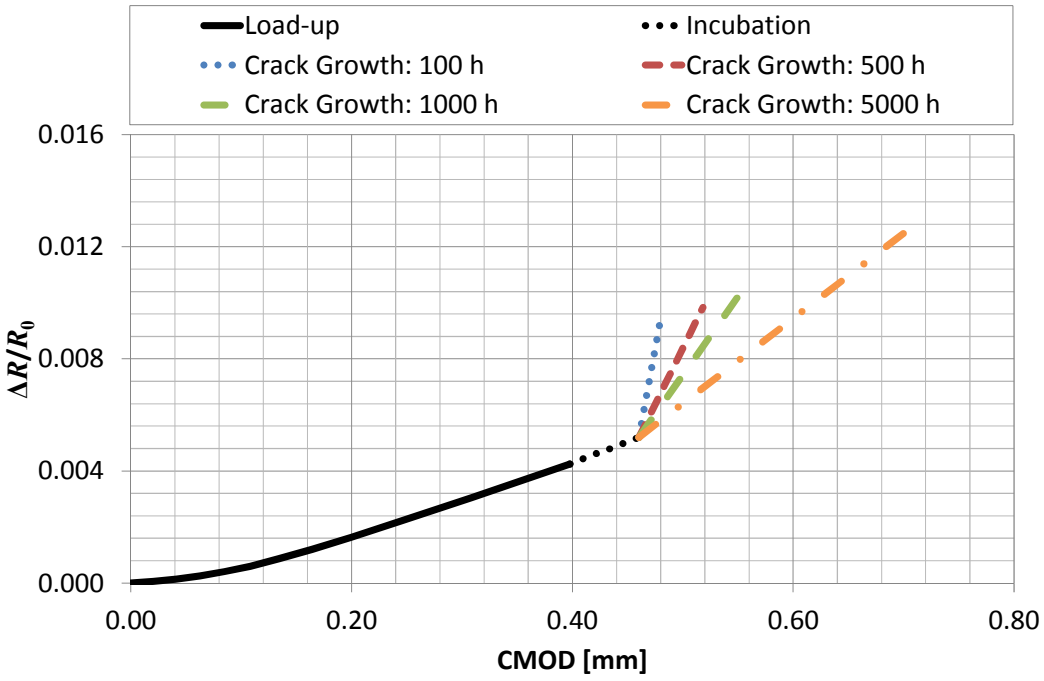

Figure 8.25: The influence of the time for a 0.1 mm crack increment to occur on the increase in gradient used to identify the onset of crack growth.

Assuming crack extension occurs when the creep ductility is exhausted; increasing the time for crack extension to occur in an FE model of a specimen with a constant load is approximately equivalent to increasing the creep ductility of the material. To demonstrate the effect of this, model 'CCG_CG' has been rerun with a single 0.1 mm increment of crack

growth. The time for that increment to occur has been varied from 100, 500, 1000 and 5000 hours. The results of this analysis are provided in Figure 8.25.

As the time for the initial crack increment to occur increases, the corresponding increase in creep strain reduces the acuity of the change in slope. For materials with very high creep ductility the increase in gradient may be masked almost entirely, making it difficult to identify the onset of crack growth. This is similar to the limitation observed in fracture toughness testing. For the experiments presented earlier in this chapter, the initial 0.1 mm of crack extension typically occurred over a period of ~180 hours (see Figure 8.19). Figure 8.25 suggests that this would need to increase by an order of magnitude before the increase in gradient became difficult to identify. This is a significant increase, and Type 316H is already a creep ductile material, so the proposed method of interpreting CCG PD data should be suitable for most engineering materials.

8.5.3 The Influence of Stress Redistribution

During a creep crack growth test, stress redistribution will occur prior to attaining steady-state conditions. This stress redistribution is likely to influence the PD response of the specimen and could obscure the increase in gradient used to identify the onset of crack growth. To investigate the influence of stress redistribution a finite element parametric study has been performed.

8.5.3.1 Geometry and Mesh

To perform this parametric study a 2D plane strain ½ FE model was generated using Abaqus [130]. A large number of analyses were performed as part of this study, so a 2D model was used to reduce the computational expense. This assumes no out-of-plane deformation and a constant level of crack tip constraint along the crack front. A preliminary study demonstrated that a 2D plane strain model will predict a change in resistance ~20% lower than a 3D model as a result of these assumptions. This is considered adequate for the following qualitative parametric study.

The specimen geometry shown in Figure 8.1 was used, with the exception of the side grooves which could not be included in the 2D model. The model consists of 5,914 linear quad elements. Element types CPE4R and DC2D4E were used for the structural and electrical models respectively. The mesh is shown in Figure 8.26.

The inputs to this parametric study were based on the interrupted tests presented above to provide realistic deformation magnitudes. The material properties, defined in the following section, are related to those of Type 316H stainless steel at 550ºC. The load applied to the

model was 30.9kN which results in a reference stress, σ_{ref}, of 191.9MPa. This is the 0.2 % proof stress of 316H and is similar to the reference stress applied in the interrupted tests.

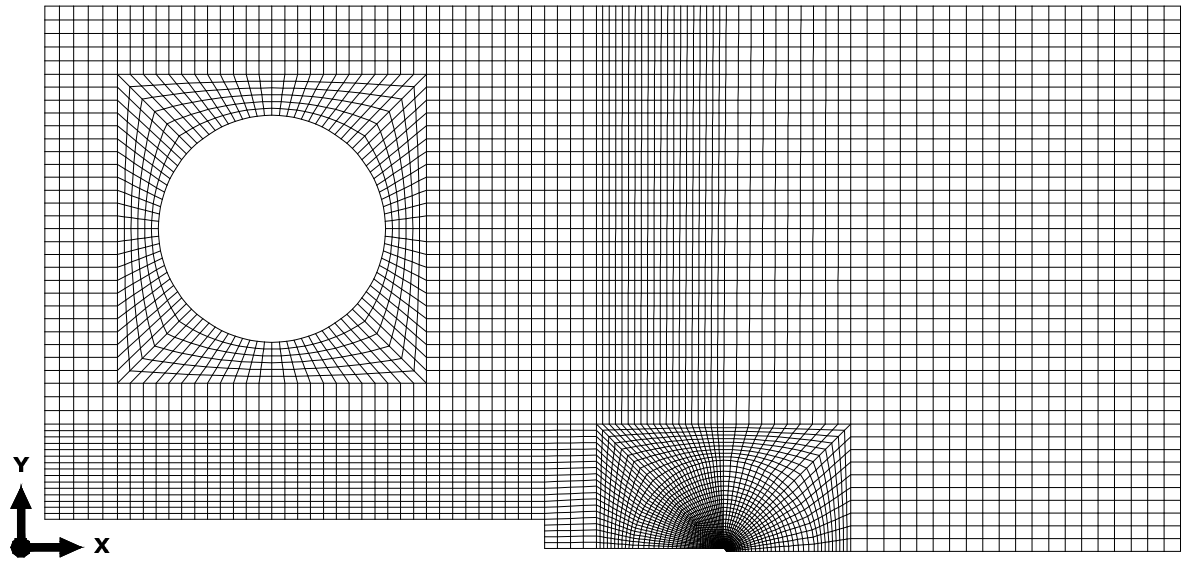

Figure 8.26: 2D Finite Element Mesh

8.5.3.2 Tensile Material Properties

A Ramberg Osgood material model, as defined in Section 2.2.2.1, has been assumed. The values of σ_{p0} and E have been taken as the 0.2% proof stress and the Young's modulus of Type 316H stainless steel at 550 ºC provided in Section 8.5.1.3. Three values of stress exponent, N, have been considered: 1, 3 and 10. For N = 1, the material is assumed to be elastic, so α = 0. For the other two stress exponents, the value of α has been calculated such that 0.2% plastic strain occurs at σ_{p0}. The material constants for each material are provided in Table 8.10.

N	E [GPa]	σ_{p0} [MPa]	α
1	159.75	191.9	0.000
3	159.75	191.9	1.665
10	159.75	191.9	1.665

Table 8.10: Tensile material properties considered in the parametric study to investigate the influence of stress redistribution

8.5.3.3 Creep Material Properties

A power-law creeping material model has also been assumed as defined in Section 2.2.3.3. Three creep stress exponents, n_A, have been considered: 1, 3 and 10. For each stress

exponent, the corresponding value of material constant A_A has been calculated such that the creep strain rate at the reference stress (191.9 MPa) is 2.26×10^{-6} h^{-1}. This is the average creep strain rate for austenitic Type 316H stainless steel at 550 ºC for the same reference stress [8]. The material constants for each material, including the average creep properties for Type 316H at 550 ºC, are provided in Table 8.11.

Material	n_A	A_A
Type 316H Stainless Steel at 550 ºC [8]	8.17	5.02×10^{-25}
Stress redistribution study, n = 1	1	1.18×10^{-08}
Stress redistribution study, n = 3	3	3.19×10^{-13}
Stress redistribution study, n = 10	10	3.33×10^{-29}

Table 8.11: Creep properties for the materials considered in the parametric study to investigate the influence of stress redistribution and the average creep properties for austenitic type 316H stainless steel at 550 ºC.

8.5.3.4 Analysis Time

The stress redistribution time, t_{red}, for elastic-creep conditions can be estimated from Equation (8.11) [6]. At the reference stress and reference strain rate defined above stress redistribution is estimated to take just over 500 hours. To ensure the full effect of stress redistribution was captured, each analysis was run for 2,000 hours.

$$t_{red} = \frac{\sigma_{ref}}{E\dot{\varepsilon}^{c}_{ref}} \qquad \textbf{(8.11)}$$

8.5.3.5 Results

Figure 8.27 shows the relationship between relative change in resistance and CMOD during load-up and creep for each combination of material properties considered. In Figure 8.27(a), where elastic-creep conditions are assumed (N = 1), the predicted stress redistribution time according to Equation (8.11) is shown by the "+" symbol.

When the tensile stress exponent, N, and the creep stress exponent, n, are equal, the linear relationship which occurs during load-up (after the initial elastic region) continues into the creep phase. This is because there is no stress redistribution, so the evolution of the strain field due to creep is equivalent to increasing the applied load in the absence of creep. The constant gradient in Figure 8.27 should make the increase in gradient at the onset of crack growth relatively easy to identify.

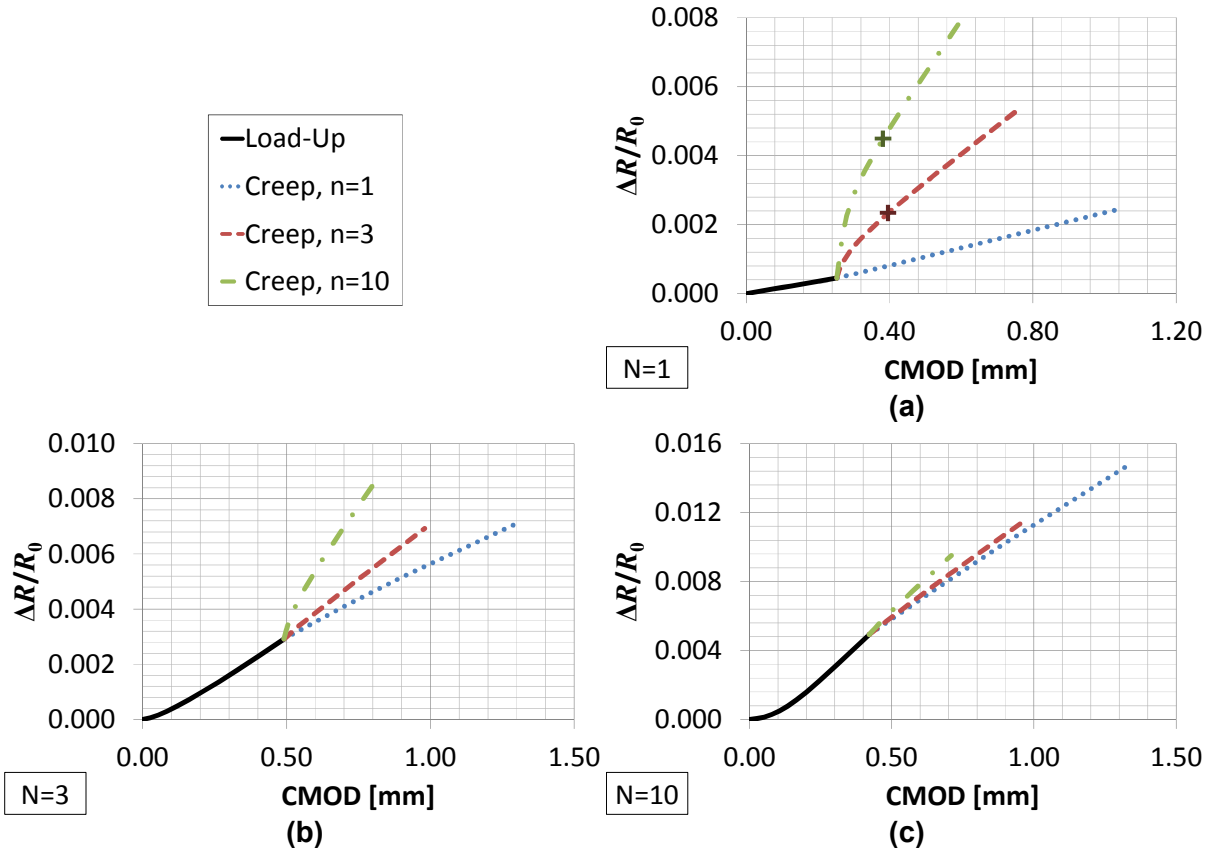

Figure 8.27: Relative change in resistance against CMOD for a range of tensile and creep material properties

When $n < N$ the gradient of Figure 8.27 reduces gradually during the creep phase. This occurs over a very long period of time and the 2,000 hour duration of the analysis is not sufficient for the stresses to fully redistribute. For tests which replicate these conditions, crack initiation is likely to occur prior to the completion of stress redistribution however due to the very gradual change in gradient, the increase in gradient associated with the onset of crack growth should still be easily identified.

When $n > N$ the gradient of Figure 8.27 increases instantaneously at the start of the creep phase before steadily reducing to a constant value. For $N = 1$, the stress redistribution times predicted from Equation (8.11) are in good agreement with the start of the constant gradient confirming that the change in gradient is indeed due to stress redistribution. If crack initiation occurs during this period of stress redistribution, it may be difficult to identify a change in slope due to the already steep gradient however, after stress redistribution, it should be easily observed.

8.6 Discussion

During a creep crack growth test, crack initiation can be identified from an abrupt increase in gradient on a plot of resistance (or PD) against CMOD. This corresponds to damage, in the form of micro-cracks, ahead of the crack tip first linking up with the pre-crack. Based on this experimental observation, a modified method of interpreting the PD data from a creep crack growth test has been proposed which is analogous to the 'COD' method used to measure stable tearing during fracture toughness testing. This approach has been validated through a series of interrupted creep crack growth tests.

The change in PD (or resistance) which occurs during incubation is primarily due to creep strain. Using the current method of interpreting the PD data in ASTM E1457-13, this is erroneously interpreted as crack growth. For materials with moderate creep ductility, such as Type 316H stainless steel, this spurious crack extension is relatively small but not insignificant when compared to the 0.2 mm 'engineering' definition of crack initiation. For materials with high creep ductility, such as P91 steel, the spurious crack extension can be much bigger than 0.2 mm such that incubation times are underestimated by more than a factor of 5.

When plotting the crack growth rate against the crack tip characterising parameter C^* the influence of the modified method on the steady-state crack growth rates is small for the tests performed here on Type 316H although it will be larger for materials with a higher creep ductility. The modified method does however remove a significant portion of the so-called 'tail' which is due to creep strains rather than crack growth.

The interrupted creep crack growth tests have also demonstrated that the PD technique can significantly underestimate the crack extension. This is because discontinuous cracking and asperities on the fracture surfaces prevent clean separation of the crack faces and provide alternative paths for the current. To mitigate this, a linear correction to the PD based on the final crack length measured from the fracture surface may be performed. In most cases this should provide conservative crack growth rates.

The sequentially-coupled structural-electrical FE tool developed in Chapter 6 has been extended to include creep strain and crack growth and has been validated against the experimental results. Up to crack initiation, the model is in good agreement with the experimental data and confirms that the increase in gradient corresponds to the onset of crack growth. It is not however capable of capturing the change in PD due to significant crack growth because the simplified modelling of crack extension doesn't capture the discontinuous crack morphology so it over predicts the change in resistance and CMOD compared to the experimental data. The use of the FE model as a predictive tool is

therefore limited to load-up, incubation and crack initiation, but this not a significant limitation because this is the portion of the test most influenced by strain.

This FE tool has been used to demonstrate that the increase in gradient used to identify the onset of crack growth may be difficult to discern for materials with very high creep ductility. A similar limitation was observed for fracture toughness testing of high toughness, high strain hardening materials in the previous chapter.

The FE tool has also been used to look at the influence of stress redistribution. It has been demonstrated that the relationship between resistance (or PD) and CMOD during the early part of a creep crack growth test is not always linear and depends on the combination of the tensile and creep material properties. For the case where the creep stress exponent, n, is greater than the tensile stress exponent, N, the gradient of a plot of resistance (or PD) vs. CMOD will increase instantaneously at the start of the creep phase before steadily reducing to a constant value. If crack initiation occurs during this period of stress redistribution, it may be difficult to identify the change in slope associated with the onset of crack growth but after stress redistribution, it should be easily observed. It should also be easily observed for other combinations of tensile and creep material properties.

Chapter 9: Re-analysis of Creep Crack Growth Data

9.1 Introduction

EDF Energy Nuclear Generation Limited have performed a significant number of creep crack growth tests on Type 316H for a wide range of loads and test durations [143]. Historically, the experimental data from these tests has been post-processed using a method similar to the one proposed in ASTM E1457-13 [3]. In this chapter the raw data from a selection of these tests has been reanalysed using the modified method proposed in the previous chapter and compared with measurements obtained using the current ASTM method. Consideration is given to both crack initiation times and crack growth rates although the main focus is on initiation because, as discussed in the previous chapter, it is more significantly influenced by strain and therefore the method of interpreting the PD data.

Three creep crack initiation models are provided in R5 [4]: Sigma-d, CTOD and TDFAD. Details of these models are provided in Chapter 2. These models have been previously validated by comparing predictions with experimental data that has been analysed based on the ASTM method. The implications of the proposed modified method of interpreting the PD data on this validation are assessed by comparing the reanalysed experimental data with these three models.

9.2 Re-analysis of CCG Data

9.2.1 Test Methodology

All of the tests considered in this chapter were performed on C(T) specimens manufactured from Type 316H and containing a sharp fatigue pre-crack. A brief overview of the methodology used to obtain the PD measurements is provided here. A more detailed description of the test methodology is set out in an internal company report [144].

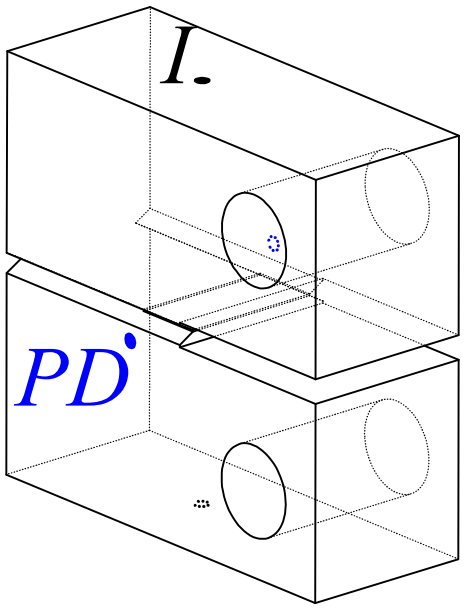

Figure 9.1: PD configuration adopted by EDF Energy Nuclear Generation Limited showing the current injection locations ('*I*') and the PD probes ('*PD*')

Crack extension was monitored using a DCPD system with the PD configuration shown in Figure 9.1. No reference measurement was taken so the measurements are sensitive to temperature fluctuations and amplifier drift. The instantaneous crack length, a, was determined from the corresponding PD, V, assuming a linear calibration function. This calibration function is provided in Equation (9.1) where a_0 and a_f are the initial and final crack lengths measured from the post-test fracture surface and V_0 and V_f are the corresponding PD measurements.

$$a = \left(a_f - a_0\right)\frac{\left(V - V_0\right)}{\left(V_f - V_0\right)} + a_0 \qquad \textbf{(9.1)}$$

9.2.2 Test Details

13 creep crack growth tests have been reanalysed covering a range of test durations from 62 to 17,850 hours. Details of the individual tests are provided in Table 9.1. The reference stress values assume plane strain conditions.

Test ID	Temp. [ºC]	Load [N]	σ_{ref} [MPa]	a_0 [mm]	Δa_f [mm]	W [mm]	B [mm]	B_N [mm]
2D2/2 CT1	550	7.86	131.9	20.68	2.97	37.91	18.85	15.27
2D2/2 CT2	550	10.17	151.6	20.03	2.63	38.01	18.92	15.62
2D2/2 CT3	550	15.50	250.7	20.49	1.21	37.82	18.98	15.57
2D2/2 CT4	550	12.83	196.4	20.14	1.24	37.90	18.98	15.59
2D2/2 CT5	550	13.68	199.6	19.79	1.42	37.97	18.98	15.50
2D2/2 CT20	550	7.75	128.4	20.56	4.52	37.97	18.86	15.13
1C2/3 CT5	550	14.40	233.7	20.48	2.21	38.02	19.00	15.20
1C2/3 CT6	550	13.25	196.9	19.87	2.86	38.10	19.02	15.21
1C2/3 CT11	550	8.75	257.5	21.24	8.26	38.01	18.96	9.32
2B1/2 CT14	550	14.58	243.7	20.63	2.96	37.97	18.93	15.14
2B1/2 CT15	550	15.43	251.8	20.42	6.36	37.94	18.95	15.12
2B1/2 CT16	550	10.00	159.7	20.26	1.89	37.99	18.93	15.10
2B1/2 CT17	550	11.25	169.2	19.86	1.21	37.99	18.95	15.15

Table 9.1: Test details of the creep crack growth tests performed on Type 316H stainless steel.

9.2.3 Interpretation of the PD Data

9.2.3.1 The ASTM Method

All of the tests listed in Table 9.1 have been analysed using the ASTM method. In five cases an initial drop in PD was observed: 2D2/2 CT1, 2D2/2 CT2, 2D2/2 CT4, 2D2/2 CT5 and 1C2/3 CT6. For these tests the value of V_0 used in Equation (9.1) was the minimum value observed throughout the test. For all other tests the value of V_0 was the value at the end of load-up. The onset of crack growth predicted by this method is, by definition, the time corresponding to V_0. For most tests this corresponds to t = 0, but for tests which experience an initial drop in PD this corresponds to t > 0. This method of addressing an initial drop in PD is merely a pragmatic method of analysing the data and is not believed to have any physical relevance so the time to the onset of crack growth, as predicted by the ASTM method, has not been reported here. The time for 0.2 mm of crack extension to occur is herein denoted $t_{0.2}^{ASTM}$.

9.2.3.2 The Modified Method

All of the tests listed in Table 9.1 have also been analysed using the modified method proposed in the previous chapter. For each of the tests an increase in gradient was

successfully identified which has been attributed to the onset of crack growth. The time at the increase in gradient is denoted t_0^{MOD}, and the time for 0.2 mm of crack extension to occur is denoted $t_{0.2}^{MOD}$. Despite all of the tests demonstrating an increase in gradient, some variation in the shape of the plots was observed as demonstrated by the examples provided in Figure 9.2. These four plots are typical of all 13 tests so details of the interpretation of the PD data are only provided for these tests.

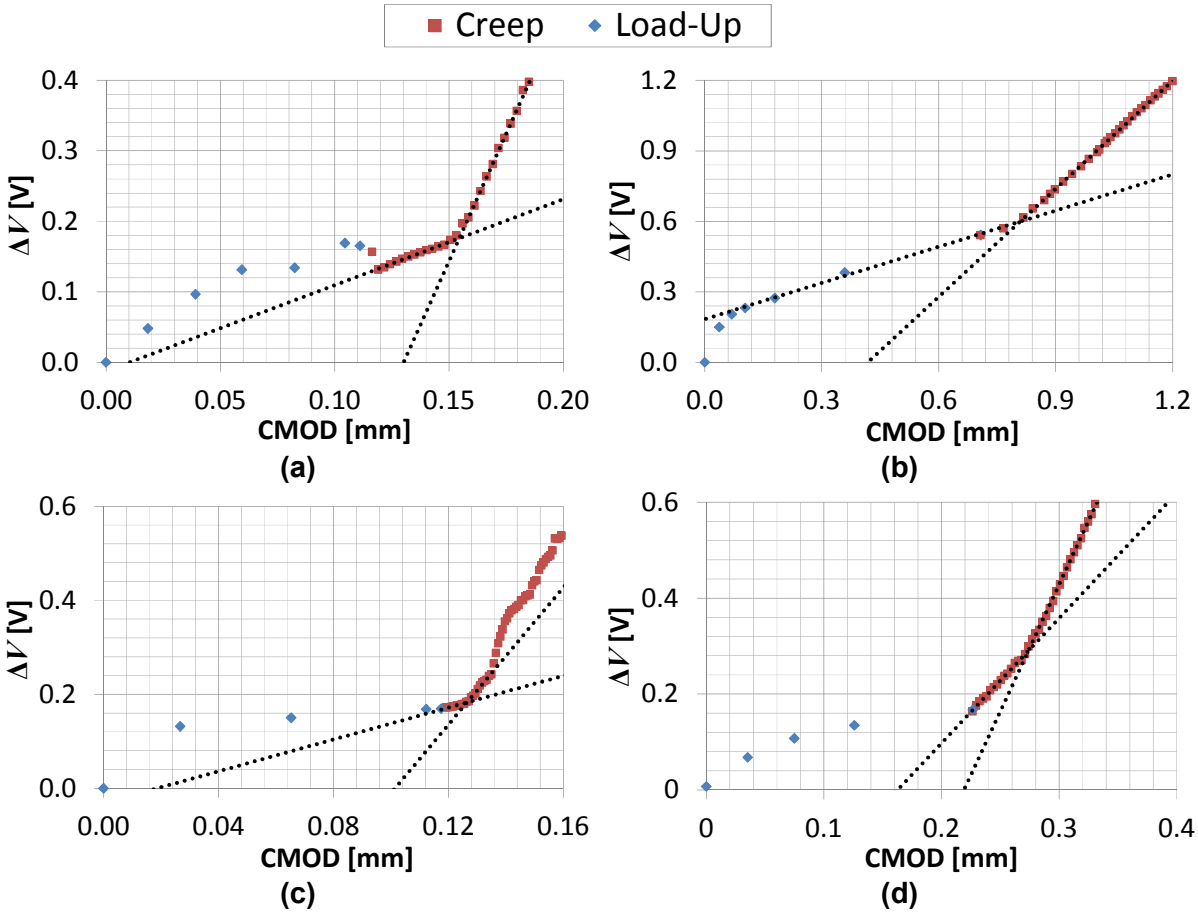

Figure 9.2: Increase in gradient used to identify the onset of crack growth in specimens (a) 2D2/2 CT1, (b) 2B1/2 CT14, (c) 2D2/2 CT20, and (d) 2B1/2 CT16.

The load-up behaviour of the four tests shown in Figure 9.2 is generally similar. There is a large increase in PD when the initial load is applied as the two faces of the fatigue pre-crack are separated. This is followed by an approximately linear region as observed in the interrupted tests in the previous chapter. The main differences between the four tests occur during the early part of the creep phase.

The PD vs. CMOD plot for specimen 2D2/2 CT1 is shown in Figure 9.2(a). Although there is an initial drop in PD, the subsequent behaviour is consistent with the FE predictions and interrupted tests in the previous chapter. The initial slope is approximately parallel to the load-up data, before an obvious increase in gradient.

The plot for specimen 2B1/2 CT14, shown in Figure 9.2(b), demonstrates similar behaviour but the increase in gradient occurs very early in the test such that there are only two data points prior to it. This highlights the need to increase the frequency with which experimental data is recorded in the early part of the test in order to accurately capture the change in slope.

The increase in gradient is more difficult to identify in Figure 9.2(c) which is for specimen 2D2/2 CT20. Two points of inflection can be observed early on in the test and, unlike the other tests, the subsequent data demonstrates significant fluctuations. Possible reasons for this are the stability of the test temperature or the measuring equipment which are likely to fluctuate over the duration of such a long term test (~18,000 hours). If this is the cause then it could have been suppressed by a suitable reference measurement. To analyse this test, the first increase in gradient has been assumed to correspond to crack initiation.

The data for specimen 2B1/2 CT16, shown in Figure 9.2(d), demonstrates an immediate increase in slope at the start of the creep phase relative to load-up. This behaviour is similar to one of the interrupted tests presented in the previous chapter where observations from the fracture surface confirmed that this increase in gradient does not correspond to instant crack growth. It does however make the increase in gradient less evident but it is still observed nonetheless. Similar behaviour was also demonstrated by specimen 2B1/2 CT17.

9.2.4 Results

9.2.4.1 Creep Crack Growth Rates

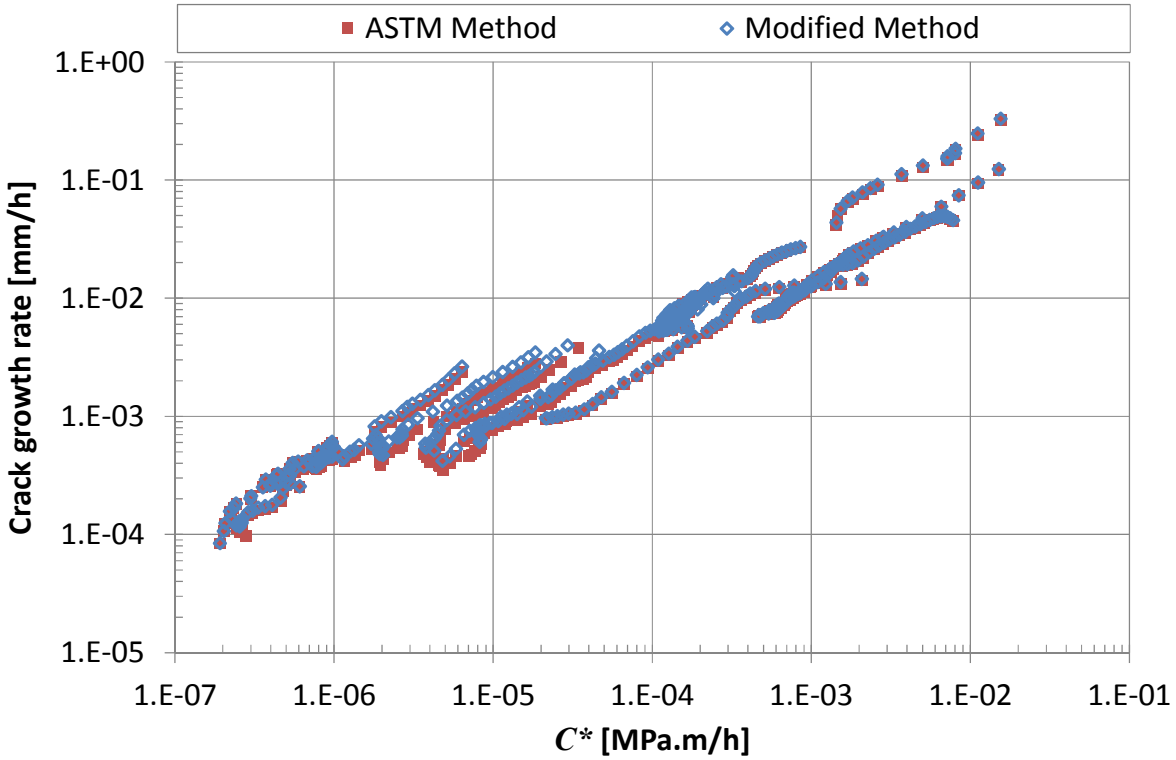

Figure 9.3: Correlation between crack growth rate and C^* for all specimens.

Figure 9.3 shows the correlation between the steady-state creep crack growth rate and C^* for all of the tests listed in Table 9.1. Both methods of interpreting the PD data are included. For some of the tests the modified method results in a small increase in the measured crack growth rate, but for many, the difference is negligible. The tests with the largest difference are 1B1/2 CT16 and 1B1/2 CT17. These are the tests which demonstrate an instantaneous increase in the gradient of a plot of PD vs. CMOD after load-up, as shown in Figure 9.2(d). This results in a larger increase in PD prior to the change in slope and therefore a larger difference between the two methods of interpreting the PD.

The results in Figure 9.3 are in good agreement with the original analysis of the data [143]. They are also consistent with the interrupted tests performed in the previous chapter. In general it may be concluded that for this material, the modified method of interpreting the PD data does not significantly influence the measured crack growth rate compared to the current method in ASTM. For other, more ductile materials however, the difference between the two methods will be larger and may become significant. Larger differences are also expected when measuring small amounts of crack growth such as those associated with initiation.

9.2.4.2 Creep Crack Initiation

The different initiation times and the transition time, t_T, as a proportion of the test duration, t_f, are provided in Table 9.2. On average, the time for 0.2 mm of crack extension to occur based on the modified method of interpreting the PD data, $t_{0.2}^{MOD}$, is approximately double the value based on the ASTM method, $t_{0.2}^{ASTM}$. This is because the ASTM method erroneously interprets the change in PD due to creep strain as crack growth. Similar to the creep crack growth rates in Figure 9.3, the maximum difference in initiation times correspond to tests 2B1/2 CT16 and 2B1/2 CT17. For these two tests the difference is a factor of 4.5 and 3.0 respectively.

The time for the onset of crack growth, identified from the increase in gradient, t_0^{MOD}, is on average 80% of the time for 0.2 mm of crack extension to occur as measured using the ASTM method, $t_{0.2}^{ASTM}$. This suggests that for this material, the "engineering definition" of initiation in ASTM E1457-13 [3] provides a reasonable approximation of the time to the onset of crack growth which is generally conservative.

Test ID	σ_{ref} **[MPa]**	t_f **[h]**	$\frac{t_T}{t_f}$ **[%]**	$\frac{t_0^{MOD}}{t_f}$ **[%]**	$\frac{t_{0.2}^{MOD}}{t_f}$ **[%]**	$\frac{t_{0.2}^{ASTM}}{t_f}$ **[%]**
2D2/2 CT1	131.9	16630	10.9	7.3	19.6	9.4
2D2/2 CT2	151.6	4698	8.1	26.8	38.1	20.6
2D2/2 CT3	250.8	170	8.2	7.6	37.6	36.5
2D2/2 CT4	196.4	1921	10.0	20.5	45.0	26.4
2D2/2 CT5	199.7	1589	8.0	15.4	39.7	24.8
2D2/2 CT20	128.4	17850	43.3	0.8	8.4	5.5
1C2/3 CT5	234.4	146	1.4	7.5	24.0	19.9
1C2/3 CT6	196.9	1081	4.1	5.7	23.9	14.9
1C2/3 CT11	257.3	287	2.8	3.1	9.1	7.0
2B1/2 CT14	243.8	140	2.1	4.3	22.1	17.1
2B1/2 CT15	251.9	62	1.6	12.9	19.4	9.7
2B1/2 CT16	159.3	3572	9.6	30.1	44.8	10.0
2B1/2 CT17	169.3	1537	15.1	11.8	38.7	12.9

Table 9.2: Predicted crack initiation times for a range of creep crack growth tests performed on austenitic Type 316H stainless steel at 550ºC.

Power-law correlations between the various definitions of initiation time in Table 9.2 and experimental values of C^* have been derived in the form of Equation (9.2).

$$t_i = \gamma C^{*-q} \tag{9.2}$$

Values of the correlation coefficient, γ, and power-law exponent, q, are provided in Table 9.3 along with 2 standard deviations to the fit.

Initiation Time	Δa [mm]	γ	q	×/÷ 2SD
t_0^{MOD}	0.0	0.066	0.685	3.19
$t_{0.2}^{MOD}$	0.2	0.309	0.619	2.54
$t_{0.2}^{ASTM}$	0.2	0.252	0.600	2.76

Table 9.3: Power law fit parameters for predicting the initiation time (in h) from C* (in MPam/h).

Figure 9.4 compares the two correlations for 0.2 mm of crack extension. The two mean lines are approximately parallel and both data sets demonstrate similar scatter. For both data sets, the largest outlier is due to specimen 2D2/2 CT20 (circled). Fluctuations in the PD data were observed for this test as shown in Figure 9.2(c). These fluctuations are the probable cause of this relatively low experimental measurement.

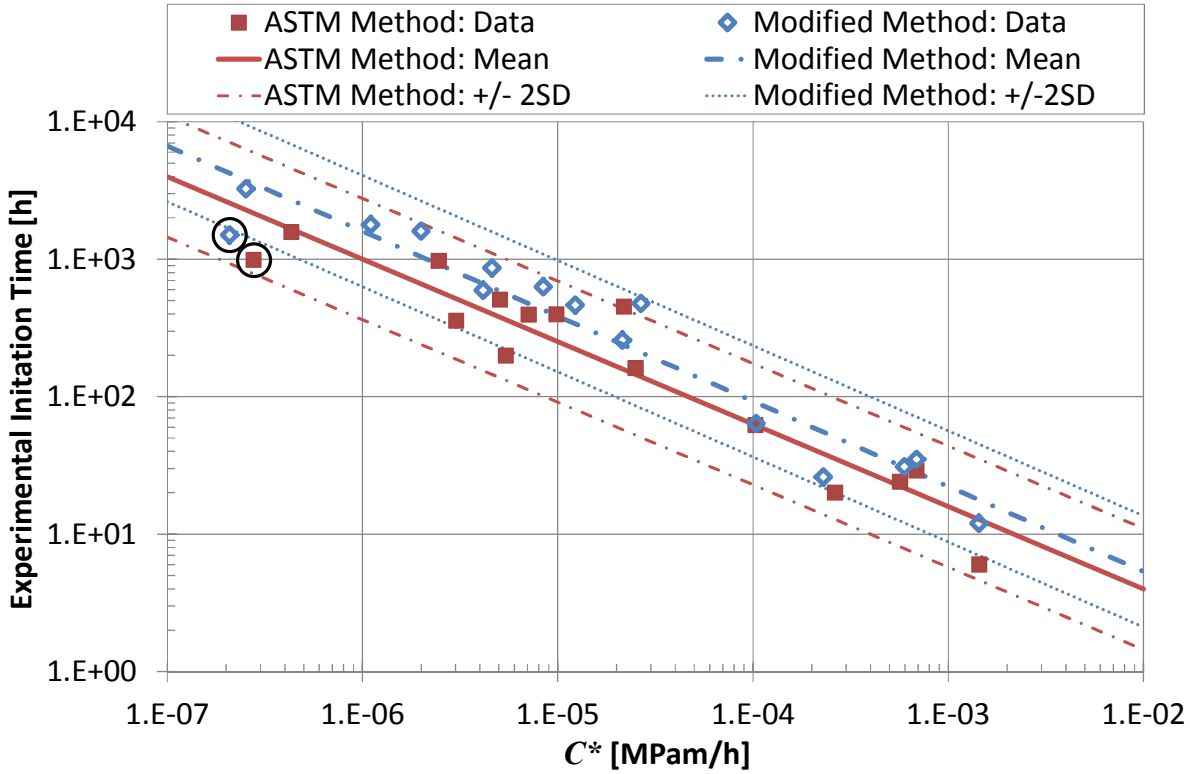

Figure 9.4: Experimental correlation between the initiation time (based 0.2 mm of crack extension) and C^* for the two different methods of interpreting the PD data.

Comparisons of the correlations between t_0^{MOD}, $t_{0.2}^{MOD}$ and C^* are provided in Figure 9.5. Again the two mean lines are nearly parallel but the scatter in the t_0^{MOD} data is slightly higher. This can again be attributed to specimen 2D2/2 CT20 (circled) for which fluctuations were observed in the PD data. By removing this data point, the scatter for the two data sets is similar. In this study the initial increase in gradient, shown in Figure 9.2(c), was used to predict the onset of crack growth but the correlations in Figure 9.5 suggest that this is more likely due to a fluctuation in the PD data and the onset of crack growth occurs much later. This highlights the importance of implementing a reference measurement to remove these fluctuations.

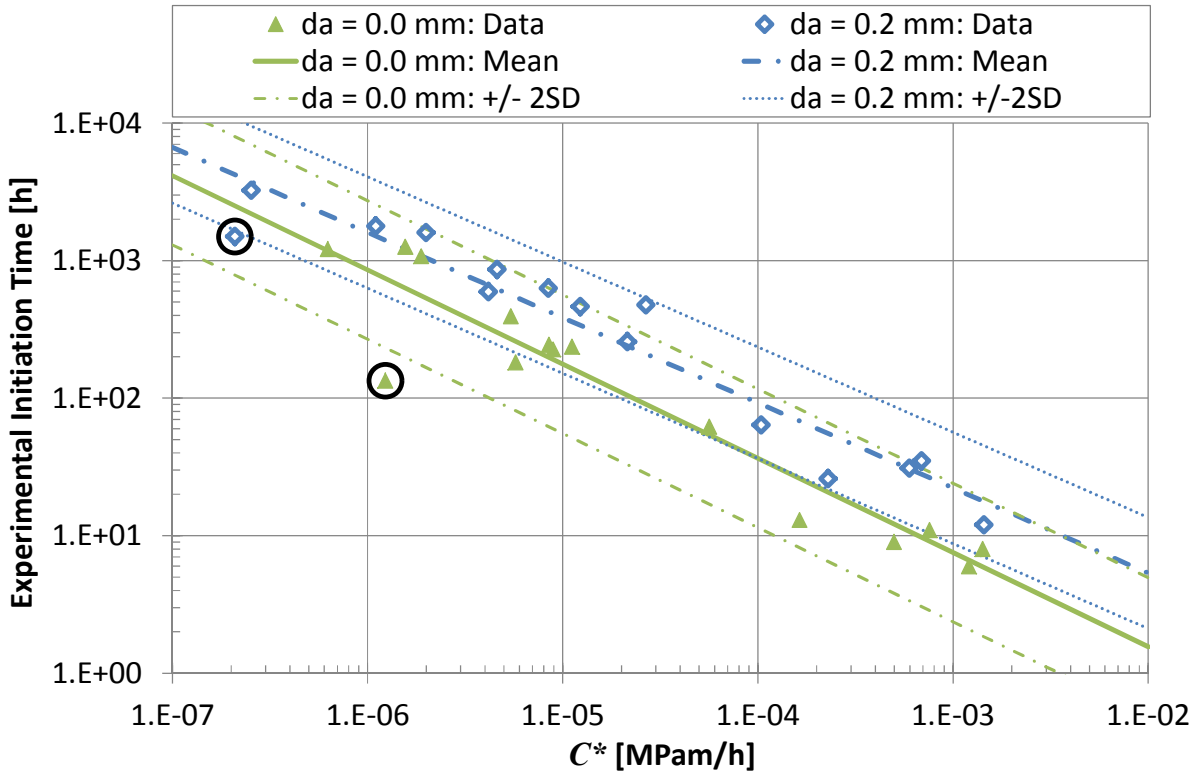

Figure 9.5: Experimental correlation between the initiation time and C^* for the two definitions of initiation obtained from the modified method of interpreting the PD data.

Interpreting the PD data using the modified method typically results in the data points in Figure 9.4 moving up and to the left compared to the ASTM method. The vertical shift is due to the increase in initiation time whilst the horizontal shift is due to a reduction in C^*. The latter is because the ASTM method sometimes predicts 0.2 mm of crack extension occurs before steady-state conditions are established whilst the modified method consistently predicts 0.2 mm of crack extension occurs during steady-state creep conditions.

A typical example of this is shown in Figure 9.6(a) which shows the correlation between crack growth rate and C^* for specimen 2B1/2 CT16. The ASTM method of interpreting the PD data predicts a significant tail, and 0.2 mm of crack extension occurs within this tail. The

modified method however discards most of the tail, attributing it to creep strain, and predicts 0.2 mm of crack growth occurs approximately at the onset of steady-state conditions. Conversely, specimens which demonstrate small changes in PD prior to the increase in gradient, such as 2B1/2 CT14, generally have a much smaller tail as shown in Figure 9.6(b). In this case, both methods of interpreting the PD predict 0.2 mm of crack extension occurs approximately at the onset of steady-state conditions. This supports the suggestion made in the previous chapter that when large tails are observed, this is most likely due to the effects of strain rather than crack growth.

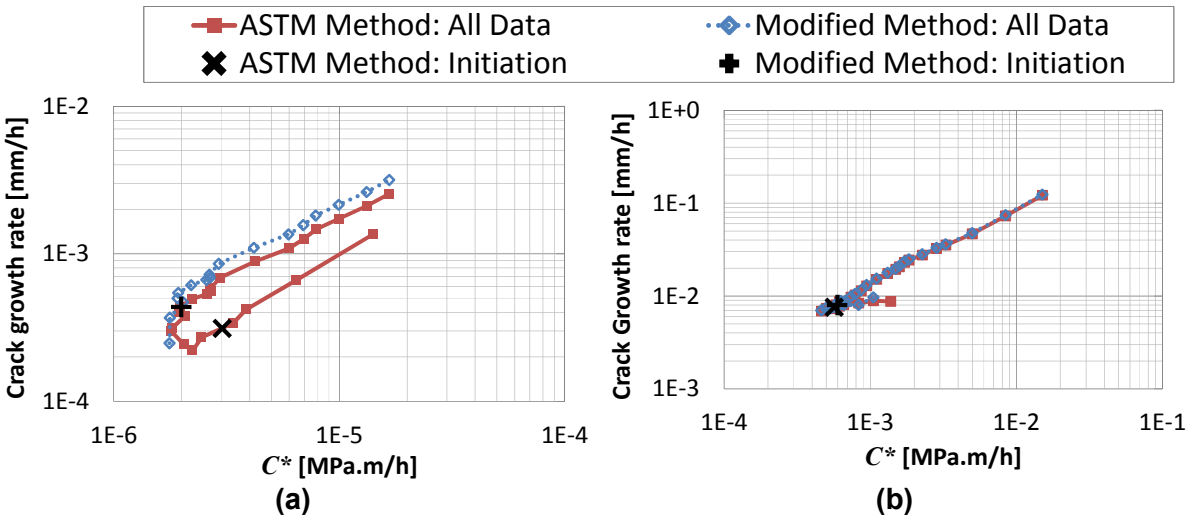

Figure 9.6: Correlation between crack growth rate and crack tip characterising parameter C^* for (a) specimen 2B1/2 CT16, and (b) specimen 2B1/2 CT14. Initiation corresponds to Δa = 0.2 mm.

9.3 Re-validation of CCI Models

Various CCI models have been proposed in the literature and are reviewed in Chapter 2. These models have been previously validated by comparison with experimental times for 0.2 mm of crack extension to occur based on the ASTM method of interpreting PD data. The implications of the proposed modified method of interpreting PD data on the validation of these models are investigated here by comparing predictions from these models with the experimental results in Table 9.2.

The three creep crack initiation models included in R5 [4] have been considered. These are the sigma-d model, the CTOD model and the TDFAD model. Each of these models requires different material properties as inputs which are usually obtained from uniaxial tensile and creep tests. This test data is provided in the following section.

9.3.1 Material Properties

9.3.1.1 Uniaxial Tensile Data

Uniaxial tensile data for Type 316H stainless steel is provided in the previous chapter and was originally obtained from the validation section of R6 [35]. This data is provided in a piece-wise linear format but it is much easier to incorporate into analytical initiation models in the form of a Ramberg-Osgood material model (see Section 2.2.2.1). A single Ramberg-Osgood fit cannot accurately capture the full stress-strain behaviour, so two fits have been applied, as shown in Figure 9.7. One fit provides an accurate representation of the experimental data for low strains (<2.4%) and the other for high strains (≥2.4%). The relevant fitting parameters are provided in Table 9.4.

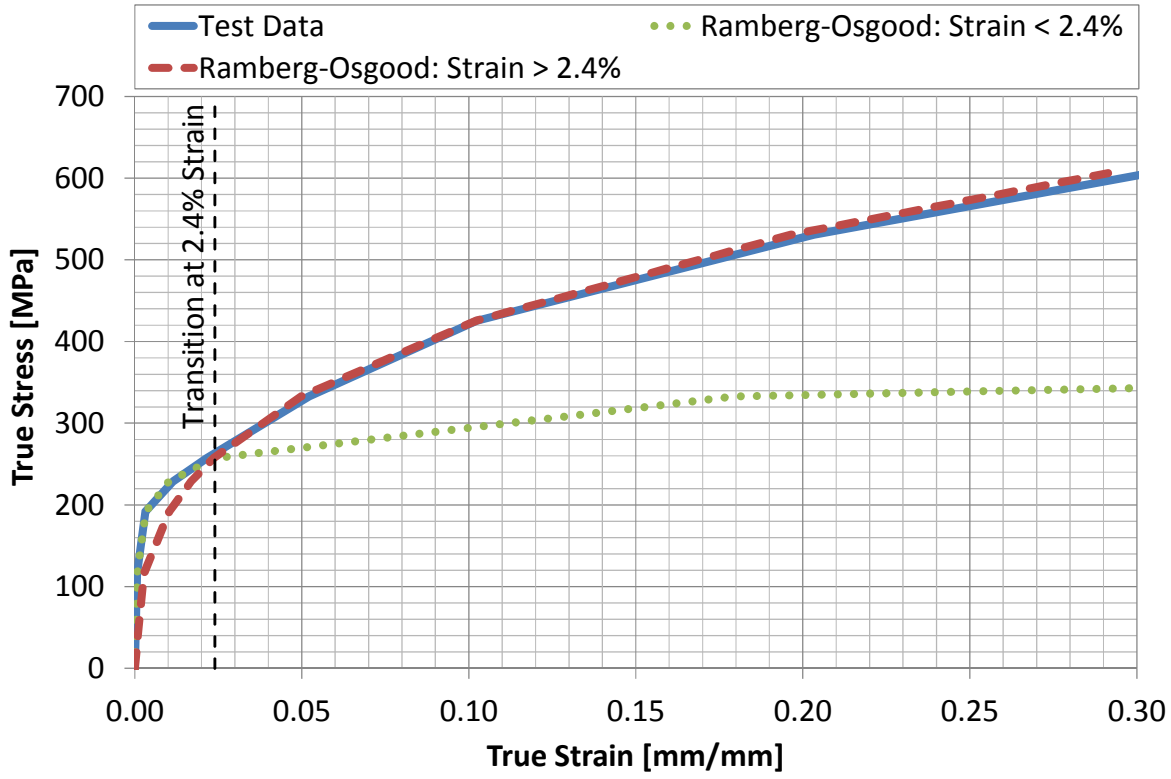

Figure 9.7: Ramberg-Osgood fits to the uniaxial tensile test data for Type 316H at 550ºC.

Valid Strain Range	σ_{p0} [MPa]	ε_{p0} [mm/mm]	α	N
$\varepsilon^e + \varepsilon^p < 2.4\%$	191.9	1.20×10^{-3}	1.80	8.0
$\varepsilon^e + \varepsilon^p \geq 2.4\%$	191.9	1.20×10^{-3}	7.60	3.0

Table 9.4: Ramberg Osgood fitting parameters for Type 316H stainless steel.

9.3.1.2 Uniaxial Creep Data

Webster et al. [8] has analysed creep rupture data for a large number of uniaxial tests performed on Type 316. These tests were performed for a range of stresses between ~170 MPa and ~380 MPa and test durations from ~30 to ~100,000 hours. This data was collated from a wide range of sources and incorporates different variants of Type 316 [145]. Different variants of Type 316 are likely to demonstrate slightly different creep properties, but any such variations should be outweighed by the robust power-law fits obtained from such a large data set. The empirical fits to the data are provided in Table 9.5. The various parameters are described in Section 2.2.3.

Parameter	Value	×/÷ 2SD
n_A	8.45	-
A_A	1.05×10^{-25}	9.25
v_r	8.45	-
B_r	1.09×10^{24}	5.33
ε_f	11.3%	4.12

Table 9.5: Creep strain rate and rupture properties for Type 316 at 550 ºC [8]. Stresses are in MPa, time in hours, strain rate in mm/h and strain in %.

Significant scatter was observed in the creep ductility data so a mean value of 11.3% was selected. For a creep ductility that is independent of stress, it follows that the average stress exponent, n_A, should be equal to the stress rupture exponent, v_r. Power-law regression fits to the data produced values of n_A and v_r of 8.17 and 8.72 respectively. For consistency with the constant creep ductility, a mean value of 8.45 was assumed for both. The corresponding coefficients A_A and B_r were calculated accordingly.

9.3.2 Sigma-d Predictions

The Sigma-d model, as defined in R5 [4], has been used to predict initiation times for the specimens in Table 9.1. The characteristic distance, d, ahead of the crack tip was taken as 50 μm and a Neuber construction was used to predict the equivalent stress at this distance ahead of the crack tip. Initiation predictions based on this model are compared to experimental measurements of the time for 0.2 mm of crack extension to occur in Figure 9.8. Only predictions based on plane stress conditions are provided which is implied in R5 (see Section 2.4.3) by the definition of the equivalent elastic stress. This is a conservative assumption since under plane strain conditions the stress triaxiality suppresses plasticity so the plastic collapse load is higher. This results in a lower reference stress, a lower value of σ_d and therefore a longer initiation time.

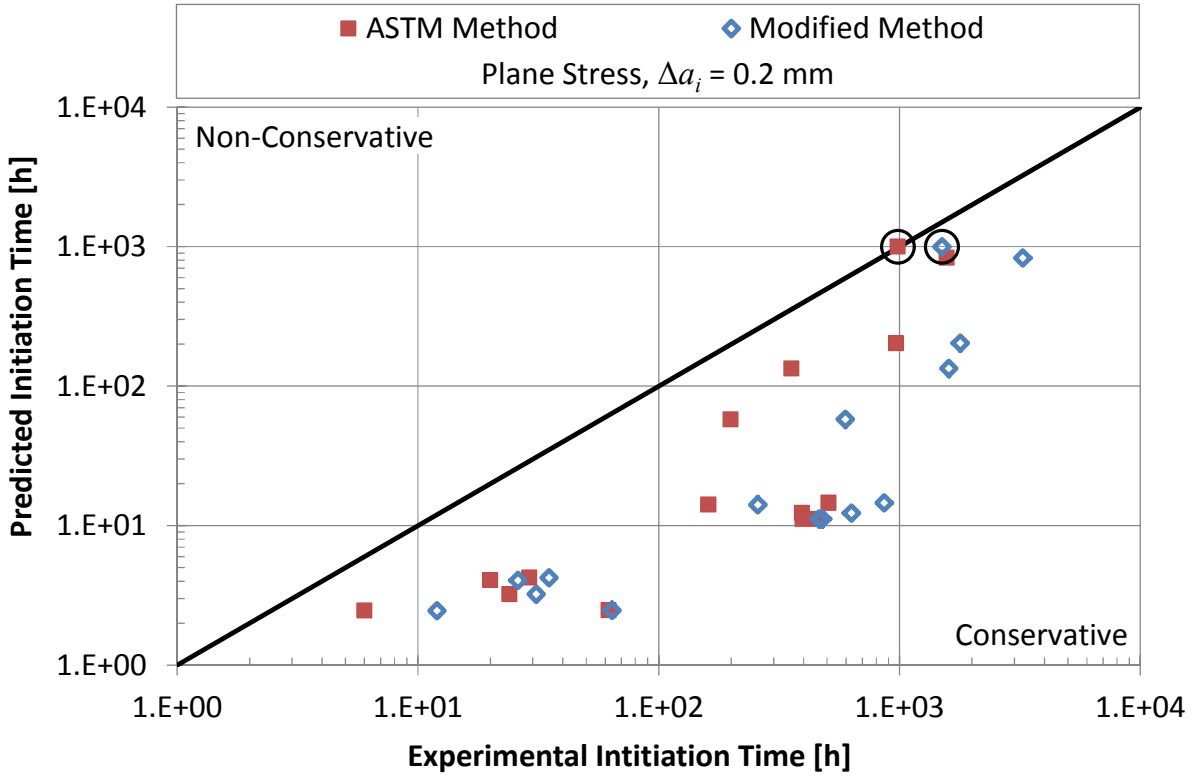

Figure 9.8: Comparison of crack initiation predictions, based on the Sigma-d, model with experimental measurements of 0.2 mm of crack of crack extension.

Predictions based on the Sigma-d method are conservative for all specimens irrespective of the method of interpreting the PD data but the level of conservatism is considerably higher when the modified method is used to interpret the PD. This is because it increases the measured time for 0.2 mm of crack growth to occur without influencing the predictions from the Sigma-d model. The least conservative predictions are obtained for specimen 2D2/2 CT20 (circled) which is the outlier observed in Figure 9.4 and Figure 9.5. Fluctuations in the experimental PD data are the probable reason for this.

This Sigma-d method does not explicitly model crack extension but its predictions are assumed to correspond to 0.2 mm of crack extension in R5 [4]. This is based on empirical validation using the ASTM (or similar) method of interpreting the PD data. Figure 9.9 compares the Sigma-d predictions with the onset of crack growth identified from the increase in gradient on a plot of PD vs. CMOD. It demonstrates the predictions remain conservative for all specimens except 2D2/2 CT20 (circled).

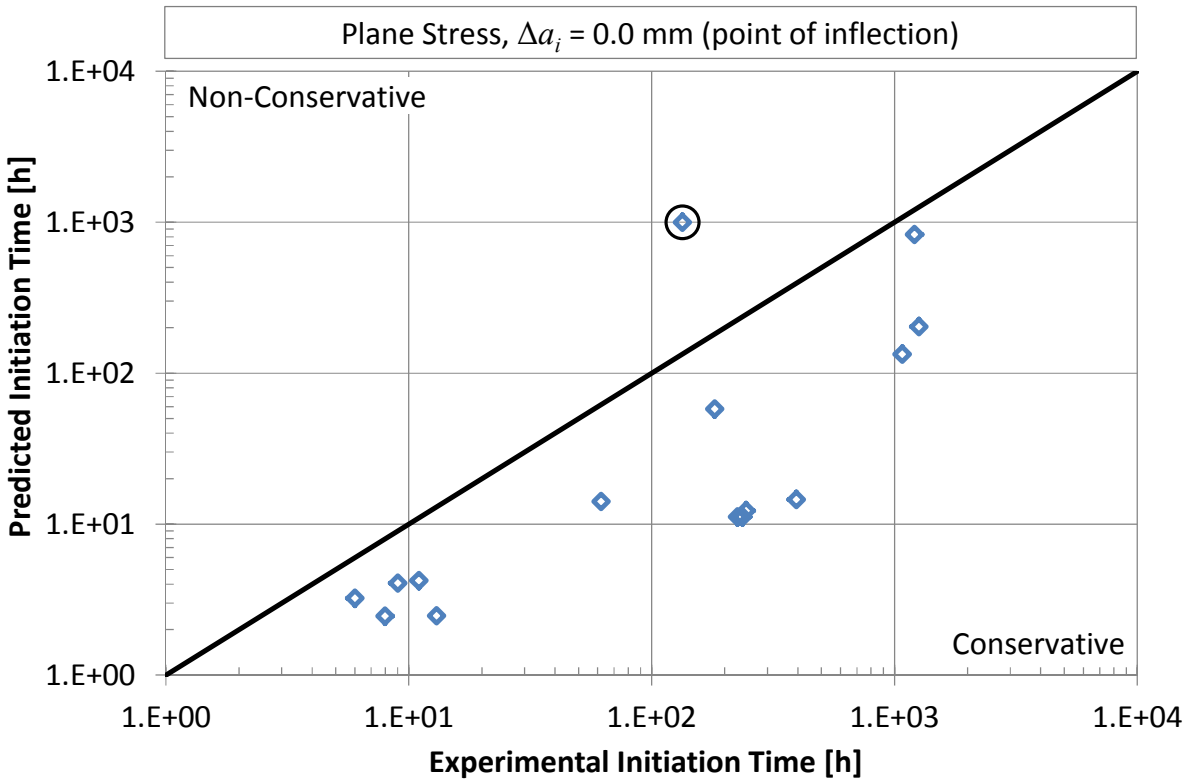

Figure 9.9: Comparison of crack initiation predictions, based on the Sigma-d model, with experimental measurements of the onset of crack growth (increase in gradient).

9.3.3 CTOD Predictions

The CTOD model, as originally described by Ainsworth [48] and in its current form in R5, requires a value of the critical CTOD obtained from experimental measurements. For many materials this data is not available. Where this is the case, an alternative version of the model may be applied as described in Chapter 2, although it is not currently included in R5. Critical values of CTOD are not available in the literature for Type 316H and insufficient measurements may be obtained from the interrupted tests performed in the previous chapter to obtain a value with any confidence so the alternative version has been applied here.

Crack growth was assumed to occur at the location around the crack tip which corresponds to the maximum ratio of the equivalent strain to multi-axial creep ductility. The variation of normalised equivalent strain around the crack tip, $\tilde{\varepsilon}_{ij}(\theta,n)$, was obtained from tables of the HRR field solution for a stress exponent, n, of 8 [25]. The same data was also used to calculate the ratio of hydrostatic stress to equivalent stress (triaxiality) at all points around the crack tip, which in-turn was used to calculate the variation in multi-axial creep ductility, ε_f^*, based on the Cocks and Ashby model [12]. For plane stress conditions this approach predicts crack growth occurs in the plane of the crack (θ = 0°) and a multi-axial creep ductility

of $\varepsilon_f/2$. For plane strain conditions it predicts crack growth occurs at an angle, θ, of 52º to the crack plane and a multi-axial creep ductility of $\varepsilon_f/38.4$. Initiation predictions based on this model are compared to experimental measurements of the time for 0.2 mm of crack extension to occur in Figure 9.10.

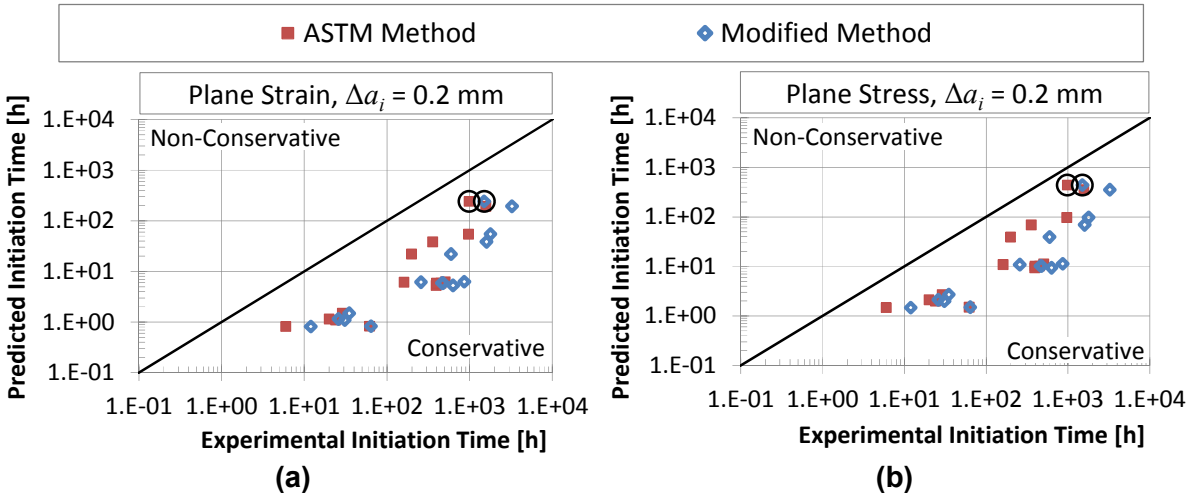

(a) (b)

Figure 9.10: Comparison of crack initiation predictions, based on the CTOD model, with experimental measurements of 0.2 mm of crack of crack extension. Predictions are provided for (a) plane strain, and (b) plane stress conditions.

The predictions remain conservative for both plane stress and plane strain conditions although those based on plane strain are more conservative as a result of the lower multi-axial creep ductility. Similar to the Sigma-d method, the modified method of interpreting the PD data increases the measured time for 0.2 mm of crack growth to occur without influencing the predictions based on the CTOD method. This increases the conservatism in the predictions. The least conservative predictions are again obtained for specimen 2D2/2 CT20 (circled).

Predictions from the CTOD model are compared to the onset of crack growth identified from the increase in gradient on a plot of PD vs. CMOD in Figure 9.11. Although the CTOD model explicitly models 0.2 mm of crack growth, the predictions remain conservative compared to the experimental data with the exception of specimen 2D2/2 CT20 (circled).

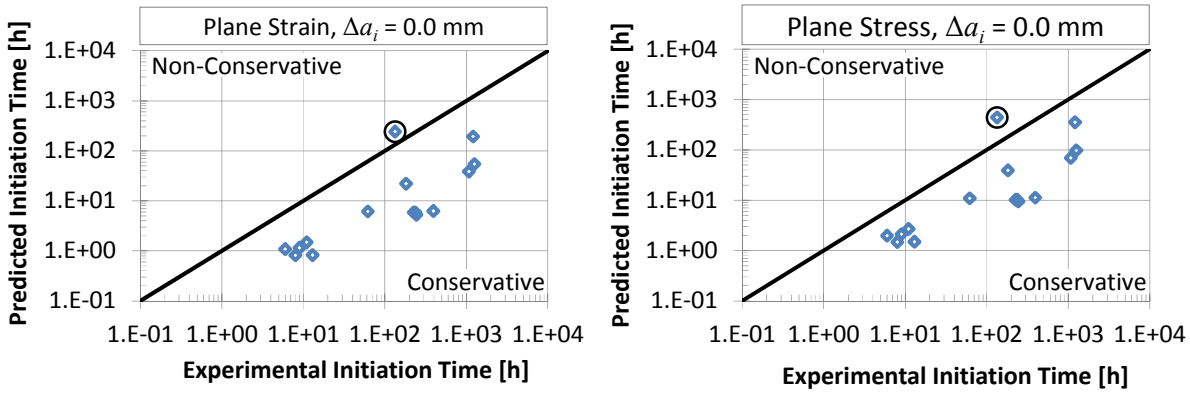

Figure 9.11: Comparison of crack initiation predictions, based on the CTOD model, with experimental measurements of the onset of crack growth (increase in gradient). Predictions are provided for (a) plane strain, and (b) plane stress conditions.

9.3.4 TDFAD Predictions

Unlike the other methods of predicting crack initiation which are entirely based on material properties obtained from uniaxial tests, the TDFAD approach requires the variation of creep toughness, K_{mat}^{c}, with time as an input. This is often obtained from creep crack growth tests rather than uniaxial data, so the method of interpreting the PD data will influence the predicted initiation times as well as the experimental values.

The creep toughness for a crack extension of 0.2 mm was obtained from each of the creep crack growth tests listed in Table 9.1. This process was performed twice: once interpreting the PD data using the ASTM method, and once using the modified method. For each test, the force-displacement plot was obtained and the creep toughness calculated from the total area under the plot based on the procedure in ESIS P2-92 [1]. This approach calculates the creep toughness from the total strain energy thus negating the need for separate elastic, plastic and creep components. A previous TDFAD assessment [50] applied this approach to Type 316H and demonstrated that it provides similar results to the more onerous procedure in ASTM E1820-13 [27].

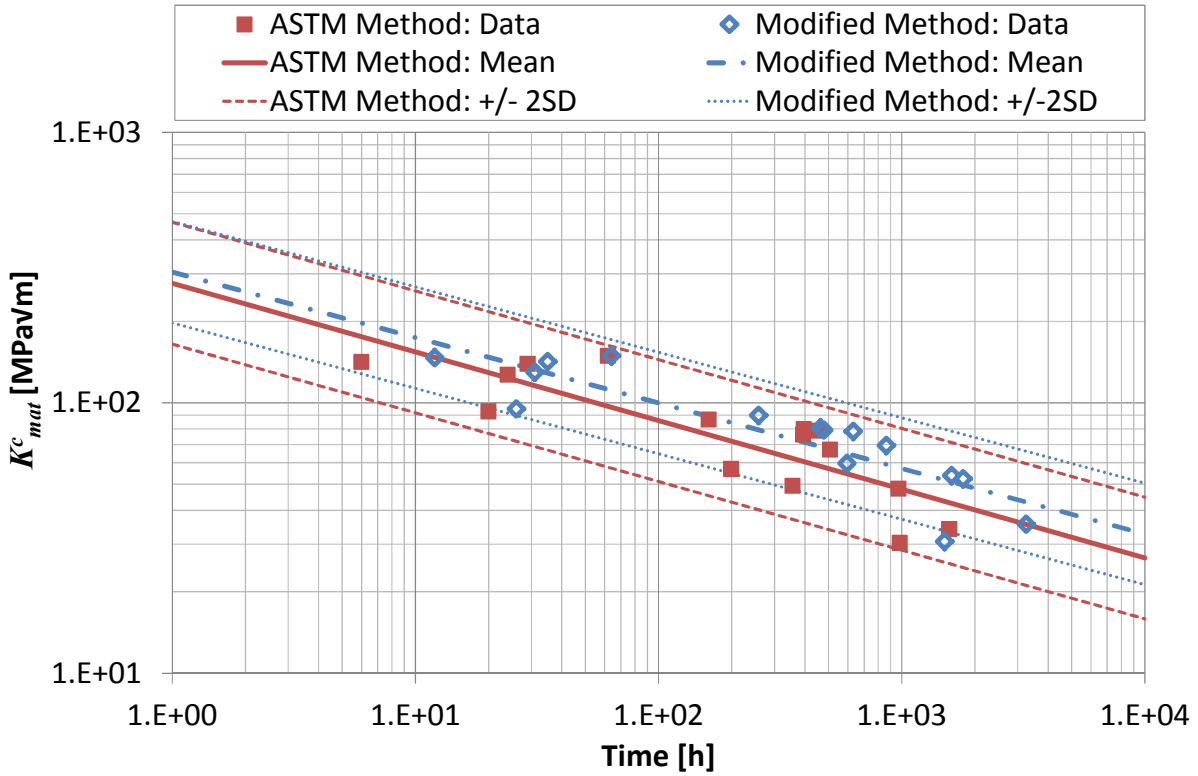

Figure 9.12: Variation of creep toughness (corresponding to 0.2 mm of crack growth) with time for both methods of interpreting the experimental PD data.

The variation of creep toughness with time (corresponding to 0.2 mm of crack growth) is shown in Figure 9.12 for the two different methods of interpreting the PD data. A power-law regression analysis has been performed on the two data sets in the form of Equation (9.3).

$$K^c_{mat} = Ht^{-j} \tag{9.3}$$

Values of the coefficient, H, and the time exponent, j, are provided in Table 9.6 along with two standard deviations. Lines corresponding to these fits are shown in Figure 9.12. A similar level of scatter is observed for both methods of interpreting the PD data.

Method of Interpreting PD Data	H	j	×/÷ 2SD
Modified	303.98	0.242	1.54
ASTM	276.70	0.254	1.68

Table 9.6: Constants used to calculate creep toughness in MPa√m (corresponding to 0.2 mm of crack growth) from time in hours.

The TDFAD is constructed from isochronous stress-strain data. This was calculated from the Ramberg-Osgood tensile stress-strain data provided in Table 9.4 and the average

power-law creep properties in Table 9.5. The TDFAD at a range of times is compared to the R6 Option 1 curve in Figure 9.13.

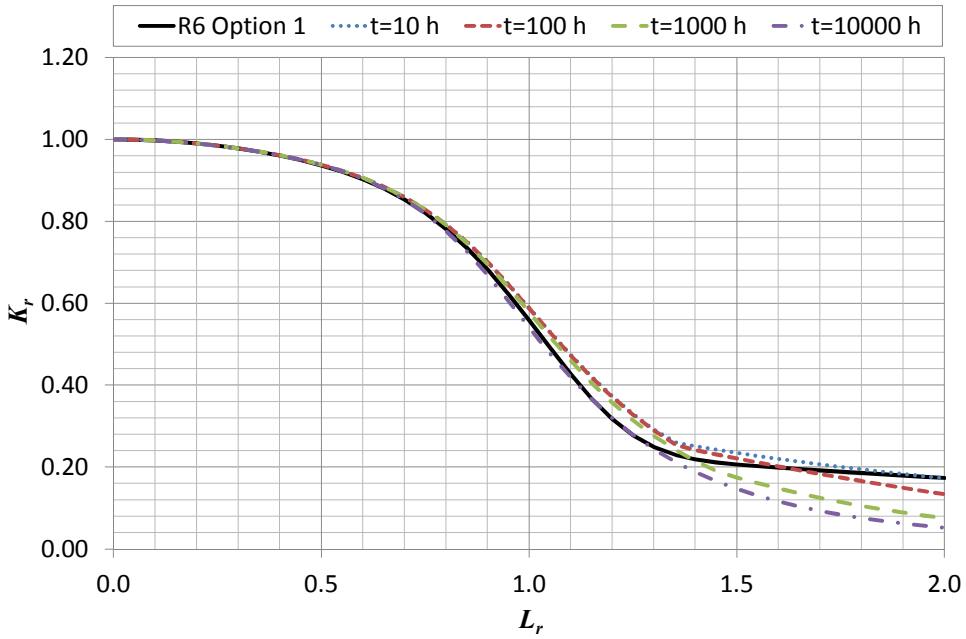

Figure 9.13: TDFAD for Type 316H compared to the R6 Option 1 curve.

TDFAD predictions of the time for 0.2 mm of crack extension to occur, based on the mean creep toughness data, are compared to the experimental measurements in Figure 9.14 for plane stress and plane strain conditions. There are fewer data points for plane stress conditions because instant failure due to plastic collapse is predicted for five specimens as a result of the large reference stress. The specimens predicted to fail immediately are 2D2/2 CT3, 1C2/3 CT5, 1C2/3 CT11, 2B1/2 CT14 and 2B1/4 CT15. These are the specimens with the highest reference stresses and the shortest failure times in Table 9.2.

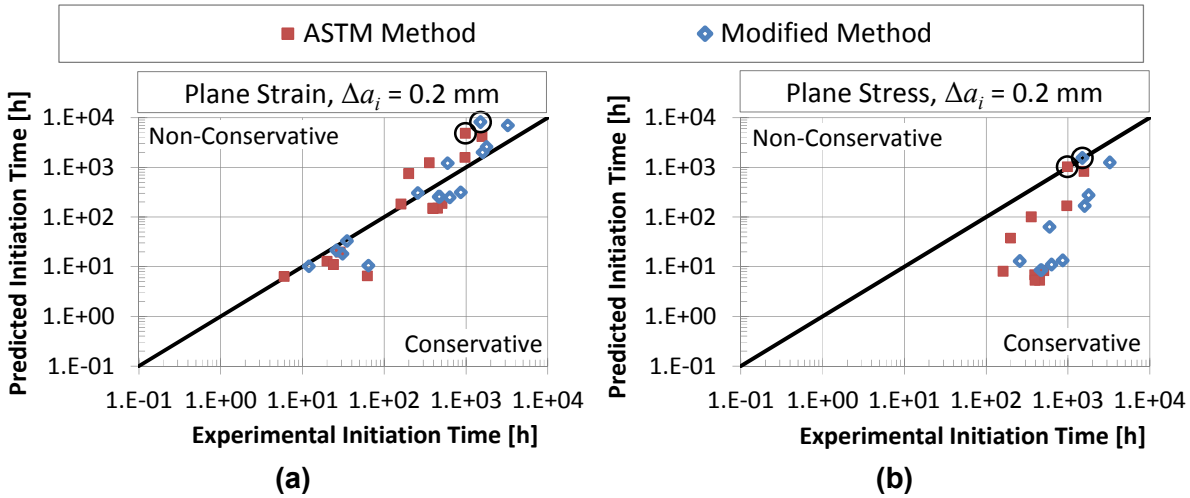

Figure 9.14: Comparison of crack initiation predictions, based on the TDFAD, with experimental measurements of 0.2 mm of crack of crack extension. Predictions are provided for (a) plane strain, and (b) plane stress conditions.

The results presented in Figure 9.14, based on the ASTM method, are consistent with a previous assessment [146]. The level of conservatism in the predictions is only slightly smaller for the modified method of interpreting the PD data. This is because the increase in experimental initiation time is offset by an increase in creep toughness. The plane stress predictions are approximately equal to or less than the experimental initiation times but some of the plane strain predictions are greater than the experimental values. If lower bound creep toughness data is applied, this non-conservatism is avoided for all specimens except 2D2/2 CT20 (circled).

The additional conservatism in the plane stress predictions is a result of the higher reference stresses which significantly increases the value of L_r. For plane strain conditions, the values of L_r when 0.2 mm of crack growth occurs at the assessment time are between 0.8 and 1.4 for all specimens. This corresponds to the steepest part of the TDFAD, as demonstrated in Figure 9.13, so the predictions are very sensitive to changes in L_r and therefore the assumed stress state.

The TDFAD has also been used to predict the time for crack initiation to occur from the increase in gradient on a plot of PD vs. CMOD using the corresponding values of creep toughness. The predictions for plane stress and plane strain conditions are compared to the experimental measurements in Figure 9.15.

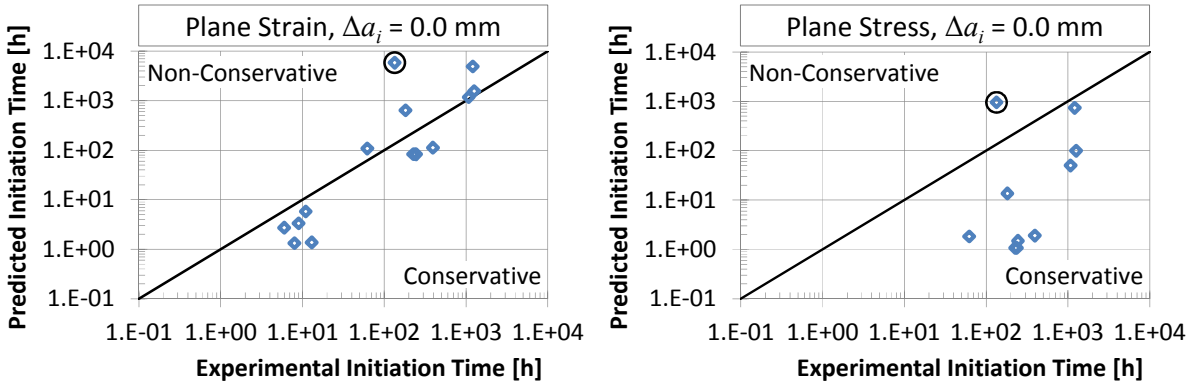

Figure 9.15: Comparison of crack initiation predictions, based on the TDFAD, with experimental measurements of the onset of crack growth (increase in gradient). Predictions are provided for (a) plane strain, and (b) plane stress conditions.

The results are similar to those for 0.2 mm of crack growth. With the exception of specimen 2D2/2 CT20 (circled), the plane stress predictions are all conservative but some of the plane strain predictions are non-conservative. Excluding this one data point, conservative predictions are obtained for both plane stress and plane strain if they are based on lower bound creep toughness data.

9.3.5 Summary of CCI Models

Table 9.7 provides a summary of the factors which must be applied to the experimental initiation times (Δa = 0.2 mm) to obtain the time predicted by each CCI model. Factors less than unity identify conservative predictions, and factors greater than unity (highlighted red) identify non-conservative predictions. For each model and stress state considered, the mean, maximum and minimum factors are provided. The values without parentheses omit specimen 2D2/2 CT20 which, due to fluctuations in the PD data results in a measured initiation time that was lower than the trend from the other 12 specimens and is not considered reliable. The values in parentheses include this test for comparison.

Initiation Model	Stress State	PD Interpretation	Mean	Maximum	Minimum
Sigma-d	Plane Stress	ASTM	0.181 (0.237)	0.529 **(1.016)**	0.025 (0.025)
		Modified	0.094 (0.132)	0.255 (0.666)	0.017 (0.017)
Modified CTOD	Plane Strain	ASTM	0.057 (0.069)	0.136 (0.246)	0.012 (0.012)
		Modified	0.030 (0.039)	0.068 (0.161)	0.007 (0.007)
	Plane Stress	ASTM	0.102 (0.125)	0.245 (0.447)	0.022 (0.022)
		Modified	0.054 (0.070)	0.123 (0.293)	0.013 (0.013)
TDFAD	Plane Strain	ASTM	**1.218** **(1.466)**	**3.747** **(4.931)**	0.105 (0.105)
		Modified	0.944 **(1.242)**	**2.134** **(5.414)**	0.163 (0.163)
	Plane Stress	ASTM	0.091 (0.155)	0.526 **(1.045)**	0.000 (0.000)
		Modified	0.062 (0.127)	0.385 **(1.031)**	0.000 (0.000)

Table 9.7: Mean, maximum and minimum factors on the experimental crack initiation times (Δa = 0.2 mm) necessary to obtain the predictions for the various CCI models. Non-conservative predictions are highlighted red. Factors without parentheses exclude specimen 2D2/2 CT20. The factors in parentheses include specimen 2D2/2 CT20.

Excluding specimen 2D2/2 CT20, all three models provide conservative predictions of the time for 0.2 mm of crack extension to occur with the exception of the TDFAD for plane strain

conditions however, as discussed above, conservative predictions may be obtained if lower bound creep toughness data is used. In general, the modified method of interpreting the PD data identifies increased levels of conservatism in the CCI models because it increases the experimental initiation times. For the tests considered here it approximately doubles the time for 0.2 mm of crack extension to occur, as identified in Section 9.2.4. For the Sigma-d and CTOD models this doubles the mean factors in Table 9.7 because the method of interpreting the PD data only influences the experimental measurements. For the TDFAD model, the mean factors in Table 9.7 are only increased by ~30% for plane stress and ~40% for plane strain compared to the ASTM method. This is because the increase in the measured initiation time is partially offset by a corresponding increase in creep toughness. In a few cases the TDFAD predictions based on the modified method of interpreting the PD data are less conservative than the predictions based on the ASTM method.

Table 9.8 provides a summary of the factors which must be applied to the experimental initiation times at the increase in gradient (Δa = 0.0 mm) to obtain the predicted values for each of the CCI models. The values without parentheses omit specimen 2D2/2 CT20 whilst the values in parentheses include this test. Factors less than unity identify conservative predictions, and factors greater than unity (highlighted red) identify non-conservative predictions.

Initiation Model	Stress State	Mean	Maximum	Minimum
Sigma-d	Plane Stress	0.255 (0.735)	0.685 **(7.454)**	0.037 (0.037)
CTOD	Plane Strain	0.083 (0.198)	0.181 **(1.808)**	0.016 (0.016)
	Plane Stress	0.149 (0.358)	0.330 **(3.279)**	0.029 (0.029)
TDFAD	Plane Strain	**1.040** **(3.872)**	**4.044** **(43.521)**	0.105 (0.105)
	Plane Stress	0.061 (0.531)	0.608 **(7.101)**	0.000 (0.000)

Table 9.8: Mean, maximum and minimum factors on the experimental crack initiation times (Δa = 0.0 mm) necessary to obtain the predictions for the various CCI models. Non-conservative predictions are highlighted red. Factors without parentheses exclude specimen 2D2/2 CT20. The factors in parentheses include specimen 2D2/2 CT20.

Again, excluding specimen 2D2/2 CT20, all of the models provide conservative predictions of the time to the onset of crack growth with the exception of the TDFAD model for plane

strain conditions although conservative predictions may be obtained using lower bound creep toughness data. For Type 316H the three CCI models considered here are therefore not only appropriate for predicting the time for 0.2 mm of crack extension to occur, but also appear to provide conservative predictions of the time to the onset of crack growth.

The predictions for specimen 2D2/2 CT20 are consistently less conservative than the other specimens. In Table 9.8 the factors for this specimen are an order of magnitude larger than the next biggest factor. This dramatic difference supports the suggestion that the fluctuations in the PD data observed for this specimen prevent the accurate measurement of initiation.

9.4 Discussion

An abrupt increase in gradient has been consistently identified on a plot of PD vs. CMOD for a series of thirteen creep crack growth tests performed on Type 316H stainless steel. PD data for these tests has been reanalysed assuming this corresponds to the onset of crack growth and compared to measurements based on the current method of interpreting the PD data in ASTM E1457-13 [3].

The correlation between C^* and the steady state crack growth rate is not significantly influenced by the modified method of interpreting the PD data for this material, but significant differences are observed when measuring small amounts of crack growth such as those associated with crack initiation. On average the time for 0.2 mm of crack extension to occur, based on the modified method is approximately double the time measured based on the ASTM method. This difference is due to creep strains which accumulate at the crack tip prior to the onset of crack growth which are erroneously interpreted as crack growth by the ASTM method.

For one of the tests (specimen 2D2/2 CT20) significant fluctuations in the PD data were observed which resulted in low crack initiation times compared to the trends observed from the other 12 tests. The results for this test have therefore been treated with caution. If these fluctuations were caused by changes in temperature or amplifier drift a reference measurement would have improved the quality of the test data. The reduced noise and thermal stability of the low frequency ACPD system may also have improved the data.

In some of the tests an increase in the gradient of the PD vs. CMOD record was observed immediately after load-up. This results in a significant over-estimation of the crack length and an under-estimation of the initiation time when the PD data is interpreted using the ASTM method compared to the modified method. These tests also demonstrated a particularly large tail on a plot of C^* vs. crack growth rate when interpreted using the ASTM

method. Similar behaviour was observed in one of the interrupted tests in the previous chapter which demonstrates that it is specimen, not material, specific. In this regard it is similar to the drop in PD which is also sometimes observed at the start of a creep crack growth test and may even be caused by the same mechanism (which is currently unknown).

The experimental CCI times have been compared to the three prediction models provided in R5 [4]: Sigma-d, CTOD and TDFAD. An alternative version of the CTOD model has been used here due to the lack of critical CTOD measurements available for Type 316H. In general all three models provide conservative predictions of the time for 0.2 mm of crack extension to occur although lower bound creep toughness properties are required for the TDFAD model for plane strain conditions. This conservatism is sufficient that the predictions remain conservative even when compared the onset of crack growth obtained from the increase in gradient on a plot of CMOD vs. PD. These conclusions are currently only applicable to Type 316H. Further validation is necessary to extend them to other materials.

Chapter 10: Conclusions and Further Work

10.1 Conclusions

In this study a detailed review of the common errors associated with the PD technique has been performed. It has been demonstrated that when applied to ductile materials, large inelastic strains are often the most significant source of error, particularly during the early stages of the test, prior to the onset of crack growth. Appropriate methods of mitigating these errors have been identified which facilitate the accurate measurement of crack initiation and growth in the presence of large strains.

In order to obtain accurate measurements of crack extension it is essential to use an appropriate PD configuration. Configurations for C(T) and SEN specimens have been identified which are optimum for a wide range of structural materials whether measuring small or large amounts of crack growth. These configurations may also be read-across to other similar specimen geometries. Suitable configurations for additional measurements used to supress proportional changes in PD due to, for example, fluctuations in specimen temperature, have also been identified.

Even when adopting these optimum PD configurations, errors in the measurement of extension are inevitable due to slight misplacement of the electrical connections and noise on the measurement signal. These errors are most significant when measuring small amounts of crack extension. For a specimen with high resistivity e.g. stainless steel, measured using a typical DCPD system, these errors are low (<5%) but for a specimen with low resistivity e.g. aluminium, they can be an order of magnitude higher due to the reduced signal-to-noise ratio. To mitigate these additional errors a low frequency ACPD system has been used in this study, which incorporates a lock-in amplifier to filter out much of the noise. It also demonstrates improve thermal stability compared to a typical DCPD system so it is less susceptible to fluctuations in ambient conditions e.g. lab temperature.

Geometric assumptions in the derivation of the calibration function used to correlate PD measurements with crack length are another common source of error. When measuring small amounts of crack extension errors >60% can occur. Crack tunnelling can account for a large part of this error when the calibration function assumes a straight fronted crack, but differences between the actual and assumed notch geometry can also be significant. In order to obtain accurate measurements of crack extension it is necessary to apply appropriate side-grooves to the specimen and derive a calibration function for the specific test geometry rather than using a calibration function from the literature for which the exact input assumptions are often unknown.

When the derivation of a calibration function is not practical, and one is not available in the literature, Johnson's calibration function [58] may be applied to most common specimen geometries using the PD configurations derived in Chapter 5. Although this will introduce additional errors in the measurement of crack extension, they are relatively modest compared to the other sources of error identified above so this approach should provide a reasonable approximation of crack extension. Despite this it is always preferable to derive a calibration function specifically for the geometry being tested wherever possible.

The influence of plastic strain on PD has been measured experimentally and can result in very large spurious crack extensions although this can be reduced by selecting an appropriate PD configuration. Suitable configurations for C(T) and SEN(T) specimens have been identified. For C(T) specimens it is important that the PD probes are not on the opposite side of the loading holes to the crack tip to avoid the influence of the large strains around the hole. This is contrary to the recommended configurations in many standards [3, 4]. Although the influence of strain may be reduced by selecting an appropriate PD configuration it cannot be avoided altogether and spurious crack extensions multiple times greater than the 0.2 mm 'engineering' definition of crack initiation are possible. This is much larger than the other sources of error identified above. It is therefore of vital importance to develop experimental methods capable of suppressing the influence of strain on PD measurements.

To help develop these experimental methods a sequentially coupled structural-electrical FE based tool has been produced which is capable of predicting the influence of strain on PD measurements. For simplicity, the modelling approach only considers geometric effects which dominate when the strains are inelastic. The only material data required to implement this model is a uniaxial stress-strain curve because, by appropriate normalisation the model predictions are independent of the electrical material properties. This FE tool has been validated by comparison with experimental measurements performed on uniaxial, SEN(T) and C(T) specimens. The FE results consistently under-predict the influence of strain on

PD. This is because the variation in electrical resistivity due to strain is not included which, although secondary to the geometric effects, remains significant. Despite this limitation, this FE tool has been demonstrated to accurately predict trends in PD due to strain which is adequate for the studies performed in this research where it has been used to determine the general PD response rather than the magnitude of this response.

The PD technique is often used to measure crack extension during fracture toughness testing where the influence of strain can be significant. During these tests two different mechanisms increase the crack length: blunting and stable tearing. Two methods of interpreting the PD data are included in some standards e.g. [1, 2]. One method uses it to measure both of these mechanisms whilst the other only uses it to measure stable tearing. Using the FE tool developed above in conjunction with experimental data it has been demonstrated that the PD technique is not suitable for measuring crack extension due to blunting and is only suitable for measuring stable tearing. This is because significant strain occurs during blunting and the PD is sensitive to the entire strain field and not just the crack tip geometry. For stable tearing the change in PD due to strain is generally small compared to that due to crack extension. The onset of stable tearing can be identified from an abrupt increase in gradient on a plot of PD vs. COD and the prior crack extension due to blunting may be predicted using a suitable blunting line. For materials which demonstrate significant strain hardening the blunting lines provided in ESIS P2-92 [1] and ISO 12135 [2] are appropriate. Using this approach measurements of stable tearing are in good agreement with the post-test fracture surface measurements and the elastic unloading compliance technique.

An experimentally observed limitation of this approach is that the increase in gradient on a plot of PD vs. COD becomes difficult to discern for high toughness, high tearing resistant, high strain hardening materials. To investigate this limitation the FE tool for predicting the influence of strain on PD measurements has been extended to incorporate crack extension. The FE analysis confirmed that this is a fundamental limitation of the PD technique. In such materials, small increases in crack length are accompanied by large increases in strain which can obscure the change in slope. For such materials, the elastic unloading compliance technique may be more suitable.

Unlike fracture toughness testing, there is currently no method of separating blunting from crack growth in creep crack growth tests. As such, creep strain which occurs during the initial incubation period is erroneously interpreted as crack extension when the PD data is interpreted in accordance with the procedure in ASTM E1457-13 [3]. To investigate whether a similar method to that used during fracture toughness testing may be applied, a series of interrupted creep crack growth tests have been performed. The results demonstrate that an

abrupt increase in gradient on a plot of PD vs. COD consistently occurs and that this corresponds to the point where micro-voids ahead of the crack tip first link up with the pre-crack. Prior to this point, the change in PD is primarily due to the accumulation of creep strains. In creep ductile materials, such as P91 steel, these strains can produce spurious crack extensions much greater than 0.2 mm which will result in very conservative initiation times. A modified method of interpreting the PD data analogous to that used for fracture toughness testing has been proposed.

The interrupted creep crack growth tests also demonstrate that the PD technique can struggle to accurately measure creep crack growth in the presence of discontinuous cracking. In one case the PD only predicted ~30% of the crack extension measured from the post-test fracture surface. It is recommended that the PD data should always be corrected based on fracture surface measurements. In the presence of discontinuous cracking this should generally result in conservative crack growth rate measurements.

Potential limitations of the proposed method of interpreting the PD data from creep crack growth tests have been investigated using the FE based tool. It has been demonstrated that similar to fracture toughness testing the increase in gradient may become difficult to observe for materials with very high creep ductility. It has also been demonstrated that stress redistribution will cause non-linearity in the plot of PD vs. COD which may also make the change in slope more difficult to discern. Despite these limitations, the results suggest that for most engineering materials an increase in gradient should be observed.

The proposed method of interpreting the PD data has been used to reanalyse a series of 13 creep crack growth tests performed on Type 316H stainless steel at 550°C. For all tests an increase in gradient was observed on a plot of PD vs. COD. On average the modified method increased the measured time for 0.2 mm of crack extension to occur by a factor of 2 compared to the current method in ASTM E1457-13 and the onset of crack growth, identified from the change in slope, occurred after ~40% of the time for 0.2 mmm of crack extension to occur. These measurements have been compared to predictions based on the three CCI models provided in R5 [4]: Sigma-d, CTOD and TDFAD. An alternative version of the CTOD model was used due to the lack of critical CTOD measurements available for Type 316H. The modified method of interpreting the PD data increases the level of conservatism in these models compared to the time for 0.2 mm of crack extension to occur although lower bound creep toughness properties were required to obtain conservative predictions for the TDFAD model under plane strain conditions. For Type 316H, the models remain conservative when compared the onset of crack growth obtained from the abrupt increase in gradient on a plot of CMOD vs. PD, but this may not apply to all materials.

10.2 Further Work

The method proposed for interpreting PD data during creep crack growth testing has only been applied to specimens manufactured from Type 316H stainless steel with the exception of a single test performed on P91. To fully validate the proposed method, it should be applied to a wide range of materials. This should include materials with very high creep ductility in order to identify the maximum errors which could occur due to creep strain when using the current ASTM method of interpreting the PD data. It will also demonstrate if the increase in gradient becomes more difficult to identify as predicted in this work. Materials which demonstrate significant stress redistribution should also be tested to validate the PD response predicted by the FE models. The assessment of a wide range of materials need not require significant additional testing because the PD data from existing tests may be reanalysed but some interrupted tests performed on other materials would be prudent.

Most of the tests performed as part of this research used homogenous specimens but one of the most common sources of defects in real structures are welds. The fracture toughness and creep crack growth properties of welds are therefore of particular interest and tests should be performed on suitable specimens to identify if the proposed PD methods remain applicable. The PD response of a specimen containing a weld is likely to be significantly more complex than a homogenous specimen due to the combination of primary and secondary loading as well as the different material properties. The FE tool developed in this work can be used to help interpret this response.

Further work could also be performed to improve the accuracy of the FE model. Strain dependent electrical properties would significantly improve the predictions albeit at the expense of a much more complicated model. Also, a more detailed model of the interaction between creep and plasticity may also improve the predictions. These are currently modelled as independent mechanisms but it is widely known that they interact [142]. Both are driven by dislocations so the introduction of dislocations by either mechanism will influence the subsequent deformation behaviour due to strain hardening. By improving the accuracy of the FE predictions, the tool developed in this study could be used to predict the magnitude of the changes in PD due to strain and not just the general trends. Changes in PD due to strain predicted from the FE could then be subtracted from experimental measurements to allow the PD technique to be applied in situations where an increase in gradient is not easily observed.

This work has raised significant questions with regards to how creep crack growth tests are analysed. The interrupted tests presented in this work are not valid in accordance with ASTM E1457-13 [3]. This is due to the discontinuous cracking which is typical of creep

crack growth so many tests are likely to be invalid. This is unsatisfactory, particularly for long term tests which can last months or even years. In the presence of discontinuous cracking the PD technique alone is not suitable for measuring crack extension without some form of correction. It is suggested in this work that the linear correction currently included in ASTM E1457-13 may be sufficient to produce conservative crack growth rates. Further work should be performed to help understand the evolution of discontinuous creep cracks and identify the most appropriate method of monitoring them. Tomographic imaging techniques could be used for this purpose.

Finally, it has been demonstrated that there is more conservatism in the CCI models presented in the R5 assessment procedure than originally thought which could lead to components being removed from service prematurely. Many of the models are based on simplified assumptions such as steady-state conditions which are often not applicable during incubation. The experimental techniques proposed in this work could be used to justify revisiting these models to remove some of this conservatism by incorporating more realistic assumptions.

References

1. ESIS P2-92, *ESIS Procedure for Determining the Fracture Behaviour of Materials*, European Structural Integrity Society, 1992.
2. ISO 12135:2002, *Metalic Materials - Unified Method of Test for the Determination of Quasistatic Fracture Toughness*, International Organization for Standardization, Geneva, Switzerland, 2002.
3. ASTM E1457-13, *Standard Test Method for Measurement of Creep Crack Growth Times in Metals*, ASTM International, West Conshohocken, PA, USA, 2013.
4. R5 Issue 3 Revision 1, *Assessment Procedure for the High Temperature Response of Structures*, EDF Energy Nuclear Generation Ltd, 2012.
5. Evans, R. W. and Wilshire, B., *Creep of Metals and Alloys*, The Institute of Metals, 1985.
6. Webster, G. A. and Ainsworth, R. A., *High temperature Component Life Assessment*, Chapman and Hall, 1994.
7. RCC-MR Appendix 16, *Guide for Leak Before Break Analysis and Defect Assessment*, AFCEN, 2002.
8. Webster, G. A., Davies, C. M., Skelton, R. P. and Nikbin, K. M., *Comparison of R5 Volume 4/5 Procedures for Determining Creep-Crack Incubation Periods in Type 316H Stainless Steel*, I.C. Consultants, ME 115/01, 2008.
9. Saxena, A., *Nonlinear Fracture Mechanics for Engineers*, CRC press, 1998.
10. Benham, P. P., Crawford, R. J. and Armstrong, C. G., *Mechanics of Engineering Materials*, Second Edition, Longman Group Limited, 1996.
11. Rice, J. R. and Tracey, D. M., *On the Ductile Enlargement of Voids in Triaxial Stress Fields*, Journal of the Mechanics and Physics of Solids, 1969, **17**(3), pp. 201-217.
12. Cocks, A. C. F. and Ashby, M. F., *Intergranular Fracture during Power-Law Creep under Multiaxial Stresses*, Metal Science, 1980, **14**(8-9), pp. 395-402.
13. Oh, C., Kim, N., Kim, Y., Davies, C. M., Nikbin, K. M. and Dean, D. W., *Creep Failure Simulations of 316H at 550 C: Part I – A Method and Validation*, Engineering Fracture Mechanics, 2011, **78**(17), pp. 2966-2977.

14. Yatomi, M., Nikbin, K. M. and O'Dowd, N. P., *Creep Crack Growth Prediction Using a Damage Based Approach*, International Journal of Pressure Vessels and Piping, 2003, **80**(7), pp. 573-583.

15. Davies, C. M., Dean, D. W., Yatomi, M. and Nikbin, K. M., *The Influence of Test Duration and Geometry on the Creep Crack Initiation and Growth Behaviour of 316H Steel*, Materials Science and Engineering: A, 2009, **510-511**, pp. 202-206.

16. Griffith, A. A., *The Phenomena of Rupture and Flow in Solids*, Philosophical Transactions of the Royal Society of London, Series A, 1921, pp. 163-198.

17. Anderson, T. L., *Fracture Mechanics: Fundamentals and Applications*, Third Edition, CRC press, 2005.

18. Tada, H., Paris, P. C. and Irwin, G. R., *The Stress Analysis of Cracks Handbook*, Third Edition, American Society of Mechanical Engineers, 2000.

19. Irwin, G. R., *Plastic Zone Near a Crack and Fracture Toughness*, in *Seventh Sagamore Ordnance Materials Research Conference*, New York, USA, August 16-19, 1960,

20. Kumar, V., German, M. D. and Shih, C. F., *Engineering Approach for Elastic-Plastic Fracture Analysis*, General Electric Company, EPRI NP-1931, 1981.

21. Irwin, G. R., *Analysis of Stresses and Strains Near the End of a Crack Traversing a Plate*, Journal of Applied Mechanics, 1957, **24**, pp. 361-364.

22. Rice, J. R., *A Path Independent Integral and the Approximate Analysis of Strain Concentration by Notches and Cracks*, Journal of Applied Mechanics, 1968, **35**(2), pp. 379-386.

23. Hutchinson, J. W., *Singular Behaviour at the End of a Tensile Crack in a Hardening Material*, Journal of the Mechanics and Physics of Solids, 1968, **16**(1), pp. 13-31.

24. Rice, J. R. and Rosengren, G. F., *Plane Strain Deformation Near a Crack Tip in a Power-Law Hardening Material*, Journal of the Mechanics and Physics of Solids, 1968, **16**(1), pp. 1-12.

25. Shih, C. F., *Tables of Hutchinson-Rice-Rosengren Singular Field Quantities*, Division of Engineering, Brown University, MRL E-147, 1983.

26. Wells, A. A., *Unstable Crack Propagation in Metals: Cleavage and Fast Fracture*, in *Proceedings of the Crack Propagation Symposium*, Cranfield, UK, 1961,

27. ASTM E1820-13, *Standard Test Method for Measurement of Fracture Toughness*, ASTM International, West Conshohocken, PA, USA, 2013.

28. Heerens, J., Cornec, A. and Schwalbe, K., *Results of a Round Robin on Stretch Zone Width Determination*, Fatigue & Fracture of Engineering Materials & Structures, 1988, **11**(1), pp. 19-29.

29. Shih, C. F., *Relationships Between the J-Integral and the Crack Opening Displacement for Stationary and Extending Cracks*, Journal of the Mechanics and Physics of Solids, 1981, **29**(4), pp. 305-326.

30. Landes, J. D. and Begley, J. A., *Test Results from J-Integral Studies: An Attempt to Establish a J_{IC} Testing Procedure*, Fracture Analysis, ASTM STP 560, 1974, pp. 170-186.

31. Heerens, J., Schwalbe, K. and Cornec, A., *Modifications of ASTM E 813-81 Standard Test Method for an Improved Definition of J_{IC} Using New Blunting Line Equations*, Fracture Mechanics: Eighteenth Symposium, ASTM STP 945, 1988, pp. 374-389.

32. McMeeking, R. M., *Finite Deformation Analysis of Crack-Tip Opening in Elastic-Plastic Materials and Implications for Fracture*, Journal of the Mechanics and Physics of Solids, 1977, **25**(5), pp. 357-381.

33. Landes, J. D., *The Blunting Line in Elastic-Plastic Fracture*, Fatigue and Fracture of Engineering Materials & Structures, 1995, **18**(11), pp. 1289-1297.

34. BS 7448-4:1997, *Fracture Mechanics Toughness Tests - Part 4: Method for Determination of Fracture Resistance Curves and Initiation Values for Stable Crack Extension in Metalic Materials*, British Standards Institute, London, 1997.

35. R6 Revision 4, *Assessment of the Integrity of Structures Containing Defects*, EDF Energy Nuclear Generation Ltd., 2000.

36. Dowling, A. R. and Townley, C. H. A., *The Effect of Defects on Structural Failure: A Two-Criteria Approach*, International Journal of Pressure Vessels and Piping, 1975, **3**(2), pp. 77-107.

37. Bloom, J. M., *Prediction of Ductile Tearing Using a Proposed Strain Hardening Failure Assessment Diagram*, International Journal of Fracture, 1980, **16**(2), pp. R73-R77.

38. Ainsworth, R. A., *The Assessment of Defects in Structures of Strain Hardening Material*, Engineering Fracture Mechanics, 1984, **19**(4), pp. 633-642.

39. Rice, J. R., Paris, P. C. and Merkle, J. G., *Some Further Results of J-Integral Analysis and Estimates*, Progress in Flaw Growth and Fracture Toughness Testing, ASTM STP 536, 1973, pp. 231-245.

40. Davies, C. M., Kourmpetis, M., O Dowd, N. P. and Nikbin, K. M., *Experimental Evaluation of the J or C* Parameter for a Range of Crack Geometries*, Fatigue and Fracture Mechanics: 35th Volume, ASTM STP 1480, 2007, pp. 321-340.

41. Riedel, H. and Rice, J. R., *Tensile Cracks in Creeping Solids*, Fracture Mechanics, ASTM STP 700, 1980, pp. 112-130.

42. Haigh, J. R., *The Mechanisms of Macroscopic High Temperature Crack Growth Part I: Experiments on Tempered Cr-Mo-V Steels*, Materials Science and Engineering, 1975, **20**, pp. 213-223.

43. Nikbin, K. M., Smith, D. J. and Webster, G. A., *Influence of Creep Ductility and State of Stress on Creep Crack Growth*, Advances in Life Prediction Methods at Elevated Temperatures, 1983, pp. 249-258.

44. Nikbin, K. M., Smith, D. J. and Webster, G. A., *Prediction of Creep Crack Growth from Uniaxial Creep Data*, Proceedings of the Royal Society of London A: Mathematical and Physical Sciences, 1984, **396**(1810), pp. 183-197.

45. Mehmanparast, A., Davies, C. M., Webster, G. A. and Nikbin, K. M., *Creep Crack Growth Rate Predictions in 316H Steel Using Stress Dependent Creep Ductility*, Materials at High Temperatures, 2014, **31**(1), pp. 84-94.

46. Webster, G. A., *Lifetime Estimates of Cracked High Temperature Components*, International Journal of Pressure Vessels and Piping, 1992, **50**(1), pp. 133-145.

47. Neuber, H., *Theory of Stress Concentration for Shear-Strained Prismatical Bodies with Arbitrary Nonlinear Stress-Strain Law*, Journal of Applied Mechanics, 1961, **28**(4), pp. 544-550.

48. Ainsworth, R. A., *The Initiation of Creep Crack Growth*, International Journal of Solids and Structures, 1982, **18**(10), pp. 873-881.

49. Ainsworth, R. A., *The Use of a Failure Assessment Diagram for Initiation and Propagation of Defects at High Temperatures*, Fatigue & Fracture of Engineering Materials & Structures, 1993, **16**(10), pp. 1091-1108.

50. Davies, C. M., O'Dowd, N. P., Dean, D. W., Nikbin, K. M. and Ainsworth, R. A., *Failure Assessment Diagram Analysis of Creep Crack Initiation in 316H Stainless Steel*, International Journal of Pressure Vessels and Piping, 2003, **80**(7), pp. 541-551.

51. Davies, C. M., *Crack Initiation and Growth at Elevated Temperatures in Engineering Steels*, Ph.D. and D.I.C. Thesis, Department of Mechanical Engineering, Imperial College London, 2006.

52. Wilkowski, G. M. and Maxey, W. A., *Review and Applications of the Electronic Potential Method for Measuring Crack Growth in Specimens, Flawed Pipes and Pressure Vessels*, Fracture Mechanics: Fourteenth Symposium-Volume II: Testing and Applications, ASTM STP 791, 1983, pp. 266-294.

53. Merah, N., *Detecting and Measuring Flaws Using Electric Potential Techniques*, Journal of Quality in Maintenance Engineering, 2003, **9**(2), pp. 160-175.

54. Madhi, E., Sposito, G., Davies, C. M., Cawley, P. and Nagy, P. B., *In-Situ Creep Monitoring Using The Potential Drop Method*, in *AIP Conference Proceedings*, San Diego, USA, **1335**, pp. 1631-1638, 18-23 July, 2010,

55. ASTM E647-13a, *Standard Test Method for Measurement of Fatigue Crack-Growth Rates*, ASTM International, West Conshohocken, PA, USA, 2013.

56. Aronson, G. H. and Ritchie, R. O., *Optimization of the Electrical Potential Technique for Crack Growth Monitoring in Compact Test Pieces Using Finite Element Analysis*, Journal of Testing and Evaluation, 1979, **7**(4), pp. 208-215.

57. Saxena, A., *Electrical Potential Technique for Monitoring Subcritical Crack Growth at Elevated Temperatures*, Engineering Fracture Mechanics, 1980, **13**(4), pp. 741-750.

58. Johnson, H. H., *Calibrating the Electric Potential Method for Studying Slow Crack Growth*, Materials Research and Standards, 1965, **5**(9), pp. 442-445.

59. Donald, J. K. and Ruschau, J., *Direct Current Potential Difference Fatigue Crack Measurement Techniques*, Fatigue Crack Measurement: Techniques and Applications, K.J. Marsh, R.A. Smith, and R.O. Ritchie (Eds), Engineering Materials Advisory Services Ltd., 1991, pp. 11-37.

60. McCartney, L. N., Irving, P. E., Symm, G. T., Cooper, P. M. and Kurzfeld, A., *Measurement of Crack Lengths in Compact Tension and Single Edge Notch Specimens using a New Electrical Potential Calibration*, National Physical Laboratory, DMA(B)3, February, 1977.

61. Paul, C. R. and Nasar, S. A., *Introduction to Electromagnetic Fields*, Second Edition, McGraw-Hill, 1987.

62. Clark, G. and Knott, J. F., *Measurement of Fatigue Cracks in Notched Specimens by Means of Theoretical Electrical Potential Calibrations*, Journal of the Mechanics and Physics of Solids, 1975, **23**(4–5), pp. 265-276.

63. Vanstone, R. H. and Richardson, T. L., *Potential-Drop Monitoring of Cracks in Surface-Flawed Specimens*, Automated Test Methods for Fracture and Fatigue Crack Growth, ASTM STP 877, 1985, pp. 148-166.

64. Gangloff, R. P., *Electrical Potential Monitoring of Crack Formation and Subcritical Growth from Small Defects*, Fatigue & Fracture of Engineering Materials & Structures, 1981, **4**(1), pp. 15-31.

65. Gilbey, D. M. and Pearson, S., *Measurement of the Length of a Central or Edge Crack in a Sheet of Metal by an Electrical Resistance Method*, Royal Aircraft Establishment, 66402, 1966.

66. Schwalbe, K. and Hellmann, D., *Application of the Electrical Potential Method to Crack Length Measurements using Johnson's Formula*, Journal of Testing Evaluation, 1981, **9**(3), pp. 218-221.

67. Gandossi, L., Summers, S. A., Taylor, N. G., Hurst, R. C., Hulm, B. J. and Parker, J. D., *The Potential Drop Method for Monitoring Crack Growth in Real Components Subjected to Combined Fatigue and Creep Conditions: Application of FE Techniques for Deriving Calibration Curves*, International Journal of Pressure Vessels and Piping, 2001, **78**(11–12), pp. 881-891.

68. Hicks, M. A. and Pickard, A. C., *A Comparison of Theoretical and Experimental Methods of Calibrating the Electrical Potential Drop Technique for Crack Length Determination*, International Journal of Fracture, 1982, **20**(2), pp. 91-101.

69. Ritchie, R. O. and Bathe, K. J., *On the Calibration of the Electrical Potential Technique for Monitoring Crack Growth Using Finite Element Methods*, International Journal of Fracture, 1979, **15**(1), pp. 47-55.

70. Hill, M. R. and Stuart, D. H., *Direct Current Potential Difference Correlation for Open-Hole, Single-Crack Coupons*, Engineering Fracture Mechanics, **99**, pp. 141-146.

71. Klintworth, G. C. and Webster, G. A., *Optimization of Electrical-Potential Methods of Measuring Crack Growth*, The Journal of Strain Analysis for Engineering Design, 1979, **14**(4), pp. 187-192.

72. Ke, Y. and Ståhle, P., *Crack Length Measurements with a Potential Drop Method: A Finite Element Simulation*, International Journal for Numerical Methods in Engineering, 1993, **36**(18), pp. 3205-3220.

73. Wei, R. P. and Brazill, R. L., *An Assessment of AC and DC Potential Systems for Monitoring Fatigue Crack Growth*, Fatigue Crack Growth Measurement and Data Analysis, ASTM STP 738, 1981, pp. 103-119.

74. Li, D. M. and Bakker, A., *Fracture Toughness Evaluation using Circumferentially-Cracked Cylindrical Bar Specimens*, Engineering Fracture Mechanics, 1997, **57**(1), pp. 1-11.

75. Lowes, J. M. and Fearnehough, G. D., *The Detection of Slow Crack Growth in Crack Opening Displacement Specimens Using an Electrical Potential Method*, Engineering Fracture Mechanics, 1971, **3**(2), pp. 103-104.

76. McIntyre, P. and Priest, A., *Measurement of Sub-Critical Flaw Growth in Stress Corrosion, Cyclic Loading and High Temperature Creep by the DC Electrical Resistance Technique*, MG/54/71, 1971.

77. Merah, N., Bui-Quoc, T. and Bernard, M., *Calibration of DC Potential Technique using an Optical Image Processing System in LCF Testing*, Journal of Testing and Evaluation, 1995, **23**(3), pp. 160-167.

78. Freeman, B. L. and Neate, G. J., *The Measurement of Crack Length During Fracture at Elevated Temperatures Using the D. C. Potential Drop Technique*, The Measurement of Crack Length and Shape During Fracture and Fatigue, C.J. Beevers (Ed.), Engineering Materials Advisory Services Ltd., 1980.

79. Venkatsubramanian, T. V. and Unvala, B. A., *An AC Potential Drop System for Monitoring Crack Length*, Journal of Physics E: Scientific Instruments, 1984, **17**(9), pp. 765-771.

80. Hartman, G. A. and Johnson, D. A., *D-C Electric-Potential Method Applied to Thermal/Mechanical Fatigue Crack Growth*, Experimental Mechanics, 1987, **27**(1), pp. 106-112.

81. Marandet, B. and Sanz, G., *Experimental Verification of the J_{IC} and Equivalent Energy Methods for the Evaluation of the Fracture Toughness of Steels*, Flaw Growth and Fracture, ASTM STP 631, 1977, pp. 462-476.

82. Bicego, V., Liviero, D., Fossati, C. and Lucon, E., *JR Curve Testing Utilizing the Reversing Direct Current Electrical Potential Drop Method*, Applications of

Automation Technology to Fatigue and Fracture Testing, ASTM STP 1092, 1990, pp. 143-166.

83. Ljustell, P., *The Effect of Large Scale Plastic Deformation on Fatigue Crack Length Measurement with the Potential Drop Method*, Journal of Testing and Evaluation, 2011, **39**(6), pp. 985-1002.

84. Ritchie, R. O., Garrett, G. G. and Knott, J. F., *Crack-Growth Monitoring: Optimisation of the Electrical Potential Technique using an Analogue Method*, International Journal of Fracture Mechanics, 1971, **7**(4), pp. 462-462.

85. Arlt, G., *The Sensitivity of Strain Gauges*, Journal of Applied Physics, 1978, **49**(7), pp. 4273-4274.

86. Sciammarella, C. A. and Sciammarella, F. M., *Experimental Mechanics of Solids*, Wiley-Blackwell, 2012.

87. Neubert, H. K. P., *Strain Gauges Kinds and Uses*, Macmillan & Co. Ltd., 1967.

88. Hannah, R. L. and Reed, S. E., *Strain Gauge User's Handbook*, Elsevier Science Publishers Ltd., 1992.

89. Madhi, E. and Nagy, P. B., *Sensitivity Analysis of a Directional Potential Drop Sensor for Creep Monitoring*, NDT & E International, 2011, **44**(8), pp. 708-717.

90. Brinnel, V., Döbereiner, B. and Münstermann, S., *Characterizing Ductile Damage and Failure: Application of the Direct Current Potential Drop Method to Uncracked Tensile Specimens*, Procedia Materials Science, 2014, **3**, pp. 1161-1166.

91. Bakker, A., *A DC Potential Drop Procedure for Crack Initiation and R-Curve Measurements During Ductile Fracture Tests*, Elastic-Plastic Fracture Test Methods: The User's Experience, ASTM STP 856, 1985, pp. 394-410.

92. Hollstein, T., Blauel, J. G. and Voss, B., *On the Determination of Elastic-Plastic Fracture Material Parameters: A Comparison of Different Test Methods*, Elastic-Plastic Fracture Test Methods: The User's Experience, ASTM STP 856, 1985, pp. 104-116.

93. Krompholz, K., Grosser, E. D., Ewert, K. and Moritz, E., *Application of the DC Potential Drop Technique in the High Temperature Regime*, Advances in Crack Length Measurement, Engineering Materials Advisory Services Ltd., 1982, pp. 231-250.

94. Madhi, E., *In-Situ Creep Monitoring Using Directional Potential Drop Sensors*, Ph.D. Thesis, Department of Aerospace Engineering, University of Cincinnati, 2010.

95. Dai, Y., Marchand, N. J. and Hongoh, M., *Fatigue Crack Growth Measurements in TMF Testing of Titanium Alloys Using an ACPD Technique*, Special Applications and Advanced Techniques for Crack Size Determination, ASTM STP 1251, 1995, pp. 17-32.

96. Verpoest, I., Aernoudt, E., Deruyttere, A. and Neyrinck, M., *An ACPD Method for Detection and Measurement of Surface Microcracks during Fatigue Testing of Wires*, Advances in Crack Length Measurement, B. C.J. (Ed.), Engineering Materials Advisory Services Ltd., 1982.

97. Unvala, B. A., *Method, Test Probe and Apparatus for the Measurement of Alternating Current Potential Drop by Confining Test Current to a Skin Region of a Test Specimen*, Google Patents, 1993.

98. Tikui, S., Marchand, N. J. and Unvala, B., *An Advanced Multiple Frequency ACPD System for Crack Detection and Calibration*, Nontraditional methods of sensing stress, strain, and damage in materials and structures, ASTM STP 1318, 1997, pp. 56-70.

99. Gibson, G. P., *The use of Alternating Current Potential Drop for Determining J-Crack Resistance Curves*, Engineering Fracture Mechanics, 1987, **26**(2), pp. 213-222.

100. Okumura, N., Venkatasubramanian, T. V., Unvala, B. A. and Baker, T. J., *Application of the AC Potential Drop Technique to the Determination of R Curves of Tough Ferritic Steels*, Engineering Fracture Mechanics, 1981, **14**(3), pp. 617-625.

101. Gibson, G. P., *Evaluation of the AC Potential Drop Method to Determine J-Crack Resistance Curves for a Pressure Vessel Steel*, Engineering Fracture Mechanics, 1989, **32**(3), pp. 387-401.

102. Satyanarayana, D. V. V., Omprakash, C. M., Sridhar, T. and Kumar, V., *Effect of Microstructure on Creep Crack Growth Behavior of a Near-α Titanium Alloy IMI-834*, Metallurgical and Materials Transactions A, 2009, **40**(1), pp. 128-137.

103. Inuil, M., Watanabe, Y., Kondo, T., Suzuki, K. and Kano, K., *Crack Growth Behavior of Ferritic Steel for USC Boilers in Pressurized Superheated Steam*, Materials at High Temperatures, 2001, **18**(2), pp. 119-124.

104. Collins, R. and Lugg, M. C., *Use of AC Field Measurements for Non-Destructive Testing*, Fatigue Crack Measurement: Techniques and Applications, Engineering Materials Advisory Services Ltd., 1991, pp. 39-67.

105. Wei, R. P. and Brazill, R. L., *An A.C. Potential System for Crack Length Measurement*, The Measurement of Crack Length and Shape During Fracture and Fatigue, C.J. Beevers (Ed.), Engineering Materials and Advisory Services Ltd., 1980, pp. 190-201.

106. Neale, B. K. and Priest, R. H., *On the Unloading Compliance Method for Crack Length Measurement*, Engineering Fracture Mechanics, 1984, **19**(3), pp. 441-448.

107. Saxena, A. and Hudak Jr, S. J., *Review and Extension of Compliance Information for Common Crack Growth Specimens*, International Journal of Fracture, 1978, **14**(5), pp. 453-468.

108. Houssin, B., *Rotation Corrections for Stainless Steel Specimens in the Unloading Compliance Method*, in *Ductile Fracture Test Methods: Proceedings of a CSNI Workshop*, Paris, France, 1983,

109. Richards, C. E., *Some Guidelines to the Selection of Techniques*, The Measurement of Crack Length and Shape During Fracture and Fatigue, C.J. Beevers (Ed.), Engineering Materials and Advisory Services Ltd., 1980, pp. 461-468.

110. Yang, H., Bao, R., Zhang, J., Peng, L. and Fei, B., *Crack Growth Behaviour of a Nickel-Based Powder Metallurgy Superalloy under Elevated Temperature*, International Journal of Fatigue, 2011, **33**(4), pp. 632-641.

111. Hollstein, T. and Voss, B., *Experimental Determination of the High-Temperature Crack Growth Behavior of Incoloy 800H*, Nonlinear Fracture Mechanics: Time-dependent fracture, ASTM STP 995, 1988, **995**, pp. 195.

112. Bensussan, P. L., Jablonski, D. A. and Pelloux, R. M., *A Study of Creep Crack Growth in 2219-T851*, Metallurgical and Materials Transactions A, 1984, **15**(1), pp. 107-120.

113. Dogan, B., Ceyhan, U., Nikbin, K. M., Petrovski, B. and Dean, D. W., *European Code of Practice for Creep Crack Initiation and Growth Testing of Industrially Relevant Specimens*, Journal of ASTM International, 2006, **3**(2), pp. 20.

114. James, M. A. and Newman, J. C., *The Effect of Crack Tunneling on Crack Growth: Experiments and CTOA Analyses*, Engineering Fracture Mechanics, 2003, **70**(3), pp. 457-468.

115. Prij, J., *Some Finite Element Results of CTS Specimen*, in *Ductile Fracture Test Methods: Proceedings of a CSNI Workshop*, Paris, France, pp. 169-180, 1983,

116. De Vries, M. I., *Experimental Aspects of Unloading-Compliance J-Tests*, in *Ductile Fracture Test Methods: Proceedings of a CSNI Workshop*, Paris, France, 1983,

117. Voss, B., *On the Problem of "Negative Crack Growth" and "Load Relaxation" in Single Specimen Partial Unloading Compliance Tests*, in *Ductile Fracture Test Methods: Proceedings of a CSNI Workshop*, Paris, France, 1983,

118. Schwalbe, K. and Setz, W., *R Curve and Fracture Toughness of Thin Sheet Materials*, Journal of Testing and Evaluation, 1981, **9**(4).

119. Sadananda, K. and Shahinian, P., *The Effect of Environment on the Creep Crack Growth Behavior Several Structural Alloys*, Materials Science and Engineering, 1980, **43**(2), pp. 159-168.

120. Bao, R., Yang, H., Zhang, J., Peng, L. and Fei, B., *Fatigue Crack Growth Measurement in a Superalloy at Elevated Temperature*, International Journal of Fatigue, 2013, **47**, pp. 189-195.

121. Cortie, M. B. and Garrett, G. G., *A New Look at an Old Technique for the Measurement of Fatigue Crack-Growth Rates*, Experimental Mechanics, 1989, **29**(3), pp. 291-294.

122. Cegla, F. B., Jarvis, A. J. C. and Davies, J. O., *High Temperature Ultrasonic Crack Monitoring using SH Waves*, NDT & E International, 2011, **44**(8), pp. 669-679.

123. Chmelík, F., Lukáč, P., Janeček, M., Moll, F., Mordike, B. L., Kainer, K. and Langdon, T. G., *An Evaluation of the Creep Characteristics of an AZ91 Magnesium Alloy Composite using Acoustic Emission*, Materials Science and Engineering: A, 2002, **338**(1–2), pp. 1-7.

124. COMSOL Multiphysics v4.3a, COMSOL Ltd., Cambridge, UK.

125. Inco Databook, *Mechanical and Physical Properties of Austenitic Chromium-Nickel Stainless Steel at Ambient Temperatures*, Publication No. 2978, Nickel Development Institute, 1978.

126. Lide, D. R., *CRC Handbook of Chemistry and Physics*, http://www.hbcpnetbase.com/, CRC Press, 2005.

127. Hyde, T. H., Saber, M. and Sun, W., *Testing and Modelling of Creep Crack Growth in Compact Tension Specimens from a P91 Weld at 650°C*, Engineering Fracture Mechanics, 2010, **77**(15), pp. 2946-2957.

128. ASTM E8/E8M-13a, *Standard Test Methods for Tension Testing of Metallic Materials*, ASTM International, West Conshohocken, PA, USA, 2013.

129. ASTM E111-04, *Standard Test Method for Young's Modulus, Tangent Modulus, and Chord Modulus*, ASTM International, West Conshohocken, PA, USA, 2004.

130. ABAQUS v6.13-2, Dassault Systèmes, Vélizy-Villacoublay, France

131. Brünig, M., *Numerical Analysis and Modeling of Large Deformation and Necking Behavior of Tensile Specimens*, Finite Elements in Analysis and Design, 1998, **28**(4), pp. 303-319.

132. Aramis v6.3.0, GOM, Braunschweig, Germany

133. Mills, W. J., *Fracture Toughness of Type 304 and 316 Stainless Steels and their Welds*, International Materials Reviews, 1997, **42**(2), pp. 45-82.

134. Dixon, M. J., *The Reanalysis of AISI 316 Plate and Weld Fracture Toughness Data*, British Energy, E/REP/GEN/0053/00, 2001.

135. Bettinson, A. D., *The Influence of Constraint on the Creep Crack Growth of 316H Stainless Steel*, Ph.D. Thesis, Department of Mechanical Engineering, Imperial College, London, 2001.

136. NIMS, *Creep Datasheet 43A: Datasheet on the Elevated Temperature Properties of 9Cr-1Mo-V-Nb Steel Seemless Pipe for High Temperature Service*, National Institute for Materials Science, 43A, 2014.

137. Panait, C. G., Zielińska-Lipiec, A., Koziel, T., Czyrska-Filemonowicz, A., Gourgues-Lorenzon, A. and Bendick, W., *Evolution of Dislocation Density, Size of Subgrains and MX-Type Precipitates in a P91 Steel During Creep and During Thermal Ageing at 600 C for more than 100,000 h*, Materials Science and Engineering: A, 2010, **527**(16), pp. 4062-4069.

138. Orlova, A., Buršık, J., Kuchařová, K. and Sklenička, V., *Microstructural Development During High Temperature Creep of 9% Cr steel*, Materials Science and Engineering: A, 1998, **245**(1), pp. 39-48.

139. ImageJ v1.48, National Institute of Mental Health, Bethesda, Maryland, USA

140. Mehmanparast, A., *The Influence of Inelastic Damage on Creep, Fatigue and Fracture Toughness*, Ph.D. Thesis, Department of Mechanical Engineering, Imperial College, London, 2012.

141. Davies, C. M., Dean, D. W. and Nikbin, K. M., *The Influence of Compressive Plastic Pre-Strain on the Creep Deformation and Damage Behaviour of 316H Stainless Steel*, in *FESI Conference on Engineering Structural Integrity Assessment 2008*, Manchester, UK, 21-22 October, 2008,

142. Mehmanparast, A., Davies, C. M., Dean, D. W. and Nikbin, K. M., *The Influence of Inelastic Damage on Tensile Deformation and Creep Crack Growth Behaviour of Type 316H Stainless Steel*, in *ASME 2013 Pressure Vessels and Piping Conference*, Paris, France, July 14-18, 2013,

143. Dean, D. W. and Gladwin, D. N., *Creep Crack Incubation and Growth Behaviour of Type 316H Steels*, British Energy Generation Limited, E/REP/BDBB/0040/GEN/03, April, 2004.

144. McLennon, D. R. and Allport, L., *Measurement of Creep Crack Incubation and Creep Crack Growth Rates*, EDF Energy Nuclear Generation Limited, E/REP/BBGB/0047/GEN/09, August, 2013.

145. Coleman, S. L., *An Analysis of Type 316 Stainless Steel Creep Rupture Data*, Nuclear Electric Plc, EPD/GEN/EAN/0038/97, 1997.

146. Davies, C., *Predicting creep crack initiation in austenitic and ferritic steels using the creep toughness parameter and time-dependent failure assessment diagram*, Fatigue & Fracture of Engineering Materials & Structures, 2010, **33**(12), pp. 911-911.